Constitutive Modelling of Branched Polymer Melts in Non-linear Response

David Matthew Hoyle

Department of Applied Mathematics

University of Leeds

Submitted in accordance with the requirements for the degree of

Doctor of Philosophy

September 2010

The candidate confirms that the work submitted is his own, except where work which has formed part of jointly-authored publications has been included. The contribution of the candidate and the other authors to this work has been explicitly indicated overleaf. The appropriate credit has been given where reference has been made to the work of others.

Details of contributions to jointly authored publications:

D. M. Hoyle, O. G. Harlen, D. Auhl and T. C. B. McLeish. Non-linear step strain of branched polymer melts. *Journal of Rheology*, 53(4):917-942, 2009.
I was the lead author with D. Auhl providing experimental data and O. G. Harlen and T. C. B. McLeish providing supervision and feedback. This work forms the basis for chapter 3 of my thesis, where the experimental data was again provided by D. Auhl.

D. G. Hassell, D. Hoyle, D. Auhl, O. Harlen, M. R. Mackley and T. C. B. Mcleish. Effect of branching in cross-slot flow: the formation of W-cusps. *Rheologica Acta*, 48:551-561, 2009.
I was a co-author providing a description of the Pompom theory and flowSolve software. Also I provided the rheological fitting and simulation results. D. G. Hassell was the lead author with D. Auhl providing the rheological data. O. G. Harlen, M. R. Mackley and T. C. B. McLeish provided me and the other co-authors with supervision and feedback on the paper. D. G. Hassell kindly provided the experimental images used in the paper along with extra images and data which are discussed in chapters 5 and 6. The rheological data provided by D. Auhl and my rheological fitting and simulation results do not appear in the thesis as they have been subsequently improved upon.

R. S. Graham, J. Bent, N. Clarke, L. R. Hutchings, R. W. Richards, T. Gough, D. M. Hoyle, O. G. Harlen, I. Grillo, D. Auhl, and T. C. B. McLeish. The long-chain dynamics in a model homopolymer blend under strong flow: small angle neuron scattering and theory. *Soft Matter*, 5:2383-2389, 2009.
For this work I contributed flowSolve simulations and the subsequent streamline analysis for various constitutive models. This work is not reproduced in this thesis.

Acknowledgements

I would like to thank my supervisors Dr. Oliver Harlen and Prof. Tom McLeish for their efforts to help, advise and support me throughout my PhD. Also, I thank Dr. Peter Olmsted for stepping into Tom's role during the latter stages of my studies.

Throughout my PhD, I had the good fortune to be involved with the microscale polymer processing group, μPP^2, and I would like to acknowledge the members of the project for their advice during my PhD. In particular Sung Ho Yoon for many useful discussions and Dr. Richard Graham for involving me in his research.

I had much experimental data provided to me though the μPP^2 project by Dr. Dietmar Auhl, Dr. John Embery, Dr. David Hassell, Dr. Tim Lord and Prof. M. R. Mackley, for which I am very appreciative for all their time and discussion. I was very lucky to receive experimental data from other research groups and I would also like to thank Dr. Vitor Borosso and Prof. Manfred Wilhelm from the Max Plank Institute and Dr. Henrik Rasmussen and Qian Huang from Danmarks Tekniske Universitet.

For helping me understand and use the *flowSolve* software and keeping it running and up to date I would like to thank Dr. Harley Klein and Dr. Tim Nicholson. Similarly for help with *euFlow* I would like to thank Dr. Mark Walkley and Dr. Rosen Tenchev.

Finally, I would like to thank my Mum and Dad and all my family and friends for their encouragement and also, my girlfriend Gemma for her support and efforts in understanding and proofreading my thesis.

The funding for my PhD was provided by the EPSRC, to which I am very grateful for the opportunity to study at Leeds.

Abstract

This thesis is concerned with modelling long chain branched polymer melts using the McLeish and Larson Pompom constitutive equations. Usually the non-linear terms in this model are fitted to uniaxial extensional data due its sensitivity to levels of branching, but in this thesis I will study a number of other non-linear flows using this model. For each flow the results are compared to experiments on a set of polyethylene melts.

The first flow types I examine are simple shear flows. In a shear step-strain flow the stress relaxation of branched polymers is observed to be time-strain separable, whereby the relaxation modulus can be separated into the product of separate functions of time and strain. I show that although the Pompom model is not time-strain separable in general, there exist subsets of parameter values for which time-strain separability is valid. For these sets a branched damping function is derived which is analogous to the Doi-Edwards damping function for linear polymer melts.

The other simple shear flow examined is oscillatory shear. Commonly, oscillatory shear is probed at low strain amplitudes over a range of frequencies to measure the usual dynamic moduli of linear viscoelasticity. In this work the effect of strain amplitude is explored up to absolute strains of order unity. The non-linear stress response is analysed from the higher harmonics in the Fourier series. In particular it is shown that the third Fourier components are dependent on the Pompom non-linear stretch relaxation time and a low-strain asymptote is obtained.

Subsequently, this thesis focuses on the stagnation point flow generated in a cross-slot geometry. The stress calculated from the Pompom constitutive model is compared to experimental flow induced birefringence images. It is shown for linear and lightly branched materials that the Pompom model predicts both the form of the birefringence pattern and stress values obtained from the stress-optical law. However, for more highly branched polymers the Pompom model fails to predict the change to birefringence patterns. Subsequent analysis shows that there could exist a transient overshoot in extension which the Pompom model cannot capture as it stands.

In the final part of my thesis I suggest an empirical alteration to the Pompom constitutive model to capture this transient extensional overshoot, which is able to resolve the differences between experimental flow induced birefringence images and theoretical simulations.

Contents

List of Figures

List of Tables

Chapter 1

Introduction

1.1 Overview

The study of *rheology* is concerned with relating an imposed deformation to a measured mechanical response and is usually focused on a structured or *complex* fluid. The rheology of a fluid is physically attributed to its structure at a microstructural or molecular level. In particular, polymers either in a solution or melt state are highly sensitive to various aspects of the architecture of the molecules. For example, the presence of long branches on a molecule has a dramatic effect on the rheology of a material. Commercial low-density polyethylenes have varied random long chain branching as a result of the synthesis technique used [Tobita (2001)]. When certain mechanical properties are needed, being able to choose the material for a specific purpose is important.

A key aspect to understanding the rheology of polymeric fluids is mathematically modelling and predicting experimentally measured stresses. A *constitutive equation* is used to relate the deformation history to the stress. To fully understand polymer rheology we aim to derive a constitutive equation from microscopic physics and deduce macroscopic conclusions. This is a vital step in a future industrial goal of synthesizing polymers by design.

Although in principle a precise knowledge of molecular structure should give a complete prediction of its rheology [Inkson et al. (2006)], in practice even constitutive equations derived from molecular theory will contain unknown parameters

that must be quantified by fitting the model to experimental data. In a molecular theory these parameters may represent unknown details of the molecular structure. A simple experimental geometry enables many parameter choices to be tested and the optimum values found, however the practicality of these experiments is a major issue and choosing an experiment that is sensitive to each of the unknown parameters is difficult.

For example, a polymer can go through several mechanisms to relax itself of stress by returning to equilibrium after an imposed strain. The polymer is characterised by the corresponding time scales and fitting them from simple experiments can be used to either test the theory or for predicting more complex flow situations.

During a typical industrial process a fluid can experience a complex strain history at high rates of deformation. Capturing the simple behaviour of a material in non-linear response is essential for modelling complex flows accurately.

In my thesis I test and build upon a generation of constitutive theories in a series of simple and complex geometries. In particular I concentrate on the level of branching in a material, as parameterising this correctly is critical in modelling non-linear flows. For each geometry the theory is compared to experimental results and is examined to see how a certain parameter set can infer the molecular structure of a material. This chapter gives an overview of polymer processing on the macroscopic level and then constitutive equations are derived from the microscopic level. Subsequent chapters detail material characterising and examine various geometries in detail.

1.2 Processing of polymer melts

Polymers commonly occur in many industrial and consumable products. They are widely used due to their versatility in being manufactured for a precise purpose, with a choice of polymer leading to differing mechanical properties. The most popular choice of polymer in industry is the thermoplastic polyethylene, with over 20 million metric tons of low density polyethylene forecast for production in Europe by 2012 [Petro-Polymers (2009)].

Polyethylenes can be produced in different ways. Each synthesis method

makes molecules with specific characteristics that define its mechanical properties. One example of an important mechanical property is strain hardening, where the apparent extensional viscosity increases with applied strain rate [c.f. section 1.5]. Polyethylenes can contain varying quantities of long chain branching (LCB) depending on the synthesis route and the consequence of LCB is the amount of strain hardening observed for a particular material.

Low density polyethylene (LDPE) is produced using high pressure polymerisation. This method produces many random long chain branches (LCB) on a molecule which inhibits crystallisation. The LCB also have a dramatic effect on the melt processing properties as they give rise to a high degree of strain hardening in flows with an extensional component. This strain hardening property is beneficial in stabilising processing flows such as film blowing or film casting, but the resulting amorphous material has relatively low mechanical strength.

High density polyethylene (HDPE), produced for example by Ziegler-Natta polymerisation, has a high level of crystallinity due to the molecules being linear, i.e. having no branches. In HDPE this gives more desirable solid state properties, such as stronger tensile strength. However, the lack of strain hardening makes its processing more difficult.

Linear low density polyethylene (LLDPE) was seen as a compromise between LDPE and HDPE, containing short branches attached to linear backbones. However LDPE remains the more popular choice of material due to its superior processing properties.

Metallocene catalysis of polyethylene is an emerging synthesis technique that produces HDPEs that contain some LCB. The synthesis process of these LCB-HDPE can be controlled very accurately giving choice over molecular structure. Das et al. (2006) used Monte-Carlo simulations to model the synthesis process and predict the linear rheology of several varieties of linear and branched metallocene HDPEs.

A general overview on production methods and mechanical properties of polyethylene can be found in Peacock (2000), for example. Further discussions on synthesis methods with respect to rheology can be found in chapter 2.

The production of many products is cheap on a mass scale, however the initial machine setup cost is high meaning it is crucial that the production process

is understood. It is potentially cheaper to change the polymer used than the machine setup.

A non-Newtonian stress response to strains imposed during processing can be 'remembered' by a fluid and frozen into a solid sate. These stresses relax over long time scales and can cause the final product to warp.

Typically in industry, a range of polymers are synthesised and are characterised in both linear and non-linear response. Using a constitutive equation a multi-dimensional flow simulation can be made of a production process and the best polymer candidate can be chosen to meet required specifications. Much attention has been focused in the area of modelling synthesis of a polymer. An overall goal is to reverse the 'design arrow' and synthesise a polymer that meets a preconceived specification. This means instead of picking from a range of available polymers, the required mechanical properties of a material for a process can be identified with the use of constitutive modelling and flow simulations and then any inferred molecular detail can be synthesised with the use of modelled reaction chemistry. This has been one of the philosophies of the research group I have been involved in during my PhD; the micro-scale polymer processing (μPP^2) project, www.mupp2.co.uk (2010).

An example of how molecular structure affects processing techniques is illustrated with the film casting process. Here a polymer melt is extruded through a die and is taken up onto a chilled roll, which pulls the polymer at a faster rate than it is being extruded.

In figure 1.1 gel permeation chromatography (GPC) and multi-angle laser light scattering (MALLS) experiments are used to show molecular differences between LCB-HDPE and LDPE. The GPC experiments elute the various volumes of polymer chain in a material and light scattering is used to measure the molecular weight of each elution volume. Also, measuring the radius of gyration provides information on the branching number, b_n, which corresponding to branches per thousand monomer. The GPC experiments show that the LDPE has a much broader molecular weight distribution than LCB-HDPE and also that the LDPE is significantly more branched than the LCB-HDPE. Further details of GCP-MALLS are discussed in chapter 2.

The contrast between these two materials is also seen in the processing during

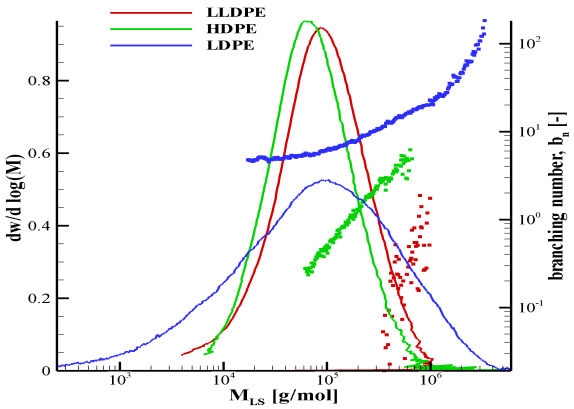

Figure 1.1: An example of GPC-MALLS, showing the contrasting structures of a linear HDPE, a lightly branched HDPE and a branched LDPE.

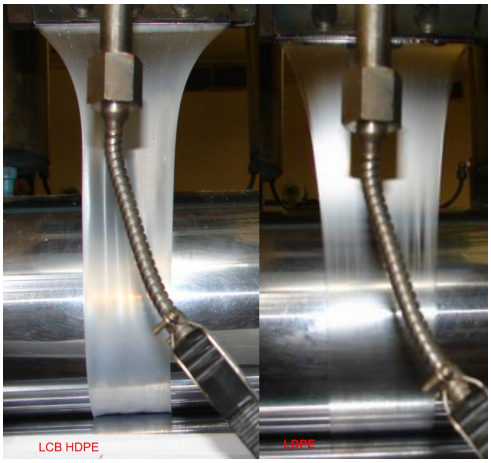

Figure 1.2: An example of the film casting process, in which a polymer melt is extruded through a die and is taken up, frozen, on a drum. The difference in the molecular structure between a LCB-HDPE (left) and a LDPE (right) affects the profile of the draw-ratio.

the film casting process. The molecular structure of the polymer affects the draw-ratio profile, giving a different shape of film between the die and roll, and differing film widths on the roll for equivalent draw speeds, seen in figure 1.2 [Auhl et al. (2008)].

The film casting process has a complex deformation history involving shear flow on the walls of the die, uniaxial extension in the centre of the film and

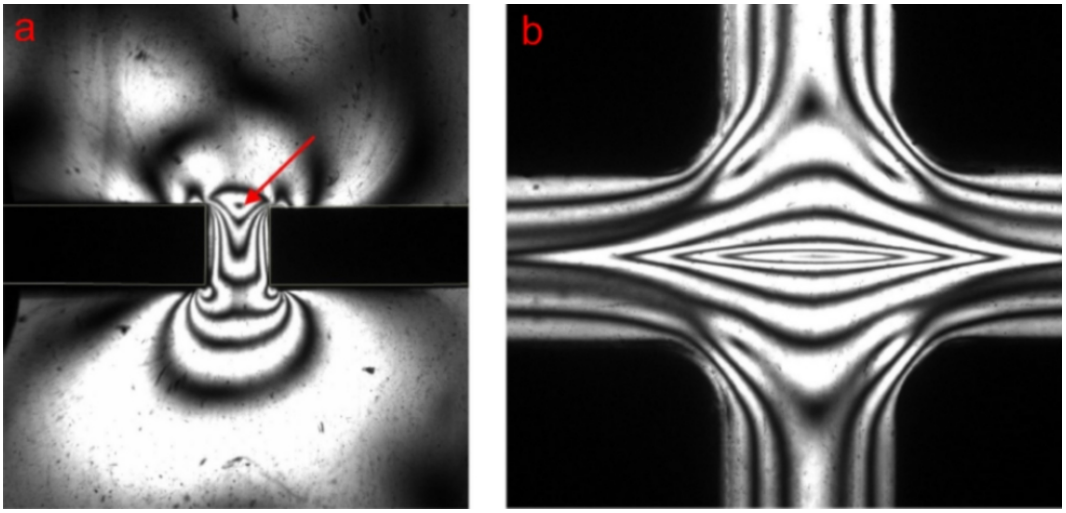

Figure 1.3: Birefringence patterns showing contours of constant principal stress difference for two complex geometries. On the left is a contraction expansion geometry and on the right a cross-slot geometry. The red arrow in figure (a) highlights the zero stress eye.

planar extension at the film edges. This requires a full 3D simulation to capture the cross-section shape of the film in free surface flow. This is a difficult and a computationally expensive simulation as there is only a 2D approximation when the aspect ratio of the film is large [Zheng et al. (2006)].

To test constitutive equations in complex flow situations an idealised geometry is used. Historically much attention has been focused on contraction-expansion and stagnation point flows. Figure 1.3 shows the flow induced birefringence (FIB) patterns of a LCB-HDPE in both contraction-expansion and cross-slot geometries. The advantage of designing an idealised geometry is the opportunity to incorporate flow measurements. FIB uses polarized light to create contour patterns of principal stress difference [c.f. chapter 5]; this method does not interact with the material and gives a non-invasive way to test constitutive theories. Furthermore, to investigate localised detail on the flow, such as orientation or velocity, techniques such as small angle neutron scattering (SANS) [Graham et al. (2009)] or laser Doppler velocimetry (LDV) can be used.

In my thesis I examine the characterisation of polymer melts to see if molecular detail can be captured by a constitutive equation. I also check the performance

of the Pompom class of constitutive equations [c.f. section 1.6.5] in complex flow geometries, not only to test the constitutive theory but also to see what macroscopic FIB can infer about molecular detail. In particular I focus on the non-linear parameters that represent branching in a material.

1.3 Continuum Mechanics

Although the flow properties of a material are governed by the molecular scale physics, in describing the large scale motion it is useful to consider the melt as a continuum in which intermolecular forces are represented by a macroscopic stress. The melt is considered a continuum medium with density, ρ, and velocity, $\underline{u}(\underline{x}, t)$.

1.3.1 Governing Equations of Fluid Motion

A fundamental principle in fluid dynamics is the *conservation of mass*. This comes from the very basic assumption that mass in a closed system is constant at all times. By matching the flux of mass into local volumes with the resulting change in density the *continuity equation* is derived as,

$$\frac{\partial \rho}{\partial t} + \nabla.(\rho \underline{u}) = 0. \tag{1.3.1}$$

Using the Lagrangian derivative, $\frac{D}{Dt} \equiv \frac{\partial}{\partial t} + \underline{u} \cdot \nabla$, equation 1.3.1 can be rewritten by expanding $\nabla.(\rho \underline{u})$ to give,

$$\frac{D\rho}{Dt} + \rho \nabla.\underline{u} = 0, \tag{1.3.2}$$

where ρ is the density of the fluid and $\underline{u}$ is the fluid velocity. For a constant density, ρ, that does not vary with either position or time,

$$\frac{D\rho}{Dt} = \frac{\partial \rho}{\partial t} + \underline{u}\, \nabla.\, \rho = 0,$$

and hence,

$$\nabla \,.\, \underline{u} = 0. \tag{1.3.3}$$

A fluid that satisfies this equation is called *incompressible*.

A second continuum equation is derived from Newton's second law of motion, the *conservation of momentum*. To derive an equation for the motion of the fluid, the forces changing the momentum of the fluid and any types of momentum flow due to boundary fluxes are accounted for. The rate of decrease of momentum in an arbitrary volume V is given by,

$$\text{(rate of decrease of momentum)} = -\int_V \frac{\partial(\rho \underline{u})}{\partial t} dV. \tag{1.3.4}$$

Momentum flow is given by advection out of V through its surface S, due to a velocity vector $\underline{u}$. Momentum of the fluid is the product of its mass and velocity, and hence the momentum flux, C_M, is given by,

$$C_M = \int_S \hat{n} \,.\, (\rho \underline{u})\, \underline{u}\, dS.$$

An equation for net rate of outward flow of momentum from V due to a flux through S is thus obtained using the divergence theorem,

$$C_M = \int_V \nabla.(\rho \underline{u}\ \underline{u})\, dV. \tag{1.3.5}$$

External body forces such as gravitational acceleration are also accounted for. The force of gravity is a product of the mass and the constant gravitational acceleration, $\underline{g}$, giving,

$$\text{(body forces on V)} = \int_V \rho \underline{g}\, dV. \tag{1.3.6}$$

Finally, we have the effect of intermolecular forces. These appear as surface forces acting on the boundary,

$$\underline{f} = f_i \hat{e}_i = \text{(stress on dS)} dS,$$

where $\underline{f}$ is the surface force density and f_i is the component of the force in the $\hat{e}_i$ direction.

The surface element $\underline{\hat{n}}dS$ over which this force acts can be be split up into component form. So defining $\tau_{ij} =$ (the stress on the i^{th} plane in the j^{th} direction), then for an elemental surface area dS,

$$\begin{aligned} f_1\, dS &= dS\, \hat{n}\,.\,(\hat{e}_1\tau_{11} + \hat{e}_2\tau_{21} + \hat{e}_3\tau_{31}), \\ f_2\, dS &= dS\, \hat{n}\,.\,(\hat{e}_1\tau_{12} + \hat{e}_2\tau_{22} + \hat{e}_3\tau_{32}), \\ f_3\, dS &= dS\, \hat{n}\,.\,(\hat{e}_1\tau_{13} + \hat{e}_2\tau_{23} + \hat{e}_3\tau_{33}). \end{aligned} \tag{1.3.7}$$

Combining all these elements together and defining the second rank stress tensor, $\underline{\underline{\tau}}$, as,

$$\underline{\underline{\tau}} = \begin{pmatrix} \tau_{11} & \tau_{12} & \tau_{13} \\ \tau_{21} & \tau_{22} & \tau_{23} \\ \tau_{31} & \tau_{32} & \tau_{33} \end{pmatrix},$$

the surface force density due to stress acting on an element of fluid is,

$$\underline{f}\, dS = dS\, \hat{n}\,.\,\underline{\underline{\tau}}. \tag{1.3.8}$$

With use of the divergence theorem, the net molecular force acting on V is,

$$\underline{f}_M = \int_V \nabla\,.\,\underline{\underline{\tau}}\, dV. \tag{1.3.9}$$

Equating the rate of decrease of momentum with the outward flux of momentum and the forces acting on the fluid, using equations (1.3.4), (1.3.5), (1.3.6) & (1.3.9) we obtain,

$$\int_V \frac{\partial(\rho\underline{u})}{\partial t}\, dV = -\int_V \nabla.(\rho\underline{u}\,\underline{u})\, dV + \int_V \nabla.\underline{\underline{\tau}}\, dV + \int_V \rho\underline{g}\, dV.$$

Eliminating the integration over the arbitrary volume, V,

$$\frac{\partial(\rho\underline{u})}{\partial t} = -\nabla.(\rho\underline{u}\,\underline{u}) + \nabla.\underline{\underline{\tau}} + \rho\underline{g}. \tag{1.3.10}$$

Using the conservation of mass equation we have the *general equation of mo-*

tion,

$$\rho \frac{D\underline{u}}{Dt} = -\nabla \cdot \underline{\underline{\tau}} + \rho \underline{g}. \tag{1.3.11}$$

For an incompressible fluid there is an isotropic component of the stress required to maintain, $\nabla \cdot \underline{u}$, and consequently the stress tensor is usually expressed as the sum of the *extra stress tensor*, $\underline{\underline{\sigma}}$, and the isotropic pressure of the fluid. The extra stress tensor is the stress caused by the deformation of the fluid,

$$\underline{\underline{\sigma}} = \underline{\underline{\tau}} - p\underline{\underline{I}}. \tag{1.3.12}$$

The equation that defines $\underline{\underline{\sigma}}$ is know as the *Stress Constitutive Equation*. It is dependent on kinematic effects of velocity, strain and their derivatives.

For Newtonian fluids the extra stress is traceless. However, in many non-Newtonian fluid constitutive models the extra stress has non-zero trace so the division between the extra stress and the isotropic stress is arbitrary.

1.3.2 Deformation Kinematics

In order to derive a constitutive equation for the extra stress tensor of non-Newtonian fluids the deformation history must be known. This local rate of deformation is found from gradients of the velocity field, $\underline{u}(\underline{r}, t)$, and is called the velocity gradient tensor, or deformation rate tensor,

$$\underline{\underline{K}}(\underline{r}, t) = \left(\bigtriangledown \underline{u}(\underline{r}, t)\right)^T. \tag{1.3.13}$$

However, only the symmetric part of equation (1.3.13) represents deformation, as the antisymmetric part represents the vorticity. The symmetric part is called the strain rate tensor,

$$\underline{\underline{D}} = \frac{1}{2}\left(\underline{\underline{K}} + \underline{\underline{K}}^T\right). \tag{1.3.14}$$

The velocity gradient only gives information about the current rate of deformation. In order to measure the deformation history it is necessary to find the accumulated deformation. The deformation gradient tensor maps the deforma-

tion from coordinates $\underline{r}$ to $\underline{r}'$ in a time $t' - t$,

$$\underline{r}(t) = \underline{\underline{E}}(t', t) \cdot \underline{r}'(t'). \tag{1.3.15}$$

If the velocity gradient tensor, $\underline{\underline{K}}$, is independent of position, $\underline{r}$, then the flow is zero dimensional and is classified as a *simple flow*. In this case the deformation gradient tensor is related to the velocity gradient tensor by,

$$\frac{\partial \underline{\underline{E}}(t', t)}{\partial t} = \underline{\underline{K}} \cdot \underline{\underline{E}}(t', t), \tag{1.3.16}$$

while in general,

$$\frac{D\underline{\underline{E}}(t', t)}{Dt} = \underline{\underline{K}} \cdot \underline{\underline{E}}(t', t), \tag{1.3.17}$$

where $\frac{D}{Dt} = \frac{\partial}{\partial t} + \underline{u} \cdot \nabla$ is the Lagrangian time derivative.

Equation (1.3.16) can be integrated,

$$\underline{\underline{E}}(t', t) = exp\left[\int_{t'}^{t} dt'' \underline{\underline{K}}(\underline{r}'', t'')\right], \tag{1.3.18}$$

where the exponential of a matrix is defined as,

$$e^{\underline{\underline{A}}} = \underline{\underline{I}} + \sum_{n} \frac{\underline{\underline{A}}^n}{n!}. \tag{1.3.19}$$

The principle of frame invariance says that a solid body rotation should not cause a stress response and as with the velocity gradient tensor, $\underline{\underline{K}}$, the deformation gradient tensor, $\underline{\underline{E}}$, contains the effects of both deformation and solid body rotation. Therefore, instead of examining stress response with respect to the deformation gradient it is often more convenient to consider the rotationally invariant *Finger tensor*,

$$\underline{\underline{B}}(t, t') = \underline{\underline{E}}(t', t) \cdot \underline{\underline{E}}^T(t', t), \tag{1.3.20}$$

and its inverse, the *Cauchy tensor*,

$$\underline{\underline{C}}(t, t') = \underline{\underline{B}}^{-1}(t, t'). \tag{1.3.21}$$

1.3.3 Examples

To demonstrate the difference between purely viscous fluids, elastic solids and viscoelastic fluids we consider simple constitutive equations for each.

The stress in a Newtonian fluid is linear in strain rate so that conventionally,

$$\underline{\underline{\sigma}}^N = 2\mu \underline{\underline{D}}, \tag{1.3.22}$$

where μ is the viscosity of the fluid.

In contrast the stress in an incompressible hyper-elastic rubber depends only on the deformation from its equilibrium,

$$\underline{\underline{\sigma}}^R = G \underline{\underline{B}}, \tag{1.3.23}$$

where G is the shear modulus.

Under a simple shear deformation the xy components of equations 1.3.22 and 1.3.23 reduce to

$$\frac{1}{\mu}\sigma^N_{xy} = \dot{\gamma} \qquad \text{and} \qquad \frac{1}{G}\frac{d\sigma^R_{xy}}{dt} = \dot{\gamma}. \tag{1.3.24}$$

Adding the two parts in equation 1.3.24 provides a combination of viscous and elastic stress. This is called a Maxwell viscoelastic model which is defined as,

$$\frac{d\varepsilon}{dt} = \frac{\sigma^M}{\mu} + \frac{1}{G}\frac{d\sigma^M}{dt}, \tag{1.3.25}$$

where ε is the total strain experienced by the fluid. The general solution in shear given given by,

$$\sigma^M_{xy} = G\int_0^t dt' \dot{\gamma}(t') e^{\frac{1}{\tau}(t'-t)}, \tag{1.3.26}$$

where $\tau \equiv \frac{\mu}{G}$ is defined as a characteristic relaxation time of the viscoelastic stress.

Two simple shear flows, an instantaneous shear step-strain and a constant shear rate flow, characterize the distinction between the three models.

In the case of the shear step-strain, an instantaneous deformation, of size γ_0, is applied at $t = 0$s, giving a shear rate of $\dot{\gamma} = \gamma_0\delta(t)$. The subsequent stress response is shown in figure 1.4. For a Newtonian fluid the stress is proportional

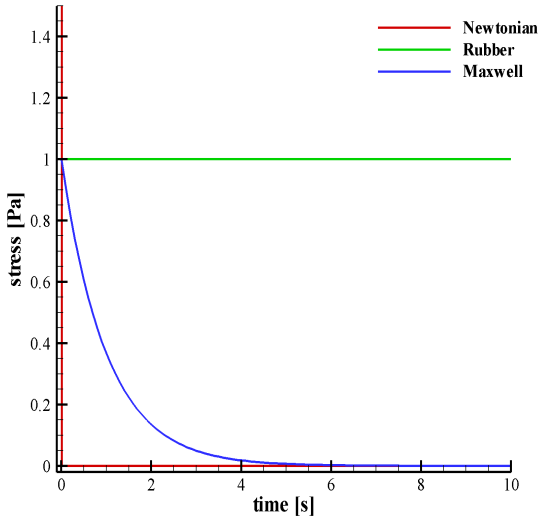

Figure 1.4: Relaxation of the shear stress after a shear step strain, for a Newtonian fluid, elastic rubber and a viscoelastic fluid.

to the applied shear rate, stress only exists at $t = 0$s and is of size $\mu\gamma_0\delta(t)$. For a hyper-elastic rubber solid the stress is proportional to the total strain applied, $\int \gamma_0\delta(t) = \gamma_0$. Hence, the stress is permanently remembered. The viscoelastic Maxwell model shows the cross-over between elastic and viscous behaviour. At early timescales the model behaves like the elastic solid. The stress decays away with characteristic timescale, $\tau = \frac{\mu}{G}$, to the viscous regime of having no memory of the stress.

For a shear flow, a constant shear rate, $\dot{\gamma} = \dot{\gamma}_0$, is applied for $t > 0$s. The stress response for constant shear rate flow can be seen in figure 1.5. The Newtonian fluid has a constant viscosity and hence constant stress, for all time. The hyper-elastic rubber has stress proportional to the total applied strain, $\dot{\gamma}_0 t$, which is linear in time. Hence the stress is linear in time with a slope of gradient, $\dot{\gamma}_0 G$. The viscoelastic Maxwell model displays a cross-over between the two regimes. The stress develops linearly with gradient $\dot{\gamma}_0 G$, at early timescales and plateaus to a constant stress, $\dot{\gamma}_0\mu$, at steady state.

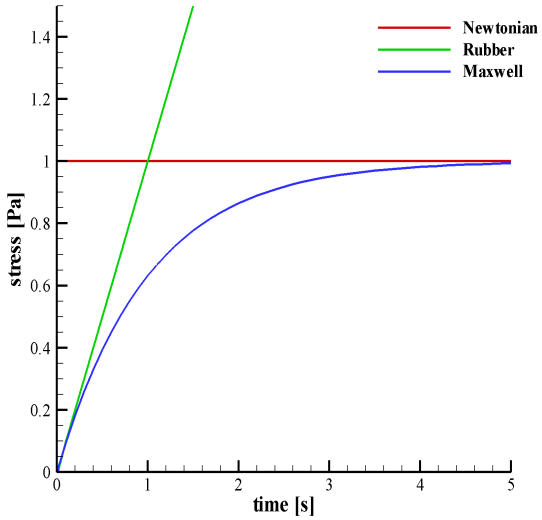

Figure 1.5: Transient shear stress, $\sigma_{xy}(t)$, for a Newtonian fluid, elastic rubber and a viscoelastic fluid.

1.4 Rheology

To test and characterise constitutive equations various simple, zero dimensional flows are commonly used. I will use these flows in chapter 2 to fit non-linear parameters to various polyethylene samples that are tested and modelled in subsequent chapters for other geometries. The three flows most commonly used are simple shear, uniaxial extension and planar extension. The velocity gradient tensors, $\underline{\underline{K}}$ and deformation gradient tensors, $\underline{\underline{E}}$ are detailed in table 1.1.

Rather than plotting the stress for various deformation rates, the stress is commonly normalised by the deformation rate to define a (time dependent) *viscosity* for each flow more properly termed *stress growth coefficients*,

$$\text{shear viscosity} \qquad \mu_S = \frac{\sigma_{xy}}{\dot{\gamma}}, \tag{1.4.1}$$

$$\text{uniaxial extensional viscosity} \qquad \mu_E = \frac{\sigma_{zz}-\sigma_{xx}}{\dot{\varepsilon}}, \tag{1.4.2}$$

$$\text{planar extensional viscosity} \qquad \mu_P = \frac{\sigma_{xx}-\sigma_{yy}}{\varepsilon}. \tag{1.4.3}$$

Flow type	Velocity gradient, $\underline{\underline{K}}$	Deformation gradient, $\underline{\underline{E}}$
Simple Shear	$\begin{pmatrix} 0 & \dot{\gamma} & 0 \\ 0 & 0 & 0 \\ 0 & 0 & 0 \end{pmatrix}$	$\begin{pmatrix} 1 & \gamma & 0 \\ 0 & 1 & 0 \\ 0 & 0 & 1 \end{pmatrix}$
Uniaxial Extension	$\begin{pmatrix} -\dot{\varepsilon}/2 & 0 & 0 \\ 0 & -\dot{\varepsilon}/2 & 0 \\ 0 & 0 & \dot{\varepsilon} \end{pmatrix}$	$\begin{pmatrix} e^{-\varepsilon/2} & 0 & 0 \\ 0 & e^{-\varepsilon/2} & 0 \\ 0 & 0 & e^{\varepsilon} \end{pmatrix}$
Planar Extension	$\begin{pmatrix} \dot{\varepsilon} & 0 & 0 \\ 0 & -\dot{\varepsilon} & 0 \\ 0 & 0 & 0 \end{pmatrix}$	$\begin{pmatrix} e^{\varepsilon} & 0 & 0 \\ 0 & e^{-\varepsilon} & 0 \\ 0 & 0 & 1 \end{pmatrix}$

Table 1.1: Flow tensors for zero dimensional simple flows. For each flow $\dot{\gamma}$ and $\dot{\varepsilon}$ are the deformation rates, with γ and ε representing the strains.

1.4.1 Linear Viscoelasticity

To measure and fit the linear Maxwell parameters, $\{G, \tau\}$, linearly oscillatory shear is often used. To capture the rheology of a polymer melt a set of Maxwell parameters, $\{G_i, \tau_i\}$, called a linear spectrum is required,

$$G(t) = \Sigma_i G_i e^{-\frac{t}{\tau_i}}. \tag{1.4.4}$$

The characteristic relaxation time for a linear Maxwell spectrum is defined as,

$$\bar{\tau} = \frac{\Sigma_i G_i \tau_i^2}{\Sigma_i G_i \tau_i}. \tag{1.4.5}$$

At small shear amplitude, oscillatory shear measurements are considered easier and more reliable than step-strain measurements. Provided the amplitude is small enough [c.f. 4 on large amplitude oscillatory shear] the measurements are far away from any non-linear response, unlike low-strain transient shear or extension. For a small amplitude oscillatory shear, the stress can be assumed to be linear in the symmetric velocity gradient, $\underline{\underline{D}}$, and linear response theory can be used,

$$\underline{\underline{\sigma}} = \int_{-\infty}^{\infty} dt' 2G(t', t)\underline{\underline{D}}(t'), \tag{1.4.6}$$

where $G(t', t)$ is the response function. Assuming that the material properties

are independent of time and integrating over the deformation history gives,

$$\underline{\underline{\sigma}} = \int_{-\infty}^{t} dt' 2G(t'-t)\underline{\underline{D}}(t'). \tag{1.4.7}$$

Equation 1.4.7 is known as Boltzmann's constitutive equation.

Under oscillatory shear the velocity gradient can be written in complex variables,

$$D_{12} = i\omega e^{i\omega t}, \tag{1.4.8}$$

which gives a shear stress of,

$$\sigma_{xy} = i\omega\gamma(t)\int_{0}^{\infty} dsG(s)e^{-i\omega s}, \tag{1.4.9}$$

where the variable of integration has been changed, $s = t - t'$.

This can be rewritten as,

$$\sigma_{xy} = \gamma(t)G^*(\omega), \tag{1.4.10}$$

where $G^*(\omega)$ is defined as the complex modulus,

$$G^*(\omega) = i\omega\int_{0}^{\infty} e^{i\omega t}G(t)dt. \tag{1.4.11}$$

The complex modulus can be split into real and imaginary parts, $G^* = G' + iG''$. The first term, G', describes stress that is in phase with the shear and is associated with elastic stress. The second term, G'' describes stress which is out of phase with the shear and is associated with viscous stresses. Here, G' is called the storage modulus and G'' is called the loss modulus. The storage and loss modulus are together termed the *dynamic moduli*.

For a Newtonian fluid, equation 1.3.22, $G' = 0$ and $G'' = \omega\mu_S$ and for a rubber solid, equation 1.3.23, $G' = G$ and $G'' = 0$. If we substitute, $\dot{\gamma} = i\omega e^{i\omega t}$ into the general solution for a Maxwell fluid, equation 1.3.26, we get a general solution of the form,

$$\sigma_{xy} = i\omega G e^{-\frac{t}{\tau}}\int_{-\infty}^{t} dt' e^{i\omega t'}e^{\frac{t'}{\tau}}, \tag{1.4.12}$$

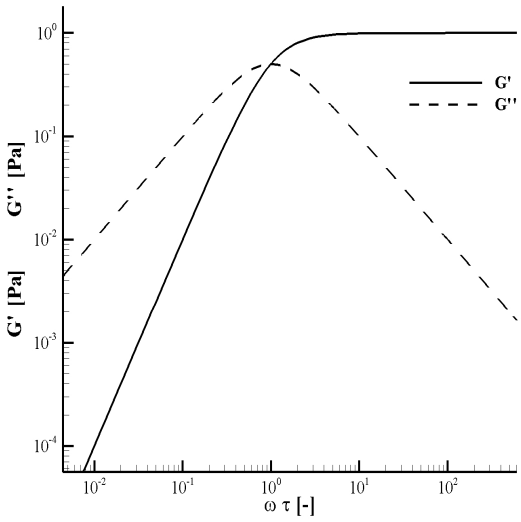

Figure 1.6: The dynamic moduli for a single Maxwell mode.

solving and taking real and imaginary parts gives the storage and loss moduli for a Maxwell fluid as,

$$G' = G\frac{\omega^2\tau^2}{1+\omega^2\tau^2}, \qquad G'' = G\frac{\omega\tau}{1+\omega^2\tau^2}. \tag{1.4.13}$$

Figure 1.6 shows the storage and loss moduli for a single Maxwell mode. For low frequencies the stress is predominantly viscous and the stress is predominantly elastic for high frequencies.

The cross-over frequency when, $G' = G''$, occurs when $\omega\tau = 1$ signifying the characteristic relaxation for this Maxwell mode. In a general fluid the reciprocal cross-over frequency identifies a characteristic relaxation time scale.

For oscillatory shear a dimensionless *Deborah number* can be defined to describe the degree of non-linearity of the strain experienced by the material. Letting, $De = \omega\tau$, shows that $De \ll 1$ gives a viscous response and $De \gg 1$ gives an elastic response. Oscillatory shear is performed at some amplitude, γ_0, and an oscillatory shear Weissenberg number can be defined as $W_i = \gamma_0\omega\tau$. This describes the validity of the linear stress response assumption (equation 1.4.6) and for this assumption to hold true, $W_i \ll 1$. In chapter 4, numerical simulations in

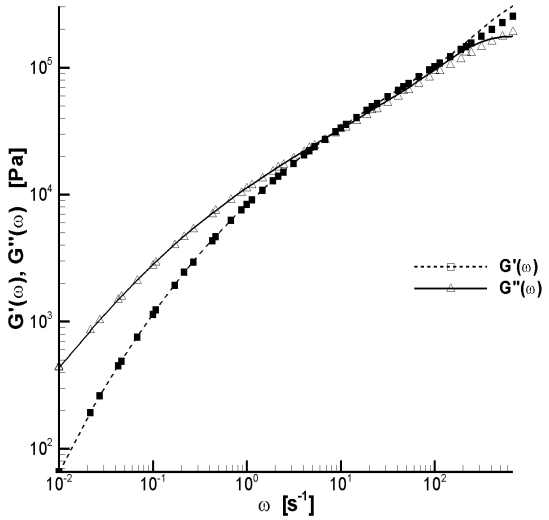

Figure 1.7: Linear Maxwell spectrum for a branched metallocene HDPE, HDB6, is fitted to experimental data.

the case of $W_i \gg 1$ show deviations from linear stress response.

A set of 12 Maxwell modes is fitted to experimental data in figure 1.7, for a branched metallocene catalysed HDPE called HDB6. Fitting was done using RepTate software [Ramirez and Likhtman (2007)] and details are given in chapter 2. For HDB6 in figure 1.7 the average relaxation time, $\bar{\tau} \sim 28s$.

1.5 Branched polymers

One important aspect of characterising a polymeric fluid is to quantify the level of LCB on molecules. The branching on a molecule is randomly distributed and is characterised by the branching number, b_n, which the number of branches per thousand carbon atoms. The amount of LCB is partly a result of the method of synthesis. The LDPEs used in this study were formed using free radical polymerisation which produces more LCB than the metallocene catalysed HDPEs and LLDPEs studies here [c.f. figure 1.1]. There are flow phenomena that arise due to branching in the simple flows defined in section 1.4. Here the difference between linear and branched materials is shown.

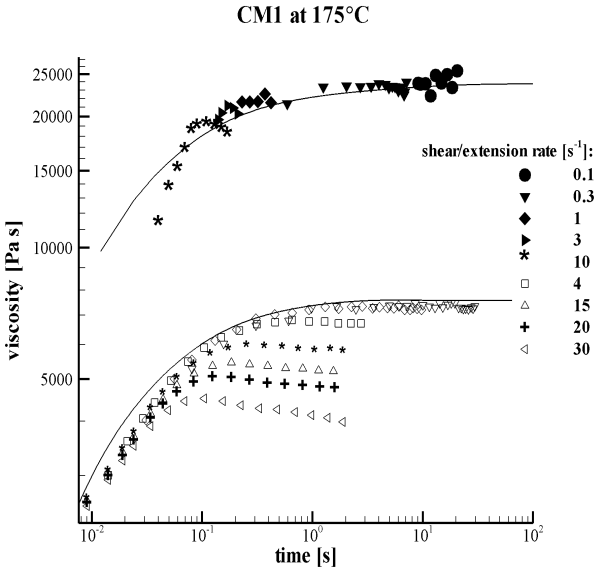

Figure 1.8: Shear viscosity data and uniaxial extensional viscosity data for a linear LDPE called CM1. The data shows non-linear thinning response in shear and in extension the stress response transitions from linear to a strain softening regime.

For both simple shear and extensional flow the stress response can be characterised by a Deborah number (which is the same as the Weissenberg number for simple transient flows). The Deborah number for each flow is the product of the deformation rate and the average relaxation time of the fluid. Linear flow behaviour is defined for each simple flow as the Deborah number, $De \ll 1$.

For Newtonian fluids the ratio between shear and extensional viscosity defined in section 1.4 is constant and is $\frac{\mu_e}{\mu_s} = 3$ for uniaxial extension and $\frac{\mu_p}{\mu_s} = 4$ for planar extension. For both linear and branched materials, the transient viscosity with Deborah number, $De \ll 1$, have the same viscosity ratios (see figures 1.8 and 1.9 for shear and uniaxial linear flow).

For simple shear flow both linear and branched materials show qualitatively the same non-linear response, i.e. when $De \gg 1$. For high enough shear rates, the non-linear steady state shear viscosity is lower than the linear shear viscosity. This is called shear thinning.

For extensional flow there is a dramatic difference between linear and LCB

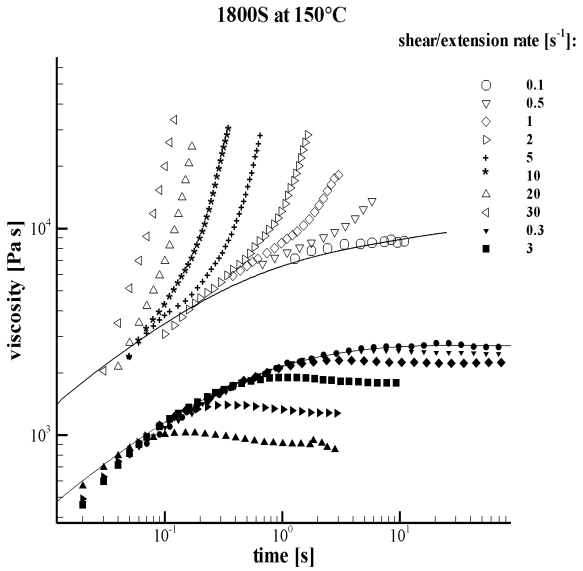

Figure 1.9: Shear viscosity data and uniaxial extensional viscosity data for a LCB LDPE called 1800S. For non-linear shear the viscosity thins but in non-linear extension we get strain hardening.

materials. In figure 1.8 uniaxial viscosity data is plotted against time for a linear LDPE called CM1. The data falls onto $3\mu_s(t)$ for all extension rates except the highest extension rate of of 10s^{-1} where the extensional viscosity falls below the linear reference. This is the opposite effect to strain hardening and is known as *strain softening*.

In figure 1.9 the transient extensional viscosity is plotted for a LCB LDPE, 1800S. For the smallest strain rate, $\varepsilon = 0.1\text{s}^{-1}$, the viscosity agrees with the relation, $\mu_e = 3\mu_s$, and has a linear deformation. For all the higher strain rates the viscosity grows above the linear flow prediction and this is called strain hardening. Notice that for each of the higher strain rates no steady state plateau is reached experimentally. It remains a challenge to ascertain the extensional steady state viscosity, although in chapter 5 the cross-slot geometry is used to determine this steady state. Non-linear rheology can also be studied in oscillatory flow if the amplitude of motion is large. In section 1.4.1 the Weissenberg number for oscillatory shear was defined as $W_i = \gamma_0\omega\tau$, where γ_0 is the amplitude of motion at a frequency of ω and τ is some characteristic time scale. This time scale is

determined by taking the viscosity average of the orientation relaxation time (c.f. 1.4.1) and so for a given frequency the amplitude can be made large enough to examine non-linearity.

1.6 Molecularly derived constitutive model

In order to explain the differences described above it is necessary to account for the stress that arises in melts of polymers with differing branching structure. This requires a constitutive model for the stress that takes account of the microscopic physics. These theories can be tested against materials with a predefined molecular structure.

In this section we discuss the molecular theory used to derive a constitutive model for branched polymers. The theories discussed in this thesis are based on the ideas of statistical mechanics where thermal averaging is considered over local conformations of polymer chains in melts. Many of the established principles covered here are reviewed in full in such books as Bird et al. (1977a,b); Doi (1995); Doi and Edwards (1986); Huilgol and Phan-Thien (1997); Phan-Thien (2002); Rubinstein and Colby (2003).

1.6.1 Gaussian Chains

Polymer molecules are composed of long chains of repeated sub-units, linked together. As a consequence of the rotational flexibility of these links the orientation correlation between neighboring units in flexible polymers such as polyethylene, decays over a small number of units. This decay length is called the persistence length ($1p \sim 6\dot{A}$) and is equal to roughly four $C-C$ bonds in polyethylene so that on length scales larger than $1p$ the polymer chain may be modelled as a free-jointed chain.

Consider a polymer made up of N freely jointed sections of length, b. Each section points in a random direction so that the distribution is isotropic. This is a random walk model, with the orientation of each section having no correlation.

This gives the mean polymer, end to end vector,

$$\langle \underline{R} \rangle = 0. \tag{1.6.1}$$

The average length of an unstretched polymer is given by [e.g. Doi and Edwards (1986)],

$$\left\langle \underline{R}^2 \right\rangle = Nb^2 \tag{1.6.2}$$

For a molecule of N segments, the end to end vector is characterised by its probability density function, $P(\underline{R}; N)$, which is the probability of an N-segment polymer having end to end vector, $\underline{R}$. Provided that N is large and $R^2 \ll N^2 b^2$ the probability density function can be approximated by a Gaussian distribution [e.g. Doi and Edwards (1986)],

$$P(\underline{R}; N) = \left(\frac{3}{2\pi N b^2} \right)^{\frac{3}{2}} \exp\left(-\frac{3\underline{R}^2}{2Nb^2} \right). \tag{1.6.3}$$

Note that the end to end vector has a maximum length of Nb, whereas the Gaussian probability is still non-zero for end to end vectors larger than the maximum. For large N, the probability of reaching this state is small, however, in extension there does exist a coil-stretch transition where the deformation-rate will be large enough to stretch a Gaussian chain beyond the maximum length. In this case it is necessary to take account of the non-Gaussian nature of the distribution [c.f. Bird et al. (1977a); Chilcott and Rallison (1988); Rallison and Hinch (1988)].

Other effects neglected with the Gaussian chain are excluded volume interactions and a maximum bond angle [c.f. Bird et al. (1977a,b); Doi and Edwards (1986)]. However, these topics are beyond the scope of this thesis.

Using the Gaussian probability density function an equation for the free energy in the chain can be derived. This is done on the basis that the probability density function is proportional to the entropy of a chain,

$$E(\underline{R}) = A(T) - k_B T \ln P(\underline{R}), \tag{1.6.4}$$

where $A(T)$ is some given function of temperature, T, and k_B is Boltzmann's

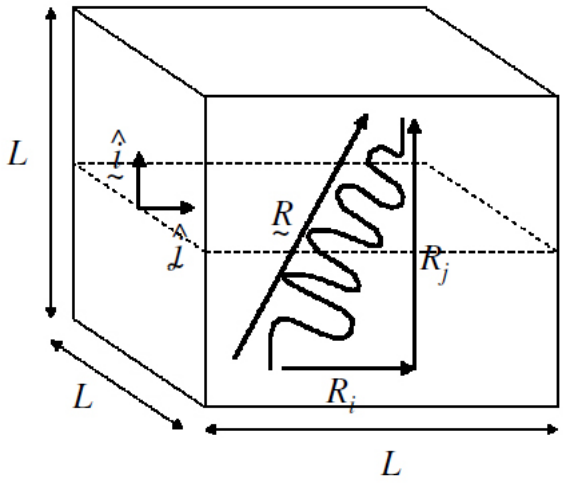

Figure 1.10: An isolated polymer in a cube, L^3. The polymer carries a tension across the surface. Taken from McLeish (2002).

constant.

For a Gaussian chain (1.6.3), the entropic tension caused by extending the chain by the vector $\underline{R}$ is,

$$\underline{F} = -\frac{\partial E}{\partial \underline{R}} = -\frac{3k_B T}{Nb^2}\underline{R}. \tag{1.6.5}$$

This implies that the tension in a Gaussian chain acts like a Hookean spring with stiffness,

$$k = \frac{3k_B T}{Nb^2}. \tag{1.6.6}$$

Initially, consider isolated chains that do not interact with each other. The thermal energy in a polymer chain causes it to exert a force when deformed. Using index notation, the extra stress tensor, $\underline{\underline{\sigma}}$ (equation 1.3.12), can be written as, σ_{ij}, where the i-th component is the total force per unit area across a plane with normal in the j-th direction.

In figure 1.10 a polymer chain with end to end, $\underline{R}$, is in a elementary volume L^3. If the chain carries a tension, $\underline{f}$, then the polymer contribution to the stress

is the sum of all chains inside the cube,

$$\sigma_{ij} = \frac{1}{L^3} \sum_{chains} f_i R_j. \tag{1.6.7}$$

Typically, a polymer chain is considered on some coarse-grained level, where a polymer chain is split into N sections. Each length is chosen to be the Kuhn step length, b. If the monomer concentration is c in the cube, L^3, then the cube contains, $\frac{cL^3}{N}$ polymer chains.

If the cube contains a large amount of chains, the sum in the above equation can be approximated by an ensemble average, $\langle \cdots \rangle$, giving the stress inside the cube as,

$$\sigma_{ij} = \frac{c}{N} \langle f_i R_j \rangle . \tag{1.6.8}$$

Thus for a Gaussian chain (1.6.5), the extra stress can be written as,

$$\sigma_{ij} = \frac{ck}{N} \langle R_i R_j \rangle = \frac{3k_B T}{N^2 b^2} c \langle R_i R_j \rangle , \tag{1.6.9}$$

which is the ensemble average of the dyadic product, $\underline{R}\,\underline{R}$.

1.6.2 The upper convected Maxwell model

Thus to derive an equation for the extra stress it is necessary to obtain an expression for the evolution of the end to end vector, $\underline{R}$. Let us begin by considering a single molecular chain in which the tension of the chain is equated with the solvent drag and random Brownian force arising from collisions with solvent molecules so that,

$$\zeta \left(\frac{d\underline{R}}{dt} - \underline{R} \cdot \nabla \underline{u} \right) = -2k\underline{R} + \underline{f}_b, \tag{1.6.10}$$

where ζ is a drag coefficient, k is the spring constant from equation (1.6.6) and $\underline{f}_b$ represents random Brownian forces. Hence,

$$\frac{d}{dt} \langle R_i R_j \rangle = \left\langle R_i R_k \frac{\partial u_j}{\partial x_k} \right\rangle + \left\langle R_k R_j \frac{\partial u_i}{\partial x_k} \right\rangle - \frac{4k}{\zeta} \langle R_i R_j \rangle + \frac{1}{\zeta} \langle f_{b_i} R_j \rangle + \frac{1}{\zeta} \langle f_{b_j} R_i \rangle . \tag{1.6.11}$$

The ensemble average of the correlation between the random Brownian forces

and end-to-end vector, $\left\langle \underline{f}_b \underline{R} \right\rangle$, is calculated using the Ito-Stratonovich relation,

$$\langle f_i R_j \rangle = 2k_B T \delta_{ij}. \tag{1.6.12}$$

Defining $A_{ij} = \frac{3}{Nb^2} \langle R_i R_j \rangle$,

$$\frac{d}{dt} A_{ij} = K_{ij} A_{ij} + A_{ij} K_{ij}^T - \frac{1}{\tau} \left(A_{ij} - \delta_{ij} \right), \tag{1.6.13}$$

where $\tau = \frac{\zeta}{4k}$ and $K_{ij} = \frac{\partial u_i}{\partial x_j}$. The extra stress is given by,

$$\underline{\underline{\sigma}} = G \underline{\underline{A}}, \tag{1.6.14}$$

where $G = \frac{c k_B T}{N}$, is defined as the elastic modulus. Equations (1.6.13) and (1.6.14) are known as the upper convected Maxwell (UCM) model and are a generalised form of the Maxwell model defined in section 1.3.3.

1.6.3 Rouse Dynamics

The UCM model only accounts for the overall end-to-end length and a more detailed model is the Rouse model for polymer chains. This was first proposed by Rouse (1953) and consists of a polymer chain with a large number, $(N+1)$, of beads connecting a line of springs each with the same spring constant, $k' = \frac{3k_B T}{b^2}$ (c.f. figure 1.11). The drag from the solvent on each bead is constant per monomer with friction coefficient, ζ_0. Labeling each bead with an index $s = 0 \cdots N$ and assuming that N is large so that we can take the continuum limit on s, the equation for the motion of the bead in the middle of the chain is,

$$\zeta_0 \left(\frac{\partial \underline{R}_s}{\partial t} - \underline{v}(\underline{R}_s) \right) = k' \frac{\partial^2 \underline{R}_s}{\partial s^2} + \underline{f}_s. \tag{1.6.15}$$

Each Rouse chain has $N+1$ normal modes, one mode represents translation and each of the other N modes represents a contribution to the extra stress acting like the dumbbell model. Concentrating on stress relaxation in the absence of flow (i.e. neglect the velocity, $\underline{v}$), the normal modes and relaxation times can be derived. The random force terms, $\underline{f}_s$ on each segment are uncorrelated with

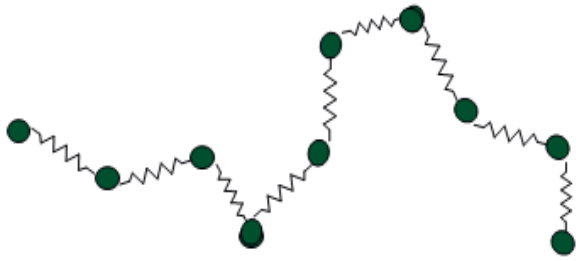

Figure 1.11: An isolated Rouse chain.

each other. Since the ends of the chains are free the tension must vanish so that $\frac{\partial \underline{R}}{\partial s} = 0$ at $s = 0, N$. Hence writing $\underline{R}(s)$as a Fourier series, the position of the beads, $\underline{R}_s$, can be written as the sum of sinusoidal normal modes,

$$\underline{R}_s = \sum_p \underline{X}_p \cos\left(\frac{\pi p s}{N}\right), \quad p = 1, 2, 3, \cdots, \tag{1.6.16}$$

giving a constitutive model for a Rouse chain as,

$$\underline{\underline{\sigma}} = G \sum_p \underline{\underline{A}}_p, \tag{1.6.17}$$

where for each p the tensor $\underline{\underline{A}}_p$ satisfies the UCM evolution equation (1.6.13),

$$\frac{d}{dt}\underline{\underline{A}} = \underline{\underline{K}} \cdot \underline{\underline{A}}_p + \underline{\underline{A}}_p \cdot \underline{\underline{K}}^T - \frac{1}{\tau_p}\left(\underline{\underline{A}}_p - \underline{\underline{I}}\right). \tag{1.6.18}$$

Subsequently, the stress relaxation time of the pth mode is given by,

$$\tau_p = \frac{\tau_1}{2p^2} = \frac{\zeta_0 N^2 b^2}{6\pi^2 k_B T p^2}, \tag{1.6.19}$$

The relaxation modulus for the Rouse model is simply a sum over UCM modes, i.e linear Maxwell modes (c.f. section 1.3.3), and is of the form,

$$G(t) = G \sum_p e^{-\frac{p^2 t}{\tau_1}}. \tag{1.6.20}$$

This can be thought of as the progressive relaxation of the p modes and so at early times, $t \ll \tau_1$, the majority of modes contribute to the relaxation modulus. In this case taking the continuous limit of the sum in equation (1.6.20) it is found that at early times, $G(t) \sim t^{-\frac{1}{2}}$ [Doi and Edwards (1986)].

Taking the Fourier transform of equation (1.6.20) will also give the storage and loss modulus for the Rouse model,

$$G^* = \int_0^\infty ds\, i\omega G \sum_{p=1}^{\infty} e^{-\frac{p^2 s}{\tau_1} - i\omega s}, \tag{1.6.21}$$

giving the storage and loss modulus, respectively as,

$$G' = G \sum_{p=1}^{\infty} \frac{\omega^2 \tau_1^2}{p^4 + \omega^2 \tau_1^2} \qquad \text{and} \qquad G'' = G \sum_{p=1}^{\infty} \frac{p^2 \omega \tau_1}{p^4 + \omega^2 \tau_1^2}. \tag{1.6.22}$$

In figure 1.12 the storage and loss modulus are plotted against dimensionless frequency, $\omega\tau_1$. In the limit of low frequencies we can assume that $p^4 + \omega^2\tau_1^2 \sim p^4$, then $G' \sim \omega^2$ and $G'' \sim \omega$. Similarly, in the limit of high frequencies the sum over p modes can be taken in the continuous limit and for both the storage and loss modulus, $G', G'' \sim \omega^{\frac{1}{2}}$. These results are indicated in figure 1.12.

The Rouse model assumes a simple coupling between the polymer chain and the background solvent which ignores hydrodynamic interactions. For polymer solutions hydrodynamic interactions are an important physical process and are included in the model of Zimm [Zimm (1956); Zimm et al. (1956)]. Despite this both the dumbbell and Rouse model, both derived from Gaussian chain statistics, are important theories in the study of polymer melts. In particular, Rouse dynamics capture the rheology of low molecular weight polymer melts, where interactions between molecules are not dominant.

1.6.4 Entanglements and Reptation

The constitutive models in the previous two subsections consider only isolated chains. In a melt of sufficiently long chain polymers there is a significant overlap between the polymer chains that dominates the rheology. The theory for entan-

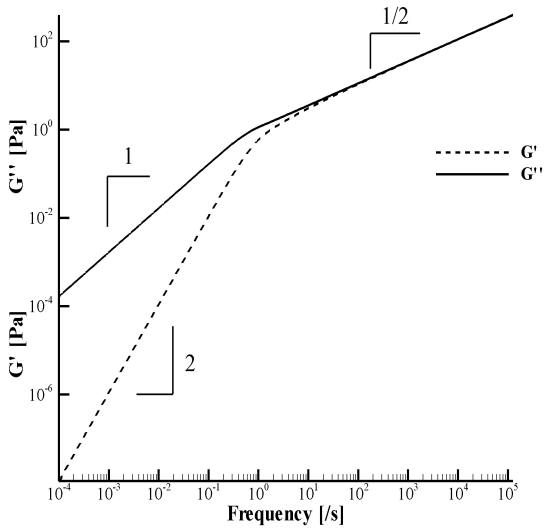

Figure 1.12: The storage and loss modulus for the Rouse model.

gled polymer melts is based upon the Doi-Edwards tube model [Doi and Edwards (1986)].

Considering one polymer chain, if it experiences many overlaps, or *entanglements*, with other chains then the lateral movements of the polymer chain is restricted. This leads to the idea of a tube of confinement around a polymer chain. This idea was first introduced by de Gennes (1971) and Edwards (1998).

For entanglements to be a dominant feature in the rheology of a material the molecular weight of each polymer chain has to be large enough to experience multiple entanglements. This was first shown by Berry and Fox (1968) and subsequently discussed by Colby et al. (1987); Doi (1983). Berry and Fox (1968) measured the zero shear viscosity for many types of polymers and varied the molecular weight of each type. In these experiments the authors found two regimes of molecular weight, characterised by some critical molecular weight, M_C. Below M_C the zero shear viscosity was proportional to the molecular weight of the polymers, $\eta_0 \sim M$, as predicted by the Rouse model. However, above M_C the zero shear viscosity scales as $\eta_0 \sim M^{3.4}$ which is attributed to polymer chains becoming entangled. The Doi-Edwards tube model [Doi and Edwards (1986)] provides a molecular model for chains with molecular weight exceeding

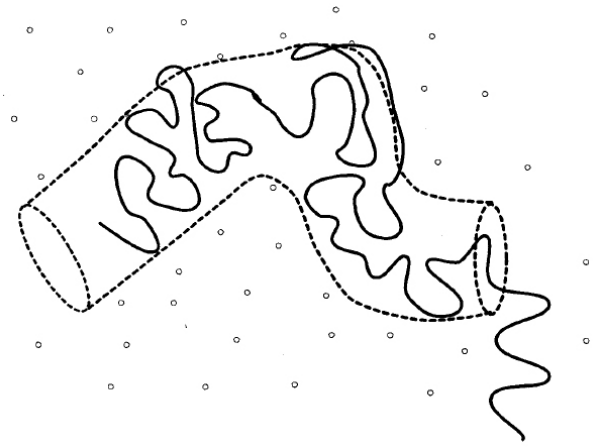

Figure 1.13: An entangled chain diffusing from its tube. The tube is a continuum of topological constraints caused by entanglements (circles). Taken from McLeish (2002).

M_C. This critical molecular weight is defined as the molecular weight at which entanglements become important to the rheology of the material.

The tube model adopts a mean field approach, that simplifies the multi-chain system to a single chain confined with a 'tube' that represents the effect of neighboring polymer chains. The tube constrains the lateral movement of a polymer chain, however the chain is free to explore its own path length. In this way a polymer chain can relax stress by diffusing along its contour and out of its initial tube, in order to adopt an isotropic distribution in its subsegments. This stress relaxation is characterised by the average time it takes a polymer to escape its tube. The relaxation process of a polymer chain diffusing out of a tube is named *reptation* [de Gennes (1971)] in reference its snake like motion.

The exact nature of entanglements is still a current research area with much activity [for example see Sukumaran and Likhtman (2009)]. However, the assumption made is that entanglements affect the lateral dynamics of a polymer chain beyond some length scale, a. This length scale, a, measures the distance between entanglements and in equilibrium, where the polymer chain can be approximated as a Gaussian walk, is given by the relationship,

$$a^2 = \frac{3}{\nu} N_e b^2, \tag{1.6.23}$$

where $N_e \propto M_e$ is the number of Rouse beads in an entanglement segment, b is the Kuhn step length and ν is a dimensionless number relating the step lengths a and b.

The relaxation of fundamental segments, M_e, follows Rouse dynamics with,

$$\tau_e = \frac{\zeta_0 N_e^2 b^2}{3\pi^2 k_B T}, \tag{1.6.24}$$

so all time scales can be expressed in terms of the Rouse relaxation time of entanglement segments, τ_e. Similarly, we can express molecular weights as path lengths, $s = \frac{M}{M_e} = \frac{N}{N_e}$, which is the number of entanglement lengths.

The primitive path is defined as the shortest path length through the tube with the same end to end vector as the polymer chain. Let z' be the distance of the primitive chain contour as measured from the centre of the molecule and $\underline{R}(z', t)$ be the position of the primitive chain. Then,

$$\underline{u}(z', t) = \frac{\partial}{\partial z'} \underline{R}(z', t), \tag{1.6.25}$$

is the unit tangent vector of the primitive chain. Also, if we let L be the length of the steps in a primitive chain then,

$$L = \frac{Nb^2}{a} = \frac{\nu}{3} sa. \tag{1.6.26}$$

So the step size, a, becomes the step length of the primitive path, also called the *tube diameter*.

A primitive path satisfies a one-dimensional diffusion equation as it diffuses out of its tube, with Rouse diffusion coefficient, $D_C = \frac{k_B T}{\zeta_0 N}$. The average time for the polymer chain to diffuse out of its tube, the disentanglement or reptation time, τ_d, is given by,

$$\tau_d = \frac{L^2}{\pi^2 D_C} = \frac{\zeta_0 N^3 b^4}{\pi^2 k_B T a^2} = \nu s^3 \tau_e. \tag{1.6.27}$$

This gives a shear relaxation modulus as,

$$G(t) = G_0 \sum_{p,odd} \frac{8}{p^2\pi^2} exp\left(-\frac{p^2 t}{\tau_d}\right), \tag{1.6.28}$$

where $G_0 = \frac{4\rho RT}{5M_e}$ is defined as the plateau modulus. This leads to a zero shear viscosity, $\eta_0 = \frac{\pi^2}{12} G_0 \tau_d \sim M^3$, agreeing closely with the experimental observations of $\eta_0 \sim M^{3.4}$ discussed at the beginning of this section (the full 3.4 power law is recovered by modelling contour length fluctuations [Milner and McLeish (1998)]).

In the basic Doi-Edwards model the extra stress tensor uses the second moment of the unit tangent vector, equation (1.6.25),

$$\underline{\underline{\sigma}} = \frac{c}{N_e} k_B T \nu \langle \underline{u}\,\underline{u} \rangle = G_0 \underline{\underline{S}}, \tag{1.6.29}$$

where $\underline{\underline{S}} = \nu \langle \underline{u}\,\underline{u} \rangle$.

The rate of tube reconfiguration is τ_d^{-1} which implies that the probability of a tube segment surviving from an isotropic distribution at time, t', to a later time, $t > t'$, is $exp(-\frac{t-t'}{\tau_d})$.

If $\underline{u}$ is a unit vector denoting the orientation of a tube segment at time, t', then at time t it is given by $\frac{\underline{\underline{E}} \cdot \underline{u}}{|\underline{\underline{E}} \cdot \underline{u}|}$, where $\underline{\underline{E}}(t', t)$ is the strain between times t and t'. Hence the orientation distribution at time t of tube segments with orientation $\underline{u}$ at time t' is given by,

$$\underline{\underline{Q}} = \left\langle \frac{\underline{\underline{E}} \cdot \underline{u}\, \underline{\underline{E}} \cdot \underline{u}}{|\underline{\underline{E}} \cdot \underline{u}|^2} \right\rangle_{t'}, \tag{1.6.30}$$

where the subscript t' denotes the time at which the average is taken.

The extra stress in the Doi-Edwards model at time t is then given by the sum of contributions from all the surviving tube segments created at past times t',

$$\underline{\underline{\sigma}} = G_0 \nu \int_{-\infty}^{t} dt' \frac{\exp(-\frac{t-t'}{\tau_d})}{\tau_d} \underline{\underline{Q}}. \tag{1.6.31}$$

This representation of the tube model contains a simplifying assumption called *independent alignment* which neglects the interconnection of the chain. A more detailed theory was described by Doi and Edwards (1986) which does not use

this approximation and accounts for chain stretch, which aligns with the flow. Despite this, the independent alignment provides a reasonable approximation, although discrepancies can occur in first normal stress difference or in complex flow situations such as reversing flows.

For the independent alignment approximation Doi and Edwards (1986) calculated that $\nu = 5$, however, the non-independent alignment value of $\nu = \frac{15}{4}$ will be subsequently used for the rest of this work. This is because the value, $\nu = \frac{15}{4}$, gives the correct scaling when considering star arm polymers, which is important when considering LCB in the next section [Ball and McLeish (1989)].

One important experimentally observed phenomena is that stress relaxation, after a shear step, is time-strain separable. This means that the non-linear shear relaxation modulus, $G(\gamma, t)$, can be written as the product of two functions,

$$G(\gamma, t) = G(t)\, h(\gamma), \tag{1.6.32}$$

where $G(t)$ is the time dependent, low strain, linear relaxation function and $h(\gamma)$ is strain dependent function, called the damping function. For the Doi-Edwards model this property follows from the integral representation (1.6.31) and gives,

$$h(\gamma) = \frac{1}{(1 + \frac{4}{15}\gamma^2)}. \tag{1.6.33}$$

The Doi-Edwards tube model successfully captures key rheological properties of linear polymer melts with a high molecular weight, such as shear thinning and extensional strain softening. This model has been the benchmark for subsequent, more complex models, such as the GLaMM model [Graham et al. (2003)]. The GLaMM model uses the tube model concept and included the extra concepts of contour length fluctuations and convective constraint release. The Doi-Edwards tube model is also a key concept in the theory of LCB rheology.

1.6.5 Branched Polymers: The Pompom model

In the previous section I considered linear polymer chains. I now move on to consider branched molecular architecture. Materials containing LCB exhibit dif-

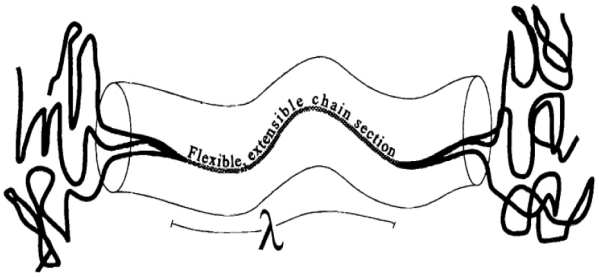

Figure 1.14: Diagram of a Pompom molecule with, $q = 3$ arms.

ferent rheology than linear materials. In particular, they exhibit strain hardening phenomena discussed in section 1.5.

Before considering a general branched molecule, I first consider the extra stress for an idealised branched molecule, *the Pompom molecule* [McLeish and Larson (1998)]. This is the simplest molecule that contains multiple branch points allowing segments of the molecule to become 'buried' and causing a hierarchy of relaxation processes. Figure 1.14 shows a typical Pompom molecule. It consists of a backbone of length, $L(t)$, connecting two sets of q identical arms at a branch point at each end of the backbone.

The Pompom molecule can be characterised by its molecular weight which comprises of the molecular weight of the backbone, M_b, and the molecular weight of each arm, M_a, so that the molecular weight of each molecule is, $M = M_b + 2qM_a$. As for linear polymers, the dynamics are controlled by the scaling of the molecular weight by the molecular entanglement weight, M_e, giving a dimensionless path length for the backbone, $s_b = \frac{M_b}{M_e}$, and arms, $s_a = \frac{M_a}{M_e}$.

It is convenient to express the molecular mass of the backbone, M_b, and arms, $2qM_a$, as molecular mass fractions of the total mass of the molecule, $M = M_b + 2qM_a$,

$$\phi_b = \frac{M_b}{M_b + 2qM_a} \qquad \text{and} \qquad \phi_a = \frac{2qM_a}{M_b + 2qM_a}. \tag{1.6.34}$$

There exist two dominant relaxation processes for the stress in the central segment of the Pompom molecule. These are the relaxation of chain stretch and the relaxation of orientation by reptation. The motion of the backbone is

inhibited by the two branch points at either end, which connect to the arms of the Pompom molecule. These prevent the backbone from moving along its tube until the arms have relaxed. The branch points are essentially star shaped molecules for which Ball and McLeish (1989) showed that the relaxation time of an arm is proportional to the exponential of the arm path length,

$$\tau_a = \tau_0 e^{\nu' s_a}, \tag{1.6.35}$$

where τ_0 is the average time for an arm to try and retract into its tube and ν' is obtained from the entropic arm retraction potential. Ball and McLeish (1989); Blackwell et al. (2000); McLeish et al. (1999) used tube dilution dynamics to derive,

$$\nu' = \frac{15\left(1-(1-\phi_a)^{\beta}(1+\beta\phi_a)\right)}{4\beta(\beta+1)\phi_a^2}. \tag{1.6.36}$$

The relaxation of the backbone, via stretch relaxation and reorientation, occurs at time scales much larger than the arm relaxation time and dominates the rheology at deformation rates of order of the backbone relaxation time. Although the arm relaxation controls the backbone relaxation, the stress contribution is negligible at time scales of order of the backbone relaxation time since relaxation is effectively instantaneous and is thus treated as Newtonian solvent. However, as segments of the molecule relax they can no longer act as entanglements to unrelaxed segments. The effect of this is to increase the tube diameter and Ball and McLeish (1989) proposed that the polymer volume fraction, Φ, scales with the entanglement molecular weight as, $M_e = \frac{M_{e,0}}{\Phi^{\beta-1}}$, with $\beta = \frac{7}{3}$ [Colby and Rubenstein (1990)]. As the relaxation of the arms is not considered before any of the backbone has relaxed, the polymer volume fraction, $\Phi = \phi_b$ [Milner and McLeish (1997)].

The two dominant relaxation processes, backbone stretch relaxation and backbone reorientation, are determined from the arm disentanglement time. The backbone stretch relaxation time, τ_s, is the time taken for the path length of the backbone to return from some displaced length to its equilibrium length. The orientation relaxation time, τ_b, is the average time it takes the backbone to reptate, via its branch points diffusing along the backbone tube, out of a tube of

unstretched length.

The dynamics of the stretch relaxation are governed by the balance of an entropically generated thermal tension and the frictional drag force at each branch point. The drag force is determined from the relative velocity of the branch point and the tube,

$$F_d = \frac{\zeta_{bp}}{2}\left(\frac{\partial L}{\partial t} - L\underline{\underline{K}} : \underline{\underline{S}}\right), \tag{1.6.37}$$

where ζ_{bp} is the drag coefficient, the velocity gradient is $\underline{\underline{K}}$, the orientation is given by $\underline{\underline{S}}$ and the contour length of the tube is given by, L. The drag coefficient, ζ_{bp}, can be obtained from the Stokes-Einstein relationship, $\zeta_{bp} = \frac{k_B T}{D_{bp}}$. By considering the diffusion of the branch points an equation is derived for the drag force of the q arms [Blackwell et al. (2000)], with diffusion coefficient given by Colby and Rubenstein (1990),

$$D_{bp} = \frac{p^2 a_{eff}^2}{2q\tau_a}, \tag{1.6.38}$$

where $a_{eff} = \frac{a}{\phi_b^{(\beta-1)/2}}$ is the effective tube diameter and p is the fraction of the tube diameter that a branch point diffusively hops when it is liberated by a retracting arm.

This drag force must balance the entropic tension in the backbone with the entropic force being Hookean in nature,

$$F_e = \frac{3k_B T}{L_0 a}\left(L - L_0\right), \tag{1.6.39}$$

where L_0 is the equilibrium length of the backbone tube and $L_0 a =< R^2 >= N_b b^2$, with the Kuhn step length related to the tube diameter with $a^2 = \frac{4}{5} N_e b^2$ [Doi and Edwards (1986)].

Defining $\lambda(t) = \frac{L(t)}{L_0}$ as the dimensionless stretch and equating the viscous drag force and entropic elastic recovery force gives,

$$\frac{D\lambda(t)}{Dt} = \lambda(t)\underline{\underline{K}} : \underline{\underline{S}} - \frac{1}{\tau_s}\left(\lambda(t) - 1\right), \tag{1.6.40}$$

as the dynamic equation for the stretch in the backbone of the Pompom molecule

with,

$$\tau_s = \frac{5}{2} q s_b \phi_b^{\beta-1} \tau_a. \tag{1.6.41}$$

Bick and McLeish (1996) noted that there is an upper bound on the elastic force and hence on the stretch, λ. Each arm with a free end carries an entropic tension, $f_0 = \frac{3k_BT}{a}$, and so the backbone can maintain a maximum tension of qf_0. At this point the branch point is withdrawn into the backbone tube reducing the effective drag coefficient and the value of the stretch will not increase. Equating the maximum tension with the tension in the backbone gives the condition, $\lambda(t) \leq q$. Originally McLeish and Larson (1998) included dynamics of the branch point withdrawal in their model. However, the timescale of this process is much faster in comparison to the stretch relaxation time, and the additional stress contribution from the aligned portion of the arms is small compared to that contributed by the backbone. Consequently, subsequent treatments of the Pompom equations [Blackwell et al. (2000); Inkson et al. (1999); Lee et al. (2001)] have neglected this term.

Blackwell et al. (2000) considered local branch point displacement. Since all relaxation processes are based on the arm relaxation process, which in turn, has dependence on the exponential of the arm path length, equation (1.6.35), even changes in the arm path length, s_a, in the order of a tube diameter, a, will have a significant effect on the arm relaxation time. Blackwell et al. (2000) assumed that there would be no significant change to the orientation relaxation time, since the withdrawn material would be orientated.

To consider the effect of branch point displacement on the relaxation times we look at the localising force on the branch point. If x is the distance along the tube contour measured from the end of the contour, then Doi and Edwards (1986) state that the Gaussian probability distribution for small scale displacements of the branch point will have a localising force with a harmonic potential,

$$\frac{U(x)}{k_BT} = (q-1)k^* \left(\frac{x}{a}\right)^2, \tag{1.6.42}$$

where k^* is an unknown dimensionless constant of order unity. This is different than the result quoted in Blackwell et al. (2000), where the case of $q = 1$ was not

treated correctly in this potential. For the value, $q = 1$, the Pompom molecule is linear and hence, has no branch points to generate Pompom stretch (note linear molecules exhibit chain stretch above critical deformation rates [Graham et al. (2003)], but this is not modelled for linear Pompom molecules) or branch point displacement. This changes $U(x) \sim q$ quoted in Blackwell et al. (2000) to $U(x) \sim (q-1)$. For large branch point displacements the branch point feels maximum force, qf_0, this gives a linear potential in agreement with McLeish and Larson (1998).

The length of a Pompom arm, $L_a = \frac{5}{4}s_a a$, and so a change in the path length of a Pompom arm with branch point displacement, x, is given by,

$$\triangle s_a = -\frac{4x}{5a}. \tag{1.6.43}$$

By balancing the elastic force, F_e, with the localising force with potential, $U(x)$, the change in path length can be expressed in terms of the stretch, $\lambda(t)$,

$$\triangle s_a = -\frac{6}{5k^*(q-1)}\left(\lambda(t) - 1\right). \tag{1.6.44}$$

From equation (1.6.35) the arm relaxation time can be expressed with respect to a dynamic path length, $s_a + \triangle s_a$, as long as the change in path length, $\triangle s_a$, is small compared to the path length of the arm, s_a, to give,

$$\tau_a = \tau_0 e^{\nu' s_a} \rightarrow \tau_0 e^{\nu'(s_a + \triangle s_a)}. \tag{1.6.45}$$

This gives a modification to the Pompom model that reduces the stretch relaxation time exponentially with branch point displacement,

$$\tau_s \rightarrow \tau_s e^{-\nu*(\lambda-1)}, \tag{1.6.46}$$

where ν^* is given by [McLeish (2002)],

$$\nu^* = \frac{2}{q-1}. \tag{1.6.47}$$

The effect of branch point displacement reduces the stretch relaxation time, τ_s,

from its initial value for $\lambda = 1$ at equilibrium, to a value of $\tau_s e^{-2}$ at maximum stretch, $\lambda = q$.

Incorporating the adjusted τ_s into the stretch equation (1.6.40) gives an ODE for the evolution of the stretch with branch point displacement,

$$\frac{D\lambda(t)}{Dt} = \lambda(t)\underline{\underline{K}} : \underline{\underline{S}} - \frac{1}{\tau_s}\left(\lambda(t) - 1\right) e^{\nu*(\lambda-1)}. \tag{1.6.48}$$

Another modification to the Pompom equations was proposed by Lee et al. (2001), whereby in the case of reversing flows the contour length of the polymer chain becomes smaller than its equilibrium length, L_0. This is particularly important in complex flows such as contraction-expansion flows [Lee et al. (2001)] and in oscillatory shear flows where the deformation rate is large, $De \gg 1$ [c.f. section 1.4.1]. This flow is a topic of much current research and in chapter 4 I discuss large amplitude oscillatory shear with respect to the Pompom equations.

Considering the case where a positive strain is followed by a rapid strain in the opposite direction the backbone tube may retract faster than the polymer chain. If there is significant chain retraction between the positive and negative strain then the contraction of the tube contour will bring the path length below equilibrium, $\lambda < 1$. From equation (1.6.48) this condition is equivalent to, $\underline{\underline{S}} : \underline{\underline{K}} - \frac{1}{\lambda}\frac{D\lambda}{Dt} < 0$. In this case the chain extension will create new isotropic portions of the backbone tube by exploration of the melt by the emerging free ends at a rate, $\underline{\underline{S}} : \underline{\underline{K}} - \frac{1}{\lambda}\frac{D\lambda}{Dt}$, which is accompanied with reptation at a rate, τ_b^{-1}. Lee et al. (2001) proposed that orientation relaxation time should be modified to capture this relaxation process with a piecewise continuous function that adjusts τ_b only when, $\lambda < 1$, to give,

$$\frac{1}{\tau_b^*} = \frac{1}{\tau_b} + \frac{\dot{\lambda}}{\lambda} - \underline{\underline{K}} : \underline{\underline{S}} \qquad \text{for } \lambda < 1. \tag{1.6.49}$$

The final element of the Pompom equations is the equation for the evolution of the orientation. As previously mentioned in this section the backbone of the Pompom model reptates out of its tube after the Pompom arms have relaxed and simply contributes as solvent drag at the branch points. The reptation time of the backbone, like for the stretch relaxation, is clearly dependent on arm relaxation.

McLeish and Larson (1998) derive the orientation relaxation as,

$$\tau_b = \frac{75}{2\pi^2} q s_b^2 \phi_b^{2(\beta-1)} \tau_a. \tag{1.6.50}$$

The orientation contribution to the extra stress tensor is given by the Doi-Edwards orientation [c.f. equations 1.6.30,1.6.31] and the extra stress for the Pompom model is,

$$\underline{\underline{\sigma}} = G_0 \phi_b^{\beta} \lambda^2(t) \underline{\underline{S}}(t), \tag{1.6.51}$$

where G_0 is the plateau modulus.

Differential Pompom models

For non-rheometric flows the numerical solution to this integral form of the Pompom model is computationally expensive, although Wapperom and Keunings (2001) perform successful numerical simulations of the integral Pompom model. This had led to the introduction of differential approximations for the orientation equation (1.6.30,1.6.31). The approximation proposed by McLeish and Larson (1998) [which is the approximation used in Blackwell et al. (2000); Hassell et al. (2009); Lee et al. (2001); McLeish (2002); McLeish and Larson (1998)] is given by,

$$\underline{\underline{\sigma}} = 3G\lambda^2(t) \underline{\underline{S}}, \tag{1.6.52}$$

with

$$\underline{\underline{S}} = \frac{\underline{\underline{A}}}{trace(\underline{\underline{A}})}, \qquad \text{where} \tag{1.6.53}$$

$$\frac{D}{Dt} A_{ij} = K_{ij} A_{ij} + A_{ij} K_{ij}^T - \frac{1}{\tau_b} \left(A_{ij} - I_{ij} \right), \tag{1.6.54}$$

where $\underline{\underline{A}}$ is an auxiliary variable satisfying the UCM model. The stretch remains given by equation (1.6.48). This approximation gives the correct asymptotic limits for S_{xy} in shear flow at high and low shear-rates. However, the transition from isotropic to aligned orientations occurs too rapidly with increasing deformation rate, so that this is a qualitative rather than a quantitative approximation to the integral solution for $\underline{\underline{S}}$.

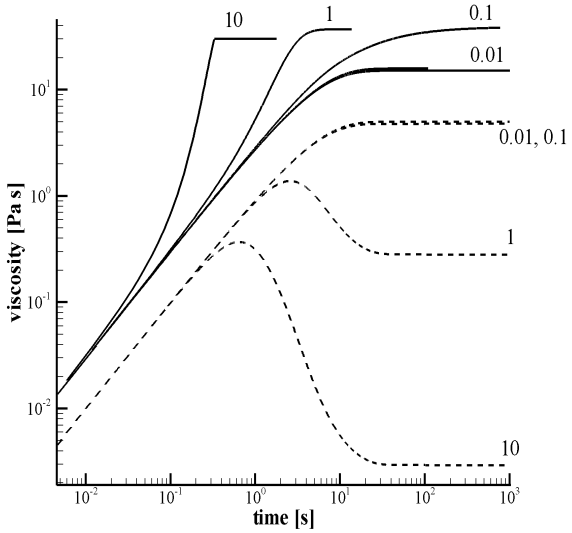

Figure 1.15: A one mode Pompom model in uniaxial extension (solid lines) and shear (dashed lines). Extension/shear rates of 0.01, 0.1, 1 and 10s^{-1} were used with Pompom parameters of $\{G = 1\text{Pa}, \tau_b = 5\text{s}, q = 10, \tau_s = 1.25\text{s}\}$.

Figure 1.15 shows the differential Pompom model, for a single mode, in uniaxial extension and simple shear flow. The parameters, $\{G = 1\text{Pa}, \tau_b = 5\text{s}, q = 10, \tau_s = 1.25\text{s}\}$, are chosen to show the qualitative behaviour of the Pompom model.

In addition this approximation gives zero second normal stress difference and the stress in both transient and steady state extension can be non-differentiable as the equations are only piece-wise continuous. Several alternative approximations for orientation tensors have been suggested to overcome these problems. Verbeeten et al. (2001) suggested an alternative approximation known as the extended Pompom model (XPP). This model gives a second normal stress difference, however it also produces unphysical mathematical artifacts. In particular, the steady shear viscosity contains multiple solutions for some shear rates [Clemeur et al. (2003)]. Clemeur et al. (2003, 2004a) suggested alterations from the XPP model know as the double convected Pompom (DCPP) model. This model creates a second normal stress difference using a ratio of upper and lower convective derivatives and has been shown to have good agreement with large am-

plitude oscillatory shear experiments (c.f. chapter 5) and predicted birefringence patterns in 3D simulations of contraction flows [Clemeur et al. (2004b)].

The XPP and DCPP models have a common limit when the parameters controlling the second normal stress difference are set to zero, known as the DPP model [Clemeur et al. (2003)]. Both models avoid the non-differentiable piecewise nature of the original models by neglecting the maximum stretch condition, $\lambda(t) \leq q$. This does make solving finite element problems easier as no penalty condition is needed (c.f. next section; 1.7) but ignores an important piece of the Pompom physics. Also both XPP and DCPP model do not gives the correct asymptotic behaviour at high shear rates.

Öttinger (2001) suggested a model from an approach based on non-equilibrium thermodynamics which does introduce a second normal stress difference and maintains the maximum stretch condition. The model is complicated by the process of having to invert matrices to solve the equations and a simplification of the model is used to avoid this when solving computational problems.

In my thesis I will focus on the original set of differential and integral Pompom equations by McLeish and Larson (1998) with the improvements discussed in this section [Blackwell et al. (2000); Inkson et al. (1999); Lee et al. (2001); McLeish (2002)]. In the subsequent chapters I will be exploring the equations in simple and complex geometries and evaluate their performance based on experimental observations.

Multimode models

The model of monodisperse Pompom molecules can be expanded to capture the rheology of randomly LCB polydisperse materials, such as LDPE. Inkson et al. (1999) introduced the multimode Pompom model which decouples a randomly LCB molecule into a series of simple Pompom molecules, which have a range of orientation and stretch relaxation times. This assumption is based on the principle that the outer branches of a randomly branched molecule must relax first, before the inner segments of a molecule can then relax. The Pompom

constitutive model now takes the form,

$$\sum_{i}^{N} \underline{\underline{\sigma}}_i = 3G_i\lambda_i^2(t)\underline{\underline{S}}_i, \tag{1.6.55}$$

where N is the number of Pompom modes. The Pompom model parameter space, $\{G_i, \tau_{b_i}, \tau_{s_i}, q_i\}$, can successfully capture the rheology of commercial polyethylenes [Blackwell et al. (2000)] and this will be discussed in the next chapter, where I detail fitting several polyethylenes with Pompom spectra.

1.7 Numerical simulations

The aim of this thesis is to analyse stress response of polymers and constitutive equations in complex flow. In particular I will examine the cross-slot geometry implemented by the Cambridge multi-pass rheometer [see for example Hassell et al. (2009)]. The cross-slot experimental apparatus allows optical measurements of principal stress difference via flow induced stress birefringence. This method will be fully discussed in chapters 5 and 6, with an investigation on mesh density carried out in chapter 5. A particular feature of cross-slot flow is the generation of a stagnation point, causing polymers to become highly extended. This stagnation point flow is a good test of constitutive equations and, to test the Pompom model in the flow, the constitutive equations coupled with the equations of motion are solved for this complex geometry.

Of course the experimental flow is three dimensional, however if the depth of the cross-slot (i.e. perpendicular to the viewing plain) is significantly more than the width of the cross-slot channel, then a two-dimensional approximation can be made (Wales (1976) suggests the ratio of depth to width be at least 10). The ratio of depth to width for the Cambridge cross-slot is 7 and so although a 2D approximation is valid, the error of ignoring the full 3D nature of the flow needs to be checked.

One popular method for solving flow through a complex geometry is the finite element (FE) method, which I use in my thesis. Finite element (FE) methods consist of dividing the solution domain into discrete elements. An example of

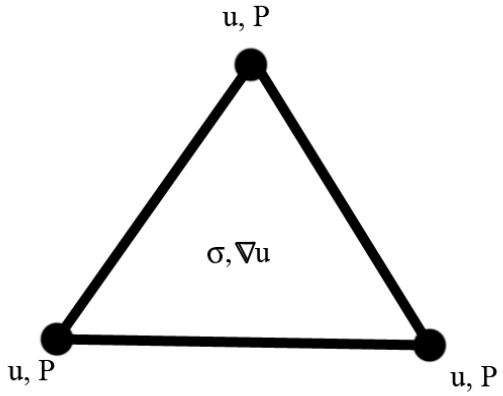

Figure 1.16: An example of an element used with the finite element method of solving complex geometries. The velocity and pressure are solved at the nodes of the element and the velocity gradient and stress are solved as constant of the area of the element.

an element can be seen in figure (1.16), where in this case a triangular element has the velocity and pressure solved at each of its three nodes and the velocity gradients and extra stress solved as a constant for the element.

I will compare two kinds of FE methods in my work. The first FE method is a split Lagrangian technique [Bishko et al. (1997, 1999); Harlen et al. (1995)] built into software called *flowSolve*. With this method the mesh moves with the fluid (c.f. figure (1.17)) and provides a very natural way of solving the velocity field, the velocity gradient field and the UCM tensor. As the mesh moves the triangles become distorted and so are split into smaller triangles. To save computation time specific regions can have the resolution of elements increased, as seen in figure (1.17), and as the mesh convects so do the refined regions so as not to loose any data points.

The second FE method I will employ is a static Eulerian mesh solver know as *euFlow* [Tenchev et al. (2008)]. This method uses quadrilateral elements to form the solution domain and the mesh does not deform with the flow. The solver scheme uses Petrov-Galerkin stream-line upwinding to stabilise the solution. Using a static mesh provides a much quicker solving method than the moving Lagrangian mesh and is expanded to 3D calculations. The speed of the

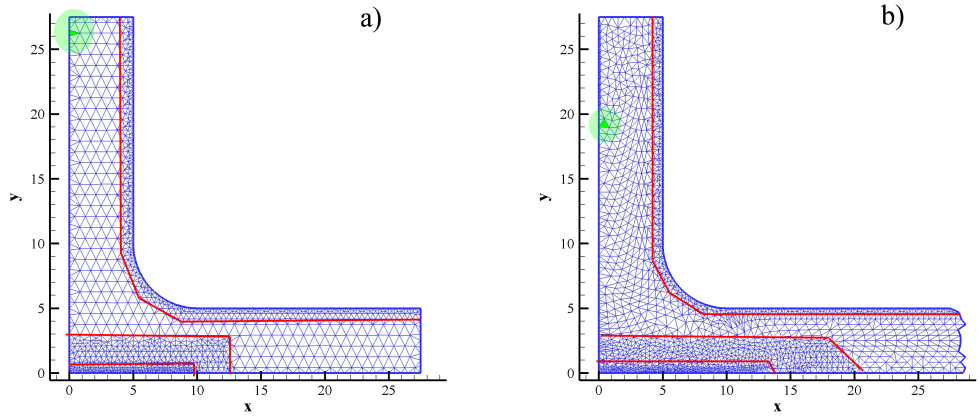

Figure 1.17: An example of a finite element mesh created by *flowSolve* in solving cross-slot flow. The red lines indicate regions of refinement. On the left is the initial mesh at time $t = 0$s and on the right the mesh at some later time. The refinement regions have been subsequently distorted and the green circle indicates the movement of one element.

method will allow me to check deviations from the 2D approximation of experiments. The discretisation of space is initially done by breaking the space down in to a series of 'super elements' (c.f. figure 1.18), these are then filled with a preset number of elements giving the final mesh.

Solving the Pompom equations requires transient constraints to be made on the solution, namely the supremum on the stretch equation (1.6.48), $\lambda(t) \leq q$, and the trace of the UCM tensor (1.6.54) needs to be constrained so that the solution remains finite. This does not affect the solution as once the trace of the UCM tensor becomes large each element of the orientation tensor (1.6.53) never exceeds unity. The solver *flowSolve* has a natural way of imposing these limits, however *euFlow* cannot impose hard limits as this makes the solution unstable. Therefore *euFlow* uses a penalty function to 'push back' any nodal values that go beyond their particular limits. This requires a predefined penalty coefficient where trial and error is needed to find the correct number. In this way there is a trade off between the speed of *euFlow* and the stability of *flowSolve*.

The experimental flow rate is set by a constant piston speed, V_p, which gives

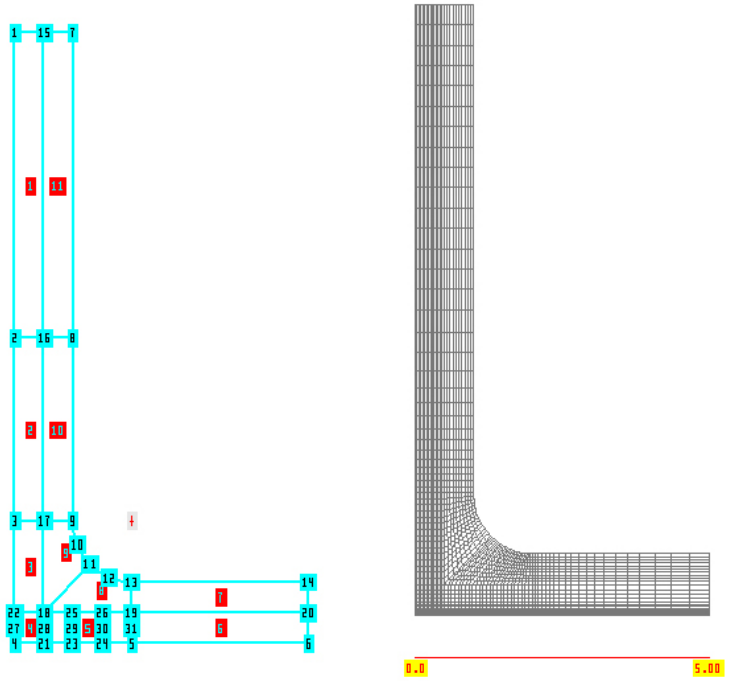

Figure 1.18: An example of the static mesh used by *euFlow*'s finite element scheme. On the left the spatial domain is constructed of super elements which are filled in with finite elements on the right.

a volume flux into the cross slot of,

$$Q = 78.5 \cdot V_p, mm^3/s \tag{1.7.1}$$

where Q is the volume flux.

The moving mesh solver, *flowSolve* requires an average velocity flux, U_Q, which is calculated from the geometry used [c.f. figure 5.2], dividing the volume flux by the surface area of the input channel. This gives the velocity input flux as,

$$U_Q = 5.2333 \cdot V_p. \tag{1.7.2}$$

For the static mesh solver, *euFlow*, the required input parameter is given as the maximum velocity of the Stokes solution across the input channel, the velocity profile is then continually updated during the simulation. For 2D geometries this

implies the maximum input velocity, V_{max}^{2D}, is given by,

$$V_{max}^{2D} = \frac{3}{2} U_Q. \tag{1.7.3}$$

The 3D input parameter is the maximum velocity, V_{max}^{3D}, of a bi-quadratic velocity profile,

$$V(x,z) = V_{max}^{3D} \left(1 - \frac{x^2}{a^2}\right) \left(1 - \frac{z^2}{b^2}\right), \tag{1.7.4}$$

where a is the channel width and b is the channel depth. Integrating the velocity profile gives the relation between the maximum 3D velocity to the velocity flux as,

$$V_{max}^{3D} = \frac{9}{4} U_Q. \tag{1.7.5}$$

I will be using and comparing both solver methods in my thesis and I would like to thank Dr Harley Klein, Dr Timothy Nicholson and Dr Mark Walkley for the help in using *flowSolve* and Dr Rosen Tenchev and again Dr Mark Walkley for their help in using and adapting *euFlow*.

1.8 Summary

In this chapter I briefly set out the motivation behind this thesis and the study of polymer rheology. I went on to introduce the basic principles that underpin the constitutive theories used in this paper, namely the Pompom constitutive equations.

In chapter 2 I will discuss the rheology of several polyethylenes with varying molecular structures and use the Pompom model to describe their behaviour in these simple flows. In doing so I will fit Pompom spectra to linear and non-linear rheological data. These spectra will then be used throughout my thesis when exploring the Pompom model's ability to correctly model certain flow situations.

In the subsequent chapters I will be focusing on particular flow situations in turn. Several key questions arise from this study; primarily can the Pompom model, with the correct parameterisation, capture the rheology of real polymer melts? Also, an important aspect of deriving a constitutive model can be to infer

molecular detail from fitting its parameters to rheological flows, so the question of what can be learned by the results of different flows is of concern.

In chapter 3 I will be examining branched polymer melts under a shear step-strain flow. The Doi-Edwards model Doi and Edwards (1986) for linear polymers predicts time-strain separation, with the result that a damping function can be derived from the model. LCB materials also exhibit time-strain separation, and in chapter 3 I look at how well the Pompom model captures this phenomena. It turns out that a branched damping function can be derived that is dependent on the non linear rheological parameters, $\{\tau_s, q\}$. I show that step strain can be used to differentiate between LCB-HDPEs and LDPEs.

In chapter 4 I will continue my investigation of shear flow by examining large amplitude oscillatory shear (LAOS) using Fourier transform rheology (FTR). This has traditionally been seen as frequency sweeps of the dynamic moduli for small amplitude. In this chapter not only strain dependency on the stress response but higher harmonics in the Fourier series are explored. In particular it is shown that in the limit of low strain amplitude the third harmonic is dependent on the two linear parameters, $\{G, \tau_b\}$, and only one non-linear Pompom parameter, the stretch relaxation time, τ_s. Even for high strain amplitudes of order unity, the dependence on the non-linear Pompom branching parameter is small making LAOS an experiment for examining the stretch relaxation time independently of the branching parameter. The Pompom model performs well with parameters fitted to uniaxial extensional data, but using simulated reaction processes which produces a highly detailed Pompom spectrum with thousands of modes provides even greater accuracy when comparing low-strain asymptotes with experimental data.

Chapter 5 and onwards is concerned with the performance the Pompom constitutive model in a complex cross-slot geometry. The Pompom model is compared to flow induced birefringence images. Flow through the cross-slot geometry causes a stagnation point and here the Pompom model shows a failing in capturing the rheology of cross-slot flow around the outflow centre line. Materials that contain long chain branching exhibit double cusping (W-Cusps) along the outflow centre line, which the Pompom model fails to capture. To explore this phenomenon further the flow induced birefringence images are transformed into

steady state extensional viscosity curves. These give smaller viscosities than seen in the maximum values obtained from stretching experiments. This leads to the conclusion that a transient overshoot in extension could exist.

To test whether a transient overshoot in extension would give W-cusps, in 6 an extra empirical stretch-relaxation term is incorporated into the Pompom model. With carefully parameterised Pompom spectra fitted to both transient uniaxial stretching data, and with the steady state fitted to cross-slot data, the rheology of several materials is modelled in cross-slot and found to give excellent predictions compared to flow induced birefringence images.

I would also like to acknowledge the many people who provided data for this thesis, making comparisons between constitutive modelling and experiment possible. I would like to thank John Embury and Dietmar Auhl for their linear oscillatory shear, transient shear and extensional data in chapter 2, and also Dietmar Auhl for the step strain data in chapter 3. In chapter 4 Vitor Borossa and Manfred Wilhelm kindly provided data for LAOS and Daniel Read and Chinmay Das the BoB spectra used for comparison. For the cross-slot birefringence images and LDV data in chapters 5 and 6, I would like to thank David Hassell, Timothy Lord and Malcom Mackley. Finally I would like to thank Henrik Rasmussen and Qian Huang for the extensional data in chapter 6, which is the only material for which I have data showing the transient overshoot in extension.

Chapter 2

Materials

In this chapter I will discuss the rheological tests commonly used to characterise polymer melts and then fit the experimental data with Pompom parameters, which will be used throughout the rest of my thesis. All experimental data in this chapter, and throughout my thesis was provided to me through the Microscale Polymer Processing project (μPP^2), in particular I would like to thank Dr. Dietmar Auhl and Dr. John Embury for the oscillatory shear, transient shear and uniaxial extensional data in this chapter and Dr. Dietmar Auhl again, for the data on molar mass distribution and branching numbers.

All the materials in my thesis are polyethylenes which can broadly be split up into three categories as previously mentioned in section 1.2. These are linear-low density polyethylenes (LLDPEs), branched high density polyethylenes (HDPEs) and low density polyethylenes (LDPEs). LDPEs are produced by high pressure, high temperature free radical polymerisation, whereas LLDPEs and HDPEs in this study are produced by metallocene catalysed polymerisation, which is produced at relatively lower pressures and temperatures compared to that for the polymerisation of LDPE. Further details of these practices can be found in, for example Peacock (2000).

For high pressure polymerisation, the high pressure forces ethylene monomers into close proximity where free radicals initiate the polymerisation process. During polymerisation free radicals can randomly extract a hydrogen atom from a pre-existing chain. This free radical then creates a site on which a new chain can grow, so forming a branch point. Branches can be short or long chained branches

(SCB or LCB, respectively) with the probability of branch point creation being proportional to molecular weight. Therefore high molecular weight LDPEs typically have more LCB. Metallocene catalysis uses a metal oxide additive to provide a smoother synthesis route than high pressure polymerisation. In contrast to the free radical catalyst, the metallocene catalyst provides a more uniform polymerisation chemistry which provides increased control over molecular architecture.

To characterise the molecular structure of a polymeric material the average molecular weight of the ensemble of polymer chains is often measured. A polymeric material will have a distribution of individual molecules with varying length. Such a material is called *polydisperse*. If all the molecules are of equal length then the material is called *monodisperse*. The molar mass of a molecule is $M_N = M_{mon}N$, where M_{mon} is the molecular mass of a monomer and N is the number of monomers in a chain. Defining the number fraction, n_N, as the number of molecules each containing N monomers the molar mass distribution can be described using moments of the number fraction distribution. The number average molar mass, M_n, is defined as the ratio between the first and zeroth moments of the number fraction distribution,

$$M_n = \frac{\sum_N n_N M_N}{\sum_N n_N} = \sum_N n_N M_N, \tag{2.0.1}$$

and the weight average molar mass is the ratio of the second and first moments of the number fraction,

$$M_w = \frac{\sum_N n_N M_N^2}{\sum_N n_N M_N} = \frac{\sum_N n_N M_N^2}{M_n}. \tag{2.0.2}$$

The polydispersity of a material can be characterised by the ratio of the weight average and number average molar mass, the polydispersity index $\frac{M_w}{M_n}$. Monodisperse materials have a polydispersity index of 1 and the larger the polydispersity index the broader the molar mass distribution will be.

Experimentally the molar mass distribution and hence the number and weight average molar masses can be measured using a combination of gel permeation chromatography and multi-angled laser light scattering (GPC-MALLS) [for further description see, for example Rubinstein and Colby (2003)]. Figure 2.1 shows

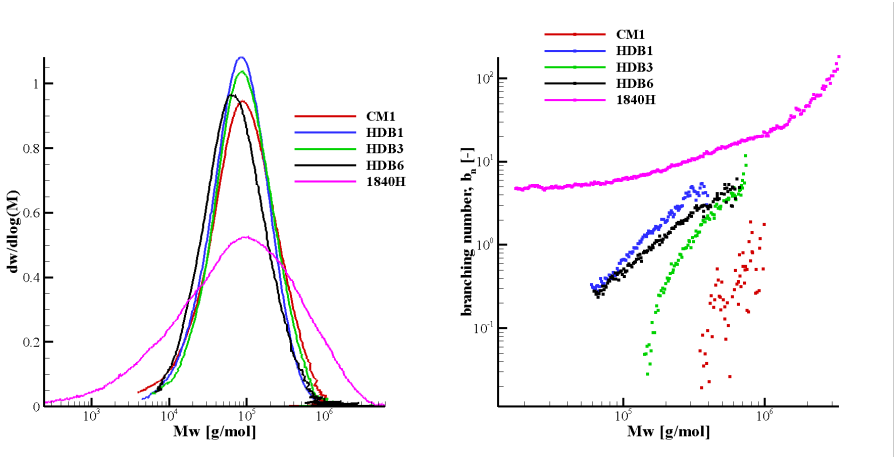

Figure 2.1: An example of molar mass distributions (left) and branching number, b_n (right) for several of the materials studied in this thesis. The molar mass distribution is broader for the LDPE 1840H than that of the HDPE materials, CM1, HDB1, HDB3 and HDB6. The branching number can clearly distinguish between the branching structure of the LDPE 1840H, the branched HDPEs and the linear HDPE CM1, but the measurements are not accurate enough to distinguish between the branched HDPEs.

the molar mass distribution of the following materials used in experiments analysed in this thesis (we refer to them using the material codes used throughout): linear HDPE CM1, LCB HDB1, LCB HDB3, LCB HDB6 and the LDPE 1840H [c.f. table 2.1] are plotted as a function of $\frac{dw}{d(log(M_w))}$ [Yau and Flemming (1968)], which is a quantity that represents the molar mass distribution of a polyethylene sample. Here, w is a weight fraction of polymer eluted. The molar mass distribution of LDPE 1840H is typical of the three LDPEs studied in this thesis, which has a much broader mass distribution compared to the metallocene catalysed materials, and hence a high polydispersity (c.f. table 2.1). The weight average molar mass of the LDPEs are all higher than any of the HDPEs in this study.

The technique of GPC-MALLS can also be used to measure the radius of gyration of polymers with respect to the distribution of molar masses, which can be used to obtain information on the degree of branching as the branching number, b_n [Zimm and Stockmayer (1949)]. The branching number is defined as the average number of branches per thousand carbons in the backbone of a molecule. In figure 2.1 the branching number as a function of molar mass

distribution is shown for several of the materials used in this thesis, detailed in table 2.1. Using GPC-MALLS the branching number can be measured sensitively enough to distinguish between the LDPE 1840H, the branched HDPEs (HDB1, HDB3 and HDB6) and the linear HDPE CM1. The GPC-MALLS branching number is in disagreement with the known branching structure of the HDPEs [Das et al. (2006)]. According to the GCP-MALLS data HDB1 is seen to have more branches per molecule than both HDB3 and HDB6, which is in contradiction to the actual branching structures where HDB1-HDB6 are labeled in order of increasing branching numbers [Costeux et al. (2002)].

Although measuring the molar mass distributions and branching number of a material provides information on the structure of the material it is not sensitive enough to parameterise constitutive theories, such as the Pompom constitutive model. This thesis is focused on the parameterisation of the Pompom model using dynamic flow measurements and finding which experiments are sensitive to certain aspects of the molecular detail.

Rheological measurements of the materials in both oscillatory and transient shear and uniaxial extensional flow were performed using a strain-controlled ARES rheometer (Advanced Rheometric Expansion System, Rheometric Scientific) with a force-rebalanced transducer (2K-FRT). The specimens were compression moulded at $170 - 190°C$ with the dimensions corrected for the thermal expansion. The rheological tests were repeated to assess the thermal stability and showed that no detectable molecular structure changes took place during the experiments.

Oscillatory shear test were carried out using 10mm parallel plates, while transient shear tests were carried out using various cone and plate geometries with cone angles between 2 and 10 degrees and a diameter of 10mm. Frequency sweeps were performed at a range of temperatures and the data shifted to the same temperature as the non-linear rheology using Williams-Landel-Ferry (WLF) theory [Ferry (1961)].

The non-linear elongational flow behaviour was characterised using the uniaxial stretching device SER (Sentmanat Elongational Rheometer, Xpansion Instruments [Sentmanat (2004)]) attached to the ARES rheometer. Different Hencky strain rates between $0.001s^{-1}$ and $10s^{-1}$ were applied to compression molded

Table 2.1: Material properties of polyethylenes investigated. The values for the HDB, CM series and Dow150R are consistent with previous studies [Wood-Adams and Dealy (2000), Crosby et al. (2002), den Doelder et al. (2005), Das et al. (2006), and Hassell et al. (2008)].

Sample	Code	M_W [kg/mol]	M_W/M_N [-]	T [°C]	η_0 [kPa s]	$\bar{\tau}_b$ [s]
Tubular	1800S	146	7	150	2.5	1.15
				140	3.0	1.38
				160	2.1	1.07
Tubular	1840H	240	9	150	51	50
Tubular	Dow150R	242	11	160	368	428
LCB-met.	HDB1	77	2.1	155	11	5.6
LCB-met.	HDB2	82	2.1	155	27	14.8
LCB-met.	HDB3	86	2.1	155	43	22.1
LCB-met.	HDB4	96	2.1	155	200	56
LCB-met.	HDB6	68	2.2	155	50	28
Lin-met.	CM1	104	2.1	155	11	1.09
				175	7.9	0.58
LCB-met.	CM2	92	2.2	155	32	16.3
LCB-met.	CM3	84	2.2	160	35	18

specimens with a width from 3mm to 10mm and a thickness of about 1mm [c.f. for example Münstedt and Auhl (2005)].

2.1 Pompom characterisation

In my thesis I analyse eleven polyethylene samples, three LDPEs, five LCB HDPEs and three LLDPEs, one of which (CM1) is linear. In chapters three to six the Pompom model will be analysed in various simple and complex flow types. Although each material will not appear in every chapter (only materials where experimental data is available for a particular flow type will be investigated in the relevant chapter), each chapter will compare materials of all three types.

The linear and non-linear Pompom parameters were fitted to data using *Reptate* software [Ramirez and Likhtman (2007)]. This software provides an automated fitting tool which uses the downhill simplex method and searches for the minimum error between experimental data points and theory.

The multimode Pompom model described in section 1.6.5 contains four parameters per mode. The linear Maxwell parameters are fitted to the dynamic moduli obtained from oscillatory shear measurements and as a further check the Maxwell parameters are then checked against the same data in the form of the complex viscosity (c.f. figure 2.2). Where available frequency sweeps at various temperatures are used to create a master curve using time-temperature superposition theory with two parameters [Ferry (1961)]. The shift to a different temperature consists of a horizontal shift and a vertical shift. The horizontal shift of frequency is of the form,

$$\omega(T_0) = a_T \omega(T), \tag{2.1.1}$$

where T is the original temperature and T_0 is the temperature which the data is shifted to, in degrees Celsius. The value of a_T is given by,

$$log_{10} a_T = \frac{-C_1(T - T_0)}{T + C_2}, \tag{2.1.2}$$

where C_1 and C_2 are material parameters. The vertical shift of modulus is given by,

$$G(T_0) = \frac{G(T)}{b_T}, \tag{2.1.3}$$

with,

$$b_T = \frac{\rho(T)T}{\rho(T_0)T_0} = \frac{(\rho_0 - TC_3)(T + 273.15)}{(\rho_0 - T_0C_3)(T_0 + 273.15)}, \tag{2.1.4}$$

where ρ is the density of the fluid at a given temperature, ρ_0 is the density of the polymer at $0°C$ and C_3 is a material parameter. For this study *Reptate* is used to minimize the χ^2 fit of the temperature dependence of frequency shifts with respect to C_1 and C_2 and the parameters $C_3 = 6.9 \times 10^{-4}\text{kg.m}^{-3}.\text{K}^{-1}$ and $\rho_0 = 0.95\text{kg.m}^{-3}$ are fixed.

Due to the broad molecular weight distribution of the polyethylene samples relaxation modes spanning four to six decades are required to capture their rheology. Thus in order to provide two to three relaxation times per decade nine to fifteen modes linear modes are required. The actual values of the orientation relaxation times, τ_{b_i}, are arbitrary but they are usually equally spaced on a logarithmic axis, which is the approach employed here. The upper and lower bounds

of τ_{b_i} are set to the limits of the oscillatory frequency data. In this thesis I have normally used twelve relaxation modes for each material. The exceptions to this are the fits to CM2 which has thirteen modes and Dow150R-b which is taken from a previous study [Hassell et al. (2008)] and has eleven modes. To obtain the relaxation moduli, G_i, I first use *Reptate* to obtain an automated fit. Then manual alterations are made to smooth out oscillations in the moduli, G_i, which occur due to the ill-posed nature of the inverse problem of finding G_i from measurements of the complex moduli [Davies and Anderssen (1998)]. These manual adjustments do not reduce the quality of the fit to the data and the fit between experimental data and fitted theory is shown for each material in the left hand columns of figures 2.5 to 2.8. Also plotted in the figures 2.5 to 2.8 (left) is the complex viscosity which is defined as $\eta^* = \frac{G^*}{\omega}$[Pa s] and in the case of limiting frequency, $\omega \to 0$, the zero shear viscosity, η_0, seen in table 2.1 is calculated. The complex shear viscosity for all materials can be seen in figure 2.2. In the limit of low frequency the zero shear viscosity for certain materials plateaus to a constant value, for example CM1 or 1800S. For these materials the lowest relaxation time is well defined. For materials where the zero shear viscosity does not plateau, for example Dow150R, the lowest relaxation time is not well defined. Also from figure 2.2, Dow150R at $160°C$ is the most viscous sample compared to 1800S at $150°C$ which is the least.

Commonly small amplitude oscillatory shear is used to fit Maxwell modes to the dynamic moduli, G', G'', the fits of which are shown in figures 2.5 to 2.8.However, other results for variables such as phase angle are defined from these variables and provide further information about material parameters [e.g. Malmberg et al. (2002); Vega et al. (1998, 1999)]. In chapter 4 the materials HDB3, HDB6 and 1840H are considered in further detail with respect to oscillatory shear in small and large amplitudes. For these materials we consider two plots that infer this extra materials detail; the Cole-Cole plot and the van Gurp-Palmen plot.

The Cole-Cole plot is a graph of $\eta^{'} = \frac{G^{'}}{\omega}$ against $\eta^{''} = \frac{G^{''}}{\omega}$ parameterised by Deborah number and can be used as an indicator of LCB [Schlatter et al. (2005)]. Figure 2.3 shows Cole-Cole plots for the three materials, HDB3, HDB6 and 1840H, which are studied in chapter 4. The point $\frac{d\eta^{''}}{d\eta^{'}} = 0$ gives a maximum point in the curve. The shift of this maximum point is attributed to LCB, however

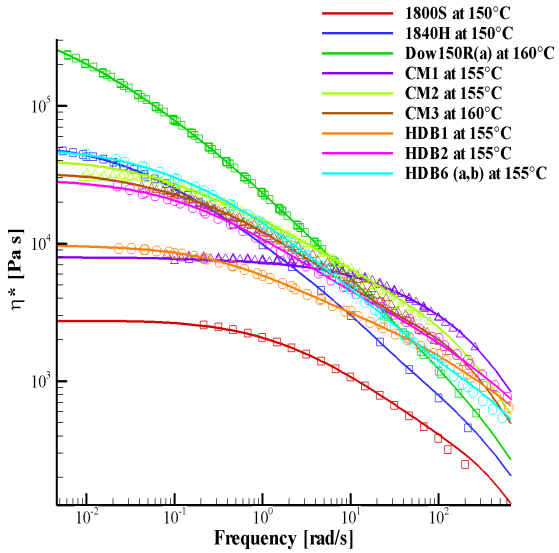

Figure 2.2: A plot of complex viscosity for all materials. The symbols represent the data and lines are linear Maxwell modes fitted to the dynamic moduli for each material

polydispersity can mask the LCB [Wood-Adams et al. (2000)]. For the three polyethylene materials the Cole-Cole plots do show increased LCB from LCB-HDPE to LDPE as expected. The Cole-Cole plots also indicate a dominant relaxation time, which is the inverse frequency at which the maximum point on the curve is achieved.

Another plot which uses standard linear rheology to show potential levels of LCB present in a material is the van Gurp-Palmen plot [Fleury et al. (2004); Malmberg et al. (2002); Schlatter et al. (2005); Trinkle et al. (2002)]. The van Gurp-Palmen plot shows the phase shift plotted as a function of complex modulus, G^*. The presence of LCB in indicated by a lower phase angle relative to the complex modulus.

The three materials featured in chapter 4 are again discriminated by branching structure as expected. For the HDPEs, HDB3 and HDB6, differences are only seen at higher values of G^*. The LDPE 1840H has a lower curve than the two HDPEs for all experimental values of G^*.

The Cole-Cole and van Gurp-Palmen plots both indicate the level of LCB in

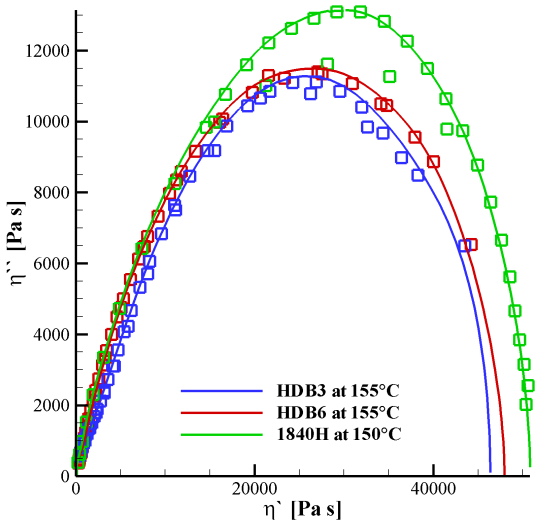

Figure 2.3: A Cole-Cole plot showing $\eta^{''}$ plotted against $\eta^{'}$, parameterised by Deborah number for the three materials studied in chapter 4. The peak of the curve shows the Cole-Cole relaxation time and the shift in peaks indicates increasing levels of LCB.

three polyethylenes that agrees with the other discussions about the materials in this chapter, however these indicators are modelled with linear Maxwell parameters and thus don't directly infer any quantitative detail about the molecular structure of of a material. As previously mentioned these results can also be a result of molecular weight distribution as well as LCB [e.g. Wood-Adams et al. (2000)]. It is impossible to tell the difference between molecular weight distribution and LCB without the molecular weight distribution information. Coupled with the fact that the non-linear Pompom parameters have no influence on modelling these results provides the motivation for non-linear measurements, such as strain hardening seen in extensional experiments. In chapter 4 it is shown that a low strain asymptote can be derived for the third harmonic which is dependent on the linear Maxwell parameters and the non-linear Pompom stretch relaxation time.

The non-linear Pompom parameters, τ_{s_i} and q_i, are fitting using the protocol set out by Inkson et al. (1999). The authors suggest physical constraints on

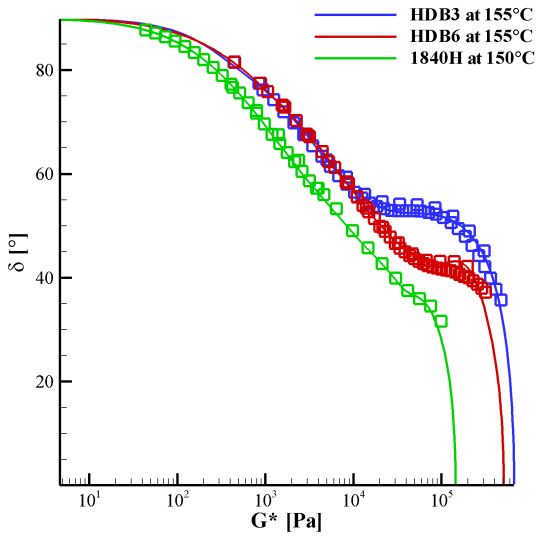

Figure 2.4: A van Gurp-Palmen plot indicating levels of LCB for the three materials studied in chapter 4. The more LCB is present in a material the smaller the value of the phase shift for the relative value of complex modulus. The figure indicates that HDB3, HDB6 and 1840H have increasing levels of LCB, respectively.

Table 2.2: The symbols used for transient shear and transient uniaxial extension plots in figures 2.5 to 2.8. Other strain rates are specified in the plots.

strain rate $[s^{-1}]$	0.01	0.03	0.1	0.3	1.0	3.0	10	30
symbol	□	△	○	▽	◇	▷	∗	◁

the choice of non-linear Pompom parameters (τ_{s_i},q_i). Namely, that the priority of branching must increase towards the centre of a molecule, i.e. the q_i is an increasing function in τ_{b_i} and that the ratio of relaxation times, $r_i = \frac{\tau_b}{\tau_s}$, is proportional to the number of entanglements in the backbone section. Although the number of entanglements is unknown the limit of $r_i = 1$ implies an unentangled backbone section. Inkson et al. (1999) also suggests that $\tau_{b_{i-1}} < \tau_{s_i}$, however this rule is not strictly adhered to and in the interests of improving the fit between experimental data and theory the relaxation time ratios are varied in the range,

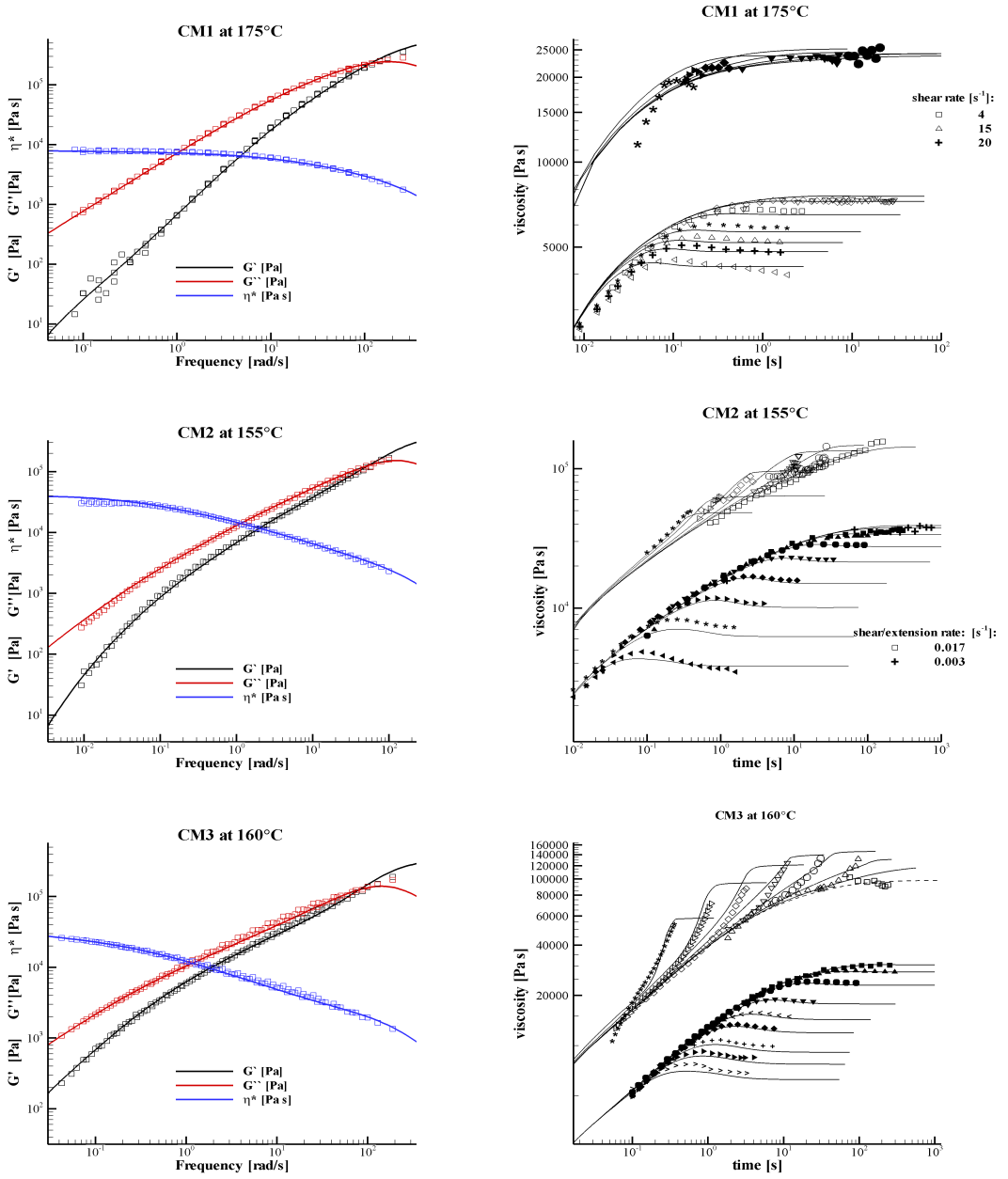

Figure 2.5: A comparison between theory fitted to oscillatory shear, transient shear and transient uniaxial extension for three LLDPE metallocene catalysed materials. Left: the dynamic moduli and complex viscosity fitted to a linear Maxwell spectrum. Right: transient shear and transient uniaxial extension data used to fit the non-linear parameters (τ_s and q) of the Pompom model. Data symbols correspond to shear/extension rates given in table 2.2.

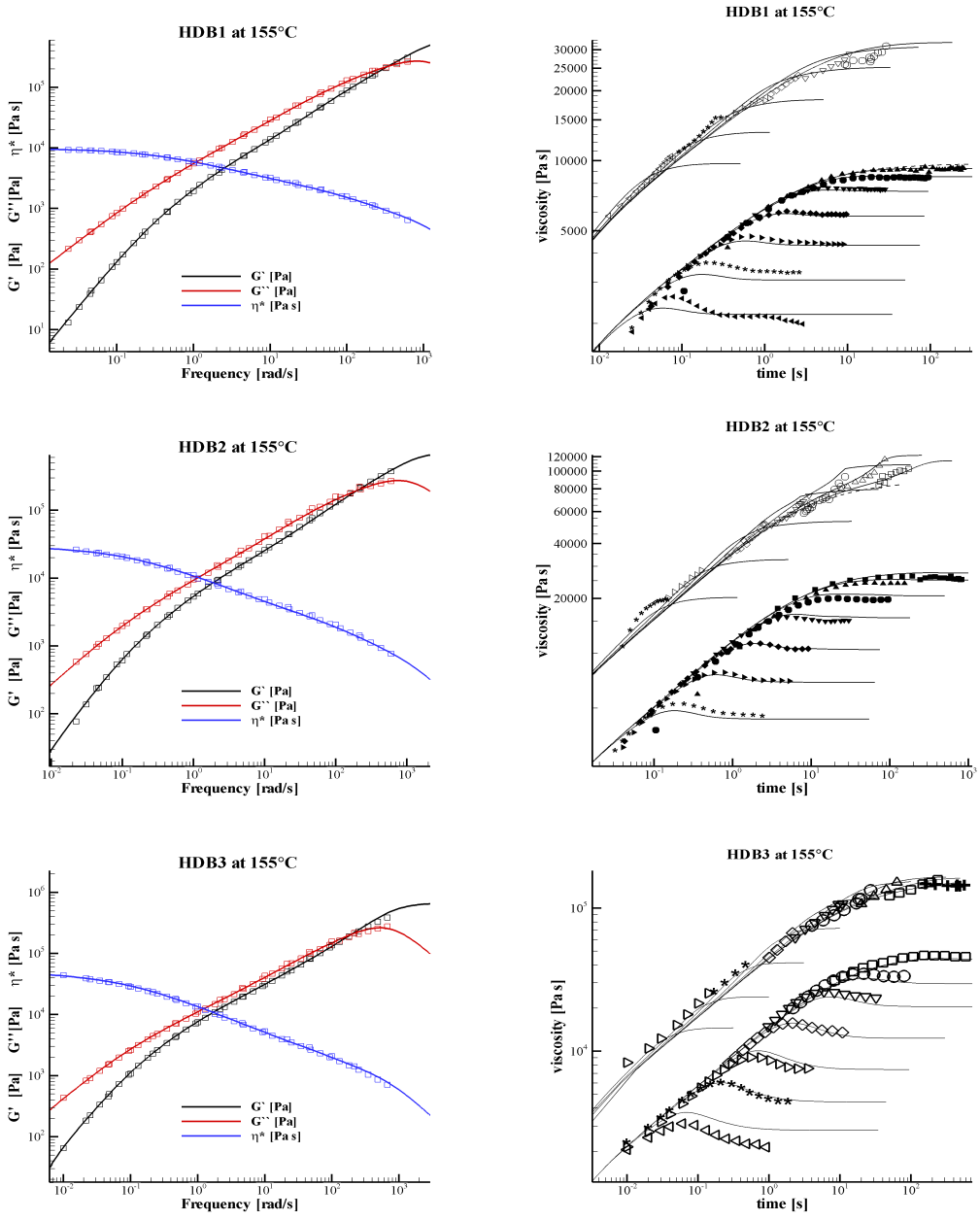

Figure 2.6: A comparison between theory fitted to oscillatory shear, transient shear and transient uniaxial extension for three of five HDPE metallocene catalysed materials. Left: the dynamic moduli and complex viscosity fitted to a linear Maxwell spectrum. Right: transient shear and transient uniaxial extension data used to fit the non-linear parameters (τ_s and q) of the Pompom model. Data symbols correspond to shear/extension rates given in table 2.2.

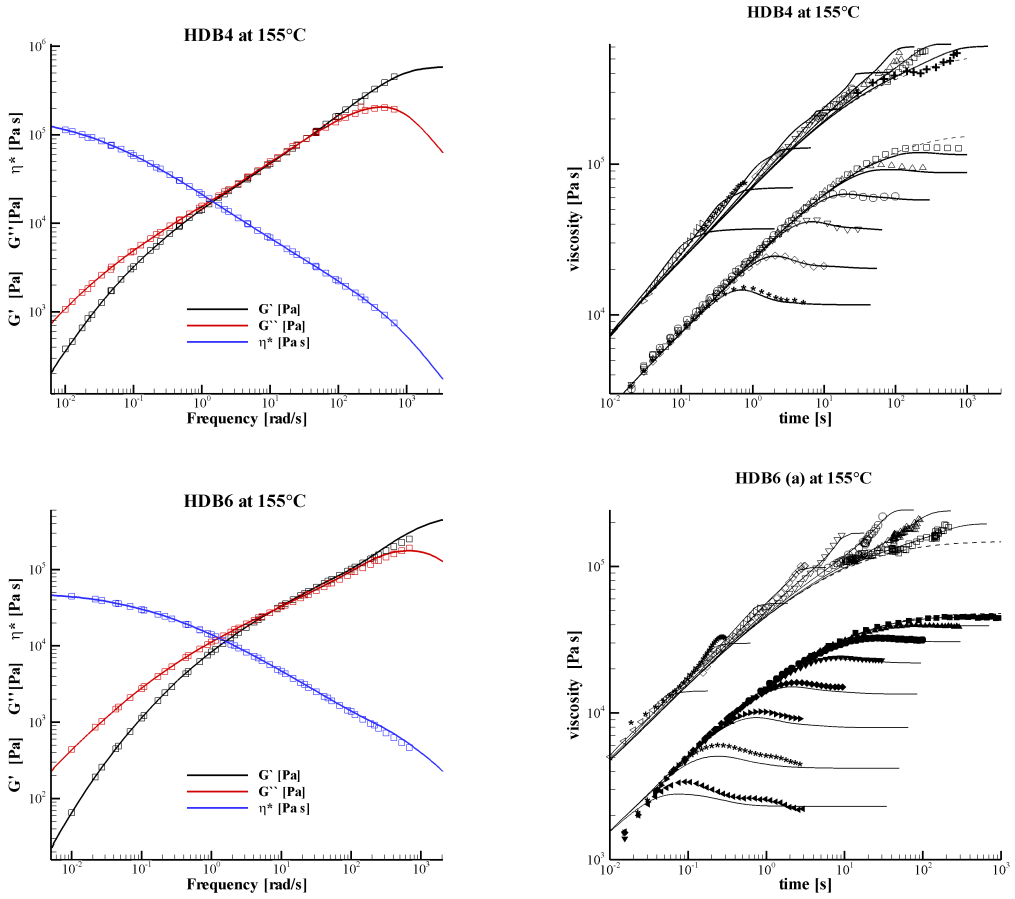

Figure 2.7: A comparison between theory fitted to oscillatory shear, transient shear and transient uniaxial extension for two of five HDPE metallocene catalysed materials. Left: the dynamic moduli and complex viscosity fitted to a linear Maxwell spectrum. Right: transient shear and transient uniaxial extension data used to fit the non-linear parameters (τ_s and q) of the Pompom model. Data symbols correspond to shear/extension rates given in table 2.2.

$1 < r_i < 10$.

The non-linear parameters are fitted to the extensional data and then against shear predictions. The value of q_i is mainly determined from the estimated limiting value in extensional viscosity at large strains. However, the extensional data obtained from the SER never reaches a steady state plateau as stretching experiments are prone to sample inhomogeneity and sample rupture [c.f McKinley and

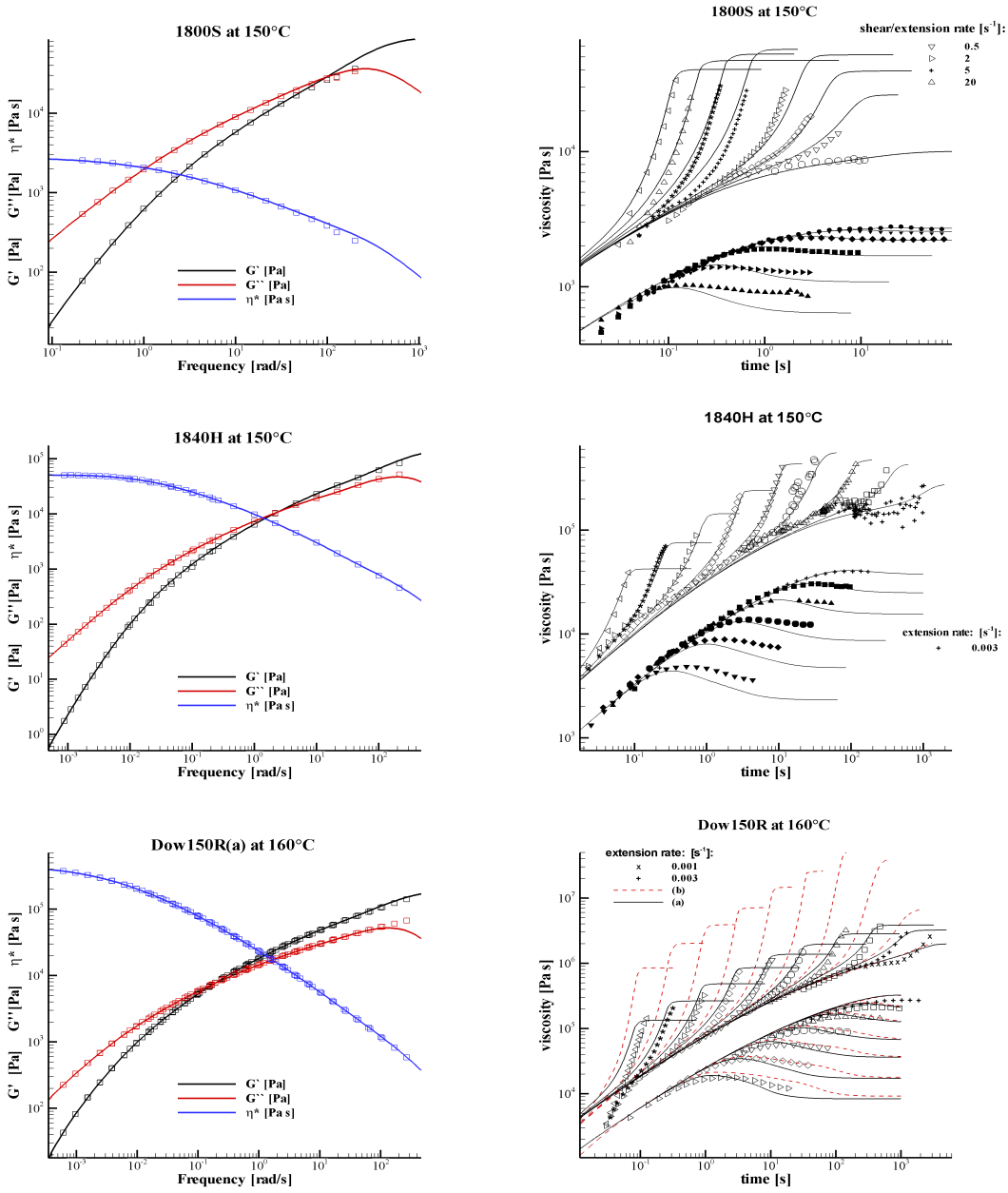

Figure 2.8: A comparison between theory and data for three LDPE materials. Left: the dynamic moduli and complex viscosity fitted to a linear Maxwell spectrum. Right: transient shear and transient uniaxial extension data used to fit the non-linear parameters (τ_s and q) of the Pompom model. For Dow150R two fits are proposed where an alternative fitting technique used for Dow150R(b) is examined. Data symbols correspond to shear/extension rates given in table 2.2.

Sridhar (2002); Minoshima and White (1986a,b) and Aho et al. (2010a,b)] and experiments are limited to Hencky strains less than four. This leaves an open question as to how to fit the Pompom theory to the data. I have chosen to fit the Pompom steady state plateau to equal the maximum SER data value reached before sample rupture.

This assertion will be tested within this thesis and in particular an alternative approach will be tested. A Pompom parameter set Dow150R(b) is taken from Hassell et al. (2008), where the approach to fitting was to estimate the degree of strain hardening that occurs after sample rupture to be higher than experimentally measured. This seems to be a reasonable approach, however the choice of steady state plateau is arbitrary. During the subsequent chapters both my fit (Dow150R(a)) and the alternative fit (Dow150R(b)) will be tested in various flow situations with the aim of determining the best fitting approach. It is important to ascertain which fitting procedure provides the most accurate flow modelling since parameterising the amount of strain hardening is important when considering complex flows containing an extensional component. A prediction of both Dow150R(a) and (b) in transient extensional and shear flow can be seen in figure 2.8, which shows the extensional viscosity steady state plateau to be considerably higher for Dow150R(b) than for Dow150R(a). Also, the spectrum Dow150R(a) matches the transient development of the data much more closely than Dow150R(b).

Figure 2.9 shows a plot of the moduli and branching priority for each Pompom spectra plotted as a function of τ_{b_i}. These parameters are detailed in appendix 2.A. Since the Pompom constitutive model is formed with a sum of modes, knowing the level of contribution from each mode can give insight into parameterising the Pompom model. Performing experiments at different flow rates is used to investigate the parameterisation of various modes, for example in uniaxial extensional flow the Weissenberg number characterising linear or non-linear flow is defined as, $W_i = \dot{\varepsilon}\bar{\tau}_b$. However, each Pompom mode has its own Weissenberg number for orientation and stretch relaxation, W_{i_b} and W_{i_s}, respectively. Thus modelling and experiments performed at low strain rates will only stretch the Pompom modes with the longest stretch relaxation times, i.e. where $W_{i_s} > 1$. For increasingly larger strain rates more Pompom modes will have orientation

and stretch Weissenberg numbers greater than one. Each mode makes a different contribution in shear and extensional flow. Figure 2.10 shows the contribution of each mode in shear flow, which can be measured by the product, $G_i \cdot \tau_{b_i}$. In extension the Pompom model predicts the same stress response for uniaxial and planar extension for a Weissenberg number $W_i = \dot{\varepsilon}\bar{\tau}_b \gg 1$ and the contribution to the stress from each mode is given by $G_i \cdot q_i^2$. Figure 2.10 shows the contribution from Pompom modes for three materials (CM3, HDB6, Dow150R) in this study. For both shear and extensional high Weissenberg number flows the contribution to the stress is dominated by the intermediate modes, making these modes important to parameterise correctly. In general the modes with the longest relaxation times contribute little to the total stress and this makes fitting the non-linear Pompom parameters to these modes difficult as the sensitivity in extension to the branching priority is reduced.

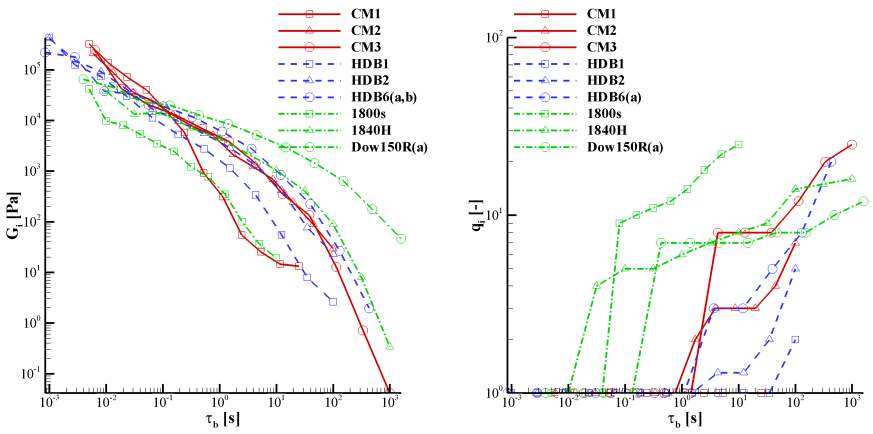

Figure 2.9: A plot of fitted linear modulus, G_i, and the non-linear branching priority, q_i, plotted against relaxation time τ_b. The details of these plots can be found in appendix 2.A

Since the fitting of Pompom parameters to data is an ill-posed problem, i.e. multiple solutions exist, then the question arises over which fit is 'right'. In other words, as the Pompom model infers molecular detail, the question of which is the set of parameters that infers the actual molecular detail of the material arises. To investigate this three spectra with near identical fits to extensional and shear data [figure 2.11] have been produced for the material HDB6, denoted

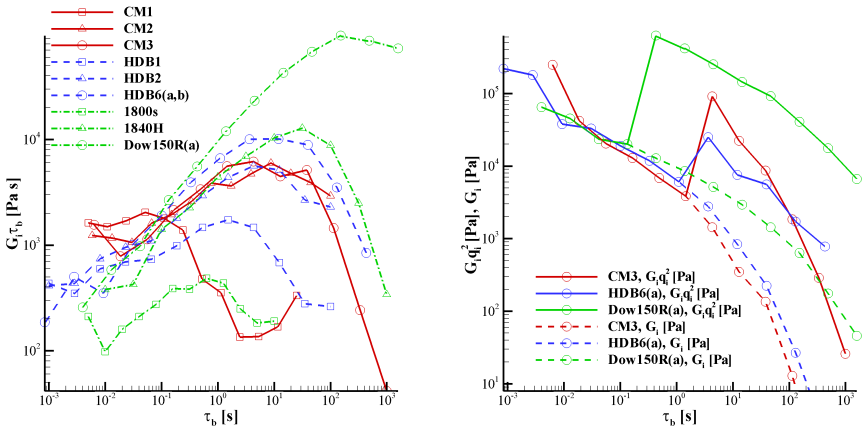

Figure 2.10: A plot of $G_i \cdot \tau_{b_i}$ and $G_i \cdot q_i^2$ against relaxation time τ_b. The two plots show the contribution each mode makes in a multimode sum in high Weissenberg number flows; on the left the shear contribution and on the right extensional contribution.

by the letters (a)-(c) in tables 2.4 and 2.5. The spectra HDB6(a) and HDB6(b) have the same linear spectrum but different non-linear parameters. HDB6(a) has generally larger q_is with faster stretch relaxation, i.e larger ratios, r_i, compared to HDB6(b). The spectra HDB6(c) has a different linear spectra with a smaller time between orientation relaxation times than HDB6(a,b) and the non-linear parameters considered to be an intermediate with medium branching and stretch relaxation parameters. Also HDB6(a,c) have five stretching modes, i.e. modes with non-linear parameters, where as HDB6(b) has six stretching modes. The spectrum for HDB6(a) has a marginally better transient fit to extensional data but there is no experimental information on the steady state plateau to fit the data to so none of the three fits can be considered to be superior to another. It should be noted that the similar stress response from three similar Pompom spectra does show the robustness of the approximation of modelling a LCB melt with the discrete sum of Pompom molecules. In subsequent sections I examine whether a particular flow type is sensitive to the subtle variations in the three spectra and whether one spectrum provides a superior prediction in the other experiments considered.

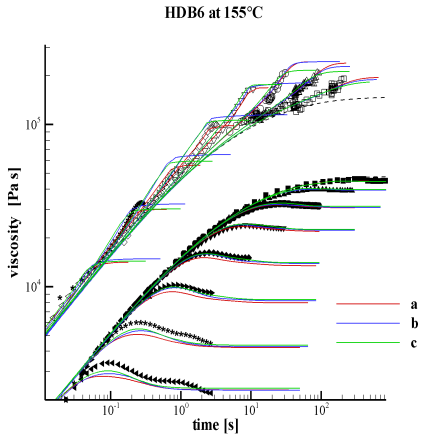

Figure 2.11: A plot showing the comparison of three spectra fitted to the material HDB6 in uniaxial extension and transient shear flow. The three spectra (detailed in appendix 2.A) show very similar agreement with experimental results, although the spectrum HDB6(a) does have slightly improved transient extensional response.

2.2 Conclusions

In this chapter I have detailed the Pompom parameters used to fit various polyethylene samples used throughout the rest of this thesis. In the subsequent chapters I investigate how well Pompom model performs in a variety of flows. In particular, can parameters fitted to extensional data capture the rheology of other flows? If there is discrepancy between experiment and model is this a result of the ill-posed nature of the fitting procedure, i.e is there a different set of Pompom parameters that can fit both experiments. If there is no Pompom parameterisation that can fit an experiment, then is there a deficiency in the Pompom model?

Also I will investigate several Pompom fits for the materials HDB6 and Dow150R. For Dow150R two different techniques have been used to derive Pompom non-linear parameters, namely to either fit the extensional steady state to the maximum SER results obtained, or assume a higher steady state as seen in Hassell et al. (2008). Can these two parameterisations be differentiated in different experiments and which fitting technique is most recommendable? For HDB6 three very similar spectra have been produced that all fit SER data very closely. Can any of the experiments investigated in this work help to resolve which of these

spectra is best to use, if any?

If discrepancies between experiment and theory arise through fitting errors then this is not necessarily a negative finding. In fact simply being able to reduce the size of Pompom parameter space by adding further constraints, deduced from considering experimental techniques not commonly used when fitting Pompom parameters leads further towards a more precise molecular description of a material.

2.A Pompom parameters

This appendix provides a detailed list of all the Pompom parameter sets used during this thesis, unless subsequently mentioned.

	CM1 at 155°C, 12 modes				CM2 at 155°C, 13 modes			
Mode, i	$G_i[Pa]$	$\tau_{b,i}[s]$	$\tau_{b,i}/\tau_{s,i}$	q_i	$G_i[Pa]$	$\tau_{b,i}[s]$	$\tau_{b,i}/\tau_{s,i}$	q_i
1	324041	0.00501	-	1	210295	0.00586	-	1
2	137478	0.01087	-	1	88330.4	0.01321	-	1
3	72139.8	0.02359	-	1	35687.2	0.02974	-	1
4	39856.8	0.05118	-	1	24142.5	0.06700	-	1
5	16198.8	0.11103	-	1	12841.1	0.15091	-	1
6	5774.95	0.24088	-	1	7587.82	0.33993	-	1
7	914.271	0.52261	-	1	5056.59	0.76568	-	1
8	312.033	1.13382	-	1	2106.61	1.72467	4	2
9	54.6331	2.45985	-	1	1219.45	3.88476	4	3
10	25.4509	5.33670	-	1	683.099	8.75031	5	3
11	14.5771	11.5781	-	1	243.090	19.7098	5	3
12	13.2977	25.1189	-	1	88.2695	44.3958	5	4
13					29.1552	100.000	5	7
	CM3 at 155°C, 12 modes				HDB1 at 155°C, 12 modes			
Mode, i	$G_i[Pa]$	$\tau_{b,i}[s]$	$\tau_{b,i}/\tau_{s,i}$	q_i	$G_i[Pa]$	$\tau_{b,i}[s]$	$\tau_{b,i}/\tau_{s,i}$	q_i
1	247540	0.00631	-	1	433472	0.00100	-	1
2	41955.2	0.01874	-	1	122601	0.00285	-	1
3	20339.9	0.05565	-	1	73615.9	0.00811	-	1
4	12961.3	0.16527	-	1	30072.1	0.02310	-	1
5	6872.94	0.49080	-	1	11178.2	0.06579	-	1
6	3841.27	1.45759	-	1	5265.64	0.18738	-	1
7	1430.96	4.32876	6	8	2749.20	0.53367	-	1
8	347.444	12.8556	6	8	1143.61	1.51991	-	1
9	134.989	38.1784	6	8	338.297	4.32876	-	1
10	12.8201	113.382	4	12	55.1885	12.3285	-	1
11	0.71838	336.723	4	20	7.94840	35.1119	-	1
12	0.04156	1000.00	4	25	2.61684	100.000	1	2

Table 2.3: A list of Pompom parameters for materials CM1, CM2, CM3 and HDB1 used throughout this study. Linear Maxwell parameters are fitted to oscillatory shear and non-linear parameters are fitted to transient shear and uniaxial flow.

	HDB2 at 155°C, 12 modes				HDB3 at 155°C, 12 modes			
Mode	$G_i[Pa]$	$\tau_{b,i}[s]$	$\tau_{b,i}/\tau_{s,i}$	q_i	$G_i[Pa]$	$\tau_{b,i}[s]$	$\tau_{b,i}/\tau_{s,i}$	q_i
1	413109	0.0010	-	1	422713	0.0016	-	1
2	152056	0.0028	-	1	116060	0.0043	-	1
3	91389.6	0.0081	-	1	62123.9	0.0118	-	1
4	41271.5	0.0231	-	1	30703.6	0.0323	-	1
5	16646.6	0.0658	-	1	16501.1	0.0882	-	1
6	9659.77	0.1874	-	1	9527.73	0.2409	-	1
7	5507.88	0.5337	-	1	5934.25	0.6579	-	1
8	2876.60	1.5199	-	1	3362.16	1.7970	2	1.3
9	1296.61	4.3289	10	1.3	1770.38	4.9081	9	1.4
10	417.052	12.329	9	1.3	688.780	13.405	9	1.5
11	75.9657	35.112	8	2	147.668	36.613	9	1.8
12	23.0226	100.00	1.2	5	64.4183	100.00	7	5
	HDB4 at 155°C, 12 modes				HDB6a at 155°C, 12 modes			
Mode, i	$G_i[Pa]$	$\tau_{b,i}[s]$	$\tau_{b,i}/\tau_{s,i}$	q_i	$G_i[Pa]$	$\tau_{b,i}[s]$	$\tau_{b,i}/\tau_{s,i}$	q_i
1	288814	0.0016	-	1	219226	0.0009	-	1
2	148263	0.0048	-	1	179387	0.0028	-	1
3	73732.9	0.0146	-	1	37873.9	0.0093	-	1
4	35850.5	0.0442	-	1	32981.4	0.0306	-	1
5	21573.4	0.1341	-	1	18896.9	0.1009	-	1
6	10424.4	0.4065	6	1.2	11820.4	0.3333	-	1
7	8137.79	1.2328	7	1.4	6053.40	1.1009	-	1
8	4211.77	3.7388	7	1.4	2767.03	3.6361	9	3
9	2345.31	11.338	7	1.5	840.575	12.009	9	3
10	978.088	34.385	8	1.6	224.024	39.662	3	5
11	248.950	104.28	7	2	26.7746	130.99	2	8
12	98.4469	316.23	3	6	1.94559	432.63	7	20

Table 2.4: A list of Pompom parameters for materials HDB2, HDB3, HDB4 and HDB6 (a) used throughout this study. Linear Maxwell parameters are fitted to oscillatory shear and non-linear parameters are fitted to transient shear and uniaxial flow.

	HDB6b at 155°C, 12 modes				HDB6c at 155°C, 12 modes			
Mode	$G_i[Pa]$	$\tau_{b,i}[s]$	$\tau_{b,i}/\tau_{s,i}$	q_i	$G_i[Pa]$	$\tau_{b,i}[s]$	$\tau_{b,i}/\tau_{s,i}$	q_i
1	219226	0.0009	-	1	332848	0.0010	-	1
2	179387	0.0028	-	1	58677.2	0.0029	-	1
3	37873.9	0.0093	-	1	52262.7	0.0081	-	1
4	32981.4	0.0306	-	1	31683.5	0.0231	-	1
5	18896.9	0.1009	-	1	18795.6	0.0658	-	1
6	11820.4	0.3333	-	1	13806.8	0.1873	-	1
7	6053.40	1.1009	5	2	7762.11	0.5337	-	1
8	2767.03	3.6361	5	2	4576.71	1.5199	5	2
9	840.575	12.009	5	3	1929.19	4.3288	5	3
10	224.024	39.662	2	5	826.986	12.329	5	3
11	26.7746	130.99	4	5	175.380	35.112	5	4
12	1.94559	432.63	4	5	64.0465	100.00	2.3	8
	1800S at 140°C, 12 modes				1800S at 150°C, 12 modes			
Mode, i	$G_i[Pa]$	$\tau_{b,i}[s]$	$\tau_{b,i}/\tau_{s,i}$	q_i	$G_i[Pa]$	$\tau_{b,i}[s]$	$\tau_{b,i}/\tau_{s,i}$	q_i
1	42020.9	0.0050	-	1	56339.6	10.000	-	1
2	9803.49	0.0100	-	1	12305.3	4.8064	-	1
3	7989.03	0.0200	-	1	8755.15	2.3101	-	1
4	5305.43	0.0398	-	1	5978.29	1.1103	-	1
5	3444.06	0.0794	2.2	9	4082.17	0.5337	2.2	9
6	2448.64	0.1585	2.2	10	2529.70	0.2565	2.2	10
7	1209.93	0.3162	2.2	11	1564.11	0.1233	2.2	11
8	768.726	0.6310	2.2	12	722.701	0.0593	2.2	12
9	346.388	1.2589	2.2	14	313.623	0.0285	2.2	14
10	99.1665	2.5119	2	18	108.407	0.0137	2	18
11	36.4592	5.0119	2.1	22	27.2916	0.0066	2.1	22
12	18.9970	10.000	2.5	25	11.8188	0.0032	2.5	25

Table 2.5: A list of Pompom parameters for materials HDB6 (b), HDB6(c), 1800S at $140°C$ and $150°C$ used throughout this study. Linear Maxwell parameters are fitted to oscillatory shear and non-linear parameters are fitted to transient shear and uniaxial flow.

	1800S at 160°C, 12 modes				1840H at 155°C, 12 modes			
Mode, i	$G_i[Pa]$	$\tau_{b,i}[s]$	$\tau_{b,i}/\tau_{s,i}$	q_i	$G_i[Pa]$	$\tau_{b,i}[s]$	$\tau_{b,i}/\tau_{s,i}$	q_i
1	56463.0	0.0025	-	1	64373.3	0.0032	-	1
2	10126.2	0.0053	-	1	37846.4	0.0100	-	1
3	8280.15	0.0113	-	1	13408.4	0.0316	1.3	4
4	6876.31	0.0241	-	1	14121.9	0.1000	4.7	5
5	3999.72	0.0512	2.2	9	7155.58	0.3162	5	5
6	2889.58	0.1087	2.2	10	4417.12	1.0000	5	6
7	1555.57	0.2310	2.2	11	2191.35	3.1622	5	7
8	674.243	0.2908	2.2	12	1034.37	10.000	5	8
9	270.474	1.0428	2.2	14	404.689	31.623	2.6	9
10	81.7654	2.2154	2	18	88.1892	100.00	2.6	14
11	22.3680	4.7068	2.1	22	7.91095	316.23	1	15
12	10.0000	10.000	2.5	25	0.34016	1000.0	1	16
	Dow150a, 160°C, 12 modes				Dow150b, 160°C, 11 modes			
Mode, i	$G_i[Pa]$	$\tau_{b,i}[s]$	$\tau_{b,i}/\tau_{s,i}$	q_i	$G_i[Pa]$	$\tau_{b,i}[s]$	$\tau_{b,i}/\tau_{s,i}$	q_i
1	64715.5	0.0040	-	1	49451.0	0.0316	-	1
2	45406.6	0.0129	-	1	21039.0	0.1000	-	1
3	23491.1	0.0415	-	1	13894.0	0.3160	1	2
4	19983.8	0.1341	-	1	9626.00	1.0000	4	18
5	12836.6	0.4329	4	7	6070.00	3.1620	4	20
6	8565.19	1.3978	5	7	3519.00	10.000	4	20
7	5152.39	4.5138	5	7	1783.00	31.620	3	20
8	2934.19	14.576	5	7	797.400	100.00	4	25
9	1436.93	47.068	5	8	288.200	316.20	2	40
10	635.072	151.99	5	8	74.0000	1000.0	3	55
11	176.198	490.81	3.5	10	13.6900	3162.0	3	20
12	45.9648	1584.9	2.3	12				

Table 2.6: A list of Pompom parameters for materials 1800S at 160°C, 1840H, Dow150R (a) and Dow150R (b) [taken from Hassell et al. (2008)] used throughout this study. Linear Maxwell parameters are fitted to oscillatory shear and non-linear parameters are fitted to transient shear and uniaxial flow.

Chapter 3

Step-Strain Flow

Long chain branched polymer melts such as LDPE and branched metallocene polyethylenes show strong time-strain separability in step strain. Constitutive models of the multimode Pompom form are highly successful in modelling the stress generated by general flow histories for these materials. However, a single Pompom mode is not time-strain separable, and reconciling this to the step-strain phenomenon has been a challenge. Indeed, McLeish et al. (1999) were able to show that melts made of single Pompom architectures do not show time strain separation as predicted by the Pompom theory. This means that time strain separability occurs with polydispersity and the multimode version of the Pompom model is required to capture the effects of polydispersity. We investigate multimode integral Pompom model and a differential approximation to compare time-strain separation, with respect to mode density. Here we show that for a wide class of branched distributions, a family of damping functions can be derived with a response that is very close to separable. We evaluate the family for both LDPE and branched HDPE melts and show that a damping function derived from the multimode Pompom model, gives an accurate prediction of the damping behaviour in step-strain experiments.

3.1 Introduction

An experimentally observed rheological property of many branched polymer melts is that the stress relaxation following a step strain satisfies time-strain separability (TSS). In these cases the relaxation modulus, $G(\gamma, t)$, after a step strain of γ can be factorised to a good approximation as,

$$G(\gamma, t) = G(t)h(\gamma), \tag{3.1.1}$$

where $G(t)$ is the linear relaxation spectrum and $h(\gamma)$ a function of strain only, is known as the 'damping function'.

This observation is used as the basis of the K-BKZ family of integral constitutive models [Bernstein et al. (1963); Wagner and Stephenson (1979)], where TSS is 'built in'. However, these models do not perform well in all geometrical flows of long-chain branched (LCB) melts. For LCB polymer melts a multimode version of the Pompom model, introduced by McLeish and Larson [McLeish and Larson (1998); McLeish (2002)] has been highly successful in modelling the non-linear rheology. This model, which is based on tube theory for a simple branched molecule does not explicitly satisfy time-strain separability. Larson has shown for a restricted class of models [Larson (1985a), Larson (1985b)] that apparent time-strain separability may arise from superposition of modes, but whether this applies to the Pompom model is still open to question.

Indeed, in a comprehensive review of an early version of the Pompom equations, Rubio and Wagner (2000) found no time-strain separable region in the non-linear relaxation modulus. However, this version of the model did not incorporate the important mechanism of branch-point withdrawal introduced by Blackwell et al. (2000). This makes a considerable difference to the smoothness of response in strong flows.

Chodankar et al. (2003) reviewed the differential and integral forms of the Pompom model and showed that by incorporating branch point withdrawal multimode versions of both models display apparent time strain separability in step strain. A numerical damping function could be produced at various times that was in better agreement with the experimentally determined damping function

of a branched LDPE, Lupolen 1810H, than the tube theory damping function for linear melts, $h(\gamma) = (1 + \frac{4}{15}\gamma^2)^{-1}$. As well as the original differential and integral forms they also analysed the Öttinger differential version of the model [Öttinger (2001)] and found that this gave a better approximation to the integral model at the terminal time than the original differential approximation of McLeish and Larson.

In further work Venerus (2005) and Venerus and Nair (2006) used the Öttinger version without the maximum stretch condition to model the stress relaxation of entangled linear polymers where the strain is imposed over a finite time interval and found good quantitative agreement for a variety of different melts and solutions, even though this model was designed for branched polymers.

However, the more sensitive technique of Fourier transform rheology [Fleury et al. (2004); Vittorias and Wilhelm (2007)] in large amplitude oscillatory shear shows that time-strain separability does not, after all, hold perfectly for branched polymers. These observations raise a series of questions related to the general issue of how apparent TSS arises:

- For what subsets, if any, of multimode Pompom models are the predictions in non-linear step strain time-strain separable?
- When these conditions are relaxed, how close to separability are the predictions for a wider class of models?
- To what extent do multimode Pompom models derived from fits to extensional data on long chain branching melts satisfy the conditions of the classes stated above?

In this chapter these issues will be addressed. We review the original integral and differential Pompom equations and assess how the range and density of modes affects the accuracy of the differential model. In section 3.2.1 we also examine how the range of relaxation times in the multimode spectrum affects the timescales over which apparent time-strain separability is observed and the behaviour at the terminal time. In section 3.3 we derive an analytic damping function approximation using certain model and material assumptions under which the Pompom model is time-strain separable. This damping function is then compared against

'idealised fluids' that incorporate some or all of the assumptions made during the derivation. Finally, in section 3.4, we survey a range of branched polyethylene melts produced by two different synthesis routes to examine how close these materials are to the conditions for time-strain separability. Comparisons are then made between the derived damping function and the modelled stress relaxation over a wide range of times and strains.

3.2 Pompom in Step Strain

A step strain flow is modelled by imposing a shear-rate, $\dot{\gamma} = \gamma\delta(t)$, so that no relaxation occurs during deformation. The calculation of the initial orientation and stretch can be found by neglecting terms associated with the characteristic relaxation times, τ_b and τ_s, in their corresponding dynamical equations. After this initial stage it is assumed that no more deformation occurs.

I employ the Pompom equations discussed in section 1.6.5 and consider both the differential and integral versions of the Pompom model, with stress given by equation (1.6.55), the stretch equation given by (1.6.48) and orientation given by (1.6.53) and (1.6.54) (differential) as well as (1.6.30) and (1.6.31) (integral). Since there is no reversing flow, the instance of the backbone tube length being less than its equilibrium length, the adjustment made by Lee et al. (2001) (equation 1.6.49) does not need to be considered. In the differential model the initial orientation is given by,

$$S_{xy}(\gamma, 0^+) = \frac{\gamma}{\gamma^2 + 3}, \tag{3.2.1}$$

with stretch given by [McKinley and Hassager (1999)],

$$\lambda(\gamma, 0^+)_D = (1 + \frac{1}{3}\gamma^2)^{\frac{1}{2}}. \tag{3.2.2}$$

For the integral Pompom model,

$$Q_{12}(\gamma) = \frac{4\gamma}{15(1 + \frac{4}{15}\gamma^2)} \qquad \text{and} \qquad \lambda(\gamma, 0^+)_I = (1 + \frac{4}{15}\gamma^2)^{\frac{1}{2}}. \tag{3.2.3}$$

Using the initial orientation as a boundary condition, the relaxation of the

fluid can be computed for the integral and differential model shear relaxation moduli, and are given respectively by,

$$G_I(\gamma,t)=\frac{\sigma_{xy}}{\gamma}=\frac{G_0\lambda_I^2(\gamma,t)e^{-\frac{t}{\tau_b}}}{1+\frac{4}{15}\gamma^2}, \tag{3.2.4}$$

and

$$G_D(\gamma,t)=\frac{\sigma_{xy}}{\gamma}=\frac{G_0\lambda_D^2(\gamma,t)e^{-\frac{t}{\tau_b}}}{1+\frac{1}{3}\gamma^2e^{-\frac{t}{\tau_b}}}. \tag{3.2.5}$$

The differences in the models become apparent at late times ($t \gg \tau_s$). The orientation of the integral model alone, appears to show TSS; this is observed at terminal times when the backbone stretch has relaxed. The differential orientation behaves differently as G_D becomes independent of strain in the long time limit. This unphysical behaviour can be observed in figure 3.1.

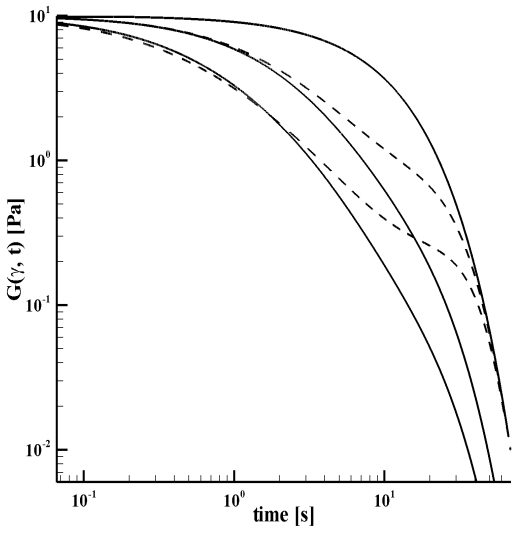

Figure 3.1: The relaxation modulus for the integral (solid) and differential (dashed) Pompom model depicting the differences in terminal time behaviour between the models. The strains used were $\gamma = 0.1, 5, 10$ with parameters $G_0 = 10$Pa, $\tau_b = 10$s, $\tau_s = 5$s and $q = 6$.

To examine this effect further it is convenient to look at the ratio of the nonlinear and linear stress relaxation modulus by defining the damping ratio, $H(\gamma,t)$,

as,

$$H(\gamma, t) = \frac{G(\gamma, t)}{G(t)}, \tag{3.2.6}$$

where $G(t) = \sum_i G_i e^{-\frac{t}{\tau_{b_i}}}$ is the linear relaxation modulus. For a time-strain separable fluid, $H(\gamma, t)$ is independent of t and is equal to the damping function.

The results for the one-mode model can be seen in figure 3.2. Note for both integral (dashed) and differential (solid) models that $H(\gamma, t)$ displays two phases of relaxation, for times $t < \tau_b$ and $t > \tau_b$. No relaxation occurs until a time of order τ_s when the stretch begins to relax. During this phase both models show a similar decay of $H(\gamma, t)$. Differences between the models appear at times beyond τ_b where the orientation relaxes. In the integral model the damping ratio tends to a plateau, which is a Doi-Edwards-like damping regime. However, the differential model shows an increase in the damping ratio and ultimately tends to the limit of $H(\gamma, t) = 1$. This occurs because the non-linear denominator in the differential relaxation modulus, (3.2.5), decays with time, unlike in the integral case, (3.2.4).

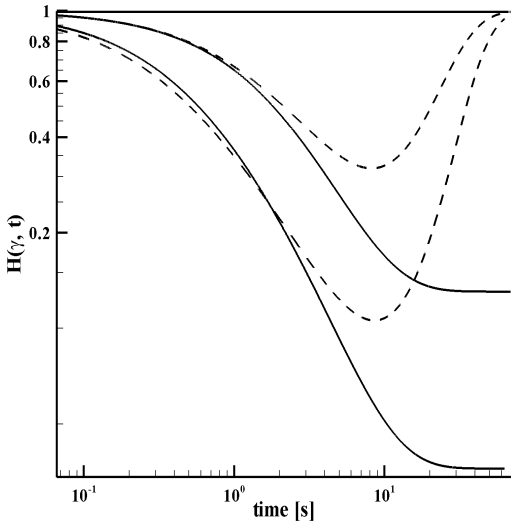

Figure 3.2: The damping ratio $H(\gamma)$ against time for a one mode integral (solid) and differential (dashed) Pompom. The strains used were $\gamma = 0.1, 5, 10$ with parameters $G_0 = 10$Pa, $\tau_b = 10$s, $\tau_s = 5$s and $q = 6$.

Clearly neither model displays TSS as found experimentally for LDPE materials, except for times beyond τ_b. This is however, to be expected since real 'Pompom' polymer melts, constructed from monodisperse controlled-architecture polymers, display exactly this failure of TSS arising from the separation of stretch and orientation [McLeish et al. (1999)]. More seriously the differential model does not properly approximate the behaviour of the integral model at long times. We need to assess the seriousness of this failure in the context of multimode models relevant to polydisperse branched melts.

3.2.1 The multimode Pompom model

The multimode Pompom model [Inkson et al. (1999)] was introduced to account for polydispersity and multi-level branching in LDPE. Rubio and Wagner (2000) used this model to describe the LDPE, IUPAC-A in step strain. This model, however, did not incorporate the modified stretch equation [Blackwell et al. (2000)] which was instrumental in achieving quantitative fits to start up flows of LDPEs.

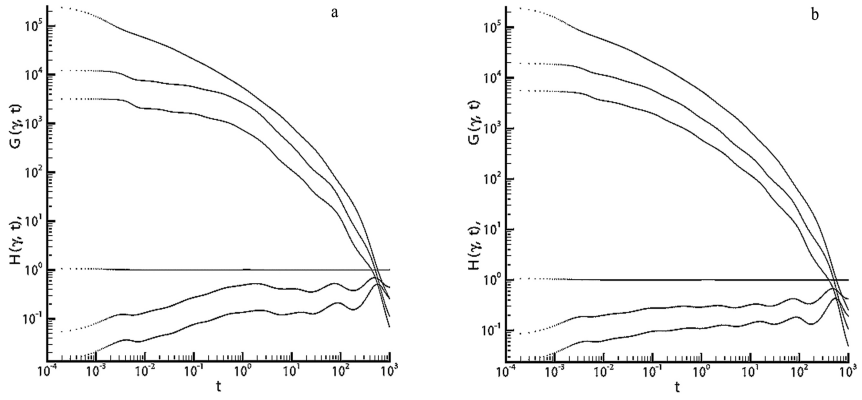

Figure 3.3: The relaxation modulus and damping ratio parameters for IUPAC A. The modifications to the equation for backbone stretch relaxation by Blackwell improve the plateau modulus showing time-strain separability over three orders of magnitude in time from 10^{-1}s to 10^{2}s (from left to right $\nu^* = 0$ and $\nu^* = \frac{2}{q-1}$). Strains of 0.1, 10 and 20 were used.

Table 3.1: Parameters used for IUPAC A. Both the cases of $\nu^* = 0$ and $\nu^* = \frac{2}{q}$ are listed. Linear data produced from Laun (1986), $\nu^* = 0$ parameters from Inkson et al. (1999) and $\nu^* = \frac{2}{q-1}$ parameters are from Blackwell et al. (2000).

			$\nu^* = 0$		$\nu_i^* = 2/q_i - 1$	
Mode no., i	G_i/Pa	$\tau_{b,i}/s$	q_i	$\tau_{b,i}/\tau_{s,i}$	q_i	$\tau_{b,i}/\tau_{s,i}$
1	1.520×10^5	1.0×10^{-3}	1.0	–	1.0	–
2	4.005×10^4	5.0×10^{-3}	1.0	–	1.0	–
3	3.326×10^4	2.8×10^{-2}	1.0	–	2.0	2.0
4	1.659×10^4	1.4×10^{-1}	1.0	–	2.0	2.5
5	8.690×10^3	7.0×10^{-1}	2.0	2.0	4.0	2.0
6	3.151×10^3	3.8×10^0	6.0	1.7	7.0	2.0
7	8.596×10^2	2.0×10^1	6.0	2.15	8.0	1.5
8	1.283×10^2	1.0×10^2	9.0	1.25	12.0	1.0
9	1.8495×10^0	5.0×10^2	22.0	1.1	30.0	1.0

Figure 3.3 compares the shear relaxation modulus and damping ratio for the two fits to IUPAC A. This shows the differences between the unmodified ($\nu^* = 0$) and modified ($\nu^* = \frac{2}{q-1}$) backbone stretch ODE, (1.6.48), given by Blackwell et al. (2000) and with Pompom parameters shown in table 3.1. Note, the parameters for IUPAC A in Blackwell et al. (2000) used a strain parameter $\nu^* = \frac{2}{q}$, which was later corrected to $\nu^* = \frac{2}{q-1}$ in McLeish (2002). In figure 3.3a, for $\nu^* = 0$, the damping ratio shows no plateau with respect to time, showing no time-strain separability. In figure 3.3b the damping ratio plateaus, after initial early relaxation of faster modes, for up to three decades of time. The damping ratio, $H(\gamma, t)$, shows clearly improved time-strain separability given by the improved modelling of branch point withdrawal.

When the faster modes have relaxed they contribute little to the total relaxation modulus. However, as the number of modes left to relax reduce, the terminal time behaviour, in which $H(\gamma, t)$ tends to one, becomes more dominant until the final mode displays the behaviour as seen in single mode relaxation. This causes spurious oscillations in the damping ratio for the differential Pompom model near the terminal time, as can be seen in figure 3.3 after the plateau of time-strain separability.

To examine the effect of different discretization of the material spectrum on

Table 3.2: Parameters used for 1840H - 9 and 12 mode models. The 9 mode parameters were used in section 3 and compared with the 12 mode model to show that an increase in the number of modes gives an increase in the period of TSS predictions.

	1840H at 150°C - 9 modes				1840H at 150°C - 12 modes			
Mode, i	G_i/Pa	$\tau_{b,i}/s$	$\tau_{b,i}/\tau_{s,i}$	q_i	G_i/Pa	$\tau_{b,i}/s$	$\tau_{b,i}/\tau_{s,i}$	q_i
1	92497	0.00316	–	1	64373	0.00316	–	1
2	27781	0.0154	1.0	2	37846	0.01	–	1
3	19747	0.0750	1.7	3	13408	0.0316	1.3	4
4	9610	0.365	4.4	3	14122	0.1	4.7	5
5	4326	1.778	5	5	7155	0.316	5.0	5
6	1583	8.660	2.3	5	4417	1.00	5.0	6
7	405.2	42.17	2.3	8	2191	3.162	5.0	7
8	30.44	205.4	1.6	11	1034	10.0	5.0	8
9	0.407	1000.0	1.6	14	404.7	31.62	2.6	9
10					88.19	100	2.6	14
11					7.911	316.2	1.2	15
12					0.3402	1000	1.0	16

the predictions of TSS, in table (3.2) we give details of two different spectra for 1840H. 1840H is a similar material to IUPAC A and its material properties are listed in table (2.1), which includes the spectra in table 2.6 for comparison and has full rheology shown in figure 2.8. The two different spectra were prepared by fitting 9 and 12 modes Pompom models to linear and extensional rheology measurements for relaxation times in the range 0.003s to 1000s. Figure 3.4 shows a comparison between both models and experimental measurements, at 150°C, in extensional and shear stress. Extension rates of 0.001, 0.003, 0.01, 0.03, 0.1, 0.3s^{-1} and shear rates of 0.003, 0.01, 0.03, 0.1, 0.3, 1, 3s^{-1} were used. Although there is little difference in the quality of the fits to the rheological data, in figure 3.5b) it can be seen that the denser 12 mode spectrum has a smoother plateau in damping ratio and later transition to terminal damping. These results are compared to the experimental damping behaviour of 1840H in figure 3.11.

Figure 3.5a) compares the differential and integral model for the 12 mode spectrum for 1840H. The damping ratio shows that in a multimode model the differential model approximates the plateau of the integral model correctly. This

happens because the oscillations in the differential model occur on a similar time scale to the integral model transitioning to a Doi-Edwards damping regime, and occur once most of the stress in the mode has relaxed. Consequently neither affect the overall stress significantly, except in the terminal zone.

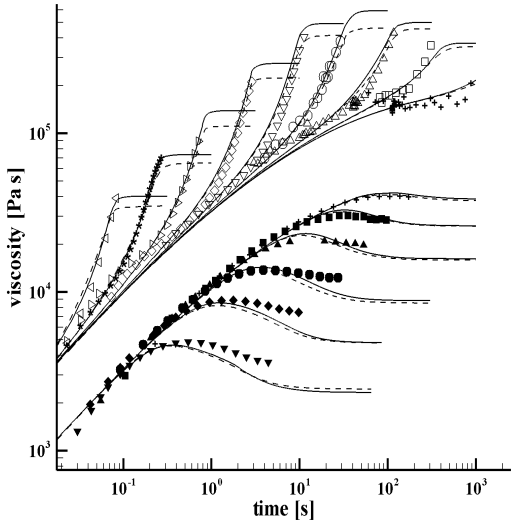

Figure 3.4: A comparison of the 9 (dashed lines) and 12 (solid lines) mode Pompom fits to extensional and shear data taken at 150°C for 1840H. Extension rates of $0.003, 0.01, 0.03, 0.1, 0.3, 1, 3, 10, 30\text{s}^{-1}$ and shear rates of $0.03, 0.1, 0.3, 1, 3, 10\text{s}^{-1}$ were used. There appears little difference between the two fits, however the increased density of modes in the 12 mode fit gives a longer region of TSS.

We conclude that empirically, a sufficiently dense mode-spectrum of either the differential or integral multimode Pompom model does exhibit TSS, over four decades of time, when parameters are extracted from representative LDPE materials. This takes us to the question of what properties of both material and model cause this behaviour to arise, when the individual modes are not TSS?

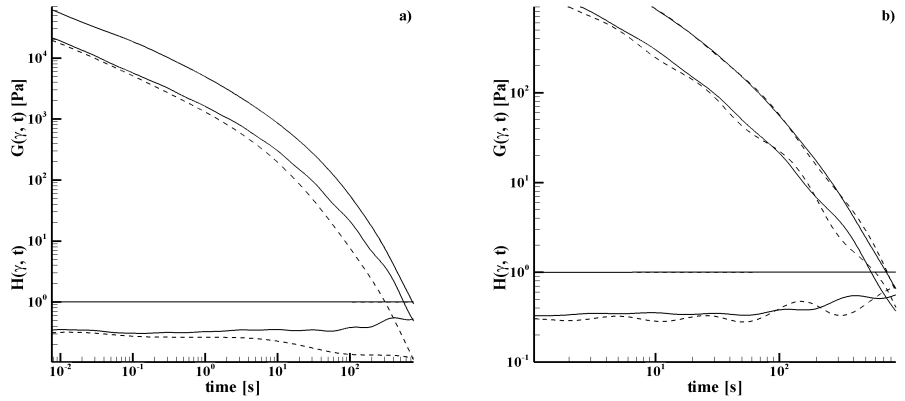

Figure 3.5: a) Relaxation modulus and damping ratio for a 12 mode model of 1840H. The comparison of differential (solid) and integral (dashed) models shows that the differential model approximates the time-strain separability of the integral model correctly until terminal time behaviour becomes dominant. b) Relaxation modulus and damping ratio for a 9 and 12 mode model of 1840H. The comparison of 9 modes (dashed lines) and 12 (solid lines) models is shown. The increase from 9 to 12 modes of relaxation improves the plateau of time-strain separability. Comparing the damping ratio near terminal time in figures a) and b), shows a reduction in oscillations for the denser 12 mode spectrum. Strains of $\gamma = 0.1$ and 7 are used.

3.3 Damping function

3.3.1 Derivation

In the previous section it was observed that increasing the number of modes in the differential Pompom equations improves the modelling of the step strain experiment. This in turn gives apparent time-strain separability over several decades of time. We now derive an approximate analytical expression for the damping function $h(\gamma)$ in the region of TSS. To proceed we need to make a number of simplifying assumptions about both the model and the material properties. The effect of deviations from these approximations will then be checked.

In order to provide an analytic solution of the backbone stretch equation [1.6.48], we initially set the parameter $\nu^* = 0$, so that we do not incorporate the improvement made by Blackwell et al. (2000). Although in general not incor-

porating branch-point withdrawal will not give TSS, the other approximations used in the derivation of the damping function, together with $\nu^* = 0$, give a special case of TSS. However, in modelling a general fluid we restore the important smoothing behaviour of $\nu^* \neq 0$. This is incorporated when we approximate the piece-wise continuous initial stretch with a fully continuous, (relaxation time)-strain separable equation.

If the material is assumed to be time strain separable then,

$$G(\gamma,t) = \sum_i \frac{G_i \lambda_i^2(\gamma,t) e^{-\frac{t}{\tau_{b_i}}}}{1 + N\gamma^2 e^{-\frac{t}{\tau_{b_i}}}} = h(\gamma) \sum_i G_i e^{-\frac{t}{\tau_{b_i}}} = h(\gamma) G(t). \tag{3.3.1}$$

The use of a sufficiently dense spectrum of modes implies the differential and integral model are equivalent, up to the factor in the denominator, N, equal to $\frac{4}{15}$ for the integral model and $\frac{1}{3}$ for the differential model.

We will now look for constraints on the family of parameters, $G_i, \tau_{b_i}, \tau_{s_i}, q_i$, that allow (3.3.1) to hold. We take the continuous limit of the sum and for convenience write $\omega = \frac{1}{\tau_b}$ so that,

$$\int_0^\infty d\omega \frac{G(\omega)\lambda^2(\gamma,\omega,t)e^{-t\omega}}{1 + N\gamma^2 e^{-t\omega}} = h(\gamma) \int_0^\infty d\omega G(\omega) e^{-t\omega}. \tag{3.3.2}$$

This effectively increases the number of modes to infinity and so suppresses the oscillations associated with the final modes of relaxation (that is reminiscent of a Gibbs phenomenon). The exponential term in the denominator of (3.3.2) is responsible for the unphysical terminal behaviour of the differential approximation. So we remove this term in order to focus on the conditions for TSS during the many decades of relaxation prior to the terminal zone.

In order to obtain an analytic solution for $\lambda(\gamma,t)$, we revert to the unmodified stretch equation with $(\nu^* = 0)$ so that,

$$\lambda(\gamma,t) = 1 + (\lambda_0 - 1)e^{-t\omega_s}. \tag{3.3.3}$$

We will restore the important smoothing behaviour provided by $\nu^* \neq 0$ below.

With these approximations equation (3.3.2) becomes,

$$h(\gamma)\int_0^\infty d\omega G(\omega)e^{-t\omega} = \frac{1}{1+N\gamma^2}\Big(\int_0^\infty d\omega G(\omega)e^{-t\omega} + \cdots$$
$$\cdots + 2\int_0^\infty d\omega G(\omega)(\lambda_0-1)e^{-t\omega-t\omega_s} + \int_0^\infty d\omega G(\omega)(\lambda_0-1)^2 e^{-t\omega-2t\omega_s}\Big). \quad (3.3.4)$$

Notice that the dependence on the q-spectrum enters (3.3.4) via the piecewise-continuous equation for the initial stretch,

$$\lambda_0 = \begin{cases} (1+N\gamma^2)^{\frac{1}{2}} & \text{for } \lambda_0 < q \\ q & \text{otherwise} \end{cases}. \quad (3.3.5)$$

In appendix 3.A we show that this function may be approximated by a continuous separable expression of the form,

$$\lambda_0 - 1 = \frac{\beta\gamma^{1+a_1/a_2}(q-1)}{(q_m^{a_2} + (\beta\gamma^{1+a_1/a_2})^{a_2})^{\frac{1}{a_2}}} = \Lambda(\gamma)\cdot(q-1). \quad (3.3.6)$$

By smoothing out the initial stretch as a function of γ in this way, we recover the smoothing behaviour of $\nu^* \neq 0$ that was lost by the approximation of equation (3.3.3).

This approximation produces separability at the level of stretch only (which is not the same as TSS for the full constitutive equation). The expression containing the damping function is now fully separable in terms of strain and time,

$$h(\gamma)\int_0^\infty d\omega G(\omega)e^{-t\omega} = \frac{1}{1+N\gamma^2}\Big(\int_0^\infty d\omega G(\omega)e^{-t\omega} + \cdots$$
$$\cdots + \frac{2\beta\gamma^{1+a_1/a_2}}{(q_m^{a_2} + (\beta\gamma^{1+a_1/a_2})^{a_2})^{\frac{1}{a_2}}}\int_0^\infty d\omega G(\omega)(q-1)e^{-t\omega-t\omega_s} + \cdots$$
$$\cdots + \frac{(\beta\gamma^{1+a_1/a_2})^2}{(q_m^{a_2} + (\beta\gamma^{1+a_1/a_2})^{a_2})^{\frac{2}{a_2}}}\int_0^\infty d\omega G(\omega)(q-1)^2 e^{-t\omega-2t\omega_s}\Big). \quad (3.3.7)$$

In order to obtain TSS it remains to choose the functions $G(\omega)$, $q(\omega)$ and $\omega_s(\omega)$ such that each of the integrals has the same time dependence. We begin by assuming that the ratio of orientation to stretch time for all modes is a constant,

α, so that,

$$\omega_s = \alpha\omega. \tag{3.3.8}$$

This ratio is proportional to the number of entanglements between branch points and might be expected to be constant if the probability of branching is independent of position in the molecule. However, the physics of dynamic dilution predicts that α should decrease slightly with increasing relaxation time. In practice, when fitting a Pompom spectrum the ratio is adjusted to best fit the transient build up of stress. Furthermore, changes in the value of α have a negligible effect on the damping function as can be seen in figure 3.8.

Next we choose $G(\omega)$ and $q(\omega)$ to satisfy power laws in ω, namely,

$$G(\omega) = B\omega^b \qquad \text{and} \qquad (q(\omega) - 1) = C\omega^c. \tag{3.3.9}$$

The equation for the damping function now looks like,

$$\begin{aligned} h(\gamma)\int_0^\infty d\omega\omega^b e^{-t\omega} = \frac{1}{1+N\gamma^2}\Big(&\int_0^\infty d\omega\omega^b e^{-t\omega} + \cdots \\ &\cdots + C\Lambda(\gamma)\int_0^\infty d\omega\omega^{b+c} e^{-t\omega(1+\alpha)} + \cdots \\ &\cdots + (C\Lambda(\gamma))^2\int_0^\infty d\omega\omega^{b+2c} e^{-t\omega(1+2\alpha)}\Big), \end{aligned} \tag{3.3.10}$$

where the integrals may now all be written as Gamma functions. Dividing by $\Gamma(b+1)$ gives the damping function as,

$$\begin{aligned} h(\gamma) = \frac{1}{1+N\gamma^2}\Big(1 + &\frac{C\Lambda(\gamma)\Gamma(b+c+1)}{t^c(1+\alpha)^{b+c+1}\Gamma(b+1)} + \cdots \\ &\cdots + \frac{(C\Lambda(\gamma))^2\Gamma(b+2c+1)}{t^{2c}(1+2\alpha)^{b+2c+1}\Gamma(b+1)}\Big). \end{aligned} \tag{3.3.11}$$

Note that this is only independent of time for the exponent $c = 0$, with $(q-1) = C = q_m$ being constant. We will see below that this is a reasonable approximation for a wide family of LDPEs, where the best fit power-law, c, is typically ~ 0.1.

The general form of the branched damping function is given by,

$$h(\gamma) = \frac{1}{1+N\gamma^2}\left(1 + \frac{2q_m\Lambda(\gamma)}{(1+\alpha)^{b+1}} + \frac{(q_m\Lambda(\gamma))^2}{(1+2\alpha)^{b+1}}\right). \tag{3.3.12}$$

For the differential Pompom model (with $N = \frac{1}{3}$), making the substitution for the best proposed choice of parameters (Appendix 3.A) for $\Lambda(\gamma)$ ($\beta = 1/4$, $a_1 = 1/2$ and $a_2 = 1$) in equation (3.3.6) gives a damping function with three material characteristics,

$$h_B(\gamma; q_m, \alpha, b) = \frac{1}{1+\frac{1}{3}\gamma^2}\left(1 + \frac{2q_m\gamma^{\frac{3}{2}}}{(4q_m+\gamma^{\frac{3}{2}})(1+\alpha)^{b+1}} + \frac{(q_m^2\gamma^3)}{(4q_m+\gamma^{\frac{3}{2}})^2(1+2\alpha)^{b+1}}\right). \tag{3.3.13}$$

As noted in appendix 3.A this damping function does become greater than one, but by less than 1% for low strain results. This provides the best smoothing behaviour at the transition to maximum stretch.

The family of damping functions represented by (3.3.13) constitutes a universal set of responses for complex branched melts in the same way that the single Doi-Edwards damping function does for linear melts. We refer to h_B as the branched damping function (BDF).

3.3.2 Ideal Model

In deriving the BDF in the previous section, we assumed that parameters in the multimode Pompom model satisfied the following conditions,

- $G(\omega) \sim B\omega^{-b} \sim B\tau^b$
- $q(\omega) - 1 \sim C\omega^{-c} \sim C\tau^c$
- $\omega_s = \alpha\omega$

In this section we consider the properties of an 'ideal damping fluid' whose parameters follow these relations, but are described by a finite set of discrete modes.

Unless otherwise stated parameters used throughout this section will be $B = 100$, $b = -0.5$, $C = q_m = 6$, $c = 0$ and $\alpha = 5$. This choice is made for illustrative purposes and all general features of the model appear with this parameter choice. We also restore the choice of $\nu^* = \frac{2}{q-1}$.

During the derivation of the BDF (3.3.13) we found that the power law coefficient for the q-distribution was required to be zero. Since the q-spectra for LDPEs generally show a slow increase in q with τ_b, we check the effect of departures from $c = 0$ to weak power laws. In figure (3.6) the damping ratios are shown for the ideal fluid for $c = 0, 0.1, 0.2$ for the differential model at strains of $\gamma = 0.1, 3, 10$. For low strains there is little difference over this range and approximate time-strain separability is observed over four decades of time. For large γ there is a more dramatic difference due to non-linear effects. As the magnitude of c is increased the time-strain separable plateau becomes less valid and a more exaggerated trough and peak occur. However, even at $\gamma = 10$, provided $|c| \leq 0.1$, $H(\gamma, t)$ is constant to within 5% over three orders of magnitude in t.

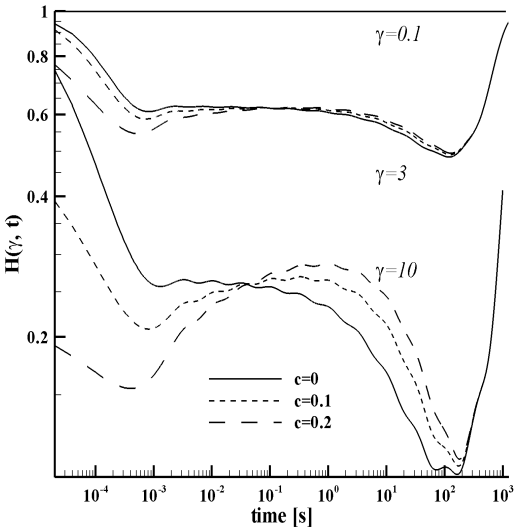

Figure 3.6: Damping ratios are shown for the ideal fluid whilst varying the parameter $c = 0, 0.1, 0.2$ for the differential model. Strains of $\gamma = 0.1, 3, 10$ are used.

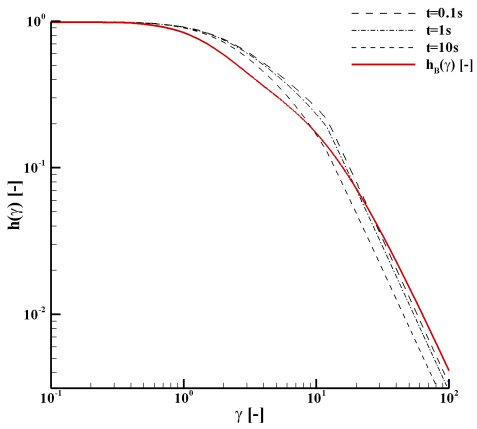

Figure 3.7: Derived BDF (solid line), plotted against strain, compared with damping ratios taken from an ideal fluid at various times, 0.1, 1, 10s (dashed lines). The picture is the case for $\nu^* = \frac{2}{q-1}$.

In figure 3.7 we compare damping estimations, $H(\gamma, t)$, produced for ideal fluids in the case of $c = 0$ and $\nu^* = \frac{2}{q-1}$ at various times, 0.1, 1 and 10s. For all times the coincidence of the damping ratios, $H(\gamma, t)$, shows almost exact TSS that is well approximated by the BDF, equation (3.3.13).

Finally in figure 3.8, we examine how the BDF, h_B, varies with the choice of parameters, b, q_m and α. Decreasing the power law of the elastic modulus from $b = -0.2$ to $b = -0.8$ has the effect of increasing the contribution from the fast relaxing modes and increases the BDF for strains in the range of 1 to 10. The BDF is also increased by the branching number, $q_m = \bar{q}_i - 1$. Choosing the average branch number, $q_m = 0$ which corresponds to $q_i = 1$ for all i, restores the Doi-Edwards damping function because there is no chain stretching in this limit. The BDF is only weakly dependent on the ratio, α, of orientation and stretch relaxation times. As α increases, the BDF decreases; figure (3.8c).

To test the performance of the BDF, $h_B(\gamma, q_m, \alpha, b)$, for a commercial material we compare it to the behaviour of the damping ratio, $H(\gamma, t)$, for the material 1840H. The damping ratios are calculated from the differential Pompom model using the 12 mode spectrum given in table 3.2 . The parameters of the BDF are taken from the material's spectrum with the non-linear parameters for the BDF

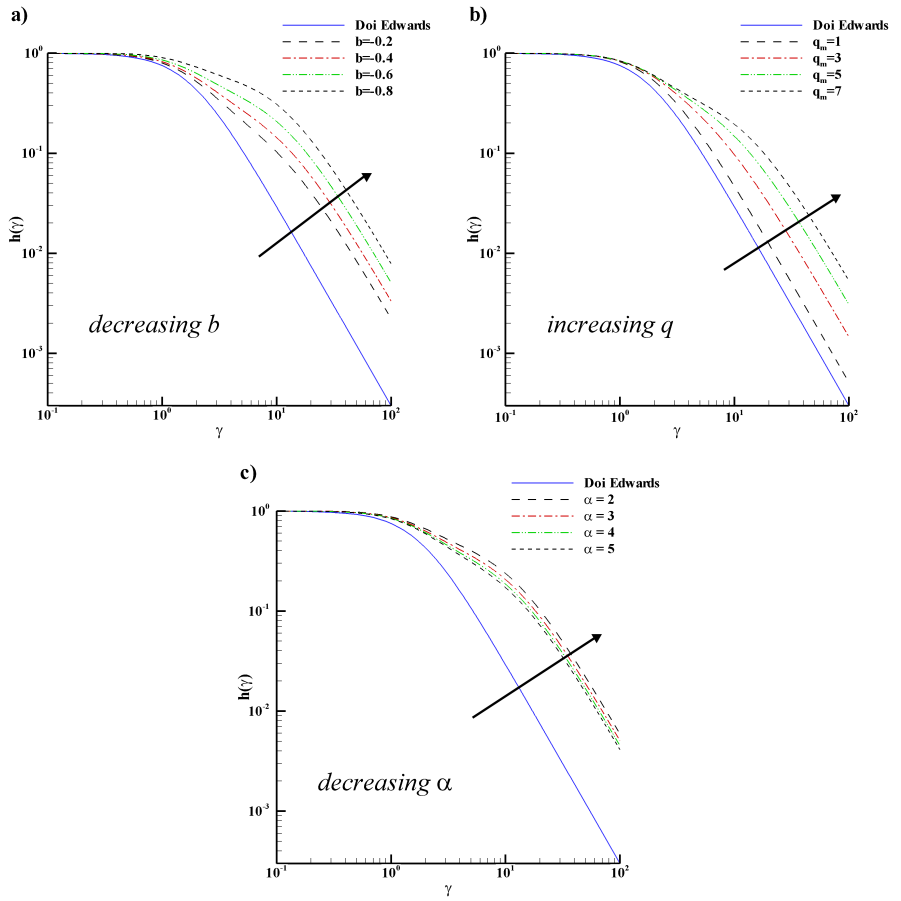

Figure 3.8: a) Variations in the BDF, $h_B(\gamma; q_m, \alpha, b)$ with power laws in b. b) Variations in $h_B(\gamma; q_m, \alpha, b)$ with values of q_m. c) Variations in $h_B(\gamma; q_m, \alpha, b)$ with values of α. Strains of $0.1 \cdots 100$ were used. The default parameters of the plots are $b = -0.5$, $q_m = 6$ and $\alpha = 5$.

chosen as the average arm number, $q_m = \bar{q}_i - 1 = 5.92$ and the average ratio $\alpha = \bar{r}_i = 3.32$, and a power law of $b = -0.4$. In figure 3.9 the 12 mode 1840H damping ratios are plotted, along with the BDF, (3.3.13), against strain for times 0.1, 1, 10s. The coincidence of the damping ratio show that TSS is valid over these times and the BDF (heavy solid line) is found to be in very good agreement with the predictions of $H(\gamma, t)$.

The time range over which the differential Pompom model model shows TSS begins much earlier than the longest existing stretch time, where $G(\gamma, t)$ transitions into terminal time unitary behaviour. Although a finite sum of differential

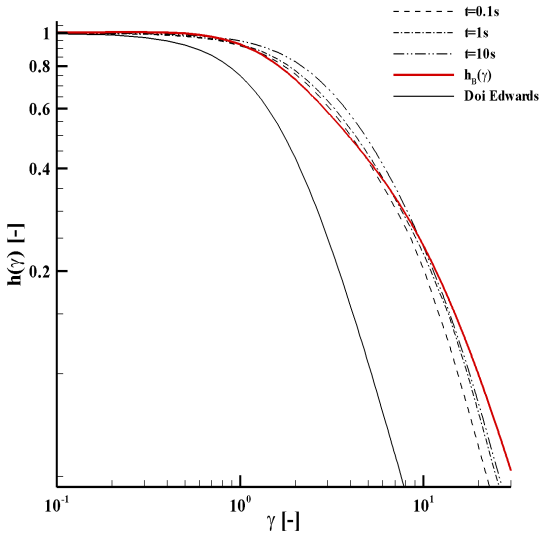

Figure 3.9: A comparison of the BDF [equation 3.3.13] (heavy solid line) and the damping predictions against strain for 1840H at times 0.1, 1 and 10s (dashed lines). Parameters used are $q_m = 5.92, \alpha = 3.32, b = -0.4$. The light solid line is the Doi-Edwards damping function.

Pompom modes will not provide any case of exact TSS it closely estimates the existence of a region of TSS. Finally, the BDF (3.3.13) still gives a good prediction to behaviour of a material even with the condition of $\nu^* = 0$ relaxed.

We now look for regions of TSS arising in Pompom spectra for a range of branched polymer melts. We then compare experimental measurements of the damping function with the predictions of BDF (3.3.13) where the parameters b, α and q_m are derived from the Pompom model fits of these materials obtained from extensional rheology.

3.4 Survey of branched polymers

In this section we compare the non-linear stress relaxation of a variety of branched polyethylenes produced by different synthesis routes. The degree of LCB dramatically affects the rheology of a material and in addition to analysing the performance of the BDF (3.3.13) in capturing TSS, where it exists in low and high

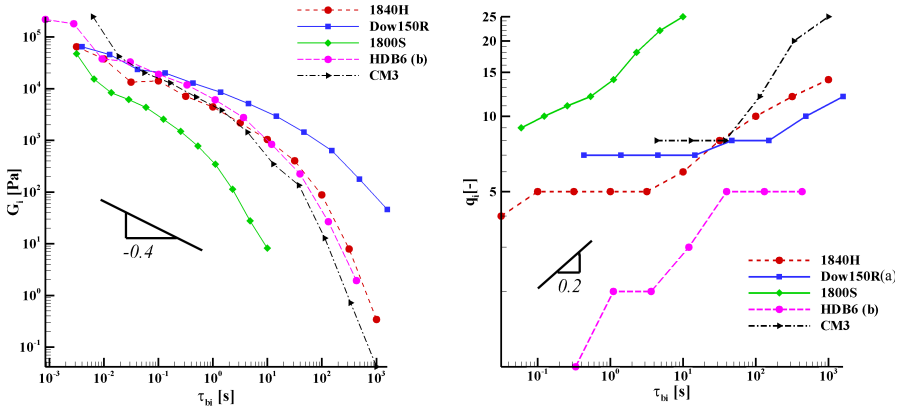

Figure 3.10: Plot of G_i (left) and q_i (right) against τ_b for various materials. On the left none of the materials satisfy the power law property used to derive the BDF. On the right we see that the q spectra show reasonable power law agreement, with powers ≤ 0.2.

density PEs, we also examine how branching structure affects the existence of TSS in step strain and the extent to which the relaxation modulus is damped.

We investigate materials produced from two different synthesis routes; low density polyethylenes (LDPEs) produced by high pressure free radical polymerisation and branched high density polyethylenes (HDPEs) produced by metallocene catalysed polymerisation. The LDPE polymers are highly polydisperse ($\frac{M_w}{M_n} \approx$ O(10)) with relatively dense branching structures, whereas the metallocene HDPE polymers have a more controlled polydispersity ($\frac{M_w}{M_n} \approx 2$) and sparse but longer branches. See table (2.1) for material properties.

Previous existence of TSS in branched materials has been well documented for LDPEs [Osaki (1993); Chodankar et al. (2003)]; we could therefore expect that the existence of dense branching structures will produce TSS. For branched HDPE the fluid will contain a proportion of linear molecules as well as LCB molecules. We might therefore expect to see a transient transition from a linear to a branched regime and not see any region of TSS with respect to time. However, experimental evidence shows that both metallocene materials display TSS for at least one decade in time.

Each material has linear rheological parameters (G_i, τ_{b_i}) and Pompom branch-

ing parameters (τ_{s_i}, q_i) fitted to experimental oscillatory and extensional data respectively, using 'Reptate' software [Ramirez and Likhtman (2007)] with twelve relaxation modes. The fits for all materials with step-strain data available are shown in figure (3.10) with parameter values detailed in tables (2.3 - 2.6). When fitting the extensional parameters to the data, the steady state plateau is never reached experimentally. This leaves a question over the accuracy of the q values in the spectra as these primarily control the steady state behaviour of LCB materials. Figure 3.10 shows a plot of the moduli, G_i, and the branch parameter, q_i, against τ_b for the materials we survey.

From figure 3.10 we can see that none of the materials perfectly satisfies the power law property used in the previous section to derive the BDF. This leads to a question in the choice of power law parameter, $b < 0$, in the BDF, (3.3.13). We choose to focus on the early relaxation time region and take $b = -0.5$ for 1800S and $b = -0.4$ for the other LDPEs and the two HDPEs, for which step strain data was available. The plot of the q_i spectra shows that for each material a reasonable power law approximation could be used, with a weak power $c \leq 0.2$. This is in agreement with the regime found for TSS in our earlier approximations in the BDF, (3.3.13).

3.4.1 Experimental

For the rheological testing of the materials in step-strain flow a strain-controlled ARES rheometer (Advanced Rheometric Expansion System, Rheometric Scientific) with a force-rebalanced transducer (2K-FRT) was employed. The specimens were compression moulded at $150°C$ and the dimensions at test temperature were corrected for the thermal expansion. Further rheological tests with respect to the thermal stability showed that no detectable molecular structure changes took place during the experiments. The step-strain data was measured by Dr Dietmar Auhl, for which I thank him.

The step-strain tests were carried out using various cone and plate geometries with different cone angles between 2 and 10 degree and a diameter of 10mm. The step imposition time was about 20ms and the maximum strain γ obtainable was 15. Similar to the procedure described in Stadler et al. (2008), a series of stress

relaxation tests with increasing deformation beginning with small and going to high strains was applied to each specimen. The stress was required to vanish below the noise level at the end of each test before the next one was started. Thus, it was ensured that the remaining stress of the previous strain step was negligible compared to the stress measured in the following step.

For reliable stress relaxation measurements it is necessary that the specimen does not suffer from any structural damage such as edge fracture. It is also necessary to ensure that no wall-slip [Archer et al. (1995)] or inhomogeneous flow [Wang et al. (2006)] occur within the sample gap. The latter is particularly difficult to rule out without optical investigation. However, a series of repeated relaxation tests with different cone angles gave almost identical stress relaxation curves indicating that the damping functions are time-independent and the time-strain separation principle is valid.

3.4.2 Results

For each of the three LDPEs and two lightly branched metallocene HDPEs we have compared the predictions of the multimode Pompom model (and the BDF derived from it) to experimental relaxation data. For all materials the experimental damping values are determined by averaging at least one decade of the experimental damping ratio where TSS exits.

For 1840H we use the 12 mode spectrum presented earlier in table (3.2). Figure (3.11) shows the 12 mode model 1840H relaxation modulus and damping ratios for strains of 0.1, 5 and 7. The solid and dashed lines show the experimental and differential Pompom model respectively. The differential Pompom model is in good agreement with experiments in the region of TSS. The discrepancies at early times are due to the effects of an imperfect strain history in the experiments, which affect the results for times up to around 0.1s.

In the right-hand graph in figure (3.11) we compare the BDF, (3.3.13), $h_B(\gamma)$ with experimental damping values. The parameters used in $h_B(\gamma)$ are taken from the 12 mode spectrum; with average $\bar{q} = 6.92$ so that $q_m = 5.92$, average ratio, $\alpha = 3.32$, and a power law of $b = -0.4$.

We have repeated the comparison for the LDPEs 1800S and Dow150R. The 12

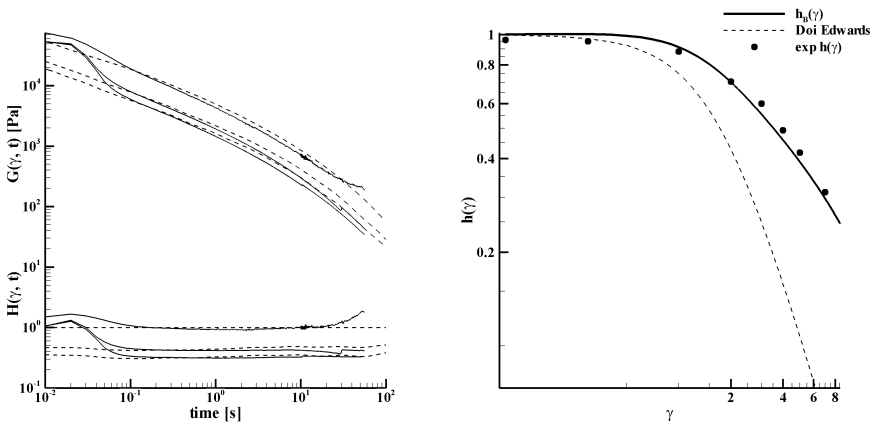

Figure 3.11: Left: is the 12 mode 1840H relaxation modulus, $G(\gamma, t)$, and damping ratio, $H(\gamma, t)$, for strains $0.1, 5, 7$. The solid lines represents the experimental data and the dashed the differential Pompom predictions. Right: a comparison of BDF (3.3.13), heavy solid line, and the damping ratio predictions against strain of 1840H for various strains. Parameters used are $q_m = 5.92, \alpha = 3.32, b = -0.4$. The dashed line is the Doi-Edwards damping function.

mode Pompom spectra used for 1800S and Dow150R (only spectrum Dow150R(a) is compared to transient data) are plotted in figure 3.10. Dow150R has a high viscosity making experimental measurements at high strains more difficult for this material. 1800S has a lower viscosity than 1840H, which allows strains of up to 15 to be measured. The results for 1800S and Dow150R can be seen in figures 3.12 and 3.13, respectively. The stress relaxation damping ratios predicted by the Pompom model show similar levels of agreement to those shown for 1840H and with TSS for times in the range 0.01s to 10s. The BDFs for all three LDPEs are shown in figure 3.16 and are in good agreement with the experimental results. The parameters used were obtained from the Pompom fit, with $q_m = 5.67$, $\alpha = 2.7$, $b = -0.5$ for 1800S. For Dow150R two spectra were compared and the damping predictions are shown in figure 3.13. The spectra used are detailed in table 2.6 and consist of one spectrum fitted to the maximum SER data value obtained, Dow150R(a), and a spectrum with showing more strain hardening and higher steady state extensional viscosity, Dow150R(b). The BDF parameters used are (a) $q_m = 4.83, \alpha = 3.90, b = -0.4$ and (b) $q_m = 19.2, \alpha = 3.1, b = -0.4$. The figure clearly shows that the fit Dow150R(a) matches the experimentally observed

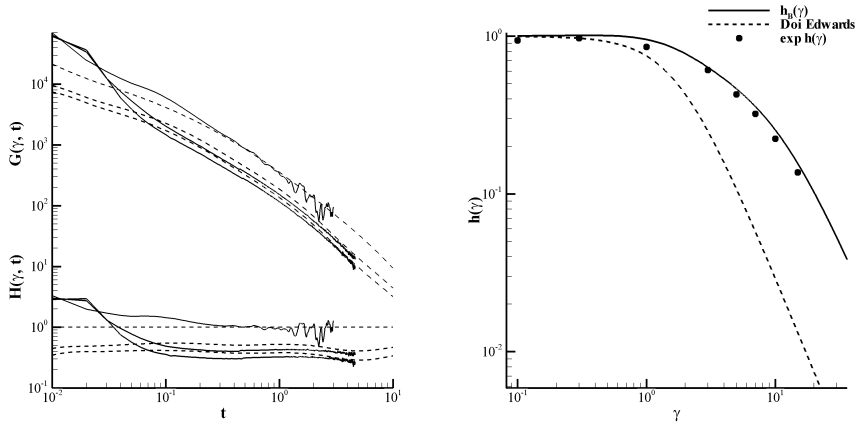

Figure 3.12: Left: is the 12 mode 1800S relaxation modulus, $G(\gamma, t)$, and damping ratio, $H(\gamma, t)$, for strains $0.1, 5, 7$. The solid lines represents the experimental data and the dashed the differential Pompom predictions. Right: a comparison of BDF (3.3.13), heavy solid line, and the damping ratio predictions against strain of 1800S for various strains. Parameters used are $q_m = 5.67, \alpha = 2.70, b = -0.5$. The dashed line is the Doi-Edwards damping function.

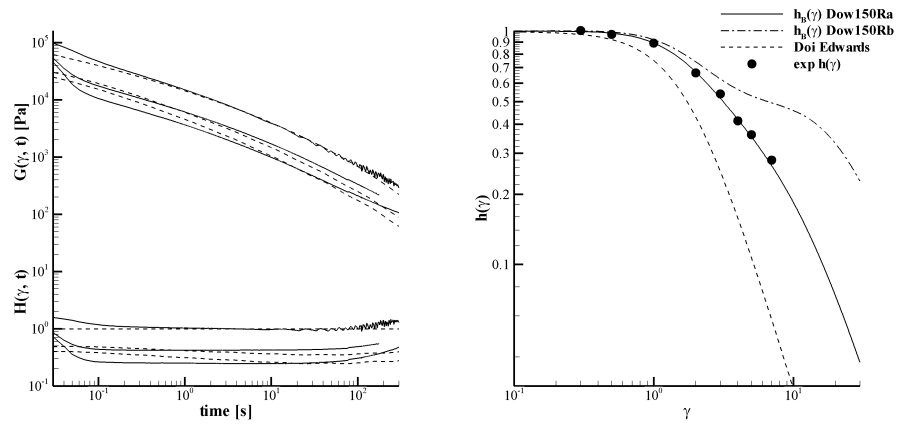

Figure 3.13: Left: is the 12 mode Dow150R(a) relaxation modulus, $G(\gamma, t)$, and damping ratio, $H(\gamma, t)$, for strains $0.3, 5, 7$. The solid lines represents the experimental data and the dashed the differential Pompom predictions. Right: a comparison of BDF (3.3.13), heavy solid line, and the damping ratio predictions against strain of Dow150R(a) and Dow150R(b) for various strains. Parameters used are (a) $q_m = 4.83, \alpha = 3.90, b = -0.4$ and (b) $q_m = 19.2, \alpha = 3.1, b = -0.4$. The dashed line is the Doi-Edwards damping function.

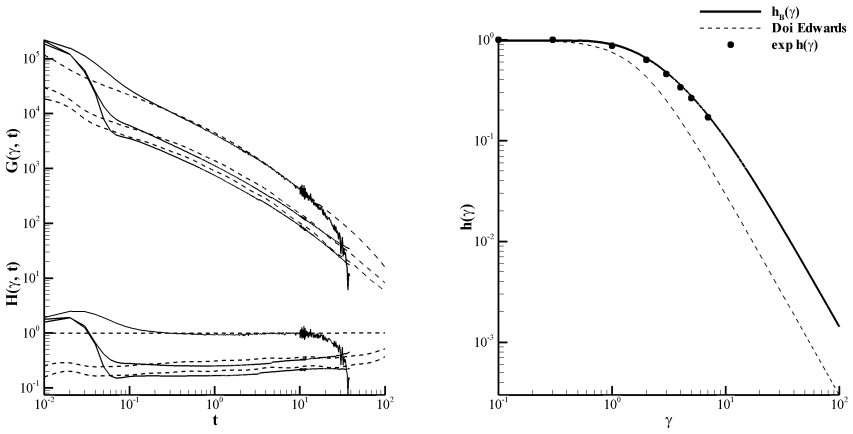

Figure 3.14: Left: is the 12 mode CM3 relaxation modulus, $G(\gamma, t)$, and damping ratio, $H(\gamma, t)$, for strains $0.1, 5, 7$. The solid lines represents the experimental data and the dashed the differential Pompom predictions. Right: a comparison of BDF (3.3.13), heavy solid line, and the damping ratio predictions against strain of CM3 for various strains. Parameters used are $q_m = 2.5, \alpha = 3.5, b = -0.4$. The dashed line is the Doi-Edwards damping function.

damping very well where as the much higher q values of Dow150R(b) produce a dramatic deviation from the data. This indicates that the spectra Dow150R(a), with its relatively lower q values is a much better choice for capturing the rheology of the material.

In contrast with the two LDPE materials the metallocene catalysed HDPE materials show less extension hardening and are not fitted as accurately by the Pompom model. The material CM3 shows strain hardening for strain rates in the range $0.01s^{-1}$ to $10s^{-1}$. Both the experimental measurements and the Pompom model for this material give TSS for times in the range of 0.1s to 30s and the BDF, with $q_m = 2.5$, $\alpha = 3.5$ and $b = -0.4$, gives excellent agreement with experimental results, seen in figures 3.14 and 3.16.

Finally we consider HDB6, which displays the least satisfactory agreement with experimental data. This is one of the reasons why several similar Pompom spectra where fitted to HDB6. However, each of the three fits give results which cannot be discriminated. I show the results for HDB6b as this is closest to the approximation of a constant power law. The extensional data for HDB6 is shown in figures 2.6 and 2.7 for extension and shear rates from $0.03s^{-1}$ to $30s^{-1}$, and

only shows extension hardening at lower strain rates (although it is possible that the experiments underestimated the extensional stress at higher strain rates due to necking). Consequently, the Pompom fit to this model, given in tables 2.4 and 2.5, has only 5 or 6 modes for which q_i is greater than unity. Thus, as can be seen in figure 3.10, the Pompom spectra for HDB6 are furthest from the ideal spectrum in which the q value is approximately constant for all modes.

For the different Pompom spectra fitted to HDB6 there are different parameters used in the damping function. For all three spectra $b = -0.4$ since there is no significant change in the linear fitting. For HDB6 a, b and c the branching parameter, $q_m = 3.83, 1.3$ and 2.25, and $\alpha = 6, 4.16$ and 4.46, respectively. There seems to be a dramatic difference in results but the relative changes in q_m and α cancel each other out to give the same BDF. This is not surprising since the parameters of the BDF are derived from the multimode Pompom parameters, which in fitting is itself an ill posed problem with multiple solutions. This problem occurs at its severest for HDB6 since there is very little extension hardening to fit a Pompom spectra to, for the other materials this problem is not so severe.

The experimental and predicted values of the relaxation modulus and damping ratios are shown in figure 3.15. The experimental data are shown as solid lines and reveal that TSS exists for times in the range 0.1s to 100s. However, the predictions of the Pompom model, shown as dashed lines, show no strict region of TSS. For the smallest strain large amounts of noise were measured beyond 100s.

At high strains the Pompom fit correctly predicts the stress at early times (but not during the step imposition), but over predicts the stress at later times, suggesting that the q parameter distribution is more uniform than any of the fitted models. Nevertheless the fitted BDF, obtained from the Pompom fit for HDB6b with $q_m = 1.3$, $\alpha = 4.16$ and $b = -0.4$, is in good agreement with results (although it does slightly under predict the experimental damping values at high strains).

Figure 3.16 shows a comparison of the damping functions and BDFs for the five materials we have analysed. The details of the parameters used are summarised in table (3.3). The BDFs from top to bottom correspond to the value of q_m from highest to lowest. This suggests that information on the extent of

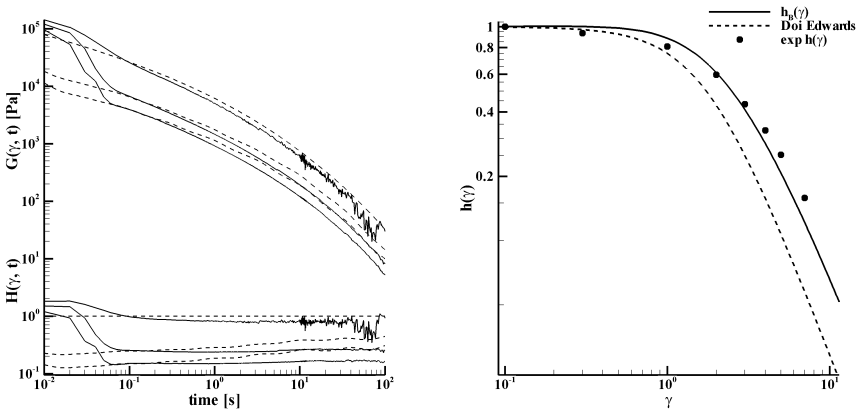

Figure 3.15: Left: is the 12 mode HDB6 relaxation modulus, $G(\gamma, t)$, and damping ratio, $H(\gamma, t)$, for strains $0.1, 5, 7$. The solid lines represents the experimental data and the dashed the differential Pompom model. Right: a comparison of BDF (3.3.13), heavy solid line, and the damping predictions data for various strains. Parameters used are $q_m = 1.3, \alpha = 4.16, b = -0.4$. The dashed line is the Doi-Edwards damping function.

Table 3.3: A summary of parameters used in producing BDFs (figure 3.16) for the various materials we survey.

Material	b	q_m	α
1840H	-0.4	5.92	3.32
1800S	-0.5	5.67	2.70
Dow150R(a)	-0.4	4.83	3.90
CM3	-0.4	2.50	3.5
HDB6b	-0.4	1.30	4.16

long chain branching can be obtained from the damping function via the BDF. In particular the experimental data is seen to divide into two groups with the LDPEs showing a slower relaxation with increasing strain than the more lightly branched HDPEs.

We have surveyed a range of materials to see which set of Pompom parameters (extracted from extensional data) showed a region of TSS in step-strain. Although none of the materials exactly satisfied the conditions for the 'ideal model' detailed

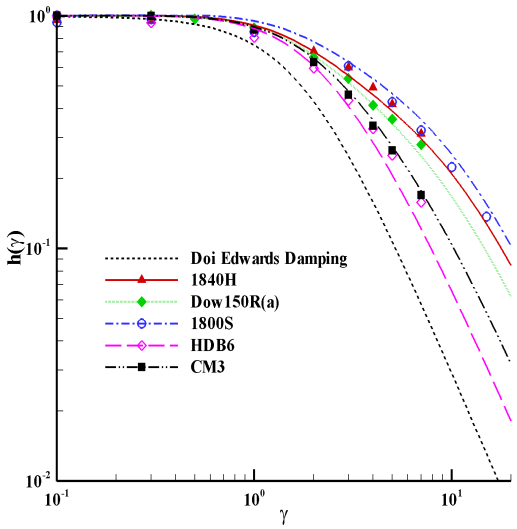

Figure 3.16: A comparison of the BDFs produced from the five materials surveyed, a summary of parameters used can be seen in table (3.3).

in section four, the differential model predicts approximate TSS for four of the five materials we surveyed, the exception being the lightly branched material HDB6. In the case of HDB6 this discrepancy could arise from errors in the extensional data to which the spectrum was fitted. Furthermore the BDF, (3.3.13), provides a good approximation of the observed damping behaviour for these materials, despite the relaxation in the conditions used to derive it.

3.5 Conclusions

We have analysed the stress relaxation following step strain in multimode Pompom models for branched polymers. A single mode Pompom model does not show TSS and the differential approximation shows qualitatively different terminal time behaviour from the integral model. However, in a multimode Pompom model this discrepancy between integral and differential versions does not appear until near the terminal relaxation time. We also find that increasing the density of modes improves the accuracy of the differential model in a manner that is analogous to the restriction of the 'Gibbs phenomena' of Fourier series with the

addition of terms to the series.

The damping ratio $H(\gamma, t)$ was defined to show how well parameterised models are time-strain separable. This tool clearly shows how well the differential model approximates the integral model and the range of timescales over which the stress relaxation is time-strain separable.

We now turn to the questions raised in the introduction. The first question was whether there exists any subsets of parameters for the multimode Pompom model that give TSS in step-strain. We have shown that a material with a power law spectrum where the ratio of orientation to stretch relaxation time and the maximum stretch, q are constant for all modes does indeed give TSS.

The second question concerned the degree of departure from separability when these conditions are relaxed. By modelling an 'ideal' fluid based on the criteria above we showed how deviations from the constant non-linear stretch parameter, q, to a weak power law in orientation relaxation time affect TSS. We find that provided this dependence is weak there is still a range of times over which the material shows approximate TSS.

The final question concerned the extent to which real materials satisfy these conditions. We have surveyed a range of branched polyethylenes produced through two different synthesis routes to look for differences between the materials. The high pressure polymerisation produces more random LCBs than the smoother metallocene catalysed route. For all five materials the experimental stress relaxation data showed a range of TSS and despite none of the materials falling in the subspace of Pompom models that predict exact TSS, a region of TSS was predicted for four of our materials. The LCB-HDPE named HDB6 was the only material where the Pompom parameterisation failed to capture the experimentally observed TSS.

To investigate the sensitivity of step-strain to the Pompom parameters the three spectra that were produced in chapter 2 for HDB6 were examined. None of the three Pompom spectra were able to capture the experimentally observed TSS. Indeed, the three spectra used could not be discriminated in step strain and it remains an outstanding problem to capture TSS for HDB6 using parameters derived from start-up rheology. This deviation arose from the step gradient in the distribution of the non-linear parameter, q, and all three spectra superimposed

to give the same result. For the LDPE Dow150R, two different spectra were compared, one with much higher q priority than the other. The BDF clearly indicated that the spectrum Dow150R(a), with lower q values, gave a much better prediction than the alternative Dow150R(b).

All BDFs predicted the attenuation in the stress relaxation well, including the BDF for HDB6 which captured the damping behaviour of the material, despite the reduced TSS predicted by the Pompom model. Thus although the parameter values for these materials do not fall into the class of exact TSS, they are close enough to this parameter space so that TSS is predicted to a good approximation.

Furthermore, both the experimental data and the corresponding BDFs split into two groups according to the synthesis route of the polyethylene concerned, with the LDPEs showing less attenuation at high strains compared with the HDPEs. This suggests that by fitting the branching parameter q_m in the branched damping function to step-strain experiments we can infer the average value of q for this material. The branching parameter is an averaged value and so further techniques, such as Fourier transform rheology, would be needed to obtain precise detail on branching structure.

In conclusion, while the materials surveyed did not fall strictly into the subspace within which the ideal BDF was derived, the BDF still predicts the experimental damping function to within experimental error. This suggests that the BDF is able to capture the damping behaviour of a wider class of multimode Pompom models that show approximate TSS. Furthermore the two different classes of branched polyethylenes show different damping behaviour demonstrating that step-strain relaxation may be used to characterise the degree of LCB in polymer melts.

3.A Approximating the initial stretch function

An essential part of deriving the BDF (3.3.13) is incorporating the piece-wise initial stretch equation (3.3.5),

$$\lambda_0 = \begin{cases} (1+\frac{1}{3}\gamma^2)^{\frac{1}{2}} & \text{for } \lambda_0 < q \\ q & \text{otherwise} \end{cases}$$

as a fully continuous function dependent on the strain and the q-spectrum.

An approximation that interpolates between the small and high strain limits is given by,

$$\lambda_0 - 1 = \frac{\beta\gamma^{1+a_1/a_2}(q-1)}{\left(q_m^{a_2} + (\beta\gamma^{1+a_1/a_2})^{a_2}\right)^{\frac{1}{a_2}}}, \tag{3.A.1}$$

where a_2 determines the rate of approach to the high strain limit, a_1 determines the strain dependence at low and moderate γ.

This particular function was chosen because it makes $\lambda_0 - 1$ a separable function of $q-1$ and γ, where (q_m+1) is the average number of arms in the spectrum. This gives a good fit of initial stretch for $(q-1)$ near q_m, (*i.e.* for modes whose q value is close to the average) but under or over predicts the gradient of equation 3.3.5 for low and high $(q-1)$, respectively. Provided that $q-1$ does not deviate far from q_m then this approximation holds.

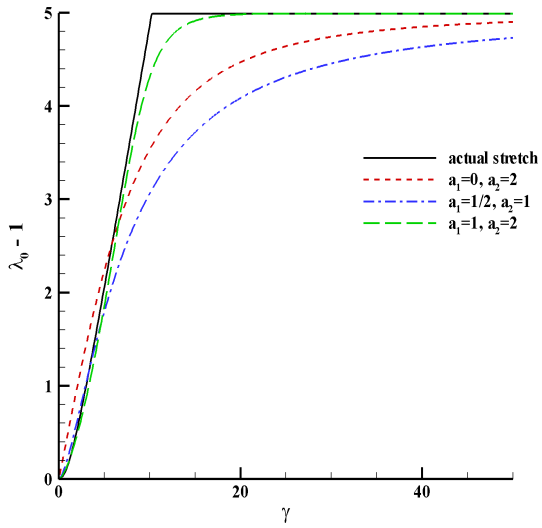

Figure 3.17: Various approximations for the initial stretch. The solid lines show the piece-wise bounded stretch. The dotted and dashed lines show predictions for $(a_1 = 0,\ a_2 = 2)$ and $(a_1 = 1/2,\ a_2 = 1)$, respectively. The dash-dotted line shows the prediction for $a_1 = 1$ and $a_2 = 2$.

Figure (3.17) shows three choices for the parameters a_1 and a_2. Choosing

$a_1 = 0$, $a_2 = 2$ (dotted line) gives a simpler form of the initial stretch equation, but looses the γ power law behaviour at low strains. A more accurate but also more complex form of the initial stretch is also pictured (dashed line) where $a_1 = 1$ and $a_2 = 2$. The dash-dotted solid line shows $a_1 = \frac{1}{2}$ and $a_2 = 1$, the ratio of a_1 and a_2 is the same as for $a_1 = 1$ and $a_2 = 2$ but the transition to maximum stretch is smoother, similar to that of the simple case, $a_1 = 0$. For; $a_1 = 0$ then $\beta = 0.5$, $a_1 = 1$ then $\beta = 0.17$ and $a_1 = \frac{1}{2}$ then $\beta = 0.25$.

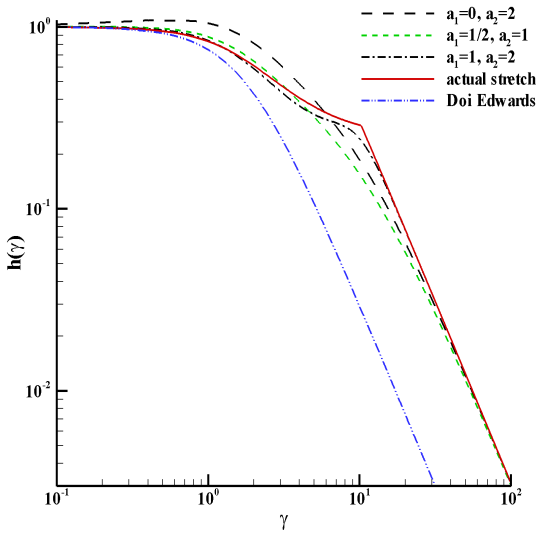

Figure 3.18: A plot of the various parameter choices used in figure (3.17) substituted into the derived BDF against strain. The solid line shows the actual stretch equation (3.3.5). The dotted, dashed and dash-dotted lines show damping functions using approximate stretch parameters $(a_1 = 0, a_2 = 2)$, $(a_1 = 1, a_2 = 2)$ and $(a_1 = 1/2, a_2 = 1)$, respectively. The dashed-double dotted line shows the Doi-Edwards damping function. We use parameters of $b = -0.5$, $\alpha = 5$ and $q_m = 6$.

We can now insert this approximation into equation 3.3.4, so that provided q is constant, the damping ratio is strain separable with the damping function given by,

$$h(\gamma) = \frac{1}{1+\frac{1}{3}\gamma^2}\left(1 + \frac{2q_m\Lambda(\gamma)}{(1+\alpha)^{b+1}} + \frac{(q_m\Lambda(\gamma))^2}{(1+2\alpha)^{b+1}}\right),$$

where $\Lambda(\gamma)$ is given by,

$$\Lambda = \frac{\beta\gamma^{1+a_1/a_2}(q-1)}{(q_m^{a_2} + (\beta\gamma^{1+a_1/a_2})^{a_2})^{\frac{1}{a_2}}}. \tag{3.A.2}$$

A plot of the derived BDF for the various parameter choices used in figure (3.17) is shown in figure (3.18). We use parameters of $b = -0.5$, $\alpha = 5$ and $q_m = 6$. The solid line shows the actual stretch equation (3.3.5), which displays a kink at the point of maximum stretch. The kink is captured by the case for $a_1 = 1$ (dashed line), but the behaviour of the other two cases displays a smoother transition to high strain results. Note this cusp is a consequence of choosing $\nu^* = 0$, and with the inclusion of branch point withdrawal, this unphysical behaviour is removed. Therefore, for cases with $\nu^* \neq 0$ it is desirable to choose parameter values that don't produce this cusp. For the case of $a_1 = 0$ (dotted line), the BDF becomes greater than one for low strains. This is because the γ power law behaviour of the initial stretch (3.3.5) for low strains is lost by the approximation with $a_1 = 0$. Since we require the damping function to be monotonic this choice of initial stretch parameters is not suitable for the BDF. The dashed double dotted line shows the Doi-Edwards damping function.

Therefore, in this paper we choose to use $a_1 = \frac{1}{2}$, $a_2 = 1$ (dash-dotted line in figure 3.18) and $\beta = \frac{1}{4}$. This choice provides the required smoothing behaviour occurring at maximum stretch and is monotonic to an accuracy of less than 1%.

Chapter 4

Large Amplitude Oscillatory Shear Flow

In this chapter the predictions of the Pompom constitutive model in large amplitude oscillatory shear (LAOS) are examined using Fourier transform rheology (FTR). FTR is commonly used with small amplitude oscillatory shear (SAOS) to fit linear Maxwell parameters to dynamic moduli and in this chapter this process is expanded to larger strain amplitudes and to further terms in the Fourier series. For both small and large amplitudes these higher harmonics are dependent on the non-linear Pompom parameters and the Pompom parameter space is explored to see how experimental oscillatory shear data can infer molecular detail.

In the regime of small strain amplitude an asymptotic solution can be found that depends only on the ratio of the orientation and stretch relaxation times, τ_b and τ_s. This asymptotic solution is found to be accurate up to strains of order unity and the branching priority, q, only affects the stress response at larger strains.

Continuing the theme of the last chapter, the Pompom parameters fitted to extensional data are compared to LAOS data for three materials; the HDPEs, HDB3 and HDB6 and the LDPE 1840H. In general the Pompom model performs well in LAOS but does tend to over predict experimental results at high strain amplitudes.

In the investigation of the Pompom model the idea of linear chain stretch

relaxation is modelled to see if the inclusion of this relaxation mechanism has any significant effect on modelling experimental LAOS results. I show that incorporating linear chain stretch relaxation into the Pompom model does not significantly affect the theoretical predictions of LAOS simulations. The question that remains is whether any inadequacies seen in fitting the Pompom parameters to extensional rheology can be overcome by adjusting the Pompom parameterisations without significantly changing the predictions in extension. We show that by simulating the reaction process of HDB6 and 1840H to obtain a distribution of molecular structures and then creating a detailed Pompom spectrum for these molecules using over 4200 modes we are able to capture low-strain asymptotes of LAOS rheology. For deviations from the low-strain asymptotes full simulation results need to be examined but these are currently unavailable.

4.1 Introduction

As has been already discussed, one challenge with using the Pompom model is to fit the non-linear parameters that cannot be obtained from linear rheology.

One challenge is to fit the free parameters of a constitutive theory to a geometrically and practically simple experiment, so that the material can then be modelled in more general complex flow situations. Such flows will typically contain a mix of shear and extensional flow and it is necessary to characterise simultaneously both flow types. In particular the degree of strain hardening seen in extensional flow is highly sensitive to LCB and makes extensional flow a good choice for fitting constitutive theories, such as the Pompom model [Münstedt et al. (1998), Inkson et al. (1999) and Malmberg et al. (2002)]. However, it is very rare that an extensional steady state viscosity can be measured and despite recent developments in extensional rheology [Sentmanat (2004)] it remains a difficult experiment and usually only transient response is measured.

As seen in chapter 2, various techniques have been developed using linear shear rheology to distinguish between linear and branched topologies. Gabriel et al. (1998) showed creep experiments can be used to distinguish between a LLDPE and a LDPE. Various authors have used small amplitude oscillatory shear with Cole-Cole [Vega et al. (1998) and Vega et al. (1999)] and vanGurp-Palmen

plots [Trinkle and Friedrich (2001); Trinkle et al. (2002); Wood-Adams and Dealy (2000); Wood-Adams et al. (2000) and Lohse et al. (2002)]. The vanGurp-Palmen plot not only distinguishes between linear and branched polymers but also indicates the degree of LCB, although this can be masked by polydispersity [Trinkle et al. (2002); Vega et al. (1999) and Wood-Adams and Dealy (2000)]. Malmberg et al. (2002) used SAOS and uniaxial extension to examine the amount of LCB in metallocene catalysed polyethylenes. They found that while vanGurp-Palmen analysis of the samples detected LCB, uniaxial extension was a more sensitive technique for detecting the amount and distribution of LCB.

To investigate non-linear shear response several transient flow types can be modelled. Inkson et al. (1999) fitted Pompom spectra to extensional data and showed this gave good agreement with transient shear data. Graham et al. (2001) showed that a Pompom model fitted to extensional data of LDPE successfully predicts the stress development in exponential shear. However, when the procedure is reversed and the Pompom model is fitted to exponential shear, there is no guarantee of being able to capture the level of strain hardening in extensional flow. In chapter 3 it was shown that step strain measurements of polyethylenes are sensitive to the level of branching and can be predicted from Pompom spectra obtained from extensional data.

The three shear flows above are all modelled well by fitting a Pompom theory to extensional data, but the converse is not true. These shear flows are less sensitive than extensional flow to details of the branching structure, and thus they are not as useful for characterising constitutive theories.

Much attention has recently been focused on Large Amplitude Oscillatory Shear (LAOS), which explores oscillatory shear experiments for a given frequency and varying strain amplitudes, typically ranging from 0.1 to 4. In particular results have been explored using Fourier transform rheology (FTR), where the stress response is analysed in Fourier space.

4.1.1 General Oscillatory Shear

In this study we compare steady state oscillatory shear flow to transient shear and transient extensional flow. For a general oscillatory flow the deformation-rate

tensor $\underline{\underline{K}}$ reduces to

$$K_{xy} = \dot{\gamma} = \varepsilon\omega\cos(\omega t), \tag{4.1.1}$$

where ε is the strain amplitude and ω is the frequency of oscillation.

We can express the stress, in the quasi-steady state, as its Fourier decomposition,

$$\sigma_{xy} = \sum_{N}^{\infty} I_N^{'}\sin(N\omega t) + \sum_{N}^{\infty} I_N^{''}\cos(N\omega t), \tag{4.1.2}$$

where the Fourier coefficients, $I_N^{'}$ and $I_N^{''}$ satisfy,

$$I_N^{'} = \frac{\omega}{\pi}\int_{-\frac{\pi}{\omega}}^{\frac{\pi}{\omega}} \sigma_{xy}\sin(N\omega t)dt, \tag{4.1.3}$$

and,

$$I_N^{''} = \frac{\omega}{\pi}\int_{-\frac{\pi}{\omega}}^{\frac{\pi}{\omega}} \sigma_{xy}\cos(N\omega t)dt. \tag{4.1.4}$$

The Fourier coefficients can be defined in terms of non-linear storage and loss moduli by,

$$I_N^{'} = \varepsilon G_N^{'} \qquad \text{and} \qquad I_N^{''} = \varepsilon G_N^{''}, \tag{4.1.5}$$

where in the limit $\varepsilon \to 0$, $G_1^{'}$ and $G_1^{''}$ become the usual complex moduli.

We can also define the phase angle of each Fourier mode, N, as

$$\tan(\phi_N) = \frac{G_N^{''}}{G_N^{'}}, \tag{4.1.6}$$

and is commonly investigated in linear rheology for the first mode, $N = 1$ [e.g. Vittorias and Wilhelm (2007)].

Oscillatory shear flow for a fluid with characteristic relaxation time, $\bar{\tau}$, can be described using both a Deborah number and Weissenberg number [c.f. section 1.4.1] which are defined as,

$$De = \omega\bar{\tau} \tag{4.1.7}$$

$$W_i = \varepsilon\omega\bar{\tau}, \tag{4.1.8}$$

where for a mulitmode Pompom spectra, $\bar{\tau} = \frac{\Sigma_i G_i \tau_i^2}{\Sigma_i G_i \tau_i}$.

It has been suggested that FTR is sensitive to differing levels of branching [e.g. Hyun et al. (2007)], and has the advantage that LAOS is easier experimentally than extensional flow. Typically, measured quantities include the real and imaginary components of the odd harmonics, I'_N and I''_N, where $N = 1, 3, 5 \cdots$. From these parameters the absolute value of each harmonic is examined as a fraction of the absolute first harmonic and can be defined as,

$$I^2_{N/1} = \frac{I'^2_N + I''^2_N}{I'^2_1 + I''^2_1}. \tag{4.1.9}$$

MacSporran and Spiers (1984) have shown that LAOS and FTR is a sensitive technique for investigating the microscopic structure of fluids, in particular the phase shift for the third harmonic, $\Phi_3 = \phi_3 - 3\phi_1$, and the third storage and loss moduli, G'_3, G''_3, are of particular interest in characterising a material and characterising both viscous and elastic non-linear rheology. Wilhelm et al. (1998) showed that applying oscillatory shear to non-Newtonian linear polymers provides a tool for investigating non-linear response independent of material. By investigating the shear response in Fourier space, higher harmonics were used to characterise non-linearities. Wilhelm et al. (1999) continued investigating at the cross-over from linear to non-linear behaviour using the relative magnitude of the third harmonic, $I_{3/1}$. The authors also looked at the difference between parallel plate and cone-plate geometries, suggesting that results are not independent of geometry. Wilhelm et al. (2000) and Wilhelm (2002) used FTR with linear polymers to characterise with respect to their molecular weight, molecular weight distribution and topology.

Debbaut and Burhin (2002) investigate high density polyethylenes (HDPE) in various oscillatory measurements including LAOS and compare them with the Giesekus model, finding reasonable agreement between experiment and theory. Neidhöfer et al. (2003) used FTR with various branched polystyrene solutions. Using the phase shift of the third harmonic, Φ_3, the authors were able to distinguish between linear and star branched molecules at large amplitudes. Fleury et al. (2004) and Schlatter et al. (2005) investigated various linear and branched materials in FTR. They compared the sensitivity of FTR to linear analyses such as van Gurp-Palmen and Cole-Cole plots and showed that it was more sensitive

to branching than linear analysis. The authors compare two constitutive models (Wagner [Wagner and Stephenson (1979)] and DCPP [Clemeur et al. (2003)]) and fit the models to the data in a range of plots. One of the more interesting plots shown is a polar plot of the real and imaginary components of the Fourier decomposed shear stress, parameterised by strain amplitude. The authors claim the Wagner model gives a better prediction of the experimental results than the Pompom model, although this may be a consequence of the way in which the model parameters were fitted.

Hyun et al. (2006) and Hyun et al. (2007) compare a range of constitutive models to strain hardening and non-strain hardening data. The authors discuss the concepts of medium amplitude oscillatory shear (MAOS) for strains amplitudes of 0.1 to 1 and the 'intercept' of the normalised absolute third harmonic, $I_{3/1}$, which is the value of $I_{3/1}$ at a strain amplitude of 0.01. In particular for branched materials the authors claim that the slope of $I_{3/1}$ scales with ε as $I_{3/1} \sim \varepsilon^n$, where n is less than 2, as opposed to $n = 2$ for linear molecules. The authors also measure transient extensional data in an attempt to link the level of strain hardening to the non-linear response of FTR. They also note that a single mode Pompom model has a power law of $n = 2$ in MAOS as must any model in the limit of small but finite strain amplitude. Schlatter et al. (2005) shows the DCPP model can successfully predict $I_{3/1}$ for a range of linear, sparsely branched and densely branched polyethylenes, and in this chapter we show that the multimode form of the original Pompom model is equally effective.

Vittorias et al. (2007) compared Fourier transform rheology (FTR), NMR and Pompom DCPP simulations. They examined $I_{3/1}$ and Φ_3 and extended the van Gurp-Palmen method to the third harmonic, $\Phi_3^0 = lim_{\varepsilon \to 0} \Phi_3$, extrapolating to zero strain amplitude and investigated optimum experimental conditions for distinguishing the branching structure of various polyethylene samples. They found that the extended van Gurp-Palmen method is sensitive to LCB and found low frequencies optimized the non-linearity. The data was modelled with the DCPP model, using only four modes. This model was able to predict $I_{3/1}$ and Φ_3 reasonably accurately although deviations from experimental data did exist. Vittorias and Wilhelm (2007) examined small amplitude oscillatory shear (SAOS), LAOS and FTR for linear and branched polyethylenes and showed that FTR is capable

of determining the degree of LCB and that LAOS is more sensitive to LCB than SAOS. However, the authors point out that FTR still needs to be explored using well characterised polymer architectures.

Wapperom et al. (2005) investigated LAOS for a high density polyethylene comparing it to the predictions of various constitutive equations, mainly focusing on the MSF but also considered the Doi−Edwards, Carreau−Yasuda, and Giesekus models. They found that the MSF model over predicted the shear stress, although fitted the phase shift well. The Doi−Edwards model gave a better prediction of the stress than the MSF model, however the MSF model is able to capture strain hardening and only requires one parameter.

In their paper deriving DPP formulation of the Pompom model, Clemeur et al. (2003) calculated the response of the model to a double step strain and LAOS with FTR. They presented the LAOS results in the form of 'Lissajous' plot, comparing stress to strain. This makes non-linear behaviour apparent by observing visual distortion of a linear ellipse. The DPP model performs reasonable well, capturing the intensity of the harmonics, but deviations in the Lissajous plot occur at strains of around 5.

More recently, Hyun and Wilhelm (2009) derive the quantities Q and Q_0, which are defined as $I_{3/1}/\varepsilon^2$ and $I_{0,3/1}/\varepsilon^2$, respectively where the 0 subscript denotes the limit of zero strain amplitude. The authors show that both Q and Q_0 are sensitive to molecular architecture and that Q_0 as a function of Deborah number can be explored using TTS to increase the experimental range available.

In this chapter we examine a variety of materials in SAOS and LAOS to see if we can successfully distinguish between levels of branching. We also plan to explore the Pompom parameter space in order to understand what characterisation of a material can be obtained from LAOS.

4.2 Numerical Methods

The stress generated in the Pompom model in oscillatory shear and its Fourier decomposition were calculated simultaneously. In shear flow the constitutive

equations for the Pompom [c.f section 1.6.5] model reduce to,

$$\frac{dA_{xy}}{dt} = \dot{\gamma} - \frac{1}{\tau_b^*} A_{xy}, \tag{4.2.1}$$

$$\frac{dA_{xx}}{dt} = 2\dot{\gamma} A_{xy} - \frac{1}{\tau_b^*} \left(A_{xx} - 1\right), \tag{4.2.2}$$

$$\frac{d\lambda}{dt} = \frac{\dot{\gamma} A_{xy}}{A_{xx} + 2} \lambda - \frac{1}{\tau_s} \left(\lambda - 1\right) e^{\nu^* (\lambda - 1)}. \tag{4.2.3}$$

The orientation equations needed to be solved numerically since the relaxation time, τ_b^* is a function of the non-analytic stretch function, $\lambda(t)$, in reversing flow [c.f. equation 1.6.49]. Equations 4.2.1 to 4.2.3 are solved using a fourth order Runge-Kutta scheme [Burden and Faires (2001)]. Quadruple precision was used to avoid round−off when solving solutions at low strain amplitude. In choosing appropriate values for the time step some calculations were performed using a fifth order Runge-Kutta-Fehlberg scheme [Burden and Faires (2001)] and solutions were checked for time-step independence for a large range of frequencies and strain amplitudes. An example of this can be seen in figure 4.1, where a one mode Pompom model with parameters $G = 1000$Pa, $\tau_b = 10$s, $q = 5$ and $r = 4$ was solved for various choices in time step ranging from 10^{-1} to $5 \cdot 10^{-4}$, at a constant Deborah number, $De = 12$. Good convergence at both low and high strain amplitudes occurs for a step size of 10^{-3} and lower. At small Weissenberg numbers the third harmonic, I_3, is of order W_i^3 making it difficult to compute accurately at very small W_i. However, for step sizes less than 10^{-3} the results in figure 4.1 for the relative third harmonic, $I_{3/1}$, shows the expected W_i^2 behaviour.

To further reduce numerical noise the time step was chosen so that the period is an integer number of steps. Convergence to steady state was checked by ensuring the maximum stress response for each period agreed to five significant figures before the start of the Fourier integral and the Fourier transform was performed over multiple cycles to increase noise cancellation. The Fourier transform was calculated using a five point extension on the trapezoid rule, known as Bode's rule, which has an error of order $h^7 f^{(6)}$ [Press et al. (1996)].

The noise level of the Fourier transform was calculated from the second harmonic, which is mathematically zero. For strain amplitudes larger than $\varepsilon = 0.1$

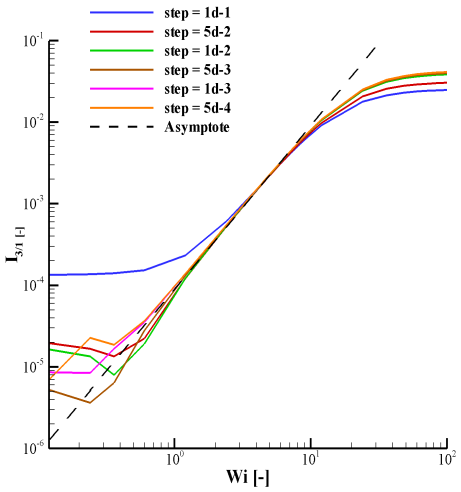

Figure 4.1: A one Pompom model in oscillatory shear with various choices of time step. The other Pompom parameters chosen are $G = 1000$Pa, $\tau_b = 10$s, $q = 5$ and $r = 4$, giving a constant Deborah number for each simulation as $De = 12$. Good convergence for both low and high strain amplitudes occurs for a step size of 10^{-3}.

the absolute value of the second harmonic was less than 10% of the absolute value of the third harmonic. The low-strain asymptotic solution detailed in the next section removes the need to calculate the solution at very low Weissenberg numbers.

4.3 The Pompom model in oscillatory shear

In this section I examine a one mode Pompom model in oscillatory shear to examine the influence of the choice of parameters on the predictions for LAOS. The Deborah number and the Weissenberg number are defined with respect to the orientation relaxation time as $De = \omega\tau_b$ and $W_i = \varepsilon\omega\tau_b$, respectively.

I begin by examining the effect of the branching priority, q_i on the shear stress response in oscillatory shear. In figure 4.2 the stress response of a one mode Pompom model with various values of q and constant ratio of $r = 4$ are shown. The is plotted against time and strain (Lissajous plots) for a constant Deborah number, $De = 12$, for $q = 1, 2, 5$ and 10. At a Weissenberg number of

$W_i = 1.2$ ($\varepsilon = 0.1$) all four models superimpose with a linear stress response. At $W_i = 12$ ($\varepsilon = 1$) all cases with $q > 1$ still superimpose, however for $q = 1$ the stress deviates slightly from linear behaviour. For a high Weissenberg number, $W_i = 120$ ($\varepsilon = 10$), the linear model with $q = 1$ is dramatically different from the branched models, $q > 1$. For $q = 1$ a double peak is observed which corresponds to cusps in the Lissajous plots. Similar shaped plots that have been observed in experiments [Li et al. (2009)] and even hysteresis loops have been shown to be evident in certain circumstances at the cusps [Ewolt and McKinley (2010); Ewolt et al. (2008)]. Even at this high amplitude there is little difference in the stress response for $q > 1$ indicating that the Pompom model in LAOS is not very sensitive to the branching priority. This is confirmed in more detail using FTR later in the chapter.

Figure 4.3 shows the same plot as figure 4.2 for constant branching priority, $q = 5$ but with the ratio of orientation and stretch relaxation times varied through $r = 1, 2, 4$ and 8. For a Deborah number $De = 12$ with increasing Weissenberg number the stress response changes more dramatically than for the case with varied q parameter. For a Weissenberg number of $W_i = 120$ the stress response is attenuated with increasing relaxation time ratio. Thus we conclude that for $q > 1$ the stress response of the Pompom constitutive model in LAOS is more sensitive to changes in the ratio of relaxation times than to changes in branching priority.

4.3.1 Fourier Transform Rheology

The stress response of the Pompom model seems to be particularly sensitive to the ratio of orientation and stretch relaxation times. This ratio is proportional to the number of entanglements along the backbone. To probe this property almost singularly would provide a unique tool for the analysis of branched materials. To study LAOS in further detail it becomes more convenient to examine the stress response in Fourier space rather than the time domain. The Fourier coefficients of the harmonic series can be studied independently to find which is particularly sensitive to molecular structure. The first harmonics of the series are already commonly used in the linear regime to fit Maxwell modes for various constitutive

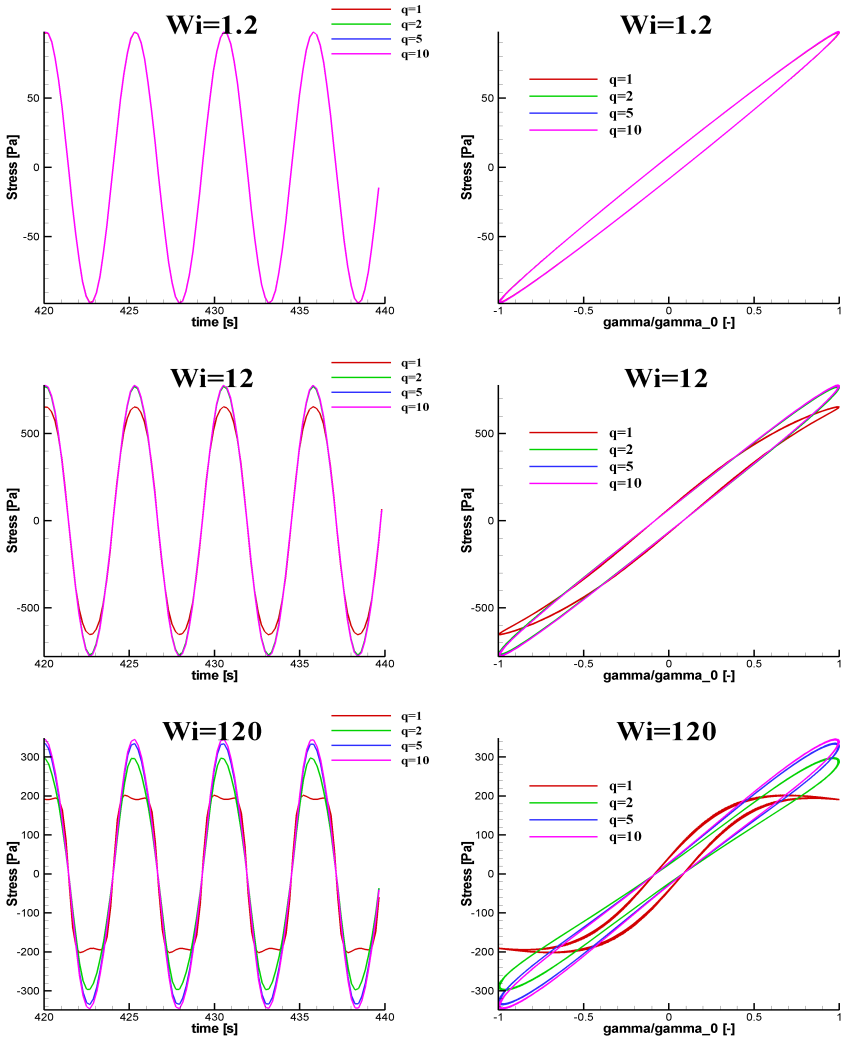

Figure 4.2: A one Pompom model in oscillatory shear with various choices of the branching parameter, $q = 1, 2, 5$ and 10. The other Pompom parameters chosen are $G = 1000$Pa, $\tau_b = 10$s and $r = 4$, giving a constant Deborah number for each simulation as $De = 12$. As the Weissenberg number increases the most noticeable difference is for the case $q = 1$. The stress response has low sensitivity to values of $q > 1$.

equations including the Pompom model where they are used to determine $\{G_i, \tau_{b_i}\}$ and hence give some information about the structure of the material. In this chapter I will focus on the third harmonic and examine its sensitivity to the non-linear Pompom parameters.

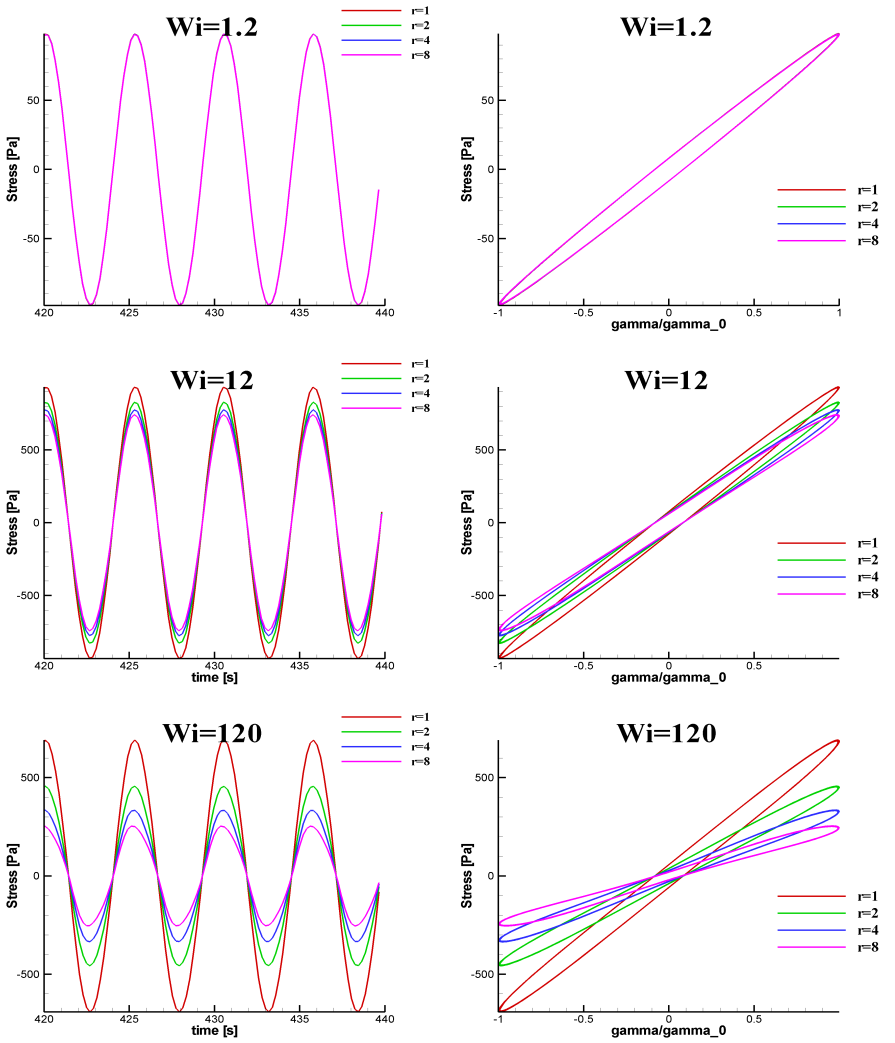

Figure 4.3: A one Pompom model in oscillatory shear with various choices of the stretch relaxation ratio, $r = 1, 2, 4$ and 8. The other Pompom parameters chosen are $G = 1000$Pa, $\tau_b = 10$s and $q = 5$, giving a constant Deborah number for each simulation as $De = 12$. Compared to the branching parameter (figure 4.2) the stress response is more sensitive to variations and stretch relaxation time.

4.3.2 Asymptotic Solutions

A series of low strain asymptotic solutions can be derived to achieve analytical solutions for equation 4.1.3 and 4.1.4. We can use these to look for deviations from linear behavior. Once verified these results can also be used to reduce

computation time for calculating the Fourier coefficients, as a very small time step is required to resolve the Fourier integrals for very low strains. A high strain asymptote for the case of $q = 1$ can also be derived to examine the high strain limit of a linear Pompom model.

To derive low strain asymptotes it is convenient to re-write the UCM tensor as an expansion in powers of the strain amplitude, ε,

$$\underline{\underline{A}} = \underline{\underline{I}} + \varepsilon \underline{\underline{a}}_1 + \varepsilon^2 \underline{\underline{a}}_2 + \cdots , \tag{4.3.1}$$

and, similarly the stretch equation can be written as,

$$\lambda(t) = 1 + \varepsilon\lambda(t)_1 + \varepsilon^2\lambda(t)_2 + \cdots \tag{4.3.2}$$

In the case of the UCM tensor for $\tau_b^* = \tau_b$ the expansion terminates after the quadratic term.

The changes to τ_b^* are negligible in the low strain limit and can be neglected. Simulations show that changes in τ_b^* affect the Pompom stress response for strain amplitudes higher than unity. The resulting shear stress can be expanded in odd powers of ε. The leading order term is,

$$\sigma_{xy} = \frac{G\tau_b\omega\left(cos\left(\omega t\right) + \tau_b\omega sin\left(\omega t\right)\right)}{1 + \tau_b^2\omega^2}\varepsilon + O(\varepsilon^3) \tag{4.3.3}$$

Taking the Fourier transform of this result restores the familiar Maxwell storage and viscous moduli,

$$I_1^{'} = \frac{GDe^2}{1 + De^2}\varepsilon + O(\varepsilon^3), \tag{4.3.4}$$

and,

$$I_1^{''} = \frac{GDe}{1 + De^2}\varepsilon + O(\varepsilon^3), \tag{4.3.5}$$

where the Deborah number is given by, $De = \omega\tau_b$, and the frequency is given in rad.s^{-1}.

Figure (4.4) shows a frequency sweep of the storage modulus ($G^{'}$) and viscous modulus ($G^{''}$), for a one mode Maxwell (Pompom) model. We see at the cross-

over frequency $\omega = \tau_b^{-1}$ that the two moduli are equivalent.

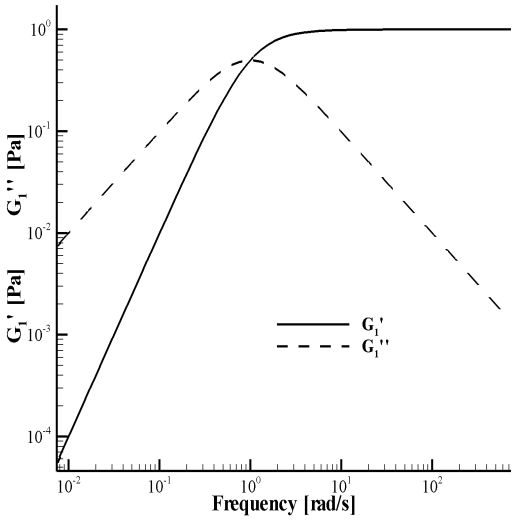

Figure 4.4: A plot of the first harmonics as a function of Deborah number which correspond to the dynamic moduli used to fit Maxwell modes. The parameters used were $G = 1$Pa and $\tau_b = 1$s.

We can go on from the first harmonic to derive subsequent low-strain asymptotic results for higher odd harmonic results (since the even Fourier coefficients are zero in value). These were calculated by hand and checked using the MAPLE symbolic algebra program. We give the result for the third harmonic and concentrate on this since higher harmonics are more complicated still. The storage and loss modulus for the third harmonic, in their low strain limit are given by,

$$I_3^{'} = -\frac{GDe^4(1-r^{-1})(De^2+5De^2r^{-1}-2-r^{-1})}{(1+4De^2r^{-2})(1+4De^2)(1+De^2)^2}\varepsilon^3 + O(\varepsilon^5), \tag{4.3.6}$$

and,

$$I_3^{''} = \frac{GDe^3(1-r^{-1})(4De^4r^{-1}-5De^2-8De^2r^{-1}+1)}{2(1+4De^2r^{-1})(1+4De^2)(1+De^2)^2}\varepsilon^3 + O(\varepsilon^5). \tag{4.3.7}$$

The two coefficients for the third harmonic are a function of Deborah number and

the ratio, r, of the orientation and stretch relaxation times. Neither asymptote is dependent on the branching parameter, q, so that the influence of branching is only present in the large amplitude regime, i.e. for $W_i \gg 1$.

The leading order term in $I_n^{'}$ and $I_n^{''}$ is of order ε^n for n odd and containing only odd powers of ε. In the limit of low strain only the leading power is of importance and so higher order terms can be neglected.

In figure 4.5 we show the variation in $I_{3/1}^{'}$ and $I_{3/1}^{''}$ with frequency, ω, where $I_{3/1}^{'}$ is defined as $\frac{I_3^{'}}{I_1}$ and similarly $I_{3/1}^{''} = \frac{I_3^{''}}{I_1}$. We plot the resulting $I_{3/1}^{'}$ and $I_{3/1}^{''}$ scaled by ε^2 on a linear axis, as there exists a regime of negative contribution. The frequency is still on a log axis. The modulus of the relative third harmonic is also overlayed.

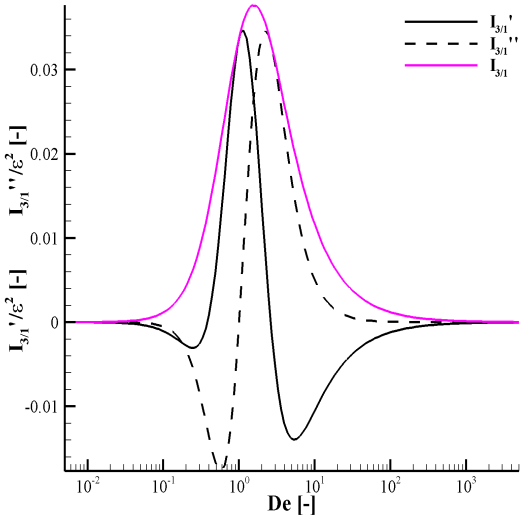

Figure 4.5: A plot of $I_{3/1}^{'}$, $I_{3/1}^{''}$ and $I_{3/1}$ as a function of Deborah number. Parameters used were $G = 1$Pa, $\tau_b = 1$s and $\tau_s = 0.25$s, with the strain amplitude chosen as, $\varepsilon = 0.01$.

For each modulus, $I_{3/1}^{'}$ and $I_{3/1}^{''}$, there exists a maximum/minimum contribution to the stress, depending on frequency. In figure 4.6 we explore the height of the maxima of $I_{3/1}$ with respect to the ratio of τ_s to τ_b.

We see in figure (4.6), that a higher ratio implies a higher maxima of $I_{3/1}$. In

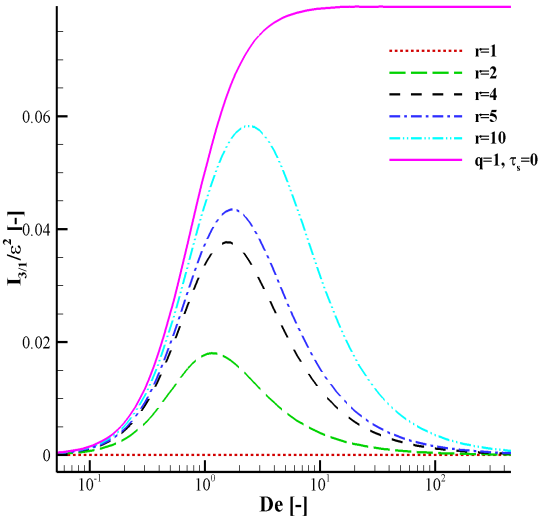

Figure 4.6: A plot of $I_{3/1}$ as a function of Deborah number for various ratios, $r = 1, 2, 4, 5, 10$ and $r = \infty$. The linear parameters are $G = 1$Pa and $\tau_b = 1$s. The maximum in I_3 increases as a function of r up to the case of $\tau_s = 0$s ($r = \infty$) which has asymptotically different behaviour compared to finite r. The strain amplitude chosen as, $\varepsilon = 0.01$.

other words, a higher ratio implies a quicker τ_s and hence a smaller contribution to stretch term in the extra stress. Note, from equations (4.3.6) and (4.3.7) for a ratio, $r = 1$, there is no contribution of the third harmonic to the total stress. In fact, the contribution is of order, $O(\varepsilon^5)$ and can be calculated analytically.

The case of $q = 1$ with the physical limit of $\lambda < q$, stretch relaxation is effectively instantaneous hence, $\tau_s = 0$s. This causes the values $I_3^{''}$ and $I_3^{'}$ to have characteristically different behaviour from the cases with stretch relaxation occurring.

Again, from equations (4.3.6) and (4.3.7) the value of $I_{3/1}^{'}$ is the most dramatically different and is non-zero in the high frequency limit. This behaviour is unphysical as this model rejects chain Rouse modes. The difference between $I_{3/1}^{''}$ for $q = 1$ and $q > 1$ occurs in the high frequency regime. For the case $q = 1$, $I_{3/1}^{''}$ does not have a second minimum as it does for the cases where $q > 1$ [c.f. figure (4.5)]. Again, this is due to the lack of any chain stretch modes in this model.

One method for incorporating the rheology of a linear molecule is to set the stretch relaxation time to the Rouse time and allow $q \to \infty$. This limit approximates to the RoliePoly constitutive equations [Graham et al. (2003)] without convective constraint release and this limit has been previous studied by Venerus (2005); Venerus and Nair (2006) to successfully model step strain flow of both finite and ideal step imposition time.

In the case of $q = 1$ we can derive high strain asymptotes for each Fourier coefficient. Using the previous expansion of the UCM tensor in powers of the strain amplitude (equation 4.3.1) it can be shown that in high strain all Fourier coefficients scale as ε^{-1}. Subsequently the Fourier coefficients for the first harmonic can be expressed as,

$$I_1' = \frac{1}{\varepsilon}\frac{\sqrt{3}G\left(2De\sqrt{(3(1+4De^2))} - 4De^2 - 1\right)}{De\sqrt{(1+4De^2)}}, \tag{4.3.8}$$

and

$$I_1'' = \frac{1}{\varepsilon}\frac{3G}{De}, \tag{4.3.9}$$

and the Fourier coefficients for the third harmonic can similarly be written as,

$$I_3' = -\frac{1}{\varepsilon}\frac{\sqrt{3}G\left(20De^4 - 6De^3\sqrt{3(4De^2+1)} - 17De^2 + 6De\sqrt{3(4De^2+1)} - 1\right)}{De(1+De^2)\sqrt{4De^2+1}}, \tag{4.3.10}$$

and

$$I_3'' = \frac{1}{\varepsilon}\frac{\sqrt{3}G\left(11De^2\sqrt{3(4De^2+1)} - \sqrt{3(4De^2+1)} - 36De^3\right)}{De(1+De^2)\sqrt{4De^2+1}}. \tag{4.3.11}$$

Unfortunately we have not been able to find an equivalent solution for $q > 1$. This requires solving the backbone stretch equation for $\lambda(t)$. Even in the limit of infinite branches, $q \to \infty$, which has the effect of making $\nu^* = 0$ and not having to impose the limit of $\lambda \leq q$, no solution has been found in the high strain amplitude limit.

In figure 4.7 the high strain asymptote for $I_{3/1}$ is plotted as a function of Deborah number for one mode Pompom model with $G = 1$Pa and $\tau_b = 1$s.

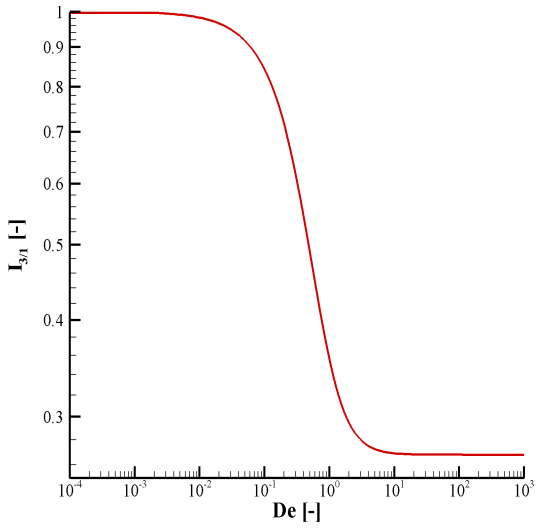

Figure 4.7: The high strain asymptote of the relative third harmonic, $I_{3/1}$, plotted as a function of Deborah number. The high strain asymptote is only analytic for a linear Pompom model, i.e. $q = 1$. This one mode model has parameters of $G = 1$Pa and $\tau_b = 1$s.

This high strain asymptote is independent of strain amplitude and so for a fixed Deborah number it is also independent of Weissenberg number, as seen in figure 4.8. Figure 4.7 shows that $I_{3/1}$ has two regimes in high strain. For low Deborah numbers, $De \ll 1$, the ratio of the third and first absolute harmonics is ~ 1, implying each harmonics contributes equally in the Fourier series. For $De \gg 1$ the value of $I_{3/1}$ plateaus at approximately 0.27 with the transition between the two regimes occurring at $De \sim 1$. This is in contrast to the low strain asymptotic results that show peaks in $I_{3/1}$ at a Deborah number ~ 2.

4.3.3 Simulation results

In this section the Pompom model is explored in LAOS with the Pompom equations solved using the numerical techniques detailed in section, 4.2.

In figure 4.8 a one mode Pompom model is compared in LAOS for $De = 12$ and a range the number of arms, $q = 1, 2, 5$ and 10. The solution agrees with the

low strain asymptote for Weissenberg numbers in the range $1 < W_i < 10$, and for the case $q = 1$ the high strain asymptote agrees with the solution for $W_i > 100$. The solution deviates from the low strain asymptote at around a $W_i \sim 10$, at which point small differences can be seen for the various choices of q, for cases with $q > 1$.

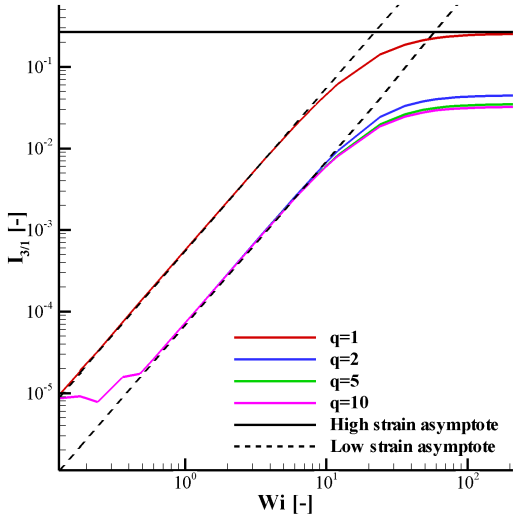

Figure 4.8: The relative third harmonic $I_{3/1}$ plotted as a function of Weissenberg number for a one mode Pompom model with variations in branching parameter, q. The other Pompom parameters are $G = 1000$Pa, $\tau_b = 10$s and $r = 4$ giving a Deborah number, $De = 12$.

In figure 4.9 a plot of $I_{3/1}$ is shown for various ratios of orientation and stretch relaxation time, $r = 1, 2, 4$ and 8, and constant branching parameter, $q = 5$. For $r > 1$ the linear response superimposes onto the low strain asymptote. For the case of $r = 1$ the leading order terms given in equations 4.3.6 and 4.3.7 are zero so that $I_{3/1}$ is of order ε^4 and not ε^2. Comparing figures 4.8 and 4.9 it can be seen that the predominant Pompom parameter that controls the stress response in LAOS is the stretch relaxation time, τ_s.

In figure 4.10 the real and imaginary parts of the absolute value of the third harmonic, $I_{3/1}$, are plotted as a function of Weissenberg number for fixed Deborah

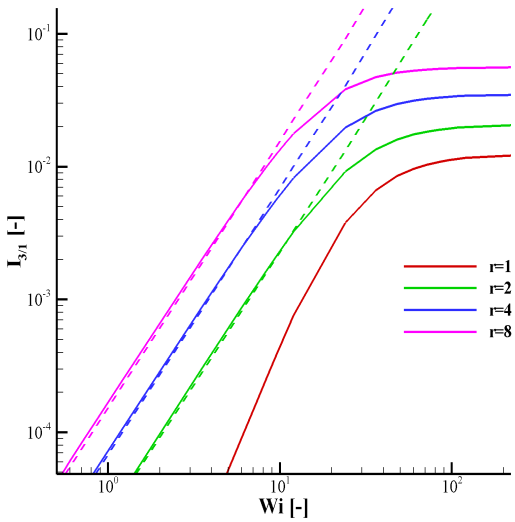

Figure 4.9: The relative third harmonic $I_{3/1}$ plotted as a function of Weissenberg number for a one mode Pompom model with variations in the ratio of orientation and stretch relaxation times, r. The dashed lines represent the low-strain asymptotic solution and the simulation was performed at a fixed Deborah number of $De = 12$. The other Pompom parameters are $G = 1000$Pa, $\tau_b = 10$s and $q = 5$.

number of $De = 12$, for various choices of branching parameter, q, and ratio of orientation and stretch relaxation time, r. The linear Pompom parameters are chosen as $G = 1000$Pa and $\tau_b = 10$s. The real and imaginary parts of $I_{3/1}$ are denoted as $I'_{3/1}$ and $I''_{3/1}$, respectively.

In figure 4.10(left) the real and imaginary parts of $I_{3/1}$ are plotted for various choices of branching parameter, q, and a fixed ratio, $r = 4$. For $q > 1$ there is only a small effect on the values of $I'_{3/1}$ and $I''_{3/1}$ with changing q. For $q = 1$, $I'_{3/1}$ is considerably larger than for the case of $q > 1$ and also for $q = 1$, $I''_{3/1}$ is positive as oppose to negative for the case $q > 1$.

As previously mentioned, there will exist a physical stretch relaxation from chain stretch of a linear molecule which is not modelled by the Pompom constitutive equations and this in the sum of multiple modes this could lead to discrepancies between constitutive model and experiment.

On the right of figure 4.10 the ratio of orientation and stretch relation times,

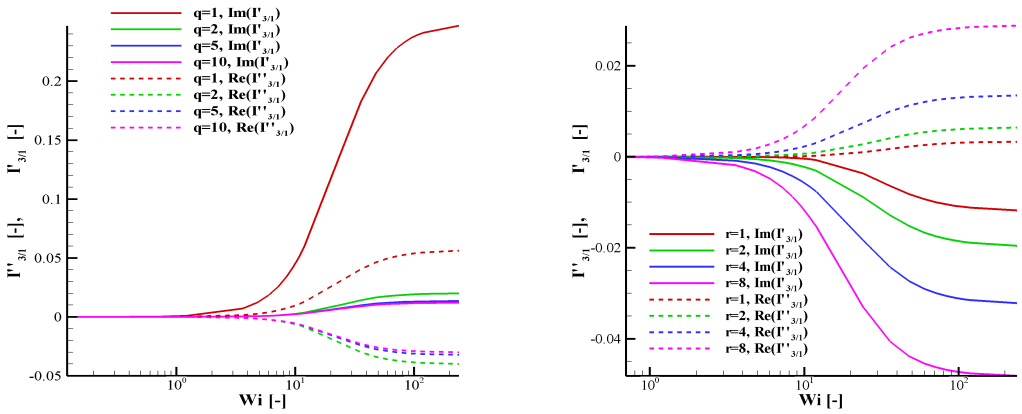

Figure 4.10: The real and imaginary parts of the relative third harmonic, $I_{3/1}$, plotted against Weissenberg number for various choices of branching priority, q, (left) and the ratio of orientation and stretch relaxation times, r (right). The linear Pompom parameters are $G = 1000$Pa and $\tau_b = 10$s with $De = 12$.

r, is varied with a fixed branching parameter, $q = 5$. The figure shows the results for a fixed Deborah number of, $De = 12$, as a function of Weissenberg number. Again it can be seen that varying τ_s and hence r has a much bigger effect on $I'_{3/1}$ and $I''_{3/1}$ than the branching parameter, q.

Studying the real and imaginary parts of $I_{3/1}$ provides a deeper insight into how a constitutive equation performs in LAOS, compared to the absolute value of $I_{3/1}$, since such quantities as the phase shift (of the n^{th} harmonic) are calculated from I'_n and I''_n. In the subsequent section the principles discussed here are used to compare simulations of multimode Pompom constitutive model to experimental results of various polyethylenes.

4.4 Experimental Results

We shall now compare the predictions of the multimode Pompom model fitted to extensional rheology in chapter 2 with experimental measurements for three materials, namely the HDPEs; HDB3 and HDB6, and the LDPE, 1840H. All three materials have similar zero shear viscosities, $\eta_0 \sim 50$[Pa s], details of which

and other material parameters can be found in table 2.1. It should be noted that unless otherwise stated the theory for HDB6 will be HDB6(a).

This will enable us to consider the question: can Pompom spectra with non-linear parameters fitted to extensional data capture the behaviour of branched materials in LAOS?

The experimental data presented in this section explores three frequencies 0.12rad/s, 1.2rad/s and 12rad/s, with absolute strain amplitudes in the range of 0.1 to 1 for each of the three materials. I would like to acknowledge and thank Vitor Barosso currently working at the Johannes Kepler University, Austria, and formally working at the Max Plank Institute working under Manfred Wilhelm, for providing me with both the experimental measurements and details of the experimental procedure used.

The Large Amplitude Oscillatory Shear (LAOS) experiments were performed on an ARES rotational rheometer (TA Instruments, New Castle-DE, USA) using a 13mm parallel plate geometry, with a gap of around 1mm. The temperature was controlled through the use of the convection oven of the ARES, with heated nitrogen being flushed to achieve the desired temperature and avoid degradation. During the LAOS experiments, a temperature of $150°C$ was used for 1840H, and $155°C$ for HDB3 and HDB6. All the samples were previously prepared on a heated press under vacuum which ensured samples free of entrapped air bubbles and stress free. For the frequencies of 0.2Hz and 2Hz, eleven strain amplitudes between 0.1 and 1 (10% and 100% strain) equally spaced on a log-scale were used. For the lower frequency (0.02Hz), only six strains (also equally spaced) were used due to possible thermal degradation derived from the extended duration of the measurement.

For the analysis of the LAOS data, the FT-Rheology framework was used [Neidhöfer et al. (2003); Wilhelm (2002)]. The raw strain and torque data were collected directly from the ARES, and externally digitised. The obtained values after Fourier analysis of the raw torque signal were the relative intensities of the higher harmonics $I_{n/1}$, and the relative phase differences Φ_n, as explained by Neidhöfer et al. (2003).

4.4.1 Small amplitude experiments

First consider the case of small amplitudes for which we can use the asymptotic formulas. Using small amplitude to measure dynamic moduli for the third harmonic has the benefit of avoiding experimental difficulty associated with performing higher strain amplitudes and it allows the stretch relaxation times in a multimode Pompom constitutive model to be determined.

Figure 4.11 shows a plot of the absolute value, $I_{3/1}$, of the low strain asymptotes (c.f. equations (4.3.6) and (4.3.7)) plotted as a function of Deborah number and normalised by ε^2 for the three materials used in this section. For each material the value of $I_{3/1}$ shows some oscillations due to the sum of multimodes. The most discernible difference is between the two HDPEs and the LDPE, where the curve of $I_{3/1}$ for the LDPE is below that of the two HDPEs. This is a result of the 1840H being modelled with more non-linear modes than the two HDPEs. Recall from figure 4.8 that the value of $I_{3/1}$ is lower for $q > 1$ than for $q = 1$ so the number of modes that have $q > 1$ is important.

In section 4.5.1 we discuss the effect of not modelling chain stretch for linear molecules and the effect that mode density has on these low strain predictions.

4.4.2 Large amplitude oscillatory shear (LAOS)

In this section a range of strain amplitudes typically larger than those used for SAOS are examined. Absolute strain amplitudes in the range $\varepsilon = 0.1$ to $\varepsilon = 1$ were accessible with the experimental technique used. Strain amplitudes beyond some critical point will depart from the low-strain asymptote which is proportional to the square of the strain amplitude, and tend to a plateau [e.g. Neidhöfer et al. (2003)]. This plateau has not been experimentally reached in this work.

In the last section it was shown that in a multimode Pompom constitutive model the number of modes with non-linear parameters (i.e. modes with $q > 1$) affects the results for higher harmonics at small strain amplitudes. On a natural progression does the number of non-linear modes affect the LAOS results and how sensitive are LAOS predictions to the branching parameter, q? Another test for LAOS is to see if measurements can be used to distinguish between materials with differing levels of LCB.

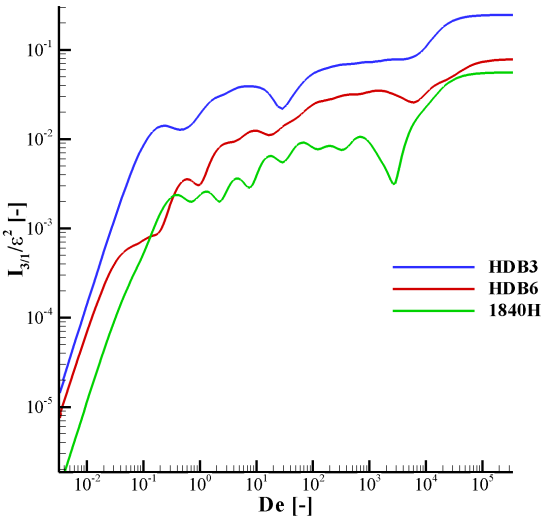

Figure 4.11: A plot of the absolute value, $I_{3/1}$, of the low strain asymptotes (c.f. equations (4.3.6) and (4.3.7)) plotted as a function of Deborah number for the three materials; HDB3, HDB6 and 1840H. The strain amplitude chosen as, $\varepsilon = 0.01$.

Figure 4.12 shows a comparison between experiment and theory for each material for the three frequencies used in this study. Since each experiment is performed at a different Deborah number the value of $I_{3/1}$ is normalised by Deborah number for clarity and is plotted as a function of Weissenberg number. To calculate Deborah and Weissenberg numbers the average relaxation time for each material was taken from table 2.1. The dotted lines represent the low strain asymptotic solution derived in the last section and the solid lines are the numerical results. The experimental results do not always depart from the small strain amplitude asymptotic prediction and where there is departure it is small. In general, the Pompom model with parameters fitted to extensional rheology is able to predict the experimental results well, even departing from the W_i^2 behaviour at the same point as experiments. The best results are for the intermediate frequency, 1.2rad/s where experiment and theory agree well. The smallest and largest frequencies are modelled less precisely, with the Pompom parameterisations used here, over-predicting the experimental results. This is possibly

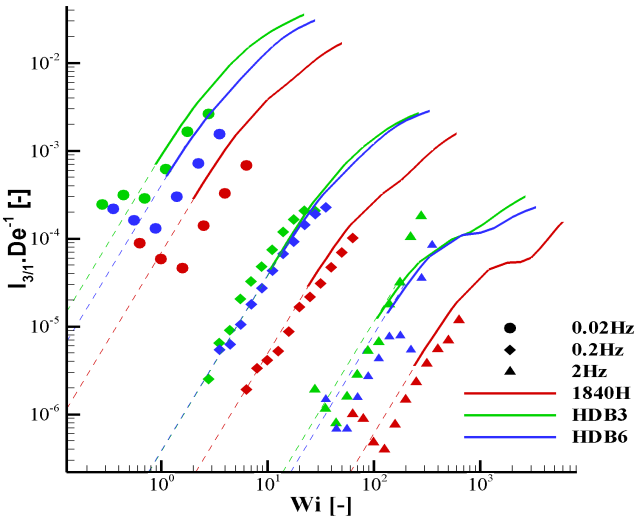

Figure 4.12: A comparison between experiment and theory for each material for the three frequencies used in this study. Since each experiment is performed at a different Deborah number the value of $I_{3/1}$ is normalised by Deborah number for clarity and is plotted as a function of Weissenberg number. The dotted lines represent the low strain asymptotic solution derived in the last section and the solid lines are the simulated results.

caused by the oscillatory behaviour occurring from the discretisation into Pom-pom modes (c.f. 4.11) and therefore increasing the mode density should smooth out the oscillations.

As noted earlier the real and imaginary parts, $I_{3/1}^{'}$ and $I_{3/1}^{''}$ respectively, contain phase information that does not appear in $I_{3/1}$. Figures 4.13 to 4.15 show the real and imaginary parts of the absolute third harmonic, $I_{3/1}$, plotted for varying Weissenberg numbers for HDB3, HDB6(a) and 1840H. Generally the real part, $I_{3/1}^{'}$, is larger and dominates the absolute modulus for each Deborah number. The initial quadratic behaviour modelled by the low strain asymptote of $I_{3/1}$ is seen in $I_{3/1}^{'}$. In contrast the imaginary part of the absolute third harmonic, $I_{3/1}^{''}$, is much smaller than $I_{3/1}^{'}$ and tends to decrease and become negative. In each plot the Pompom prediction is shown with a solid line in the experimental regime and a dotted line for Weissenberg numbers that were not experimentally available.

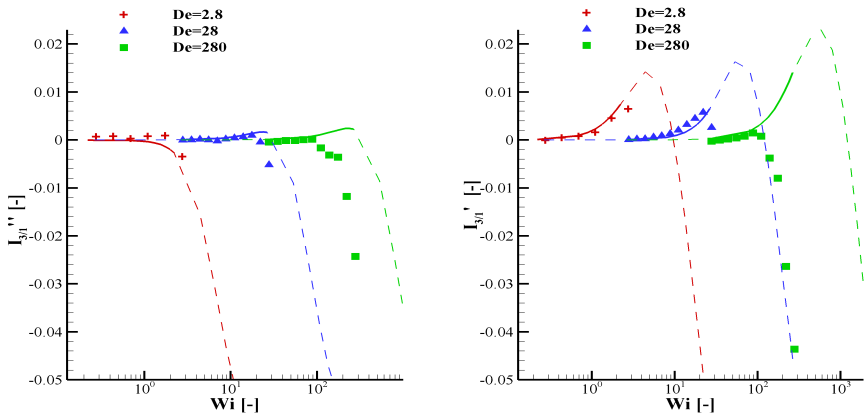

Figure 4.13: A comparison between experiment and Pompom theory of the real (right) and imaginary (left) parts of $I_{3/1}$ for HDB3. The Pompom model has reasonable agreement with data with the biggest discrepancy occurring for the largest Deborah number, $De = 280$.

All the multimode Pompom spectra show a similar pattern of behaviour with increasing W_i. The real part of $I_{3/1}$ typically grows quadratically with W_i before reaching a turning point, at which point $I'_{3/1}$ decreases and becomes negative. The imaginary part of $I_{3/1}$ is much smaller than the real component but still grows negatively as the Weissenberg number is increased. For all three materials the highest Deborah number plot of both $I'_{3/1}$ and $I''_{3/1}$ show maxima that are much higher than that observed experimentally.

For HDB3 $I''_{3/1}$ is modelled well for the lowest Deborah number ($De = 2.8$), but for the two higher Deborah numbers ($De = 28, 280$) the downturn occurs at a higher Weissenberg numbers for the model than in the experiments (c.f. figure 4.13). The real component, $I'_{3/1}$, is predicted well for low Weissenberg numbers for all Deborah numbers, but the Pompom model predicts a maximum which is much higher than the data.

The results are similar for HDB6(a) (figure 4.14) with the first two Deborah ($De = 3.8, 38$) numbers being modelled well by the Pompom model, although slightly over-predicting the experimental data. For the highest Deborah number ($De = 380$) the Pompom model over-predicts the value of the experimental data and predicts a large maximum for both the real and imaginary components, where

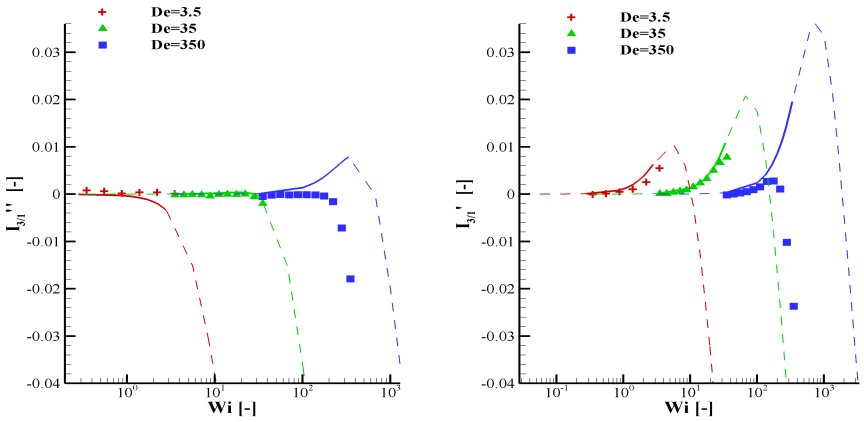

Figure 4.14: A comparison between experiment and Pompom theory of the real (right) and imaginary (left) parts of $I_{3/1}$ for HDB6(a). The Pompom model has good agreement with data with the biggest discrepancy occurring for the largest Deborah number, $De = 350$.

no maximum is seen in the experimental data.

For LDPE 1840H (figure 4.15) the lowest Deborah number experiment is predicted well by the Pompom model, however $I'_{3/1}$ is still over-predicted. For the other two Deborah numbers the Pompom model predicts a maximum in $I''_{3/1}$ which is not experimentally visible. For the largest Deborah number the experiments find a downturn in $I'_{3/1}$ which is not captured by the Pompom model until much higher Weissenberg numbers.

In chapter 2 three different spectra for the HDB6 were obtained and fitted to extensional data. In the last chapter the three spectra were found to be indistinguishable in shear step strain. However, they do show quantitative differences in LAOS. The three different spectra are compared to LAOS data for the Deborah numbers, $De = 3.8, 38$ and $De = 380$ in figures 4.16 to 4.18. For the lowest Deborah number, $De = 3.8$, all three models over-predict both the real and imaginary parts of $I_{3/1}$. The disagreement between theory and experiment is similar for each spectrum and the resulting absolute harmonics also similarly show theory over predicting experiment, as can be seen in figure 4.19.

For the intermediate Deborah number, $De = 38$, all parameterisations match the data well. In particular HDB6(a) shows good agreement for both real and

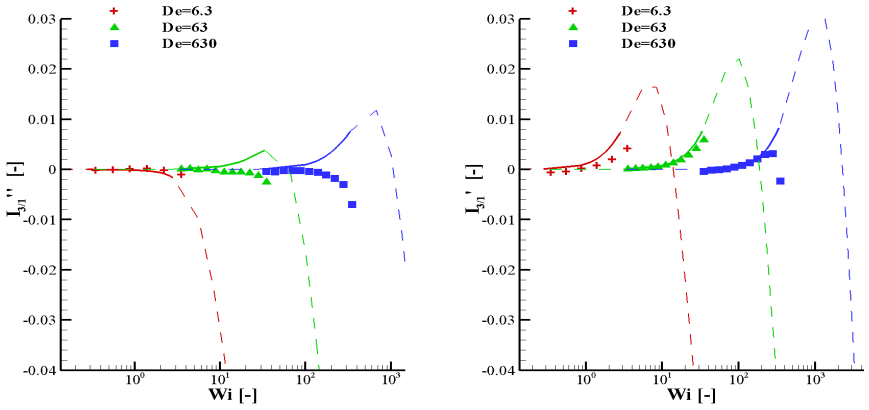

Figure 4.15: A comparison between experiment and Pompom theory of the real (right) and imaginary (left) parts of $I_{3/1}$ for the LDPE 1840H. The Pompom model has good agreement with real data with the biggest discrepancy occurring for the imaginary component, $I''_{3/1}$, for the largest two Deborah numbers, $De = 63$ and $De = 630$.

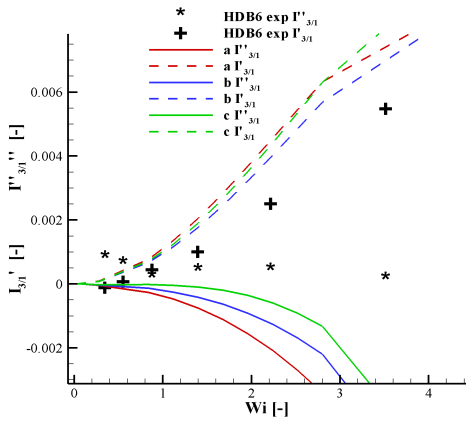

Figure 4.16: A comparison of the three different HDB6 spectra (a, b, and c) fitted to extensional data, and experimental data for the lowest of the three Deborah numbers, $De = 3.8$. Each spectra does a reasonable job in predicting the experimental data for both the real and imaginary components of $I_{3/1}$. The most discernible difference is the modelling of the real component where HDB6(c) gives the closest agreement.

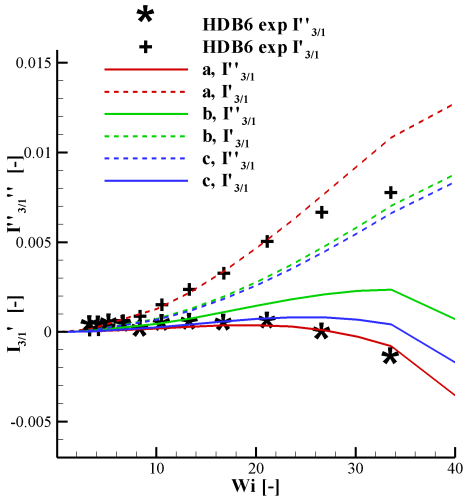

Figure 4.17: A comparison of the three different HDB6 spectra (a, b, and c) fitted to extensional data, and experimental data for the intermediate Deborah number, $De = 38$. Each spectra does a good job in predicting the experimental data for both the real and imaginary components of $I_{3/1}$. In particular HDB6(a) captures the rheology of each component very well.

imaginary parts of the third harmonic.

The Pompom parameterisations for HDB6 compared to LAOS data for the highest experimental Deborah number, $De = 380$, show a big discrepancy from the data. The Pompom model predicts both the real and imaginary parts, $I'_{3/1}$ and $I''_{3/1}$, to have a much higher maximum than experiments find and don't show a negative gradient until much higher Weissenberg numbers.

Figure 4.19 show the absolute value of the third harmonic for each of the three HDB6 Pompom parameterisations. As seen in the figure, all parameterisations perform similarly well, and despite the discrepancies for the individual real and imaginary parts the absolute third harmonic is modelled well by all three spectra. This is because it is dominated by the imaginary component and this component is best modelled by the Pompom equations.

Each of the HDB6 spectra does give a noticeably different prediction for the components $I'_{3/1}$ and $I''_{3/1}$ for the three Deborah numbers considered. From the study of the Pompom model in the previous section this differentiation between

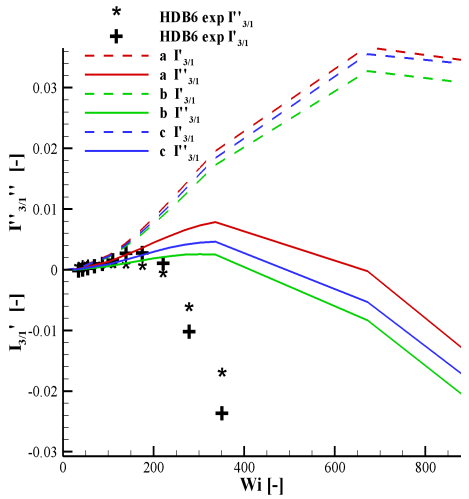

Figure 4.18: A comparison of the three different HDB6 spectra (a, b, and c) fitted to extensional data, and experimental data for the largest of the three Deborah numbers $De = 380$. Each spectra does a poor job in predicting the experimental data for both the real and imaginary components of $I_{3/1}$, failing to predict the large negative results that experimental data shows.

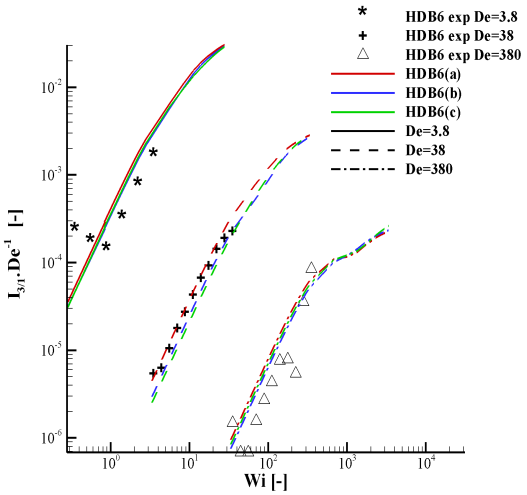

Figure 4.19: A comparison of each HDB6 spectra (a, b, and c) compared to experimental data for the absolute value of the third harmonic for each experimental Deborah number. All three spectra perform similarly well which is a consequence of the dominant imaginary component being well modelled by each spectra.

the spectra is attributed to the sensitivity of LAOS rheology to the stretch relaxation times. The value of the real component shows the largest amount of variation using the three spectra, however this is typically smaller than the imaginary component and thus the absolute value of the third harmonic is dominated by the imaginary component. The imaginary component show less variation for the three HDB6 spectra and hence so does the absolute value, $I_{3/1}$.

Examining the real and imaginary components of the absolute third harmonic separately for all three materials gives greater insight into the performance of the Pompom equations in LAOS compared to looking at the absolute value alone. The real component is much smaller than the imaginary and thus has little contribution to the absolute third harmonic thus studying this variable separately can show discrepancies not seen when studying the absolute third harmonic alone. Also both components become negative in the range of Weissenberg numbers accessible. The Pompom model captures the magnitude of the harmonic well but the prediction of the phase angle of the harmonic is poor. This can be seen, for example in figures 4.18 and 4.19 in the largest Deborah number for the material HDB6, and for all the materials investigated here. The question remains of whether this is a fundamental deficiency of Pompom model in capturing the rheology of LAOS or whether the discrepancies result from the incorrect choice of non-linear parameters when fitting to extensional rheology. In fitting parameters to extensional data both the non-linear Pompom parameters (τ_s and q) are fitted simultaneously and is most sensitive to q, if the Pompom model correctly captures the rheology of LAOS then it can be used to ascertain the stretch relaxation time independently.

In general the Pompom constitutive model with parameters fitted to extensional rheology capture the rheology of LAOS reasonably well. When discrepancies occur the Pompom model over-predicts experimental results. In the one mode Pompom model we found that the value of $I_{3/1}$ showed different rheological response for modes with a branching priority of $q = 1$ than for $q > 1$, in particular giving larger values of $I_{3/1}$. As noted earlier a linear molecule would still exhibit chain stretch relaxation that is not modelled by the $q = 1$ Pompom model. The next section looks at modelling chain stretch relaxation for linear Pompom molecules to examine if this affects the performance of the Pompom

model in LAOS.

4.5 Modelling linear chain stretch in the Pompom model

It was shown in section 4.3 that there is a qualitative difference between linear Pompom modes (i.e. modes with branching parameter, $q = 1$) and branched Pompom modes (modes with $q > 1$). This is attributed to the presence of stretch relaxation. In the $q = 1$ Pompom modes the chain stretch relaxes instantaneously and the extra stress only contains contributions from chain orientation. However, at high shear rates and frequencies stretch modes are important even in linear polymer melts [e.g. Likhtman and McLeish (2002)], and is incorporated in constitutive models such as the GLaMM model [Graham et al. (2003)]. In this section the effect of incorporating chain stretch for $q = 1$ modes in the multimode Pompom model is assessed to determine whether this can remedy the discrepancies from experimental results.

In this section a simple model for linear chain stretch is included in LAOS calculations. For the modes with $q = 1$ the polymer stretch, λ, found by solving the equation,

$$\frac{D}{Dt}\lambda(t) = \lambda(t)\underline{\underline{K}} : \underline{\underline{S}} - \frac{1}{\tau_s}(\lambda(t) - 1)e^{\nu*(\lambda_i - 1)}, \tag{4.5.1}$$

is calculated using the chain Rouse time as the value of τ_s with no limit on λ. Since for a linear molecule there is no branch point displacement the value of $\nu^* = 0$.

For HDPE materials considered here the chain Rouse time is of order $0.01\tau_b$ giving a chain relaxation ratio of order 100. However, I will also test chain stretch relaxation ratios of 3.3 and 10 as well, to determine the effect of this ratio. For each value of the chain stretch ratio (3.3, 10, 100) all modes with $q = 1$ will be given the same ratio of orientation to stretch relaxation time and the limit of $\lambda < q$ will be removed. Figure 4.20 show the SAOS predictions of the relative third harmonic (normalised by ε^2) as a function of Deborah number for the material HDB6 for the various choices of chain stretch ratio. For all values of the chain stretch ratio there is only negligible difference for Deborah numbers

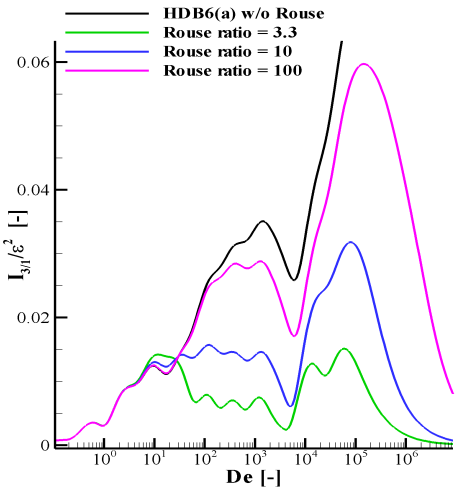

Figure 4.20: The value of the absolute relative third harmonic as a function of Deborah number predicted by the low strain asymptotes derived earlier in this chapter. The Pompom predictions are shown for various choices of Rouse chain stretch ratio for the material HDB6(a).

less than 10, which is the range of the two lowest frequencies in experiments. At high Deborah numbers $\sim O(10^6)$, the models with chain stretch relaxation ratios tend to a zero contribution from the third harmonic, as oppose to the non-zero plateau predicted by the Pompom model without chain stretch relaxation. For the intermediate regime, $10 < De < 10^6$, the effect of including chain stretch is to reduce the value of $I_{3/1}$ with larger Rouse times giving the largest reduction. However for, $r = 100$, which most resembles the Rouse motion for linear chain segments the response is nearly identical to the original model over the frequency range of the experiments.

This result is confirmed when the real and imaginary values of the relative third harmonic are compared to experimental data for various Weissenberg numbers. Figure 4.21 shows the experimental results for the real and imaginary parts of the relative third harmonic with Pompom predictions for the material HDB6, using the Pompom spectrum HDB6(a). The theory results are shown for the Pompom model without linear chain stretch relaxation and with chain stretch relaxation for ratios of $r = 3.3$ and $r = 10$. For the lowest Deborah number there

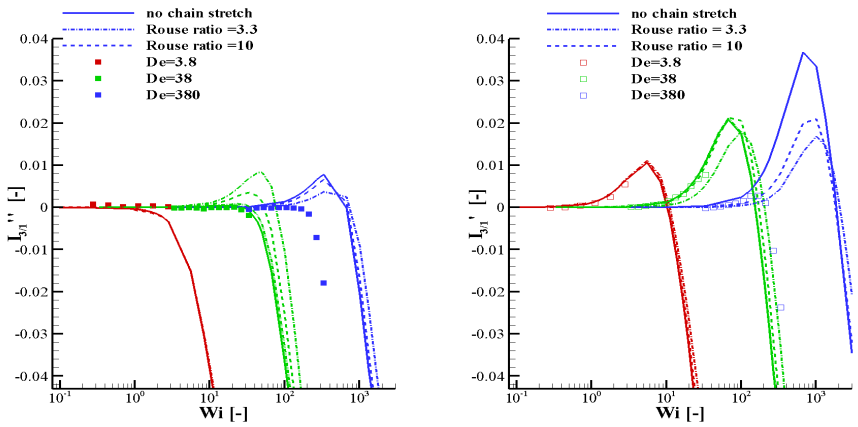

Figure 4.21: The Pompom spectrum HDB6(a) with various choices of chain stretch ratio are compared to experimental data for the real (right) and imaginary (left) components of the relative third harmonic. Ratios of $r = 3.3$ and $r = 10$ are shown with the result for $r = 100$ giving almost identical results to the original model.

is little difference between the three models and for the intermediate Deborah number modelling chain stretch worsens the prediction of the real component. The highest Deborah number is the more interesting case as this means there are more individual Pompom modes with $De > 1$. Although the real component is largely unaffected by the choice of model, the imaginary component show differences in the maximum peak with the Pompom model using a Rouse ratio of $r = 3.3$ showing a much smaller peak than the original model. As the ratio is increased the predictions tend to the original model and a Rouse ratio of $r = 100$ was examined and found to give indistinguishable results to the original model.

Modelling Rouse chain stretch relaxation for linear Pompom modes makes little difference to the model predictions when a chain stretch ratio is chosen to be of realistic value ($O(10^2)$). However, the Pompom spectra with non-linear parameters fitted to extensional data still don't predict some aspects of LAOS rheology.

4.5.1 Computational branch on branch rheology

In the previous sections of this chapter the Pompom spectra used in the LAOS calculations were obtained from fitting rheological data and not from molecular structure of the polymers. In order to make a direct link with molecular structure we need to test a Pompom spectrum derived from the molecular structure. One possibility would be to perform LAOS experiments on a melt of carefully synthesised Pompom molecules. Although such materials have been synthesised, LAOS measurements are not available. The alternative is to derive a statistical distribution of molecular shapes of the materials we have available using a model for their synthesis, and use this distribution of shapes to obtain an approximate Pompom spectrum. Such a model is currently under development [Das et al. (2006); Read et al. (2008)] from which Pompom spectra for HDB6 and 1840H have been derived.

Software is able to simulate reactor conditions for branched polyethylenes [Das (2010)] using a Monte-Carlo algorithm to model the reaction of molecules [Inkson et al. (2006)] and create an explicit ensemble where probability statistics are used to interpret the LCB architecture. From this ensemble a detailed configuration is analysed with a tube model that then predicts the linear rheology of a material using a branch-on-branch (BoB) algorithm [Das et al. (2006)]. Finally, this is mapped onto a full Pompom parameter space where the complex architecture of a material requires many different Pompom modes for each Maxwell mode to capture the correct rheology.

Although the determination of the branching priority, q, is still a topic of current research, the value of the stretch relaxation time, τ_s, is well defined in the reaction simulations. This makes LAOS a good choice of flow to test this aspect of the BoB model since we showed earlier that LAOS is strongly dependent on stretch relaxation and weakly dependent on the branching priority. In particular, the low-strain asymptotes derived in section 4.3.2 can be quickly examined to compare reaction modelling to experimental data that are in the linear regime of LAOS.

For the HDPE, HDB6, a BoB Pompom spectra was provided to analyse in LAOS. I would like to thank Daniel Read and Chinmay Das for providing this

data. The BoB Pompom spectra for HDB6 consists of 42 Maxwell modes and approximately 4200 Pompom modes. In the case of linear Pompom molecules the BoB algorithm provides Rouse stretch relaxation times so the choice of modelling Rouse stretch relaxation for linear modes can be checked. The use of so many modes makes a full LAOS simulation computationally very time consuming, however the low-strain asymptotes can be used relatively easily to examine the behaviour of the Pompom model in the linear regime.

In figure 4.22(left) the Dynamic moduli for HDB6 are plotted as a function of Deborah number, De, where for consistency the average relaxation time is taken from the Pompom spectra already used in this chapter. The figure show a comparison between the manually fitted 12 mode linear spectrum and the BoB linear spectrum. In the experimental window the two spectra are comparable but beyond this the BoB spectra gives a more realistic prediction than the 12 mode model since it has relaxation time spanning a much larger range of frequencies. The right hand figure of 4.22 show the low-strain asymptotic prediction for the absolute third harmonic, $I_{3/1}$, in the cases of the 12 mode Pompom spectra fitted to extensional data, the BoB spectra ignoring linear chain stretch and the BoB spectra including linear chain stretch. Due to a high density of modes both BoB spectra give a smoother curve than the 12 mode spectrum. Also, for Deborah numbers, $De > 10^2$, the spectrum with linear chain stretch has a significantly smaller value of $I_{3/1}$ compared to the BoB spectrum without linear chain stretch. This is analogous to the differences in $I_{3/1}$ seen in figure 4.6, where the absence of stretch relaxation caused a non-zero plateau. In general both BoB spectra predict the curve for $I_{3/1}$ to be lower than for the 12 modes spectrum.

A comparison between the BoB low-strain asymptotes (including Rouse chain stretch) and experimental data is shown in figure 4.23, along with the full predictions of the Pompom spectrum fitted to extensional data. The figure shows that the agreement between experimental data and the BoB Pompom spectrum is significantly improved compared to the 12 mode Pompom spectrum. For $De = 350$ this is expected since this is the regime where figure 4.22 showed a difference when modelling chain stretch relaxation, but there is also a significant improvement for $De = 3.5$ where the choice of modelling chain stretch relaxation is negligible. This demonstrates that at least some of the discrepancies seen in the previous

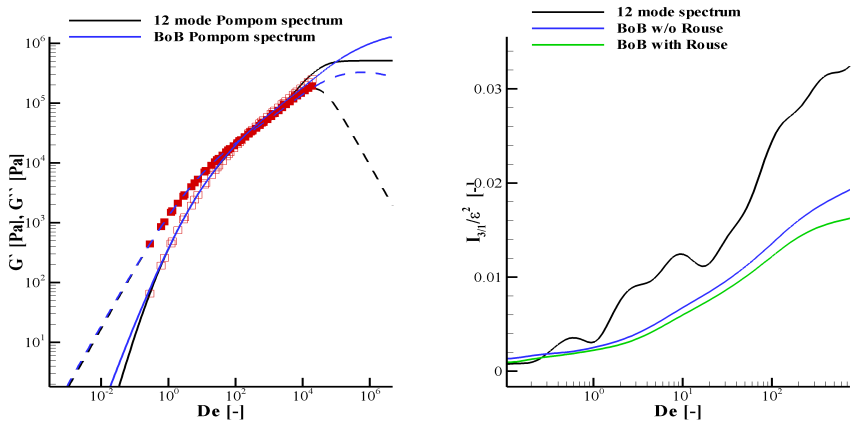

Figure 4.22: Left) The dynamic moduli for HDB6, comparing the experimental data, the 12 mode HDB6(a) spectrum and the BoB spectrum derived from reaction synthesis. Right) A comparison of the absolute relative third harmonic for the material HDB6. The parameterisations shown are the 12 mode HDB6(a) spectrum and the BoB spectrum with and without chain stretch.

sections are due to the method of fitting the Pompom spectrum to the extensional rheology, which is rather insensitive to the choice of τ_s.

The process is repeated for the LDPE 1840H, where the BoB simulated spectrum has around 10^4 modes. Similar to HDB6 the linear prediction for a frequency sweep of the low strain asymptotes [c.f. figure 4.24] shows that the 12 mode fitted Pompom spectra gives a much higher prediction than the BoB spectra for the absolute third harmonic. This would again indicate that stretch relaxation times are shorter than is predicted by Pompom spectra fitted to extensional data. Comparing the low strain asymptotes of the third harmonic to experimental data for 1840H, figure 4.25 shows that using the BoB Pompom spectrum gives an improved prediction of the absolute third harmonic and hence an improved prediction of the stress response. As for HDB6, the predictions for 1840H show the biggest differences from the 12 mode Pompom spectrum for the lowest and highest frequencies tested. For both materials however, without the full non-linear solution no conclusions can be drawn on the deviations from the low strain response with increasing strain amplitude.

Using reactor simulations and branch-on-branch rheological algorithms to pre-

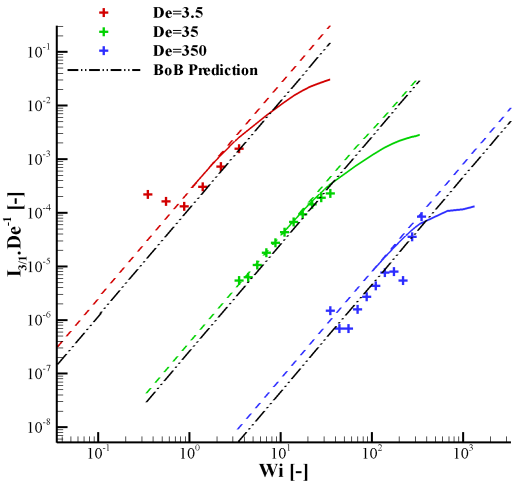

Figure 4.23: A comparison of experimental data and Pompom predictions for $I_{3/1}$ as a function of Weissenberg number. The Pompom prediction for HDB6(a) is shown for each Deborah number along with the low strain asymptote derived from the BoB Pompom spectra which shows an improved prediction with correct modelling of stretch relaxation.

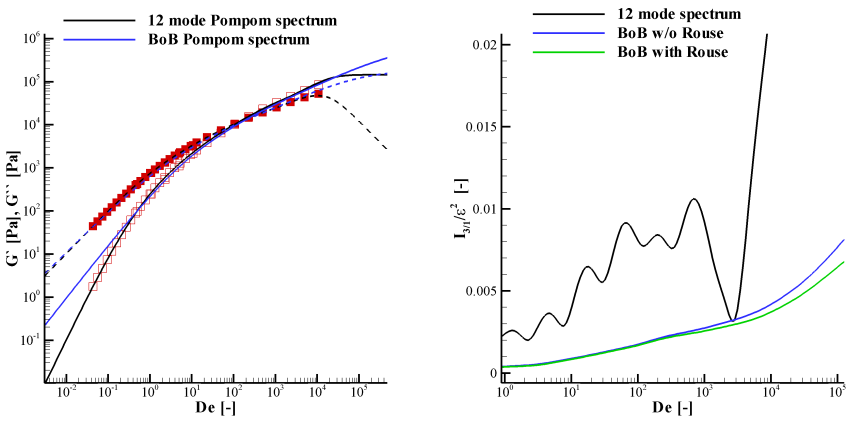

Figure 4.24: Left) The dynamic moduli for 1840H, comparing the experimental data, the 12 mode 1840H spectrum and the BoB spectrum derived from reaction synthesis. Right) A comparison of the absolute relative third harmonic for the material 1840H. The parameterisations shown are the 12 mode 1840H spectrum and the BoB spectrum with and without chain stretch.

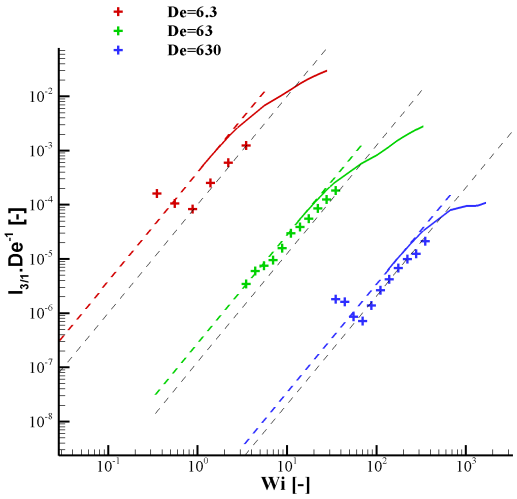

Figure 4.25: A comparison of experimental data and Pompom predictions for $I_{3/1}$ as a function of Weissenberg number. The Pompom prediction for 1840H is shown for each Deborah number along with the low strain asymptote derived from the BoB Pompom spectra which shows an improved prediction with correct modelling of stretch relaxation.

dict a detailed Pompom spectrum has indicated that the Pompom model is capable of capturing LAOS rheology with good accuracy. However, to substantiate this result further a full simulation for high strain amplitudes is required to see how a BoB Pompom spectrum predicts deviation from this linear result. This is needed to analyse the real and imaginary parts of the third harmonic, where the Pompom model fitted to extensional rheology showed the biggest discrepancy from experimental data.

4.6 Conclusions

In this chapter the Pompom constitutive model was examined in large amplitude oscillatory shear (LAOS) to see if the model can successfully predict experimental results, and to determine the sensitivity of this experiment to the Pompom non-linear parameters. In particular can a Pompom parameter set fitted to extensional data capture the behaviour of the material in LAOS?

As this is a periodic flow it is convenient to use Fourier analysis to analyse the results. Since the first harmonic is dominated by the linear viscoelastic response, the most sensitive measurements of non-linearity come from the higher harmonics (which are zero for Oldroyd and UCM models). In this study I focus my attention on the third harmonic Fourier coefficients, which are the largest non-linear coefficients and hence most easily measured.

The Pompom parameters infer detail about molecular architecture and so by analysing a one mode Pompom model it was possible to deduce which of the Pompom parameters are sensitive in LAOS. Of the two non-linear Pompom parameters the stretch relaxation time is the more dominant parameter, with the branching priority having only a minor effect on the stress response, for $q > 1$. For the Pompom model a low strain asymptotic solution was derived which showed the absolute relative third harmonic, $I_{3/1}$, as a function of Weissenberg number shows a power law of 2. The low strain asymptotes can be used to reduce computation time when simulating the full LAOS stress response and Fourier decomposition. The low strain asymptotes are independent of branching parameter, q, and so provide a method for measuring τ_s alone.

The multimode Pompom model is compared to experimental data for three materials; two HDPEs HDB3, HDB6 and the LDPE 1840H. Experiments were performed at three frequencies (0.02Hz, 0.2Hz and 2Hz) and strain amplitudes ranging from $\varepsilon = 0.1$ to $\varepsilon = 1$. The Pompom parameters for each material were fitted to the dynamic moduli and extensional rheology and each spectrum shows a reasonable degree of accuracy in predicting $I_{3/1}$. Deviations away from the low strain asymptote were hard to examine as the experimental data did not go far enough into the high strain regime.

To examine the accuracy of the Pompom model further the variation of the real and imaginary parts of the relative third harmonic were examined with increasing strain amplitude (Weissenberg number). In general the Pompom parameterisations agreed with experiments well for the two lower frequencies but large deviations occurred for the larger frequency. For the higher Weissenberg numbers both the real and imaginary components of $I_{3/1}$ showed a significant downturn, however, the Pompom model predicts a large peak and does not downturn until much higher Weissenberg numbers. This could either be caused by poor param-

eterisation of the non-linear Pompom parameters or due to inadequacies in the Pompom model.

To examine how sensitive LAOS predictions are to variations in Pompom parameterisations, the three different HDB6 spectra derived in chapter 2 were compared to the experimental data for all three frequencies. LAOS predictions discriminate the three spectra reasonably well when examining the real and imaginary components. So far in this thesis we have seen that transient shear and extension as well as shear step strain flows were not particularly sensitive to the three HDB6 spectra. In LAOS the three spectra do give differing results and in particular HDB6(c) performs best in the low frequency experiment and HDB6(a) performs best in the medium frequency experiment (All three spectra do not fully capture the third harmonic for the highest frequency experiment and so no conclusions can be drawn). The reason for this differentiation between Pompom spectra is that LAOS is the only experiment considered so far that is strongly dependent on only one of the non-linear Pompom parameters, namely the stretch relaxation ratio. Transient shear and extension, as well as shear step strain, are affected by both non-linear parameters.

For the linear Pompom modes Rouse chain stretch relaxation was modelled to examine if there was a significant effect on the response of the third harmonic. It was shown that for a realistic value of chain-stretch relaxation time the difference between the original Pompom model and the chain stretch Pompom model is negligible.

By modelling the reaction process for the material HDB6 and 1840H using the branch-on-branch (BoB) algorithm a detailed Pompom spectrum fully characterising the materials' architecture was created which contained between 4000 and 10000 modes. Although a full LAOS simulation is computationally too time consuming to perform at present, the low strain asymptotic results that were derived in section 4.3.2, showed a significant improvement on the 12 mode Pompom spectrum fitted to extensional data. This indicates that a correctly parameterised Pompom model can capture LAOS rheology, although this remains to be shown fully.

One way forward would be to use a smaller number of modes obtained from the BoB model to simulate the LAOS experiments. Also a larger range of ex-

perimental data could be used to further clarify results as well as investigating further parameters such as higher Fourier harmonics.

Large amplitude oscillatory shear experiments provide a unique tool for analysing branched polymer melts. The theme of this thesis is characterising LCB, but when trying to parameterise the Pompom model to flows such as transient extension the two non-linear Pompom parameters are fitted for each mode simultaneously. This provides multiple fits all satisfying experimental rheology equally. In LAOS the stress response is strongly dependent on only one non-linear Pompom parameter and so could be used to determine this parameter independently. The low strain asymptotes provide a powerful tool for this analysis as the experiments are easier to perform in this limit.

Chapter 5

Cross-slot Flow

To characterise material architecture several spatially homogeneous 'simple' flows have been examined. In particular the predictions of the Pompom model with parameters fitted to extensional stretching experiments have been tested against other experiments in shear step-strain and Fourier transform rheology, to assess not only the accuracy of the parameterisation but also the performance of the Pompom constitutive model itself.

In the rest of my thesis I will examine the flow in the cross-slot geometry. This contains an isolated stagnation point (SP) flow which generates a region of extensional flow, as well as shear near the walls. Experimentally the stress is measured using flow induced birefringence (FIB). In a planar flow this technique provides images of black and white contours of constant stress difference. Finite element solutions of the Pompom constitutive model are compared to the FIB images. The solution techniques are discussed in section 1.7. After an investigation into mesh choices and the performance of one and two mode Pompom models, the multimode Pompom model is compared to experimental FIB images for a range of polyethylenes.

The FIB images for a material at several flow rates will be used to generate steady state extensional viscosity measurements of LCB materials at steady state. These measurements complement transient stretching experiments, which are not always able to achieve steady state due to the finite strain achievable and sample breakage.

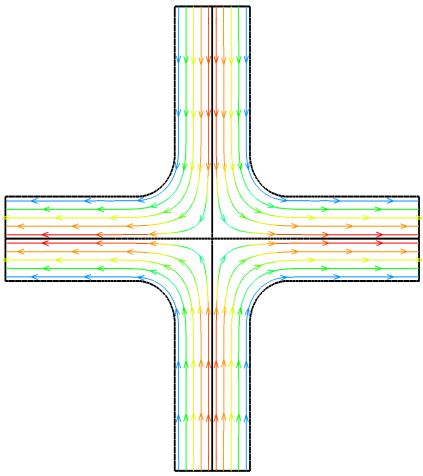

Figure 5.1: An illustration of cross-slot flow which generates stagnation point flow. The stream lines indicate the flow direction with the colours representing the magnitude of the velocity.

5.1 Introduction

The cross-slot flow consists of four channels, two opposing inlet channels and two outlet channels, illustrated in figure 5.1. This generates a stagnation point (SP) flow which has regions of high extensional stress on the symmetry lines of the outlet channels. The depth of the channels is usually chosen to be large compared to their width so that the flow can be assumed to be 2D, this approximation is checked later in the chapter [section 5.4.3]. The cross-slot flow does not suffer from the free surface instabilities that hinder shear or uniaxial extensional flow. Also, since the stress response is measured optically through birefringence once loaded a single sample can be used for many different measurements. The material at the SP experiences an arbitrarily large strain, although in practice (at least for the flow cell used at Cambridge) the strain of a particular flow rate is limited to the time taken for the sample to flow through the apparatus. This means that the extensional stress generate by the stagnation point reaches steady state and the rheological behaviour of branched materials in extension can be examined. Furthermore, the birefringence pattern generated along the upstream stagnation streamline shows the strain history at a particular flow rate.

Stagnation point (SP) flow has been used in a variety of ways to examine fluid dynamics. Taylor (1934) used a four roll mill to try and approximate [rectangular hyperbolic] stream lines, similar to the cross-slot studied here. Taylor (1934) placed a golden syrup solution containing a drop of various undissolved oils in the four roll mill and examined how the drops deformed under flow conditions. Dynamical and viscous forces on the surface of the oil drop act to distort its shape. By balancing these forces with surface tension which acts to keep the drop spherical, the author derives an analytic expression for the distortion of the oil drops which is valid for small drops being distorted at low speeds.

To examine the relationship between an induced velocity gradient and stress response of a polymeric fluid the optical anisotropy can be examined. A polymeric fluid with completely random ensemble is optically isotropic. When the ensemble average of polymer molecules become distorted then anisotropy caused by double refraction, or birefringence, can be measured [Wales (1976)].

An important relation upon which the interpretation of flow birefringence relies is the linear relation between stress and birefringence,

$$\Delta n = C\Delta\sigma, \tag{5.1.1}$$

where $\Delta\sigma$ is know as the principal stress difference and is given by,

$$\Delta\sigma = \sqrt{(\sigma_{xx} - \sigma_{yy})^2 + 4\sigma_{xy}^2}, \tag{5.1.2}$$

and C is the stress-optical coefficient.

Frank and Mackley (1976) used a two roll mill and Crowley et al. (1976) a four roll mill to investigate polyethylene oxide solutions in stagnation point flow and found birefringent strands corresponding to high values of principal stress difference along streamlines downstream of the stagnation point. Scrivener et al. (1979) found similar birefringence strands using a cross-slot flow cell. A summary of these and other flow birefringence studies can be found in Janeschitz-Kriegl (1983).

In polymer melts flow induced birefringence is usually sufficiently strong enough to rotate the plane of polarisation though more than one cycle. This means that

provided the cell depth, d, is sufficiently large (so that end effects can be ignored) the birefringent pattern is seen as contours of constant principal stress difference, with each contour representing the same increment in stress which was calculated by Coventry (2006) as,

$$\text{stress/fringe} = \frac{\lambda_{light}}{C \cdot d}. \tag{5.1.3}$$

The stagnation point causes a region of high extension downstream of the stagnation point and thus the PSD patterns show asymmetry between the inlet and outlet plane [see Coventry (2006); Coventry and Mackley (2008); Verbeeten et al. (2001)]. The stress is highest at the stagnation point and this is represented by increasingly localised fringes around the stagnation point. Early findings for polymer melts showed the stress contours cusp along the symmetry line downstream [Coventry (2006); Coventry and Mackley (2008); Verbeeten et al. (2001)]. More recent publications [Hassell and Mackley (2008); Hassell et al. (2009, 2008); Soulages et al. (2008)] show that the cusping of the PSD contours occurs away from the symmetry line and Hassell et al. (2009) termed this double cusping pattern as 'W-cusps'. In section 5.4.4 I review the PSD of single and double cusping PSDs and compare the Pompom constitutive model to experimental PSD patterns. I would like to thank David Hassell for providing the experimental data used in this work.

Since this is a complex flow the local fluid velocity and hence strain rate are not determined a priori, and will depend upon the constitutive properties of the fluid as well as the input flow-rate. Consequently, it is important to know how polymer molecules affect the velocity gradient. Harlen et al. (1992) reduced the complex geometry of stagnation point flow to a 1D problem and modelled birefringent strands and pipes using a FENE model. Incorporating hydrodynamic drag to create a coil-stretch hysteresis the authors show that highly stretched molecules from the stagnation point slow the flow down to create a birefringent pattern called *birefringent pipes* [c.f. Keller et al. (1987); Müller et al. (1988)], which are similar to the W-cusp phenomenon.

Since the depth to width ratio of the cross-slot is usually large, the flow is normally regarded as being a 2D planar flow. However this approximation neglects the effects of the viewing walls, which can affect the birefringence pattern.

Wales (1976) suggests that an aspect ratio between the depth and the width of the flow cell should be at least 10 for a valid 2D approximation. Schoonen et al. (1998) investigated deviations from a 2D approximation for aspect ratios of 2 and 8 in slit flow. The authors found that deviations between 2D and 3D flow calculations increased with increasing flow rate but were minimal for the larger aspect ratio.

Clemeur et al. (2004b) performed a numerical investigation for various aspect ratios in a slit flow and an abrupt contraction flow using the UCM model and the DCPP version of the Pompom model. For both models they agreed with Wales (1976) that a 2D approximation was acceptable for an aspect ratio of 10, although the 2D approximation became worse at higher flow rates. The results also show that the choice of constitutive model does not seem to affect the 2D approximation. Sirakov et al. (2005) looked at 3D effects of the XPP constitutive model for various contraction geometries. The authors show that complex 3D flow kinematics can be captured using the XPP model and recommend that full 3D numerical analysis is needed to correctly describe the flow behaviour in contraction geometries. For the cross-slot geometry presented in this work the aspect ratio is approximately 7 and so the validity of using a 2D approximation is checked in section 5.4.3.

In this chapter cross-slot flow is considered for various branched polyethylenes, establishing differing rheological behaviour for linear, lightly branched and densely branched materials. The Pompom constitutive model is compared to cross-slot flow using 2D flow simulations. As previously seen in this thesis, the Pompom model parameter space is explored using one and two mode models. Then the Pompom parameters fitted to uniaxial extensional data for various polyethylenes (c.f. chapter 2) are compared to the principal stress difference patterns observed in experiments.

5.2 Experimental Setup

For the complex flow experiments a Cambridge Multi-Pass Rheometer (MPR) with a cross-slot insert was used. This instrument is a dual piston capillary-type rheometer, designed for small quantities of material of about 10g, that enables si-

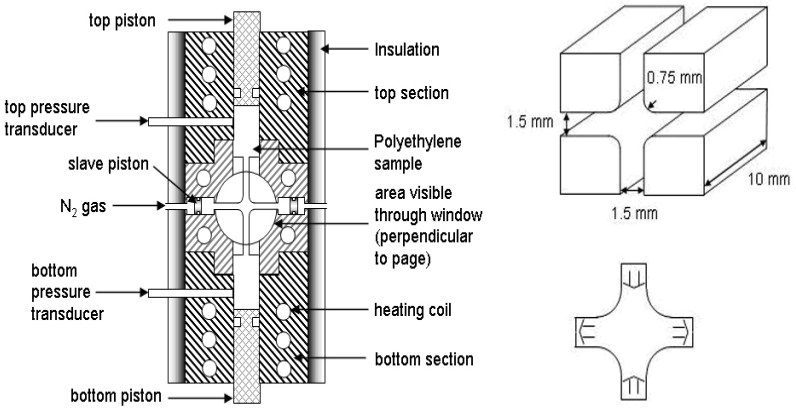

Figure 5.2: The Geometry of the MPR cross-slot.

multaneous and time-resolved pressure and optical measurements [Mackley et al. (1995)]. It was operated together with an optical configuration using monochromatic polarised light with a wavelength of 514nm and pair of stress-free quartz windows so that the stress-induced birefringence patterns were captured by a digital video camera, e.g. Collis and Mackley (2005). From the top and bottom reservoirs the polymer material is driven in opposite directions along two perpendicular channels by pistons at a controlled rate and with equal pressure through the midsection cube into two horizontal side channels with slave pistons (Figure 5.2). Thereby, the material is maintained within the MPR and can be forced back by nitrogen pressure through the cross-slot insert into the top and bottom reservoirs for subsequent runs. The cross-slot geometry insert used in this study consists of four perpendicular, intersecting coplanar channels with a depth of 10mm and aspect ratio of about 7 (Figure 5.2). The two streams, which are pumped into the cross-slot channel, generate a pure and large elongational deformation around the stagnation point and along the inlet-outlet symmetry plane, but essentially simple shear near the outer walls [Coventry and Mackley (2008); Hassell et al. (2008)].

The input condition is represented by a piston speed, V_p, and the volume flux, Q, into the two input channels is given by the relation,

$$Q = 78.5 \cdot V_p \; [mm^3.s^{-1}]. \tag{5.2.1}$$

The central extension rate in the Cross-Slot can be estimated from the flow geometry, and the relationship between the maximum extension rate and the piston speed, V_p, is given by:

$$\dot{\varepsilon}_{max} = AV_p, \tag{5.2.2}$$

where A scales as the reciprocal channel width. However, the exact numerical value of A depends on the constitutive behaviour of the melt throughout the flow. This is the reason that quantitative cross-slot extensional rheometry must be supported by self consistent flow calculations. The steady state elongational viscosity $\eta_{E,std}$ is calculated from the time-independent tensile stress σ which is determined from the number of fringes, and the steady state Hencky strain rate $\dot{\varepsilon}_{std}$ as determined from the flow field:

$$\eta_{E,std} = \frac{\sigma_{std}}{\dot{\varepsilon}_{std}}. \tag{5.2.3}$$

Stress induced birefringence was used to observe the principal stress difference (PSD) during flow. The bi-color method gives simultaneously the phase shift and extinction angle of a stressed polymer fluid according to the stress-optical relation [e.g. Chow and Fuller (1984); Janeschitz-Kriegl (1983)]. The retardation of light between the two principal axes within the polymer, represented as the difference in the refractive indices, is given by the stress-optical rule (SOR) as in equations 5.1.1 and 5.1.2, where the stress-optical coefficient, C, is given in units of Pa^{-1}. This relation has been found to be a linear function for stresses up to about $1MPa$ in the case of low-density polyethylenes [Kotaka et al. (1997); Koyama and Ishizuka (1989)] as well as polystyrenes [Luap et al. (2006); Venerus et al. (1999)]. For the work presented in the subsequent sections the stresses are below this limit and therefore, the SOR is expected to be valid and simply a linear relation. Stress-optical coefficients ranging from $1.29{\cdot}10^{-9}Pa^{-1}$ to $2.34{\cdot}10^{-9}Pa^{-1}$ were used for the experimental and computational work, which is in quantitative agreement with the range given in the literature for polyethylene of $1.2 - 2.4 \cdot 10^{-9}Pa^{-1}$ [Macosko (1994)]. According to the theory of rubber elasticity and with support from experimental data, the stress-optical coefficient is only weakly dependent

on temperature [Koyama and Ishizuka (1989)].

5.3 Numerical Methods

Details of the numerical methods used to solve the constitutive equations in cross-slot flow are given in section 1.7. In this section the details of the choice of mesh used for each method are discussed. In this section all simulation results are performed at a set input velocity flux of 1.9mm.s^{-1}. In general the input parameters for each solver are related to the velocity flux via the relations derived in section 1.7.

I would like to thank Drs Harley Klein and Timothy Nicolson for their help in working with *flowSolve* and Drs Rosen Tenchev and Mark Walkley for their work on and constant development of the *euFlow* software. Details of both solvers can be found at www.mupp2.co.uk (2010).

For both computational methods the time stepping was performed in units of strain so that the same number of time steps were used for any given flow rate. Calculations were performed using three time steps ranging from 10^{-3} to 10^{-5} units of strain. The results of these calculations show that the solution was independent of the time step chosen. Also to increase computational speed modes with $W_i \ll 1$ were treated as contributions to the Newtonian solvent stress. At most four modes were treated this way, meaning that at least eight modes would be solved as Pompom modes for any given material and flow rate. In the subsequent discussion of the various mesh refinements used the mesh densities for both computational methods were varied using a global mesh refinement. Each software package allows the mesh (including the various refinements) to be varied with one global parameter which increases the mesh density of refined and unrefined sections of the mesh uniformly.

The *flowSolve* program uses Lagrangian elements that move and deform with the fluid. Three mesh densities with mesh refinement near the downstream stagnation streamline were investigated for the material HDB6. The details of the three meshes used can be seen in table 5.1. The solution at time, $t = 0$s, which represents the Stokes solution for a viscous fluid whose viscosity is equal to $\sum_i G_i \tau_{b_i}$, where the sum is taken over the solvent modes. In table 5.1 the

Table 5.1: A comparison of various flowSolve mesh densities for the Stokes solution at a time of t=0s. The PSD and velocity gradient, $\frac{dU}{dX}$, are compared at the stagnation point. For the Stokes solution the PSD at the stagnation point can be calculated analytically; $4\frac{dU}{dX}\sum_i G_i\tau_{b_i}$, where the sum is taken over the solvent modes. There is close agreement between the simulated and analytical value of the intial PSD at the SP to within 1.2%.

mesh	nodes [-]	$\frac{dU}{dX}$ [s^{-1}]	PSD [kPa]	difference from true PSD [%]
1	1137	2.13	17.63	1.09
2	2162	2.13	17.63	1.09
3	8304	2.05	16.97	1.11

Table 5.2: A comparison of various flowSolve mesh densities for the solution at a time of t=3.5s. The PSD and velocity gradient, $\frac{dU}{dX}$, are compared at the stagnation point.

mesh	nodes [-]	$\frac{dU}{dX}$ [s^{-1}]	PSD [kPa]
1	1667	2.835	144.4
2	6544	2.824	144.6
2	25269	2.786	143.6

velocity gradient, $\frac{dU}{dX}$ and principal stress difference are probed at the stagnation point. As *flowSolve* computes the solution, elements are convected with the flow and so new points are added to retain the resolution near the SP, as a result the number of nodes increases with solution time. The details of each mesh density at a solution time of $t = 3.5$s is given in table 5.2, with velocity gradient and PSD values taken from the stagnation point. The solution times on a standard laptop with 1.8GHz processing power, for each mesh are approximately 36 hours, 96 hours and 15 weeks, respectively. A comparison of *flowSolve* solution at time $t = 3.5$s for mesh 2 and mesh 3 can be seen in figure 5.3. The figure shows the PSD for HDB6 with contour lines for comparison, also shown are the two meshes used with the result that the two meshes show visually identical results. For the remainder of this work *flowSolve* mesh 2 will be presented in simulation results.

The solver *euFlow* uses a static mesh which allows more control over local mesh refinement. The results of these mesh investigations with the velocity gradient and PSD values taken at the stagnation point are detailed in tables 5.3 and 5.4. At the solution time of $t = 9$s there are fewer mesh densities investigated due

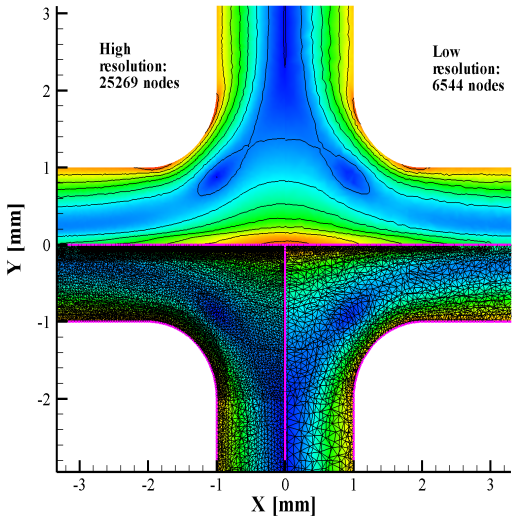

Figure 5.3: A comparison of flowSolve meshes (meshes 2 and 3 in tables 5.1 and 5.2) showing the PSD distribution and the triangular meshes used. The comparison shows that visually the solutions are almost identical.

to the solver instabilities detailed in chapter 1.7. The solution time for meshes 2 to 5 ranges from 24 hours to 48 hours.

The values detailed in tables 5.3 and 5.4 are plotted in figure 5.4 which shows good convergence for the Stokes solution and at a solution time of $t = 9$s the simulation results are independent of the meshes investigated. For the remainder of this work mesh 5 will be presented for simulation results. In figure 5.5 the simulation results for *flowSolve* and *euFlow* are compared again for HDB6 with contour lines shown every 20kPa. The agreement between the results are excellent which can be seen with the visual agreement of the contour lines. This implies that either solver method can be used without affecting any comparisons made with experimental flow induced birefringence.

A transient plot comparing the PSD and velocity gradient, $\frac{dU}{dX}$, for *euFlow* and *flowSolve* simulations of the material HDB6 can be seen in figure 5.6. The figure shows that the two solvers shown good agreement in the transient development of both the PSD and $\frac{dU}{dX}$ with *flowSolve* predicting a slightly higher PSD and slightly lower and noisier $\frac{dU}{dX}$.

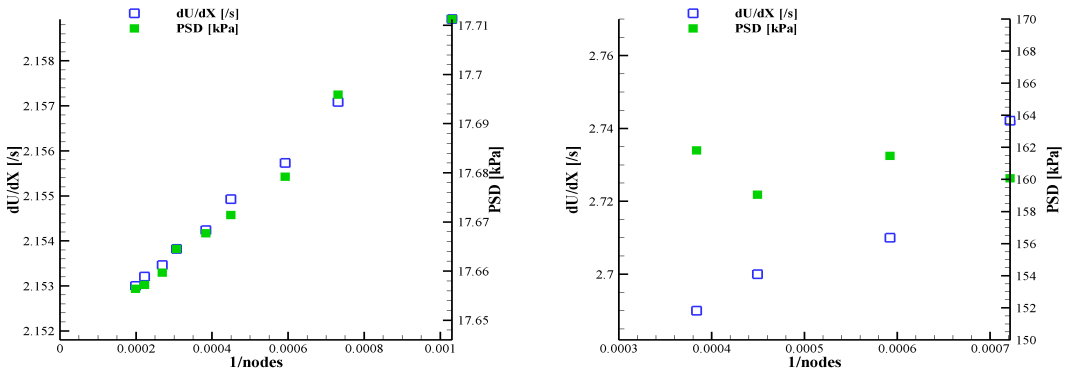

Figure 5.4: The PSD and velocity gradient, $\frac{dU}{dX}\mathrm{s}^{-1}$, probed at the stagnation point are plotted against the inverse node number of various meshes, detailed in tables 5.3 and 5.4. left) the Stokes solution, showing convergence with increasing node number. right) A solution time of $t = 9$s showing the solution is independent of mesh to within 3%.

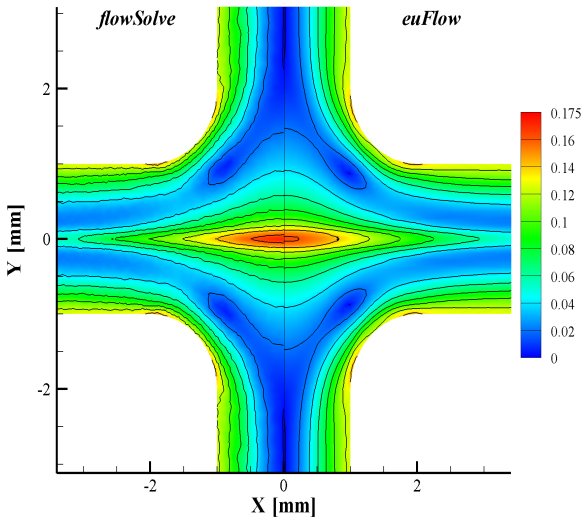

Figure 5.5: A comparison of *euFlow* and *flowSolve* solutions at steady state with contours added for comparison every 20kPa and at 175kPa. The solutions are visually very similar, with both solvers predicting the same number of fringes. The biggest difference occurs at the SP where the highest fringe is smaller for the *euFlow* solution.

Table 5.3: A comparison of various euFlow mesh densities for the Stokes solution. The PSD and velocity gradient, $\frac{dU}{dX}$, are compared at the stagnation point. For the Stokes solution the PSD at the stagnation point can be calculated analytically; $4\frac{dU}{dX}\sum_i G_i\tau_{b_i}$, where the sum is taken over the solvent modes. There is good agreement between the simulated and analytical value of the intial PSD at the SP to within 0.2%.

mesh	nodes [-]	$\frac{dU}{dX}$ [s^{-1}]	PSD [kPa]	difference from true PSD [%]
1	970	2.15893	17.7113	0.199
2	1368	2.15709	17.6959	0.197
3	1689	2.15573	17.6792	0.166
4	2226	2.15493	17.6714	0.160
5	2606	2.15424	17.6677	0.170
6	3264	2.15382	17.6645	0.171
7	3721	2.15346	17.6597	0.161
8	4500	2.15321	17.6572	0.158
9	5034	2.15300	17.6564	0.163

Table 5.4: A comparison of various euFlow mesh densities for the solution at a time of t=9s. The PSD and velocity gradient, $\frac{dU}{dX}$, are compared at the stagnation point.

mesh	nodes [-]	$\frac{dU}{dX}$ [s^{-1}]	PSD [kPa]
2	1368	2.742	160.1
3	1689	2.710	161.5
4	2226	2.700	159.1
5	2606	2.690	161.8

For the *euFlow* static mesh solver 3D simulations are presented using a reduced XY-plane mesh density to reduce computation time. To avoid computational problems associated with the Pompom model (c.f. section 1.7) a version of the DPP model is used. The details of this choice are discussed in section 5.4.3.

Figure 5.7 compares a 2D simulation of the XY-plane mesh consisting of 720 nodes, and the mesh chosen for 2D simulations (mesh 5 in table 5.4). The left hand figure shows the two meshes with some refinement removed on the outflow centre line. The right hand figure shows the predicted PSD for the LDPE 1800S with the contours of the PSD showing good visual agreement around the stagnation point.

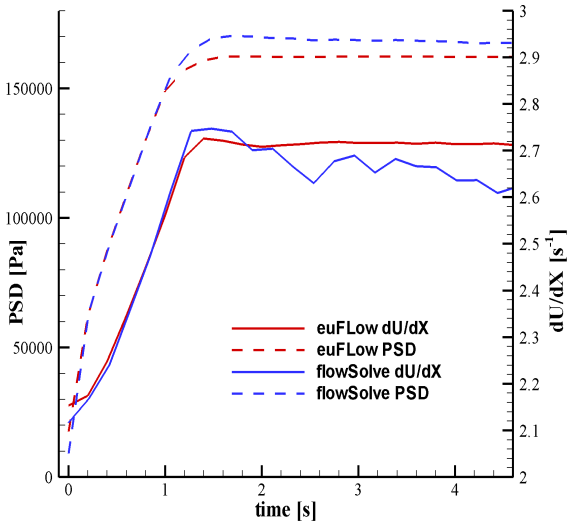

Figure 5.6: The transient solutions of *euFlow* and *flowSolve* simulations are compared at the SP. Both solutions show the same transient development of the PSD and $\frac{dU}{dX}$, however *euFlow* predicts a higher value for the velocity gradient and a lower value for the PSD compared to *flowSolve*.

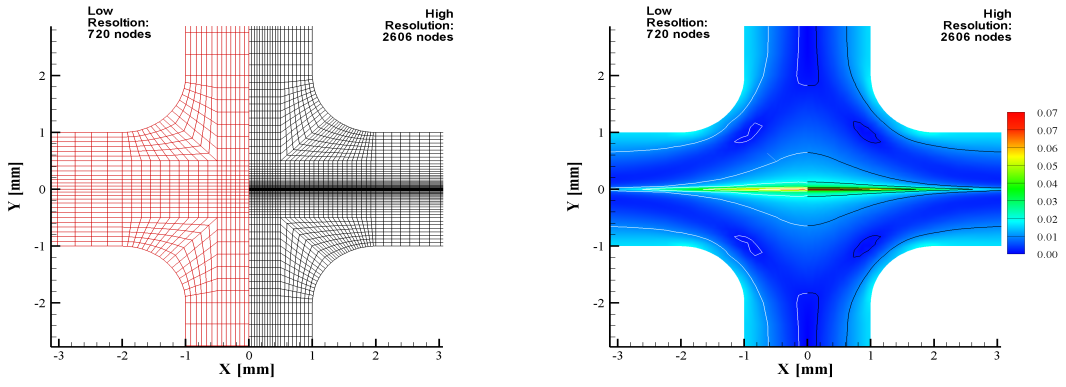

Figure 5.7: The resolution of the XY *euFlow* mesh used in 3D simulations compared to the 2D mesh. left) the high and low resolution meshes used for 2D and 3D simulation, respectively. right) the PSD for LDPE 1800S

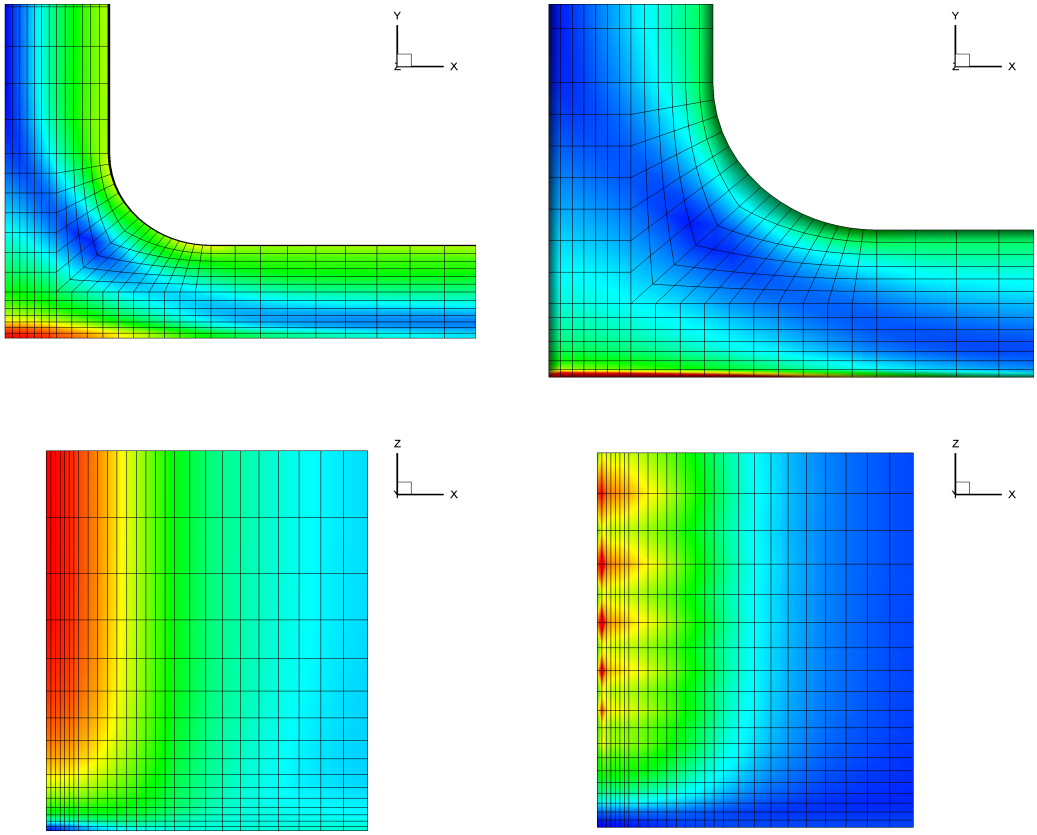

Figure 5.8: The 3D *euFlow* solutions for HDPE HDB6 (left) and LDPE 1800S (right), showing the PSD. The top figures show the XY centre plane and the bottom figures show the XZ centre plane. For the LDPE 1800S the high stress gradient near the outflow centre line causes instabilities in the Z direction at late solution times.

Figure 5.8 shows the PSD for two materials in the XY-plane and the XZ-plane. On the left the PSD of HDB6 shows a smooth distribution of stress in the XZ-plane, where there are 16 levels of discretisation in the Z-direction. For the LDPE 1800S (right) the solver produces an instability in the Z-direction, even when the Z-discretisation was increased to 19. The instability occurs as the solution approaches steady state ($t \sim 4$s) and is caused by the large stress gradient approaching the outlfow centre line. A transient comparison can be made with 2D simulations for times before the instability occurs and this is the approach used in section 5.4.3.

The validity of the 2D approximation of cross-slot FIB will be examined in section 5.4.3, where details of the DPP model used and the calculation of the true 3D birefringence will be given. Since only small discrepancies occur the remainder of simulations will be 2D and a combination of *flowSolve* and *euFlow* will be used.

5.4 The Pompom model in cross-slot flow

Similar to the previous chapters, in understanding the stress response that causes flow induced birefringence both experimentally and theoretically through the multimode Pompom constitutive model, it is helpful to investigate the stress caused by simple one and two mode Pompom models with parameters chosen to emphasize certain flow features. The Pompom model is based on the idea of two dominant independent relaxation process; orientation relaxation (with characteristic time τ_b) and stretch relaxation (with characteristic time τ_s). For cross-slot flow it is helpful to characterise these relaxation processes with two Weissenberg numbers, an orientation Weissenberg number (which is what was been used previously in this work) and a stretch Weissenberg number defined as,

$$W_{i_b} = \dot{\varepsilon}_C \tau_b, \tag{5.4.1}$$

$$W_{i_s} = \dot{\varepsilon}_C \tau_s, \tag{5.4.2}$$

where $\dot{\varepsilon}_C$ is the strain rate at the stagnation point for a Newtonian fluid.

5.4.1 One mode Pompom model

The first model investigated is a one mode Pompom model with parameters; $G = 0.9$Pa, $\tau_b = 10$s, $q = 15$ and $r = 2$. In order to maintain numerical stability a Newtonian viscosity, $\mu = 1$Pa.s, is added, giving a zero shear-rate viscosity of $\mu + G\tau_b = 10$Pa.s. The shape of the PSD for the one mode model is characterised by the two Weissenberg numbers.

In figure 5.9a the Pompom parameters in a single Pompom model and the flow rate are chosen such that $W_{i_b}, W_{i_s} << 1$. This means that the fluid behaves

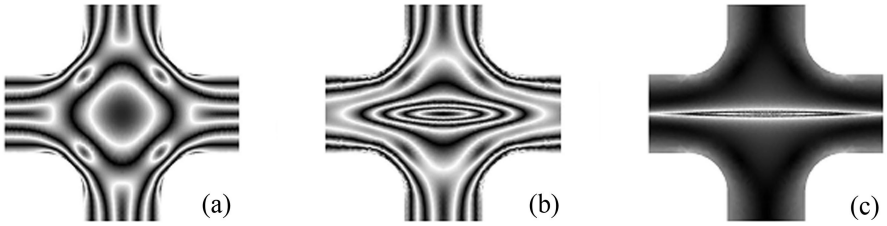

Figure 5.9: Qualitative comparison of the predicted shape of the PSD for different flow Weissenberg number regimes for a single Pompom mode: a) slow flow ($W_{i_b} = 0.1$ and $W_{i_s} = 0.05$); b) orientating but non-stretching flow ($W_{i_b} = 1.5$ and $W_{i_s} = 0.75$); c) stretching flow ($W_{i_b} = 10$ and $W_{i_s} = 5$).

as a Newtonian fluid of viscosity $\mu + G\tau_b$. In figure 5.9b the flow is orientating but not stretching, i.e. $W_{i_b} > 1, W_{i_s} < 1$. Finally, figure 5.9c shows a typical pattern where the flow is both orientating and stretching, i.e. $W_{i_b}, W_{i_s} > 1$. The molecular stretching becomes evident from the formation of very narrow and extended birefringence lines along the central outflow axis.

In the case of a stretching flow where the critical strain rate is larger than the inverse stretch time of the polymer, i.e. $\tau_s\dot{\varepsilon}_C > 1$, the most dominant material parameter for the appearance of the PSD pattern is the priority branching number q, or set of priorities, $\{q_i\}$. This parameter controls the maximum value which the backbone stretch can reach. In consequence it has very little effect on shear viscosity but a large effect on the planar elongational, as seen in the Cross-Slot PSD.

The presence of high polymeric stresses near the outflow centre line affects the fluid velocity, which changes the strain rate at the stagnation point. In Figure 5.10 we show how the x component of the fluid velocity near the SP changes with different values of q.

For high values of q, a large stress builds up along the downstream centre line, this in turn slows down the velocity in this direction therefore $\dot{\varepsilon}_C(t)$ is decreasing. In comparison with the initial velocity profile the area in which the flow slows extends a long way along the downstream centre line (5.10d).

For low values of q, the stretch parameter λ quickly reaches a maximum. In this case in a large area downstream of the stagnation point the stretch becomes saturated at $\lambda = q$. This has the effect of increasing the velocity near the

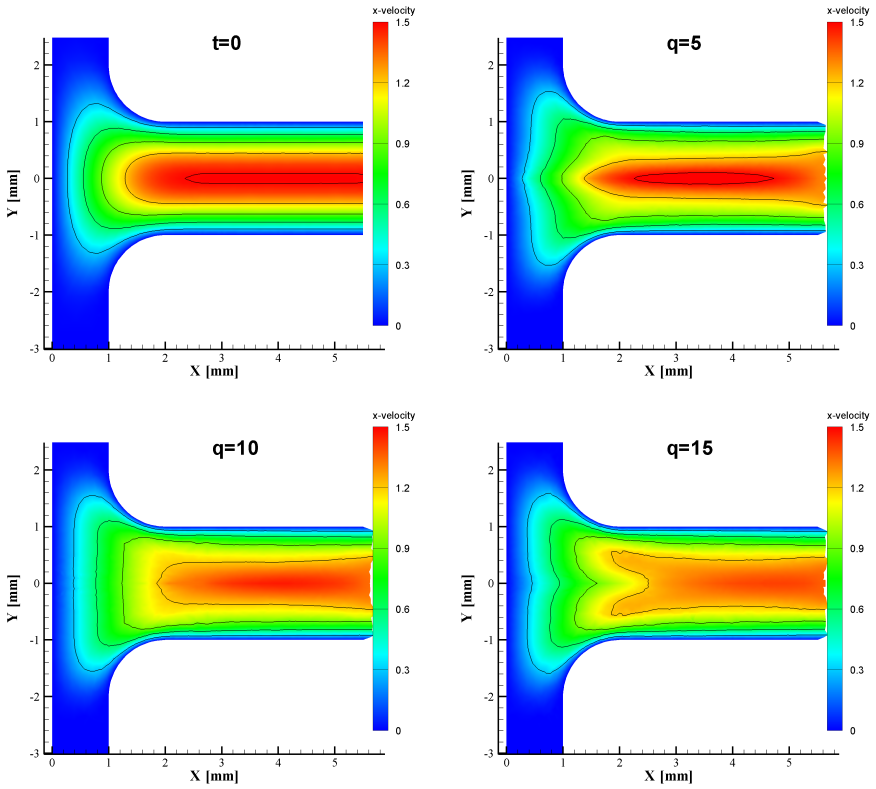

Figure 5.10: A comparison of the x-velocity shape in the right hand part of the cross-slot for different test cases: a) the initial Stokes solution velocity profile, b) during the flow the velocity near the stagnation point speeds up for low values of q, i.e. $q = 5$ c) for intermediate values of $q \sim 10$ the velocity up near the stagnation point speeds up, but slow the flow down further along the downstream centre line. d) for large values of $q > 15$ the large stretch gradient slows the flow down. Parameters chosen were; $G = 0.9$Pa, $\tau_b = 10$s, $r = 2$ with varied q, this gives an initial Weissenberg number of 5 for stretch and 10 for orientation.

stagnation when the limit $\lambda = q$ is reached (Figure 5.10b).

In figure 5.11 the value of the velocity gradient, $\frac{dU}{dX}$, and PSD at the SP are plotted as a function of solution time, with the values at t= 4.5s given in table 5.5. The figure shows how the dependence of $\frac{dU}{dX}$ and the PSD varies with q. The value of the stretch directly affects the PSD through the constitutive model, however the variation in $\frac{dU}{dX}$ is more subtly dependent on how much the stretch slows the velocity along the outlfow centre line.

In this simple model the choice of $\dot{\varepsilon}_C$ relative to τ_s is important since this

Table 5.5: A table showing how the choice of Pompom branching parameter, q, affects the *flowSolve* prediction of the velocity gradient, $\frac{dU}{dX}$, and the PSD at the stagnation point.

q [-]	$\frac{dU}{dX}$ [s^{-1}]	PSD [Pa]
t=0	1.13	4.53
5	1.07	60.1
10	0.84	118
15	0.63	164

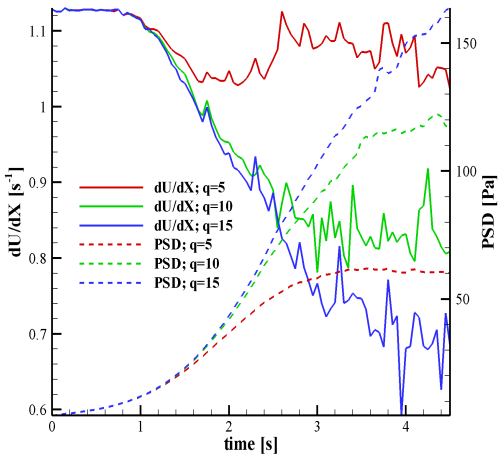

Figure 5.11: A comparison of the transient PSD and velocity gradient, $\frac{dU}{dX}$, taken at the stagnation point for various branching priorities, q. Parameters chosen were; $G = 0.9$Pa, $\tau_b = 10$s, $r = 2$ with varied q, this gives an initial Weissenberg number of 5 for stretch and 10 for orientation.

will determine not only if stretch is a dominant feature of the flow but whether a maximum stretch is reached. From this we can see that $\dot{\varepsilon}_C(t)$ is itself dependent on changes in the stretch gradient deduced by the flow on other parts of the chain. In a realistic model of a PE, with a multimode spectrum, these effects will not be so prevalent. It should be noted that although Pompom modes do not interact directly, all modes are affected by changes to the velocity gradient and so are indirectly coupled.

Table 5.6: The parameters for the two mode Pompom model used in figure 5.12. A Newtonian viscosity of $\mu = 1$Pa.s was also included in the simulation.

Mode, i	G_i [Pa]	$\tau_{b,i}$ [s]	$\tau_{b,i}/\tau_{s,i}$ [-]	q_i [-]
1	0.2	10	5	5
2	0.35	20	2	22

5.4.2 A two mode Pompom model

To study the effect of this coupling a two mode Pompom model is used to show how changes in velocity gradient caused by one mode affects the other. In particular, we are interested in whether a reduction in strain rate along the outflow centre line axis can cause chain relaxation in a mode where the stretch Weissenberg number is close to unity and whether this provides an explanation for the W-cusp patterns observed by Hassell et al. (2009). The Pompom parameters chosen can be seen in table 5.6, again Newtonian viscosity of $\mu = 1$Pa.s was included and the zero sher-rate viscosity is 10.

The initial strain rate was chosen to be $\dot{\varepsilon}_C = 1.1s^{-1}$, so that all orientation and stretch Weissenberg numbers are greater than unity. The parameters were chosen so that mode two would significantly alter the velocity gradient at the stagnation point, reducing it from $1.1s^{-1}$ to $0.6s^{-1}$.

In figure 5.12 results of the *flowSolve* simulation of the two mode Pompom model detailed in table 5.6 are shown. As with the one mode model the flow is dominated by the slowest mode which slows down the flow near the outflow centre line and produces a narrow PSD pattern. The stretch of the faster mode has less influence on the PSD. It can be seen that the reduction in strain rate at the SP causes stretch relaxation along the outflow centre line for the fast mode, with the maximum stretch occurring away from the centre axis.

For the stretch relaxation in the fast mode (mode 1) to occur the slow mode (mode 2) needs to be the dominant mode in the two mode spectrum. Reducing the modulus of the slow mode reduces the level of stretch relaxation in the fast mode and for this reason, we find that stretch relaxation cannot have enough influence in the sum of modes to cause the PSD to have a maximum away from the outflow centre line. This suggests that this coupling mechanism alone is not sufficient to cause the W-cusps.

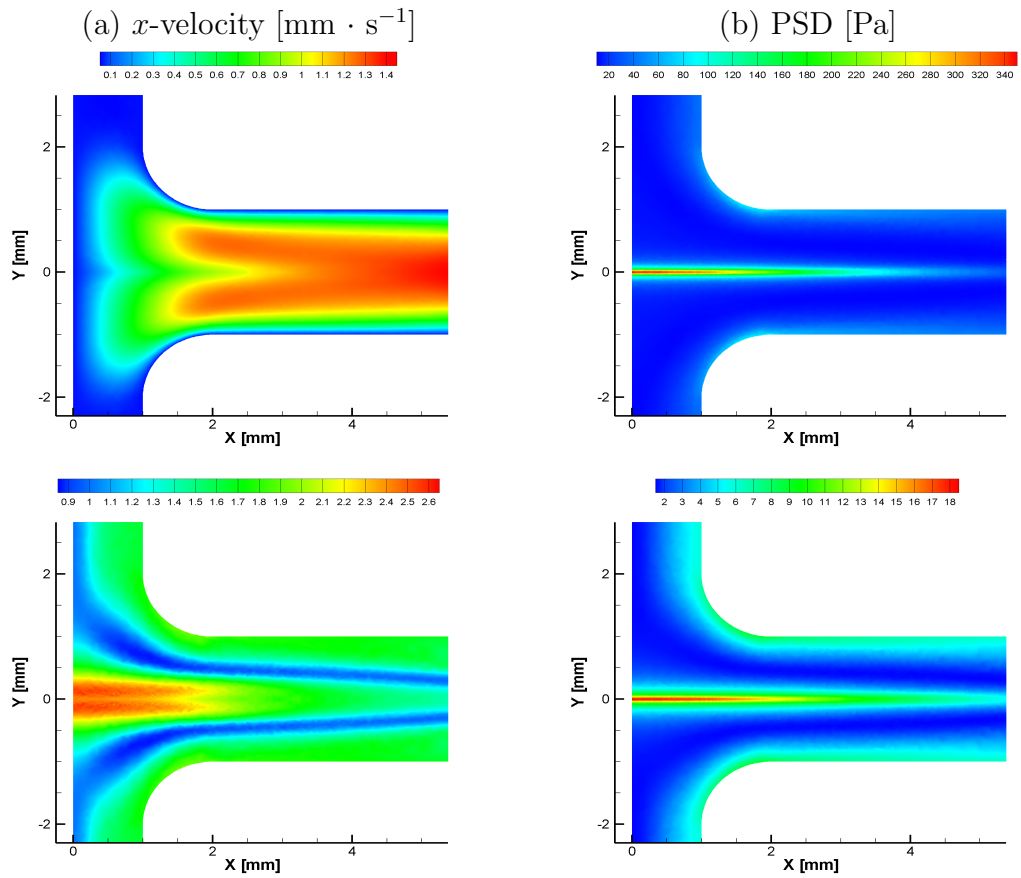

Figure 5.12: The predictions of the two mode Pompom model given in table 5.6 using *flowSolve*. The highly stretched backbone of the slow mode (d) significantly modifies the flow, slowing the velocity along the outflow centre line (a). This causes a collapse in the fast mode stretch (c) along the outflow centre line, but the collapsed pattern is not seen in the PSD (b) because of the dominance in slow mode needed to reduce the velocity.

5.4.3 Comparison of 2D approximation and 3D simulations

Unlike velocity measurements, which can be taken on the centre plane away from the walls, the observation of flow induced birefringence involves the integral of the PSD though the entire depth of the flow cell. Consequently, flow induced bire-

fringence (FIB) is always affected by the flow near the viewing windows which produce a no-slip boundary condition. To ensure that the 2D approximation is valid for birefringence measurements, in this section 2D and 3D birefringence patterns for various materials will be compared to ascertain the extent of any deviations from the 2D flow compared to a full 3D solution. Details of the numerical solvers used for this investigation can be found in section 1.7, with the meshes used detailed in section 5.3.

The 3D calculations are made using the *euFlow* static mesh solver. As explained in section 1.7, limits need to be imposed on the Pompom equations, namely the entropic limit on the stretch, $\lambda(t) \leq q$, and an arbitrarily large limit on the trace of the UCM tensor. The limits are imposed using a 'push-back' function where each push-back function requires a user-inputted weight. This requires some trial and error to find the required weight needed for each mode. This is time consuming since the 3D simulations are found to be more sensitive to the push-back weights used, making it harder for simulations to reach a steady state.

To overcome these problems a version of the Pompom model called the DPP model [Clemeur et al. (2003)] is used. The DPP model uses a variation on the differential equation for the orientation which remains finite for all shear/strain rates. To see the difference between the two orientation tensors it is convenient to write the Pompom model's orientation as an evolutionary equation in $\underline{\underline{S}}$ rather than $\underline{\underline{A}}$,

$$\frac{d\underline{\underline{S}}}{dt} = \frac{d}{dt}\left(\frac{\underline{\underline{A}}}{trace\underline{\underline{A}}}\right) = \frac{1}{tr\underline{\underline{A}}^2}\left(tr\underline{\underline{A}}\frac{d\underline{\underline{A}}}{dt} - \underline{\underline{A}}\frac{d}{dt}\left(tr\underline{\underline{A}}\right)\right). \tag{5.4.3}$$

Using the identity,

$$trace(\underline{\underline{K}} \cdot \underline{\underline{S}} + \underline{\underline{S}} \cdot \underline{\underline{K}}^T) = 2\underline{\underline{K}} : \underline{\underline{S}}, \tag{5.4.4}$$

the orientation differential equation for the original Pompom model can be written as,

$$\frac{D\underline{\underline{S}}}{Dt} = \underline{\underline{K}} \cdot \underline{\underline{S}} + \underline{\underline{S}} \cdot \underline{\underline{K}}^T - \frac{1}{\tau_b tr\underline{\underline{A}}}\left(3\underline{\underline{S}} - \underline{\underline{I}}\right) - 2\underline{\underline{S}}\left(\underline{\underline{K}} : \underline{\underline{S}}\right). \tag{5.4.5}$$

The differential equation (5.4.5) still contains a $tr\underline{\underline{A}}$ term and an approximation first suggested by Verbeeten et al. (2001) for the XPP model and used

subsequently by Clemeur et al. (2003) for the DPP model and Clemeur et al. (2004a) for the DCPP model is to make,

$$trace\underline{\underline{A}} = 3\lambda^2. \tag{5.4.6}$$

This gives the DPP orientation as,

$$\frac{D\underline{\underline{S}}}{Dt} = \underline{\underline{K}} \cdot \underline{\underline{S}} + \underline{\underline{S}} \cdot \underline{\underline{K}}^T - \frac{1}{\tau_b \lambda^2}\left(\underline{\underline{S}} - \frac{1}{3}\underline{\underline{I}}\right) - 2\underline{\underline{S}}\left(\underline{\underline{K}} : \underline{\underline{S}}\right) \tag{5.4.7}$$

Although the stretch equation remains the same the entropic limit on the stretch, $\lambda(t) \leq q$, is removed for computational ease. This means that all modes including linear, $q = 1$, modes have no upper bound on the stretch, and the only influence on q is though the exponential reducing the stretch relaxation time. Another important difference is a change to the exponential prefactor, ν^*. For the Pompom model $\nu^* = \frac{2}{q-1}$ for $q > 1$ and since there are no branch points, $\nu^* = 0$ for $q = 1$, whereas for the DPP model $\nu^* = \frac{2}{q}$ for all modes.

It should be noted that although linear modes ($q = 1$) can stretch in the DPP model, in *euFlow* the linear ($q = 1$) modes are not solved and kept constant (at $q = 1$) and so this is the approach adopted when solving transient uniaxial and shear flows. The DPP model is compared to the Pompom model using the spectra detailed in chapter 2. The temperatures of the experiments and fitted theories are $155°C$ for HDB2 and HDB6 and $140°C$ for 1800S.

Figure 5.13 show transient plots of shear and uniaxial extensional viscosities of the Pompom and DPP models. The comparison shows no significant difference between the shear viscosities and the transient development of the uniaxial extensional viscosities. The largest difference between the two models is the steady state value of the extensional viscosities. The DPP model predicts a higher steady state value due to the removal of the limit on the stretch, however the differences between the models are reasonable for a 2D-3D comparison to be made.

To compare the Pompom and DPP models further the 2D simulations of cross-slot flow are shown in figure 5.14 for each material. The comparison between the models shows that visual differences between the models are small although the original Pompom model does produce sharper cusping along the outflow centre

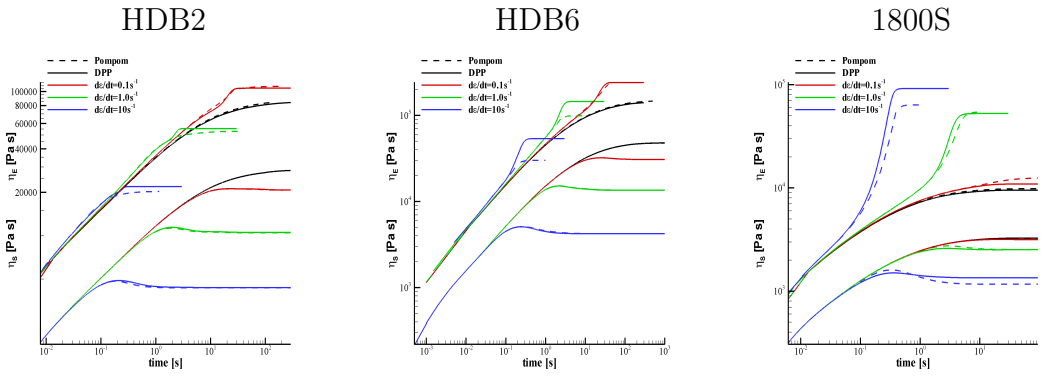

Figure 5.13: A comparison between the Pompom and DPP constitutive models for the same spectra given in chapter 2. The comparison is made for three materials; HDB2, HDB6 and 1800S in transient shear and uniaxial extension. The black line shows the linear envelope and the coloured lines show various shear/strain rates.

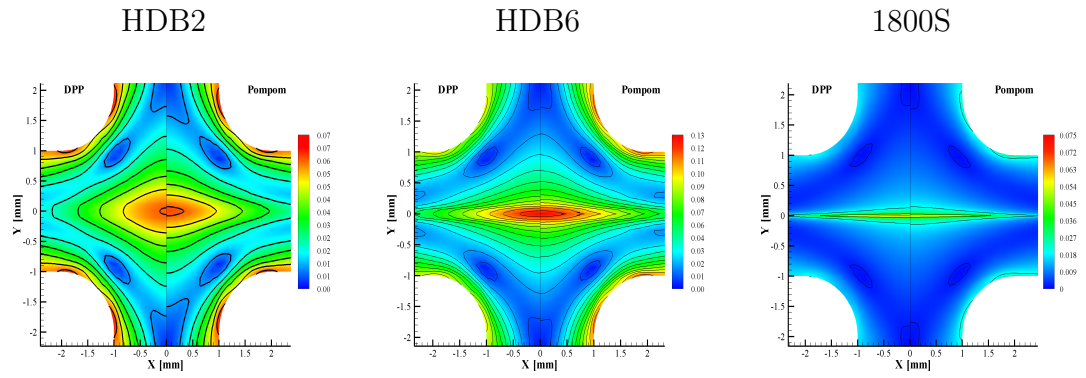

Figure 5.14: The Pompom and DPP constitutive models are compared in 2D cross-slot flow for three materials; HDB2, HDB6 and 1800S. The results show that the two models are comparable in cross-slot flow predicting the same number of contours (at 20kPa each) for each material. However the Pompom model does show sharper cusping down the outflow centre line.

line. The DPP model does produce very similar values for PSD and $\frac{dU}{dX}$ at the stagnation point, the results of which are summarised in table 5.7. In 2D cross-slot flow the Pompom model and the DPP model give very similar predictions and therefore results from 3D simulations of the DPP model are assumed to be

Table 5.7: The differences between the Pompom and DPP constitutive models in 2D cross-slot flow, with values of PSD and velocity gradient, $\frac{dU}{dX}$, taken from the stagnation point initially and after the transient development of the solution to steady state.

		t= 0.2s		t= 10s	
		Pompom	DPP	Pompom	DPP
HDB2	$\frac{dU}{dX}$ [s^{-1}]	1.29	1.29	1.51	1.43
HDB2	PSD [kPa]	29.4	28.0	62.0	60.1
HDB6	$\frac{dU}{dX}$ [s^{-1}]	1.29	1.29	1.58	1.59
HDB6	PSD [kPa]	37.3	37.2	126	125
1800S	$\frac{dU}{dX}$ [s^{-1}]	1.28	1.28	1.21	1.19
1800S	PSD [kPa]	8.37	9.03	53.7	58.8

also valid for the Pompom model.

To calculate the PSD for a 3D simulation the polarisation of the light due to the anisotropy the polymer needs to be calculated across the depth of the geometry. Azzam (1978) and Fuller (1995) proposed Mueller calculus as a mathematical method for calculating the intensity of light passed though a medium. As previously discussed by Clemeur et al. (2004b) the effect of the no-slip boundary condition at the viewing windows means that to correctly calculate the PSD there must be an integration over the light path through the medium. Each component of the a series of optical elements, or optical train, is represented by a 4x4 Mueller matrix, $\mathbf{M}$ [Fuller (1995)].

euFlow is programmed to calculate the 3D birefringence with the following equations in a post processing calculation. For the light source used in the experiments in this work the light intensity, I_f, after passing through the medium is given by,

$$I_f = \frac{1}{4} I \left(M_{11} - M_{44} \right), \tag{5.4.8}$$

where I is the intensity of the light source and M_{ii} are components of the Mueller matrix. The Mueller matrix satisfies the differential equation [Azzam (1978)],

$$\frac{d}{dz}\mathbf{M} = \mathbf{m} \cdot \mathbf{M}, \tag{5.4.9}$$

with the boundary condition that $M = \mathbf{I}_4$ at $z = 0$, where $\mathbf{I}_4$ is a 4x4 identity

matrix. For a linearly birefringent medium $\mathbf{m}$ is given by [Azzam (1978)],

$$\mathbf{m} = \begin{pmatrix} 0 & 0 & 0 & 0 \\ 0 & 0 & 0 & -2C\sigma_{xy} \\ 0 & 0 & 0 & C(\sigma_{xx} - \sigma yy) \\ 0 & 2C\sigma_{xy} & -C(\sigma_{xx} - \sigma_{yy}) & 0 \end{pmatrix}, \tag{5.4.10}$$

where C is the stress-optical coefficient.

Equations (5.4.9) and (5.4.10) reduce to solving three coupled differential equations in z across the depth of the channel;

$$\frac{dM_{24}}{dz} = -2C\sigma_{xy}M_{44} \tag{5.4.11}$$

$$\frac{dM_{34}}{dz} = C(\sigma_{xx} - \sigma_{yy})M_{44} \tag{5.4.12}$$

$$\frac{dM_{44}}{dz} = 2C\sigma_{xy}M_{24} - C(\sigma_{xx} - \sigma_{yy})M_{34}, \tag{5.4.13}$$

which is solved with initial conditions, $M_{24} = M_{34} = 0$ and $M_{44} = 1$ and hence the observed light intensity at the viewing window, $z = d$, is given by,

$$I_f(d) = \frac{1}{2}\left(1 - M_{44}(d)\right). \tag{5.4.14}$$

Clemeur et al. (2004b) used this technique in calculating FIB for channel and contraction flows using various aspect ratios. The authors show that increasing the aspect ratio improves the agreement between 2D and 3D calculations. They also conclude the an aspect ratio of 10, as suggested by Wales (1976), provides reasonable agreement. The cross-slot geometry used here has an aspect ratio of around 7 and in the rest of this section the differences between 2D and 3D flow will be examined.

All subsequent simulation presented are performed at the same input flux of 1.15mm.s^{-1} and the PSD contours are set at 20kPa per fringe. In table 5.8 the values of the PSD and $\frac{dU}{dX}$ are compared at the stagnation point, and in the case of the 3D simulation the value is taken at half the cell depth.

In figure 5.15 2D and 3D solutions of the DPP model are shown comparing the PSD contours of the three materials already seen in this section. For HDB2

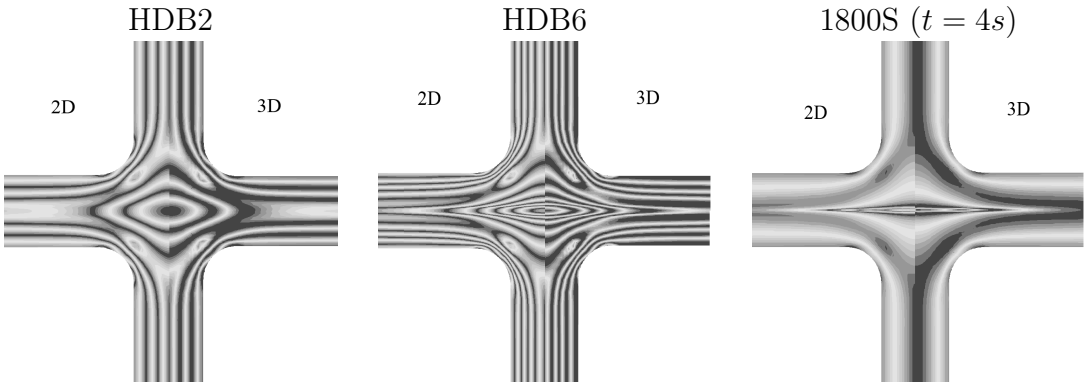

Figure 5.15: A comparison for the *euFlow* solution of the 2D approximation to the actual 3D FIB for three materials; HDB2, HDB6 and 1800S. The figures show that the aspect ratio is sufficient for the 2D approximation to accurately capture the FIB PSD contours (at 20kPa each) at the side walls and around the SP for each material. For 1800S high stress gradients on the outflow centre line meant the numerical solution was only valid until around 4s.

Table 5.8: The differences is the PSD between the 2D approximation of the full 3D flow. The values were taken at the stagnation point and for 3D flow in the centre plane of the geometry.

material	2D PSD [kPa]	3D PSD [kPa]	difference [kPa]	% difference compared to 3D PSD [-]
HDB2	60.1	65.5	5.4	8.2
HDB6	125	131	6.0	4.6
1800S	58.8	58.0	0.8	1.38

the agreement at the channel walls and the SP fringes are excellent, except for a slight discrepancy around the zero stress eye. For HDB6 the fringes at the channel walls show good agreement as do the position of the fringes around the SP. The 2D model does predict half a fringe more than the 3D model despite the value of the PSD at the SP having very similar values [c.f. table 5.8]. For the LDPE 1800S the simulation suffered from instabilities detailed in section 5.3, meaning that a comparison between 2D and 3D models could only be made where the solution was stable. The latest time that this could be done was at time $t = 4$s. At this time the solutions of the 2D and 3D simulations match very well, both predicting three PSD contours around the stagnation point.

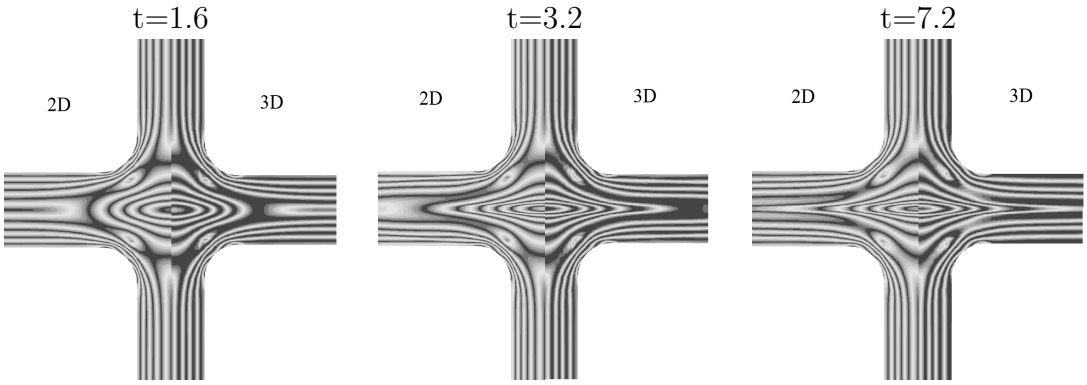

Figure 5.16: A comparison between the transient development of the FIB PSD contours (at 20kPa each) for 2D and 3D cross-slot flow for the material HDB6. At each time the 2D flow approximates the 3D birefringence well showing that the 2D simulation accurately captures the transient development of full 3D flow.

Figure 5.16 shows the transient development of the PSD for HDB6, comparing 2D and 3D birefringence patterns. The figures show that the transient development of the stress is the same for both 2D and 3D simulations. This is confirmed in figure 5.17(right) where the transient development of the PSD and $\frac{dU}{dX}$ at the centre point of the geometry are plotted. In the figure the PSD for the 3D simulation is slightly higher than in the 2D case but for both geometries the PSD reaches steady state at around, $t = 2$s. There is a slight discrepancy in the values of $\frac{dU}{dX}$ initially but at steady state the 2D and 3D model gives the same result. The behaviour of the PSD and $\frac{dU}{dX}$ along the stream line passing through the SP [shown in figure 5.25] along the centre plane are compared to the 2D simulation in figure 5.17(left) at steady state. The figures show that the 2D simulation approximates 3D flow very closely, implying the aspect ratio is large enough for the 2D approximation to be valid.

For the rest of this work experimental results are compared to 2D simulations of the original Pompom model assuming that the 2D approximation is valid for the experiments discussed.

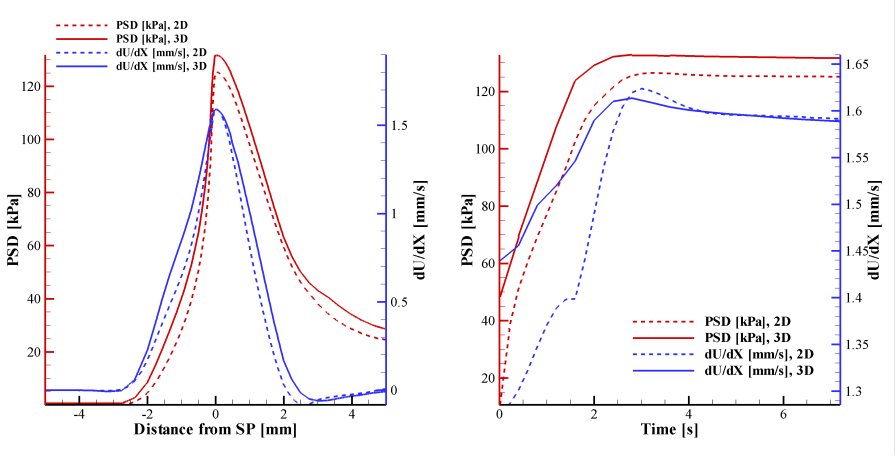

Figure 5.17: left) A comparison between the 2D and 3D solutions for the values of the PSD and $\frac{dU}{dX}$ along the stream line shown in figure 5.25. The figure shows good agreement between 2D and 3D simulations. right) The transient development of the PSD and $\frac{dU}{dX}$ at the SP (and centre plane for the 3D simulation) for the material HDB6, comparing the 2D and 3D solutions. At all times the 3D simulation predicts slightly higher PSD than the 2D model. Despite an initial discrepancy at steady state $\frac{dU}{dX}$ is the same for 2D and 3D solutions.

5.4.4 Multimode Pompom model

In this section simulated 2D birefringence patterns are compared to experimental results for a range of materials. The experimental results used in this work have been previously presented by Coventry and Mackley (2008) and Hassell et al. (2009) and I would like to acknowledge and thank Drs David Hassell and Timothy Lord for providing the experimental images and LDV data.

As in previous chapters I will compare these experimental results to numerical simulations using the Pompom parameters discussed in chapter 2. It was shown in section 5.4.3 that the aspect ratio of the flow cell is sufficiently large for the 2D approximation to be valid and so only 2D simulations are presented from here on.

In this section five materials are chosen to present how various material rheologies are observed in cross-slot flow and how well the Pompom constitutive model captures flow phenomena. The comparisons made in this chapter are made at an input flux of 1.15mm.s^{-1} unless otherwise stated [c.f. table 5.9]. The simulated

Table 5.9: The experimental conditions for each material investigated in this section. The initial strain rate is calculated from the Stokes solution and $\bar{\tau}_b$ is taken from the spectra detailed in section 2.A.

material	temperature [°C]	velocity flux [mm.s^{-1}]	initial $\dot{\varepsilon}_C$ [s^{-1}]	$\bar{\tau}_b$ [s]	W_{i_b} [-]
CM1	155°C	1.15	1.74	1.04	1.81
HDB2	155°C	1.15	1.74	14.8	25.8
HDB6	155°C	1.15	1.74	28.0	48.7
1800S	140°C	1.15	1.74	1.38	2.40
1840H	150°C	0.46	0.70	50.4	35.3

results were solved with *euFlow* and are presented as colour plots of PSD with black contour lines representing the black fringes equally spaced at a fixed stress value per fringe taken from Coventry (2006); Hassell et al. (2008).

Various constitutive equations have been examined previously in a Cross-Slot geometry. Bogaerds et al. (1999) showed that the Giesekus and PTT constitutive models fail to predict downstream principal stresses in Cross-Slot geometry for polymer solutions due to a failure to capture extensional stresses. Verbeeten et al. (2002) compared the XPP, Giesekus and PTT constitutive models in a cross-slot geometry using 2D simulations. For a LDPE melt at a low Weissenberg number ($W_i = 4.3$) all three models showed a reasonable match with experiments, although the Giesekus and XPP models perform slightly better than the PTT model. Abedijaberi et al. (2009) compared experiments and simulations of the flow of LDPE branched polymer melts in a lubricated cross-slot channel. Using the Giesekus constitutive model the authors show that the model performs well at a Weissenberg number, $W_i = 21$. However, for a high Weissenberg number ($W_i = 29$) the Giesekus model fails to capture the optical data, although it is reported that this could be due to limitations in the experimental technique.

The FIB of the LLDPE CM1 at 155°C is shown in figure 5.18. CM1 is a linear material with a average relaxation time of $\bar{\tau}_b = 1.04$s. Since the material exhibits no strain hardening and has fast orientation relaxation the PSD flow pattern is Newtonian in shape, as seen for the one-mode Pompom model with $W_b \ll 1$. The simulation of Pompom parameterisation for CM1 (which has $q_i = 1$ for all modes, i) captures the shape of the PSD well and produces the correct number

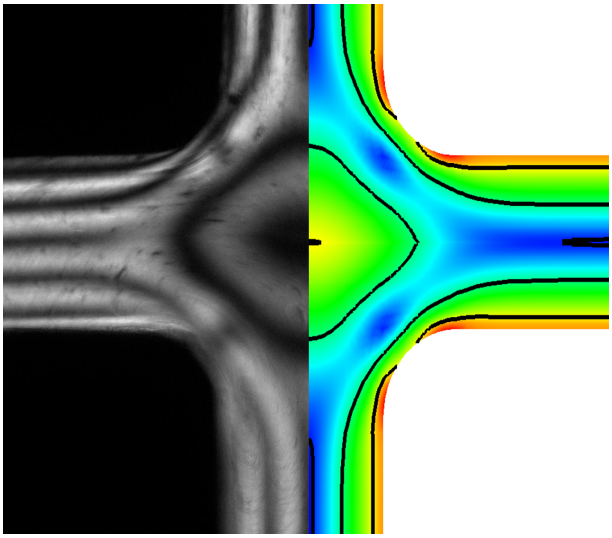

Figure 5.18: The experimental FIB for the LLDPE CM1 and 2D simulation results with PSD contours shown at every 40kPa. The shape of the simulated PSD is very similar to the experiment and the Pompom spectra used predicts the correct number of contours.

of fringes compared with the experiment.

The HDPE named HDB2 has a longer average relaxation time of $\bar{\tau}_b = 14.8$s and contains linear and sparsely branched molecules showing only a small amount of strain hardening in SER uniaxial experiments. The FIB for HDB2 at 155°C is shown in figure 5.19 where the PSD pattern shows elongated diamonds around the SP. The Pompom parameterisation used underestimates the number of fringes shown in the experiment which suggests that HDB2 is more strain hardening than SER measurements indicate. In the SER experiments all the polyethylenes experienced sample rupture before steady state is reached. As a consequence the values for q may be underestimated. This will also explain why the cusps in the simulation are not as elongated compared to the experimental PSD.

Another HDPE similar to HDB2 is HDB6, which has an average relaxation time of $\bar{\tau}_b = 28.0$s. HDB6 displays more strain hardening than HDB2 due to a larger content of LCB present. The FIB patterns for HDB6 at 155°C are shown in figure 5.20. For both HDPEs shown, the simulations predict more PSD fringes on the channel walls than present in experiments despite the good prediction in transient shear experiments seen in chapter 2. This is a general finding for all

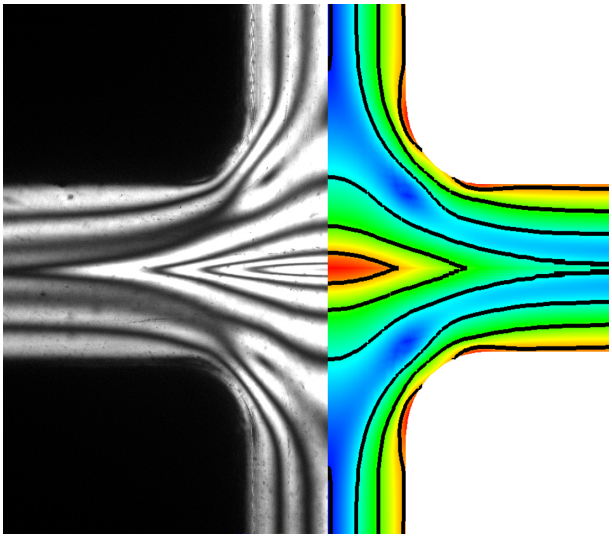

Figure 5.19: The experimental FIB for the HDPE HDB2 and 2D simulation results with PSD contours shown at every 22kPa. The Pompom spectra used predicts one less fringe than the experiment and the experiment has sharper cusping, possibly indicating that the spectra for HDB2 should include more LCB.

LCB materials and is thought to be due to the presence of an abrupt contraction upstream of the cross-slot which is discussed in Coventry (2006); Coventry and Mackley (2008). For CM1 and HDB2 each fringe around the stagnation point cusps along the outflow centre line. For HDB6 the PSD contours at steady state, cusp either side of the outflow centre line forming a double cusp. Hassell et al. (2009) called these double cusps, 'W-cusps'. The appearance of W-cusps is dependent on material and seem to be a function of branching. For HDB6 W-cusps are observed at all experimentally accessible velocity fluxes, ranging from 0.23mm.s^{-1} ($W_i = 9.74$) to 4.6mm.s^{-1} ($W_i = 195$). The appearance and formation of W-cusps is discussed in more detail in chapter 6.

Although the Pompom parameterisation for HDB6(a) captures the overall shape of the PSD contours around the SP, near the centre line the Pompom model does not display the W-cusp formation that is seen in experiments. Indeed, we have not found any Pompom parameterisations that exhibit W-cusps.

For LDPEs the PSD contours are highly concentrated on the outflow centre line. This is similar to the one-mode Pompom model with $W_s \gg 1$ [c.f. figure

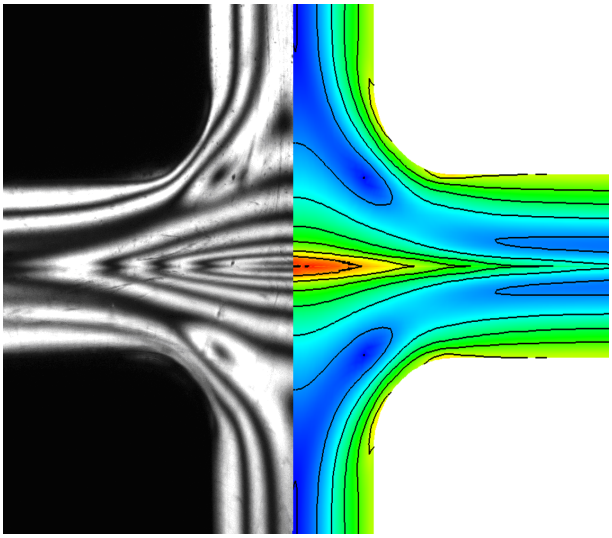

Figure 5.20: The experimental FIB for the HDPE HDB6 and 2D simulation results with PSD contours shown at every 22kPa. The number of fringes and the overall shape of the PSD is predicted well, however, the Pompom constitutive model does not predict the W-cusps along the outflow centre line.

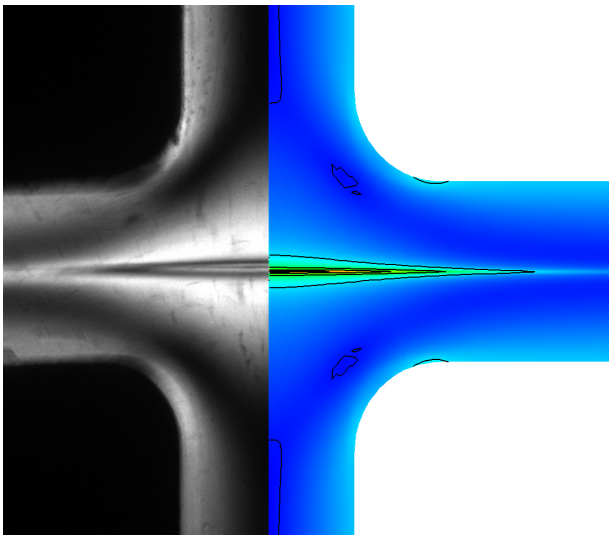

Figure 5.21: The experimental FIB for the LDPE 1800S and 2D simulation results with PSD contours shown at every 24.5kPa. The number of fringes and large stress gradient is predicted well, however, the Pompom constitutive model does not predict the W-cusps along the outflow centre line. The double cuspsing is narrow for 1800S and therefore is hard to see in this picture.

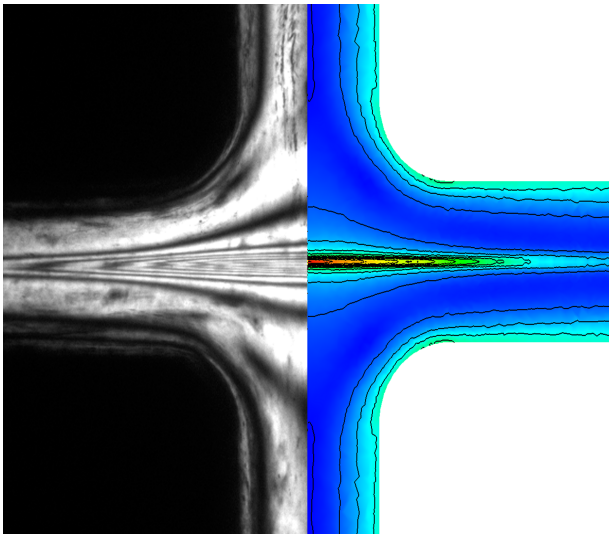

Figure 5.22: The experimental FIB for the LDPE 1840H and 2D simulation results with PSD contours shown at every 24.5kPa. The number of fringes and stress gradient is predicted well, however, the again Pompom constitutive model does not predict the W-cusps along the outflow centre line, easily seen on the outer fringes.

5.9]. The dense LCB structure of LDPEs causes high levels of strain hardening which in turn produces high stress gradients near the SP.

Figure 5.21 shows the experimental PSD for 1800S at 140°C compared to simulation results. At this flow rate 1800S does not exhibit W-cusps but they do occur at higher flow rates [c.f section 5.5 and chapter 6]. The simulation of the Pompom spectra shifted to 140°C closely matches the experimental PSD, both of which have three fringes around the SP. As discussed above, for higher flow rates when W-cusps occur the Pompom model fails to capture the phenomena.

Figure 5.22 shows the FIB pattern for the LDPE 1840H at 150°C with a velocity flux of 0.46mm.s^{-1} (W_i = 35.3). Even at this low flow rate the high viscosity and strain hardening, with $\bar{\tau}_b$ = 50.1s, produce approximately 9-12 fringes of stress concentrated on the outflow centre line. The Pompom spectrum used matches the experiment well predicting ten fringes, but the experimental PSD pattern also contains W-cusping close to the centre line which the Pompom model does not capture.

As well as steady state, transient images of the build up of the experimental

FIB can also be compared to simulations. Figure 5.23 shows the solution at six different times for HDB6 leading to the steady state FIB seen in figure 5.20. The plots show the transient nature of W-cusps, first occurring at 3.2s near the SP and travelling downstream. Although the Pompom model captures the shape of the PSD contours (but not the W-cusps) at steady state, at early times the transient build up of stress occurs much quicker than in experiments. This may be a consequence of the differences in the transient flow rate. In simulations the flow rate switches on instantaneously at start up, whereas the flow rate in the experiments grows over a finite time interval. Another discrepancy between experiments and simulations is that between $5s$ and $11s$ the experimental PSD pattern 'collapses' and the number of fringes at the SP decreases by one fringe. For all materials exhibiting the W-cusp phenomena this pattern collapse is observed, however simulations using the Pompom constitutive model fail to capture the pattern collapse. Indeed, the solutions at 5s and 11s are visually identical.

As well as comparing the PSD as obtained from FIB, we can also compare the predictions of the modification to the fluid velocity due to the polymeric stresses. Figure 5.24 show how the level of stretch along the outflow centre line is predicted to affect the fluid velocity for HDB6. The figure shows the two effects the stretch has on the velocity. Near the stagnation point, the velocity increases as there is a region of saturated maximum stretch. Further downstream the effect of gradients in the stretch component slows the velocity down. This is similar to the one mode Pompom model with intermediate q values [c.f. figure 5.10]. Figure 5.25 shows the distribution of the velocity gradient $\frac{dU}{dX}$ at steady state, which equates to the strain rate near the SP. Starting from the initial maximum value at the SP of $3.5s^{-1}$ the maximum value at steady state is $4.4s^{-1}$, which is an increase of 25%. The averaging of multiple modes means that we do not find such dramatic changes in strain rate as in the single-mode Pompom model.

The fluid velocity in the experiments were measured by laser-Doppler velocimetry (LDV) [e.g. Coventry (2006)] for HDB2 at a velocity flux of 1.15mm.s^{-1} ($W_i = 25.8$) and 1840H at 0.46mm.s^{-1} ($W_i = 35.3$) measured along the upstream and downstream centre lines as shown in figure 5.25. For HDB2 the Pompom model predicts that the fluid velocity upstream is slower than the Stokes solution at time, $t = 0$, which agrees well with the LDV data [c.f. figure 5.26]. Down-

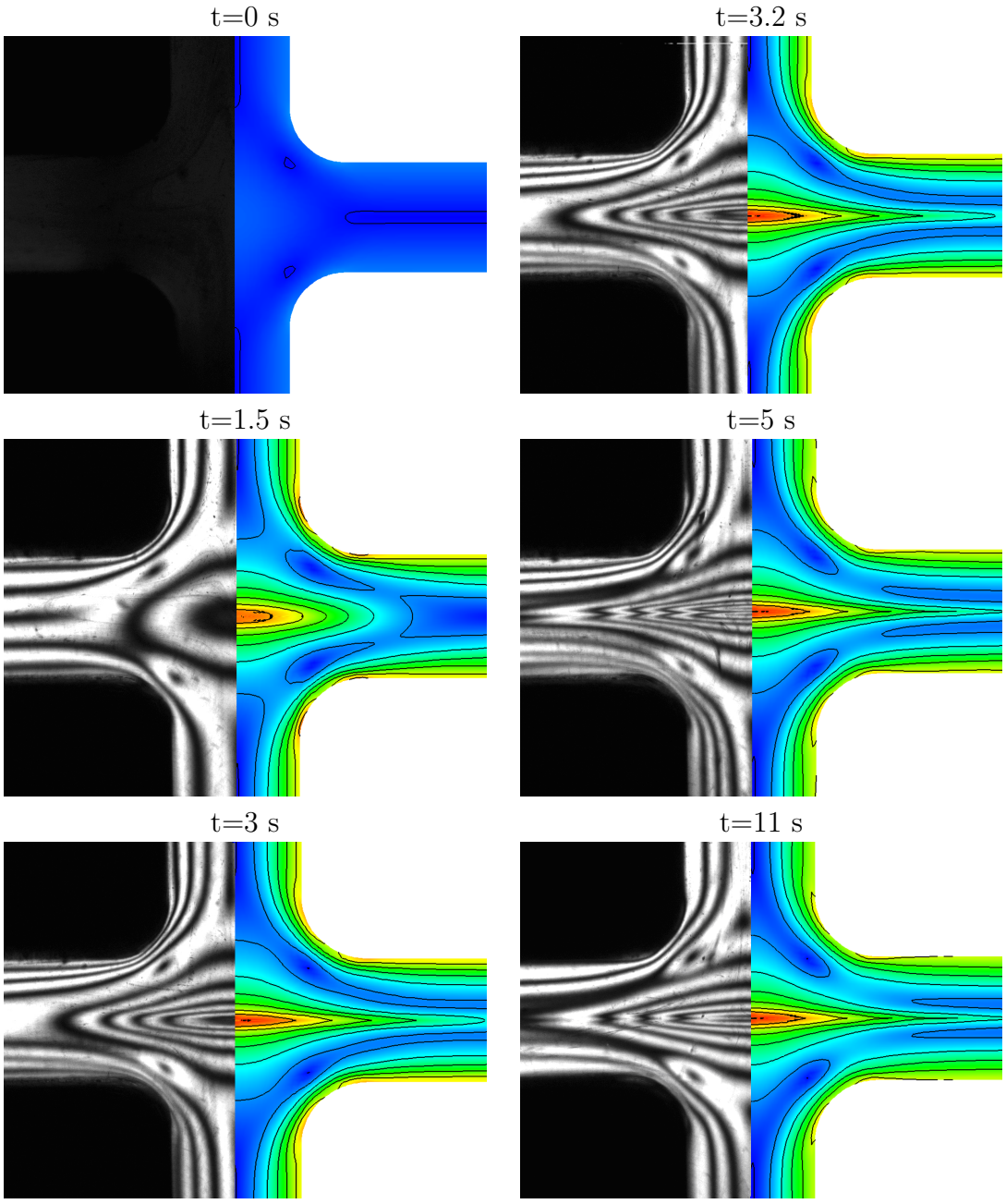

Figure 5.23: The transient development of the experimental PSD for HDPE HDB6 is compared to the transient PSD for the 2D simulated solution. In the experiments W-cusps occur at a time of 3.2s near the SP. The simulated PSD develops faster for simulations than experiment and W-cusps are not predicted for any simulated solution time.

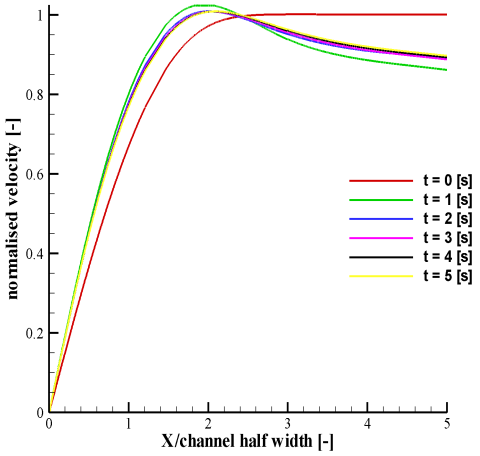

Figure 5.24: A comparison of the velocity profile along the downstream symmetry line for the simulated HDB6 Pompom spectrum as a function of time. Near the stagnation point the velocity increases where regions of constant stretch occur, but further downstream the flow is slowed by gradients in the stretch.

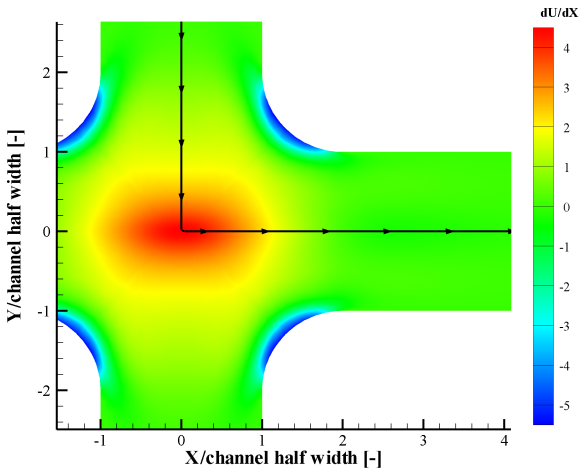

Figure 5.25: Flow patterns computed in the cross-slot for a multimode Pompom model of HDB6(a) ($155°C$) at steady state flow from simulation at a Weissenberg number of ~ 100: b) elongational flow rate distribution $\sim \frac{dU}{dx}$.

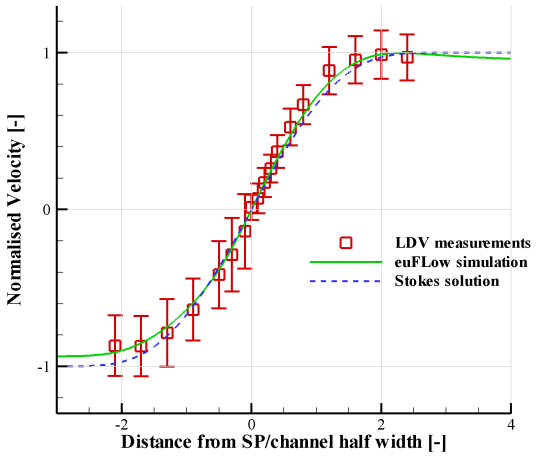

Figure 5.26: Experimental results from laser-Doppler velocimetry (symbols) and flow simulations (solid line) for the velocity profile as a function of position for the stream line along the inlet-outlet symmetry plane for HDPE HDB2 at 155°C. See figure 5.25 for a depiction of the stream line used.

stream the Pompom model predicts a slight increase in velocity gradient near the SP and a slight decrease in velocity downstream from the stagnation point, relative to the Stokes solution. This is similar to the predictions of HDB6 [c.f. figure 5.25]. The experimental data predicts the same behaviour but the velocity seems to be higher for the experiments than for simulation near the SP. However these differences are small compared to the noise levels in the LDV signal. Downstream the LDV data does show a velocity overshoot as in the simulation but there are not enough downstream data points to fully determine the velocity.

For 1840H [figure 5.27] the slower flow rate means that the data for each point is much noisier than the data for HDB2. Despite this there is a clear trend that the velocity downstream is significantly slower than the velocity upstream of the SP, with a decrease of velocity gradient near the SP. The Pompom simulation predicts the same behaviour but to a lesser extent, perhaps suggesting there needs to be more branching in the spectrum to slow the velocity down further. The discrepancies seen could be a result of the Pompom parameters being fitted incorrectly, for example HDB2 cross-slot predictions show that more strain hardening needs to be modelled.

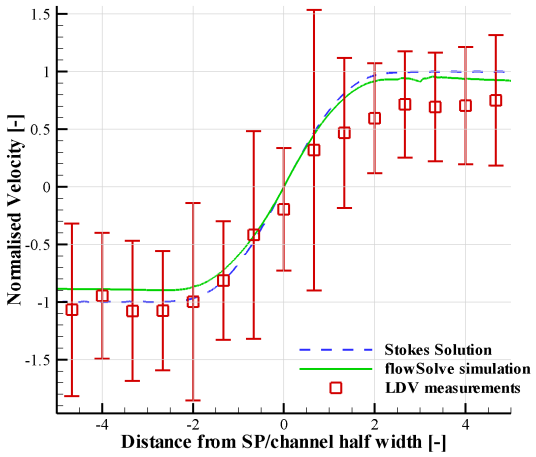

Figure 5.27: Experimental results from laser-Doppler velocimetry (symbols) and flow simulations (solid line) for the velocity profile as a function of position for the stream line along the inlet-outlet symmetry plane for LDPE 1840H at 150°C. See figure 5.25 for a depiction of the stream line used.

In general the Pompom constitutive model and the parameters fitted to simple extensional rheology perform well in cross-slot flow, apart from failing to predict the W-cusp phenomena. In the next we section examine whether the cross-slot can be used to measure extensional viscosity, using numerical simulations to determine the strain rate at the SP.

5.5 The cross-slot as a rheometer

In order to determine the steady state viscosity from cross-slot rheometry it is important to achieve a steady state stress profile. It appears that even for the highly branched LDPE, with long relaxation times, the birefringence patterns equilibrate, with no further change, within the experimental time and strain window of about 6 Hencky strain units, indicating a steady state flow condition. This steady state was observed to have been reached well before the end of the experimental time frame for all the materials in our study. These visual observations of the flow suggest that the residence times and total stains are sufficient to reach a steady state in transient rheology. The time dependence of the stress profile has

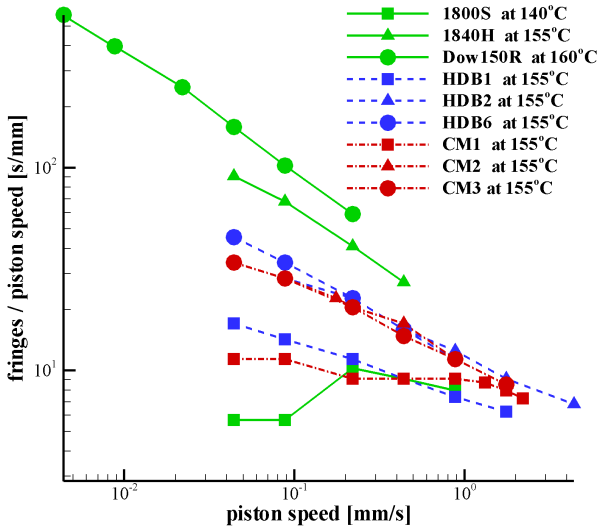

Figure 5.28: Number of fringes per piston speed as a function of piston speed for the LLDPE, HDPE and LDPE samples investigated at conditions indicated in Figures 5.29, 5.30 and 5.31.

been discussed in more detail by Hassell et al. (2008) and shown in figure 5.23.

The intensity patterns of the birefringence can be transformed from PSD into steady state extensional stress at the SP by counting the (fractional) fringe number at the flow stagnation point. The first step to obtaining quantitative data is to examine the limits of manual fringe counting. Figure 5.28 displays this recorded 'raw' data as a function of the primitive machine-proxy for the flow rate, the piston speed. The lower limit for the determination of tensile stresses from the birefringence method is given by the necessary minimum of half an established fringe. The resolution for the stress increases significantly with a growing number of fringes since an error in the order of one fringe becomes less pronounced for a higher number of fringes. Towards higher piston speeds the spatial resolution of the optical equipment limits the maximum number of fringes which can be distinguished in the $1.5mm$ wide cross-slot gap to about 40 fringes, with a possible error of ± 3 fringes. The viscosity of the chosen PE samples was high enough to obtain a reasonable number of fringes, which can be used to compute the tensile stress, yet not so high as to lose fringe resolution.

From the shape of the resulting curves one can already estimate the qualitative form of the elongational viscosity function $\eta_{E,std}(\dot{\varepsilon})$ since the viscosity is related to the number of fringes per piston speed via the stress-optical coefficient (SOC), and the elongational rate will be approximately proportional to piston speed.

In Figures 5.29, 5.30 and 5.31 the black and white fringes from stress-induced birefringence (photographs in the left part) are compared to the PSD intensity profiles from *euFlow*/*flowSolve* simulations (color images in the right part) with the PSD level increasing from blue to red. As before, for clarity black lines are drawn to coincide with the dark experimental birefringence contours. The similarity of both fringe patterns demonstrates a very good agreement and accurate description of the stress level and distribution for each material as a function of velocity flux.

The initial strain rate and material specific average relaxation times are given in the tables so that the particular Weissenberg numbers can be estimated for a particular flow condition. However, these numbers can only give an average since all materials have a relatively wide range of relaxation times due to the width of the molar-mass distribution and also the heterogeneity of the long-chain branching structure. Also the true strain rate will depend upon the fluid rheology.

For each material, the variation in FIB as a function of flow rate shows several similarities. Although the number of fringes increases with increasing flow rate [c.f. Hassell and Mackley (2009); Hassell et al. (2009, 2008); Verbeeten et al. (2002)], the overall shape of the PSD pattern for each material remains similar. For example CM1 (figure 5.30) retains the symmetric diamond pattern associated with Newtonian flow in section 5.4.1. Also, HDB1 and HDB2 retain the same asymmetric diamond contours and HDB6 exhibits W-cusps for all flow rates (figure 5.29). For the LDPEs, each material exhibits W-cusps but only for the higher Weissenberg numbers. All the LDPEs contain highly stretched material along the outflow centre line, even for Weissenberg numbers less than unity.

$\dot{\varepsilon}_C$ [s^{-1}]	HDB1 $155°C$ $\bar{\tau}_b = 5.61s$	HDB2 $155°C$ $\bar{\tau}_b = 14.8s$	HDB6 (a) $155°C$ $\bar{\tau}_b = 28.0s$
0.35	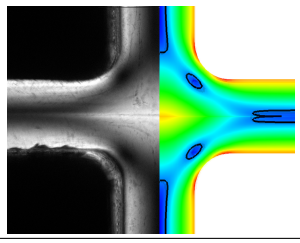	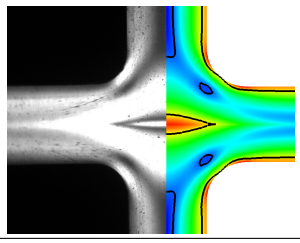	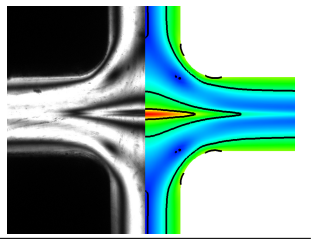
0.70	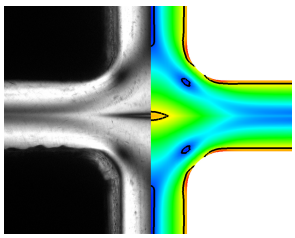	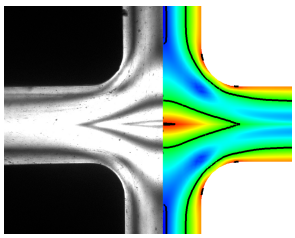	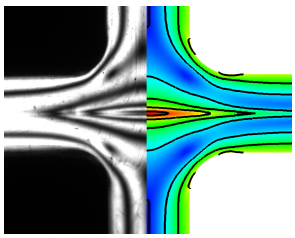
1.74	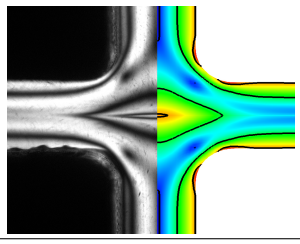	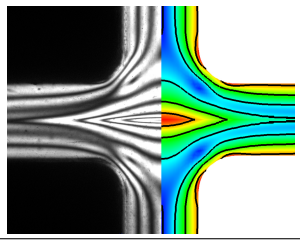	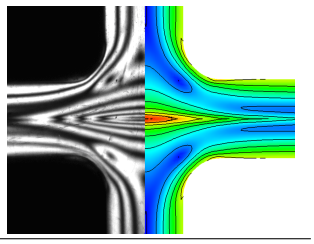
3.48	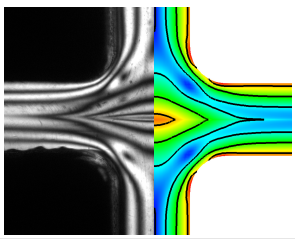	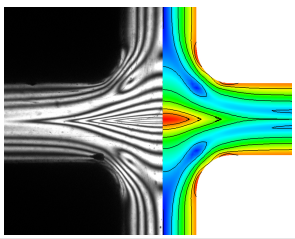	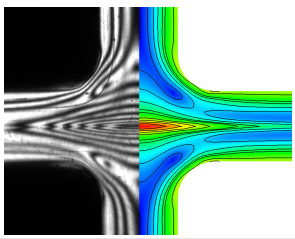
6.95	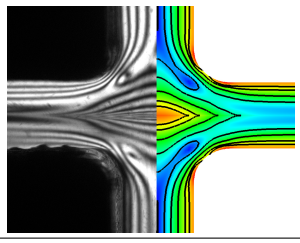	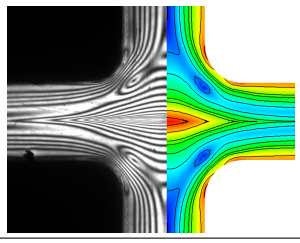	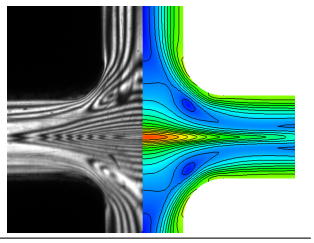

Figure 5.29: Flow-induced stress birefringence patterns at steady state flow for HDPE HDB series at different initial strain rates, or Weissenberg numbers, W_i, calculated using the average relaxation time indicated. The stress profile is evident from the fringe patterns and the simulated data are presented with a series of contours, using the same optical constant of $22kPa$ for all materials.

$\dot{\varepsilon}_C$ [s^{-1}]	CM1 $155°C$ $\bar{\tau}_b = 1.09s$	CM2 $155°C$ $\bar{\tau}_b = 16.3s$	CM3 $155°C$ $\bar{\tau}_b = 18.0s$
0.35	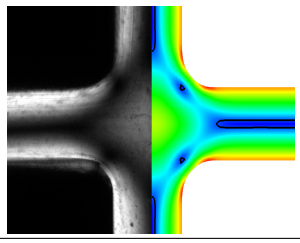	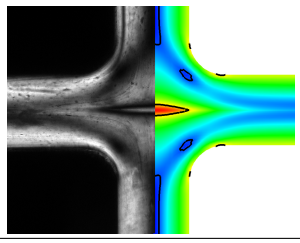	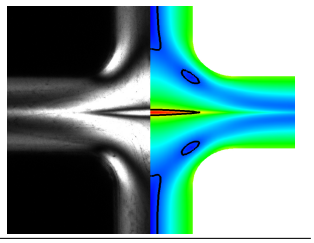
0.70	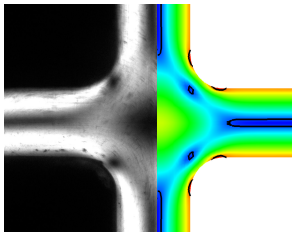	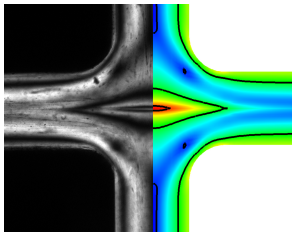	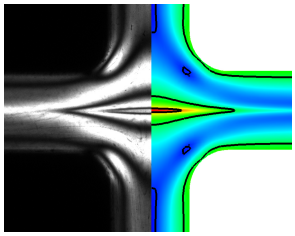
1.74	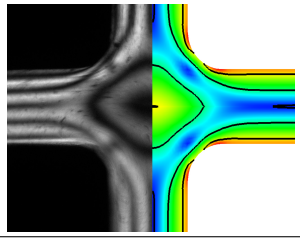	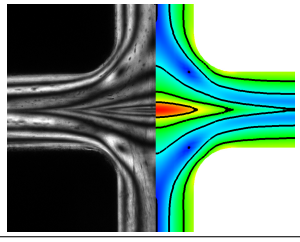	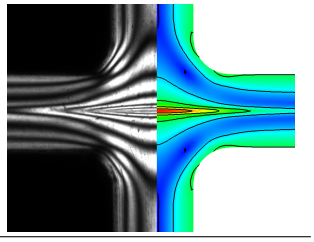
3.48	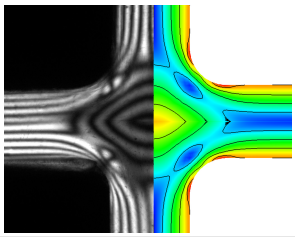	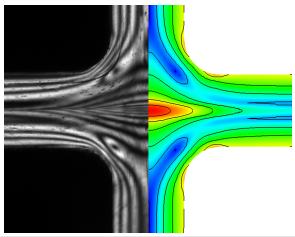	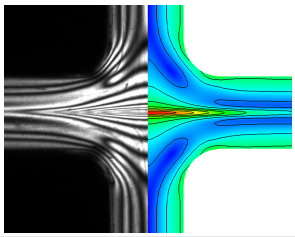
6.95	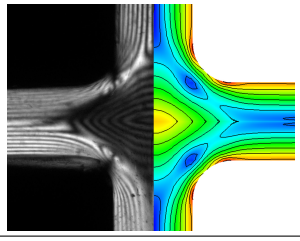	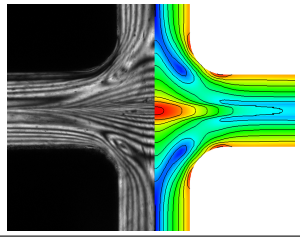	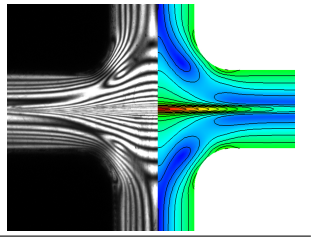

Figure 5.30: Flow-induced stress birefringence patterns at steady state flow for HDPE CM series at different initial strain rates, or Weissenberg numbers, W_i, calculated using the average relaxation time indicated. The stress profile is evident from the fringe patterns and the simulated data are presented with a series of contours, using the same optical constant of $40kPa$ for all materials.

$\dot{\varepsilon}_C$ [s^{-1}]	1800S 140°C $\bar{\tau}_b = 1.38s$	1840H 155°C $\bar{\tau}_b = 50.1$	Dow150R(a)* 160°C $\bar{\tau}_b = 428$	$\dot{\varepsilon}^*_C$ [s^{-1}]
0.35	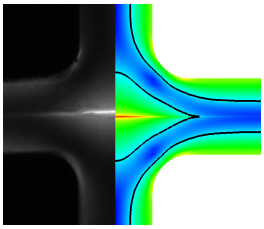	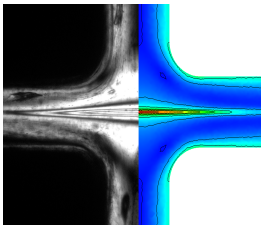	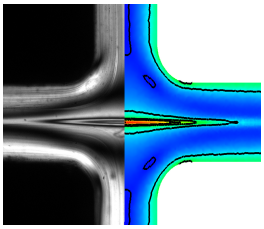	0.035
0.70	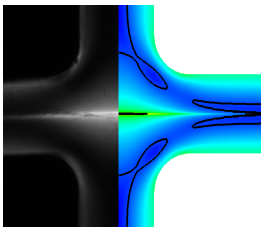	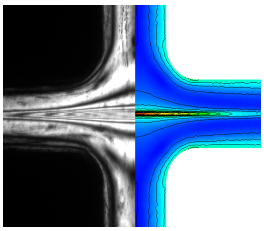	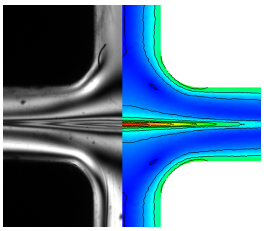	0.070
1.74	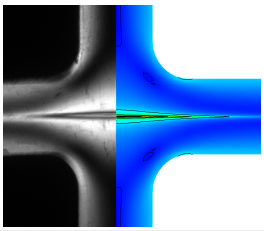	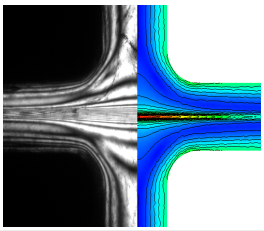	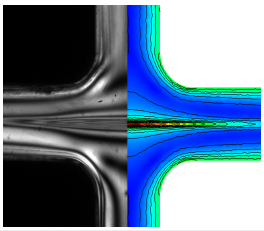	0.174
3.48	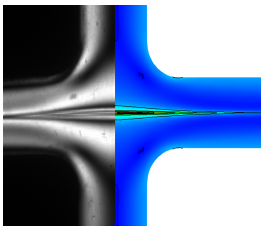	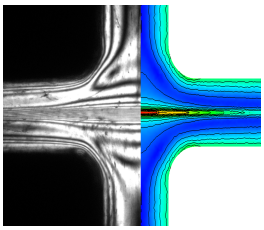	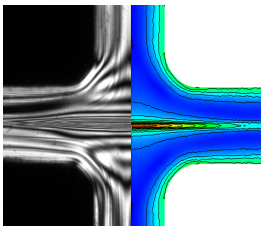	0.35
6.95	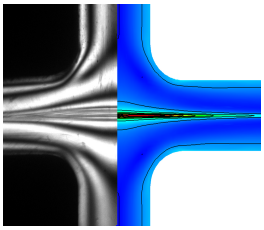	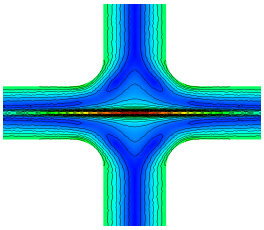	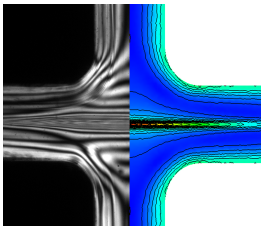	0.70

Figure 5.31: FIB stress patterns at steady state flow for three LDPEs at different initial strain rates, or Weissenberg numbers, W_i. Note, for Dow150R the strain rates are a factor 10 lower than for 1800S and 1840H. The stress profile is evident from the fringe patterns and the simulated data are presented with a series of contours, using the same optical constant of $24.5kPa$ for the three slowest flow rates, and for clarity $49kPa$ for the two fastest flow rates.

5.5.1 Steady state elongational planar viscosity from stagnation point analysis

At the SP the steady state viscosity in planar extension may be deduced from the fringe number and calculated local extension rate. Producing a steady state extensional viscosity curve from the cross-slot extensional rheometer (CSER) provides a new fitting tool to parameterise the Pompom constitutive theory. Matching the steady states in extension should improve qualitative FIB predictions. For example the materials HDB2 produces fewer PSD contours than are observed in experiments. This is probably due to sample rupture in stretching experiments and so using CSER to find the true steady state would give matching FIB predictions and HDB2 would be parameterised more accurately.

In predicting CSER steady state extensional viscosity curves various errors must be analysed to establish the precision of these measurements. Three values are needed to produce a data point, namely the number of PSD fringes, the SOC and the strain rate. The PSD fringes count has a minimum error of half a fringe, which is most significant at small fringe numbers, i.e. when < 2 fringes are visible. When the total number of fringes exceeds ~ 15, the fringe visibility at the SP is poor, with errors of ± 3 fringes, but this has less effect on the viscosity curve. For each fringe to carry a fixed stress contribution the linear stress-optical relation must be valid with a well defined SOC. A SOC of $2.34 \cdot 10^{-9}\text{Pa}^{-1}$ which is equivalent to 22kPa of stress per fringe is used for the HDPEs, $2.19 \cdot 10^{-9}\text{Pa}^{-1}$ equivalent to 24.5kPa of stress per fringe for the LDPEs and a SOC of $1.29 \cdot 10^{-9}\text{Pa}^{-1}$ giving 40kPa of stress per fringe for the LLDPEs. This agrees with previous experimental measures of the SOC using the MPR [Coventry (2006); Hassell et al. (2008)] and fall well within literature range of $1.2 - 2.4 \cdot 10^{-9}\text{Pa}^{-1}$ [Macosko (1994)]. Errors in the SOC are likely to be of order 10% which is smaller than the fringe counting error. The predicted error from CSER extensional measurements is shown on figure 5.32 and this shows that the least viscous samples (CM1, HDB1 and 1800S) have significant error at the lower strain rates, when less than two fringes are observed.

To define the viscosity the simulated strain rate is used, which can vary from the initial strain rate by up to 25%. In section 5.4.4 it was shown that the

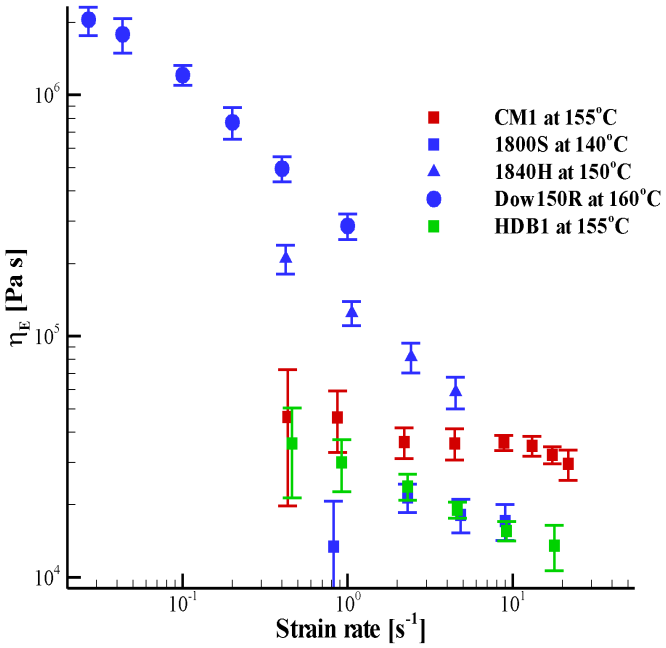

Figure 5.32: The predicted error for CSER extensional viscosity measurements for a range of materials used in this study. The largest error bars occur for the less viscous materials (CM1, HDB1 and 1800S) for the lower strain rates when less than two fringes are observed.

velocity predictions of the Pompom model showed good agreement with LDV data. Since the viscosity is a function of strain rate, errors in the strain rate will produce a 45° translation of the data. Errors up to 20% have little visible effect on the extensional viscosity predictions. The strain rate was simulated for each experimental flow rate for all the materials evaluated in this chapter and it was found that the strain rate deviated from its initial value by the almost the same factor for each material, seemingly independent of flow rate. In section 5.4.1 it was shown how the Pompom branching parameter affects the velocity field, so it is not unreasonable that the transient development of the strain rate is a function of material.

In comparing the SER and cross-slot it should be noted the two experiments measure different extensional flow types. The SER measures uniaxial extensional

flow whereas the cross-slot approximates planar extensional flow. For Newtonian fluids there is a factor $\frac{4}{3}$ difference between these two viscosities. However in non-linear response in extension the difference between the two flow types is diminished [Laun (1986); Laun and Schuch (1989); Laun and Münstedt (1978)]. At extension rates above a $W_{i_b} \gg 0.5$, the tube segments align with the extensional axis so that $\underline{\underline{K}} : \underline{\underline{S}} \simeq \dot{\varepsilon}$. The Pompom constitutive model captures this diminishing effect and in the limit of high strain rate gives the same extensional viscosity for both flow types [Inkson et al. (1999)]. For clarity of the onset of high non-linear response the Pompom predictions for both uniaxial and planar extension are shown in figures 5.33, 5.34 and 5.35.

The results from the combination of birefringence analysis and flow-rate predictions are presented in figures 5.33, 5.34 and 5.35, in terms of steady state extensional viscosity as a function of extension rate. Also plotted are the maximum values of the stress obtained in the SER extensional experiments performed on the same samples, testing the hypothesis that these values are attained at the onset of plateau stress. The steady state extensional viscosity predictions of the Pompom parameterisation for each model in both uniaxial and planar flow are included.

For the linear LLDPE CM1 (figure 5.34) and the HDPE HDB1 with little LCB content (figure 5.33) the SER and CSER extensional viscosity data are in good agreement with the small discrepancy between the data being explained by the difference between uniaxial and planar extensional flow. This is shown by the Pompom predictions agreeing with each flow type for these materials.

The discrepancy between uniaxial and planar extension is smaller for CM2 (figure 5.34) and HDB2 (figure 5.33), where the data is in the non-linear strain-hardening regime. For these two materials the CSER data is slightly higher than the SER data and the Pompom planar prediction. In the cross-slot simulations the Pompom spectra used for CM2 and HDB2 did not capture the same number of fringes as was experimentally found (c.f. figures 5.30 and 5.29). This finding supports idea that the SER stretching experiments do not reach the steady state plateau at the point where the sample breaks and so these materials are more strain hardening than the SER experiments predict. Hence, the CSER steady state extensional viscosity curves provide a tool for improving rheological testing

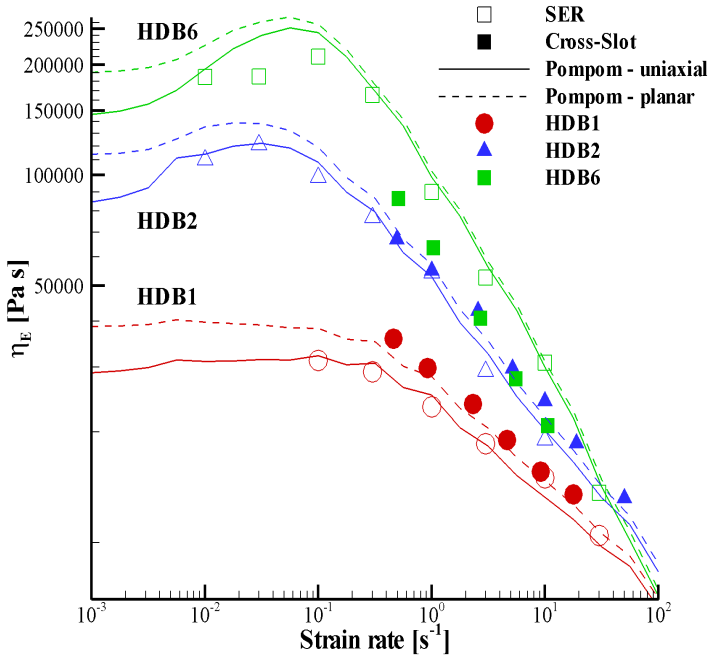

Figure 5.33: Elongational viscosity η_E as a function of strain rate from uniaxial (open symbols) and cross-slot experiments (closed symbols) for the branched HDPE HDB series. Also shown are the Pompom predictions in uniaxial (solid lines) and planar (dashed lines) extension.

and parameterising materials where sample breakup limits transient SER data.

For the materials HDB6 (figure 5.33), 1840H and Dow150R (figure 5.35) a different trend is observed. Operating in the experimental window where the difference between uniaxial and planar extension is nominal, the CSER data is significantly lower than that of the SER experiments for all strain rates. As seen in the previous analysis of CSER (figure 5.32) this discrepancy is larger than the imprecision in the CSER measurements. However, all these materials exhibit W-cusps for all flow rates (figures 5.29 and 5.31). Therefore, since one birefringence image shows the strain history of the material in that flow rate this suggests an overshoot in transient extensional flow with the maximum observed extensional viscosity being larger than the final steady state value.

The materials CM3 (figure 5.34) and 1800S (figure 5.35) provide an interest-

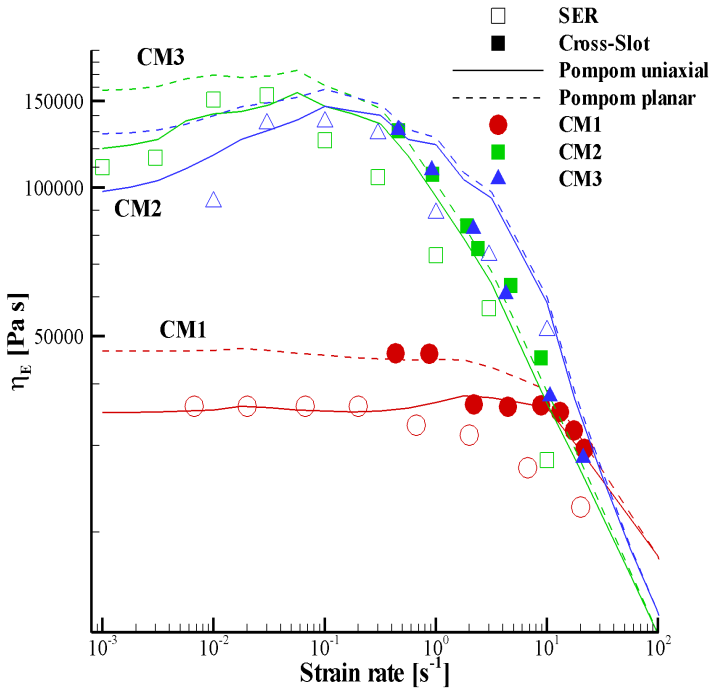

Figure 5.34: Elongational viscosity η_E as a function of strain rate from uniaxial (open symbols) and cross-slot experiments (closed symbols) for the branched HDPE CM series. Also shown are the Pompom predictions in uniaxial (solid lines) and planar (dashed lines) extension.

ing cross-over behaviour. For 1800S at low strain rates both the SER and CSER experiments, within the noise levels of the CSER, predict a linear response (confirmed by the FIB pictures (figure 5.31) showing a single cusping pattern). However, for the higher strain rates the CSER gives a lower steady state value than the SER measurements with W-cusps in the FIB pictures. For the material CM3 the experiments are within the non-linear regime and the predictions of the two experimental methods cross-over at a strain rate of around $10s^{-1}$. However, it is unclear whether the FIB pictures (figure 5.30) exhibit W-cusps at these higher strain rates as the resolution is not good enough to decipher the highly packed fringes.

One explanation for the discrepancy between the CSER and SER measurements on the more highly branched polymers is that the stress growth curves are

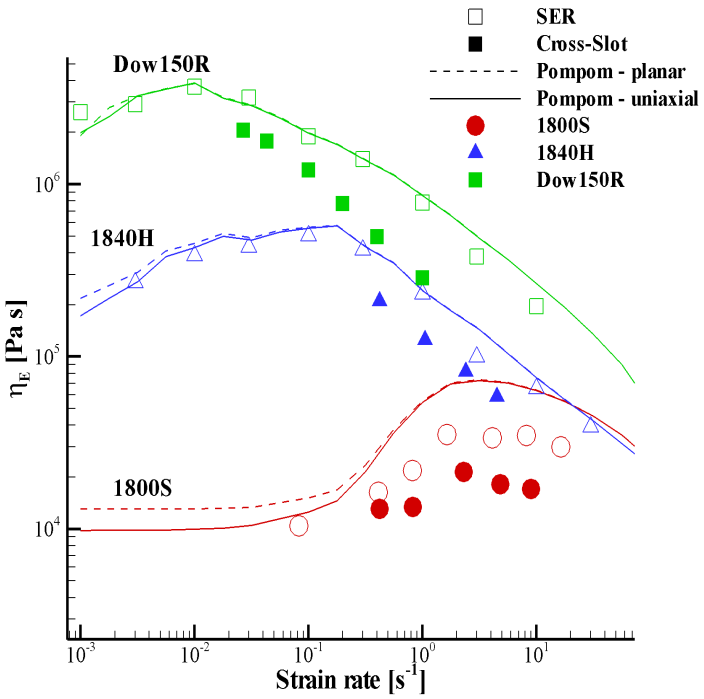

Figure 5.35: Elongational viscosity η_E as a function of strain rate from uniaxial (open symbols) and cross-slot experiments (closed symbols) for the LDPE materials used in this study. Also shown are the Pompom predictions in uniaxial (solid lines) and planar (dashed lines) extension.

non-monotonic, rising to a maximum before falling towards a lower steady state viscosity plateau. In this case, the SER measurements would pick up the transient maximum and register a higher viscosity than the steady state cross-slot value. Such an overshoot has been observed in LDPEs by Bach et al. (2003); Rasmussen et al. (2005), who found a viscosity overshoot in uniaxial elongational.

5.5.2 Discussion

Our investigation demonstrates both how the steady state flow behavior in elongation can be determined from cross-slot measurements and also that the molecular structure influences the steady state extensional response in such a way as a function of deformation rate. Analyzing polymer melts in a confined reservoir

like the cross-slot geometry using the multi-pass rheometer avoids free surface distortions.

For the steady state elongational viscosity determined in the cross-slot geometry we found a good qualitative agreement with the maximum values determined in uniaxial elongation for materials with a single cusp pattern. For materials that show W-cusps the CSER gives significantly lower values for the viscosity which is consistent with the existence transient maximum in the extensional stress of some LCB melts. This is discussed in more detail in the next chapter.

The determination of the 'priority' branching q-spectrum by the Pompom model is not a trivial task and sometimes is an ill-posed problem since, in the case of restricted data sets, there are multiple solutions to fitting a multimode Pompom spectrum that accounts for limited uniaxial elongational data equally well. However, by using a combination of CSER and sample stretching tests like the SER, the model parameter space becomes much more restricted. For this reason matching the predicted stress-induced birefringence patterns could become a highly valuable tool in analysing the branching structure of a polymer melt.

Using the rheology and flow modelling procedure described in this study it is possible to pinpoint the relaxation times and parameters which are affected by long-chain branching structure differentiating both between classes of LCB materials and between materials of different branching density within a single class. Accordingly, this technique can be used to infer information on the molecular structure of the polymeric sample.

The questions raised by new data and modelling of this work, specifically the differences in maximum extensional stress of the SER, and the steady state stress of the CSER, and specific flow features such as 'W-cusping' observed at high Weissenberg numbers of the LDPE samples and for all Weissenberg numbers of HDB6, may suggest new physics as yet not captured in molecular models.

5.6 Evaluating Pompom parameterisations

Using the cross-slot data we can now analyse how the Pompom parameterisations described in chapter 2 are able to capture the cross-slot flow and in particular

the different spectra fitted to HDB6 and Dow150R are examined to determine the sensitivity to the fitting of the Pompom non-linear parameters.

HDB1 shows good agreement between the extensional rheology from the SER and the CSER, with the discrepancy between the results accounted for with the difference between uniaxial and planar extension. This is shown by the Pompom steady state predictions which is shown in figure 5.33. However, figure 5.29 shows significantly more cusping in experimental FIB than in the Pompom predictions for all strain rates. Since the fringe number and hence the steady state viscosity are well modelled by the Pompom model, this cusping is caused by a small contribution of some high molecular weight LCB molecules. This would be parameterised in the Pompom spectra by increasing the branching numbers, q_i, for the slowest modes. In the current spectra for HDB1 only the slowest mode has $q > 1$, with a value of $q = 2$ for this mode. Increasing the branching number of this mode could be done to try and improve the visual cusping of the simulated FIB.

For the materials HDB2 and CM2 the Pompom calculations produced less FIB fringes (figures 5.29 and 5.30, respectively) than was experimentally observed for all strain rates. This is a result of the fact that the steady state extensional viscosity in the CSER is found to be higher than in the SER (figures 5.33 and 5.34, respectively). Since these materials exhibit only a small amount of strain hardening, stretching experiments are prone to sample rupture which limits the total strain achievable. CSER is not limited by the same free surface problems and larger total strains can be seen. To improve the Pompom parameterisation of HDB2 and CM2, the non-linear Pompom parameters should be fitted to the transient SER data and the steady state CSER data to fully capture the rheology of the material. This shows that the CSER is a valuable tool for further probing the extensional rheology of these materials with a low content of LCB.

For the materials that exhibit W-cusps the current Pompom model provides less insight into the their rheology since it does not capture this double cusping phenomena. This is discussed in the next chapter in more detail. However, the various spectra for the materials HDB6 and Dow150R that were fitted in chapter 2 can still be compared. Figure 5.36 shows that between the three HDB6 spectra there is little difference in the visual shape of the PSD contours, however due

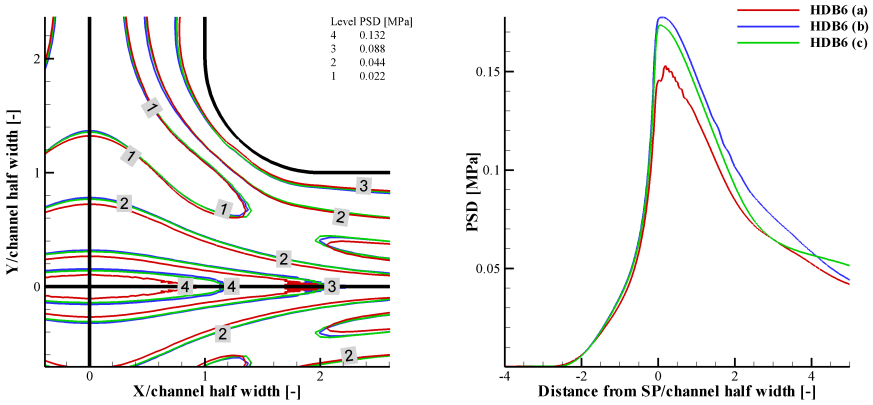

Figure 5.36: A comparison of the PSD for the three HDB6 spectra explored in this work. Only various contour levels have been selected for clarity. As none of the parameterisations show W-cusps then none of the spectra predict the experimental PSD distribution. However, away from the outflow centre line HDB6(a) (RED) predicts the PSD contours with better accuracy than HDB6(b) (BLUE) and HDB6(c) (GREEN), both of which predict an extra PSD fringe when compared to experimental FIB images.

to the slightly higher steady states of HDB6(b) and HDB6(c) these two spectra predict an extra fringe compared to HDB6(a). Thus HDB6(a) provides the best match to the experimental observations away from the outflow centre line [c.f. figure 5.20].

The differences between the two Pompom spectra fitted to Dow150R (Dow150R(a) and Dow150R(b) taken from Hassell et al. (2008)) are most clearly distinguished by looking at the steady state extensional viscosity curves. In figure 5.37 the Pompom extensional viscosity predictions of each spectra are compared to the data taken from both the SER and the CSER. As previously stated, the lower values of the CSER suggests a transient extensional overshoot so both spectra over predict the steady state, although Dow150R(a) is the closest match.

Investigating cross-slot flow with respect to LCB provides two tools for analysing extensional rheology of materials, namely, the visual FIB contours which indicate the extent to which a material is being stretched, and the quantitative steady state predictions that can provide a useful tool for parameterising Pompom spectra. In both cases the predominant Pompom non-linear parameter is the branching

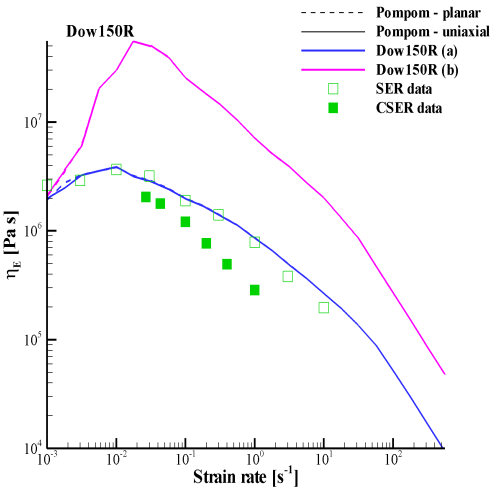

Figure 5.37: The steady state extensional viscosity for the LDPE Dow150R. The open symbols are the maximum values taken from SER experiments and the closed symbols are taken from CSER fringe counting. The Pompom predictions for two spectra, Dow150R (a) and (b), are also shown. With the CSER data indicating a transient overshoot in extension the spectra Dow150R(b) is an unreasonable estimation of the extensional rheology of the material.

number, q, which strongly contributes to the extensional state.

5.7 Conclusions

The cross-slot provides a stern test of the performance of the Pompom model in a flow with both extensional and shear components, as is commonly found in more complex geometries occurring in industrial polymer processing. The stagnation point itself provides a point of unlimited strain and so probes the limits of the deformation of the backbone segments.

Initial investigations of a one mode Pompom model showed that the two Weissenberg numbers for the orientation and stretch relaxation defined the shape of the PSD pattern. These Weissenberg numbers also characterise the flow modifications. Above a stretch Weissenberg number of one the value of the branching priority is the dominant non-linear parameter controlling how the velocity gradient at the stagnation point is modified. Such a flow modification provides an

indirect coupling of modes in a multimode model. An example of this was highlighted for a two mode Pompom model, where the parameters were chosen to show how a large reduction of the strain rate at the SP would cause faster modes to relax. Although this reduces the stress contribution from this particular mode along the outflow centre line it did not reduce the overall PSD (as this is dominated by the slower mode). In a more general case the effects of flow modifications are important for ascertaining viscosity data where a reliable strain rate needs to be known.

Another important investigation is the relevance of 3D flow effects, especially with respect to variations between the FIB of 3D experiments and 2D flow simulations. A version of the Pompom constitutive model, known as the DPP model was chosen to aid in 3D numerical simulations of cross-slot flow. It was shown that for the geometry used in this work a 2D approximation was valid and a good approximation for both the PSD and the strain rate at the SP.

A comparison was made between the Pompom cross-slot predictions and experimental results for a range of LLDPEs, HDPEs and LDPEs. The high content of LCB in the LDPEs produced much higher stress gradients near the SP and was clearly distinguishable from the other materials. For the materials with a low content of LCB, for example HDB2 and CM2, although the shape of the PSD was reproduced, the Pompom parameters used predicted less FIB contours than found in experiments. This was attributed to the much higher total strains obtained in cross-slot flow compared to stretching experiments, thus there existed more strain hardening than the SER predicted. All of the LDPEs and the more LCB HDPEs clearly exhibited W-cusping along the outflow centre line. This is not captured by the Pompom constitutive model and is a failing of the model which is not dependent on parameterisation.

To investigate this further the FIB pictures taken at steady state were translated into a steady state extensional viscosity with the use of a SOC and the strain rate at the stagnation point calculated from simulations. To give confidence in the simulated strain rate the predicted strain rate was compared to LDV experiments for a HDB2 and 1840H. The Pompom model predicted the velocity along the inflow and outflow channel and showed the dependence of LCB on the transient development of the strain rate at the SP. Further LDV data is

needed to confirm the predicted strain rate obtained from simulations, for example HDB6 has similar LCB to HDB2 but shows W-cusps similar to 1840H. If the low branching priorities of HDB6 speed the flow up as predicted, this would imply the Pompom constitutive model accurately captures flow modifications in the cross-slot and that W-cusps are not the result of flow modification but result from the constitutive behaviour.

Steady state extensional viscosity curves were produced using CSER for each material. For the materials HDB2 and CM2 the extensional steady state had a higher viscosity than predicted from the SER data, even taking into account the difference between uniaxial and planar extension, suggesting that the SER experiments did not reach steady state before the sample ruptured. Therefore, using CSER and the SER in combination would give more accurate details on the extensional rheology of these two materials. For the materials exhibiting W-cusps the CSER steady state data is lower than the SER prediction. Since the cross-slot FIB pictures show the whole strain history of the experiment, it would suggest that there is a transient extensional overshoot from the maximum extensional viscosity to a lower steady state value.

In the next chapter, the W-cusp phenomena is discussed in detail and an empirical adjustment is made to the Pompom constitutive model so that it produces an overshoot in transient extension.

Chapter 6

Cross-slot Flow: an overshoot in extension

In the previous chapter the Pompom constitutive model was compared to experimental flow induced birefringence (FIB) and it was shown that the model failed to capture the experimentally observed W-cusps. Also, it was shown how the cross-slot FIB could be used as an extensional rheometry (CSER) by counting the FIB contours around the generated stagnation point. The data taken from the CSER showed a lower steady state than the maximum viscosity measured by the SER for the cases when W-cusps appear. Furthermore, FIB pictures show the whole strain history of the one flow rate, which supports the idea that the existence of a transient overshoot in extension causes the appearance of W-cusps.

In this chapter the W-cusp phenomena is examined in detail. Noting that W-cusps are a function of long chain branching (LCB) in a material, an extra empirical relaxation mechanism is considered in the context of the Pompom model with the aim to show that modelling a transient overshoot in extension will produce W-cusps in the principal stress difference (PSD) of cross-slot simulations. This extra relaxation mechanism has a characteristic time scale which will be explored for simple transient flows. This new model will have to satisfy both the transient development of shear and extensional experiments from chapter 2 and the steady state extensional data taken from the CSER.

We will examine whether this model is able to reproduce the W-cusps seen

in FIB experiments. Although the mechanism causing a transient extensional overshoot is not derived from molecular rheology it can still confirm that this is a flow characteristic that can explain W-cusps and provides a potential base line for new molecular rheological understanding to be introduced that will naturally give rise to this overshoot.

6.1 Introduction

In the last chapter it was shown that W-cusps formed for a variety of LCB polyethylenes and this correlated to the steady state extensional viscosity data produced from cross-slot FIB being lower than the maximum extensional viscosity that was measured with the SER stretching rheometer. Some of the experimental images were taken from Hassell et al. (2009), however the simulations are not those presented in this paper. The clear observation that W-cusps occur for the materials with the highest content of LCB, for example all the LDPEs in this study, shows that W-cusps are a function of branching. In another study, Soulages et al. (2008) produced cross-slot FIB images with a lubrication layer at the viewing windows producing a slip boundary condition. The FIB for a LDPE named 1810H, which is similar to the LDPE 1840H in this study, also exhibits the W-cusp phenomena in this 2D flow and this suggests that W-cusps are not a consequence of 3D flow effects.

To show further the effect of branching on the formation of W-cusps figure 6.1 examines the FIB and steady state extensional viscosity of the HDB series which has a well characterised synthesis and LCB [Inkson et al. (2006)]. For HDB1 and HDB2 with the lowest amount of LCB, the FIB shows a single cusp with the CSER steady state viscosity values above the SER measurements. As the content of LCB increases the CSER data becomes lower than the SER maximum with HDB4 exhibiting small W-cusps, while the more branched HDB6 shows even more pronounced W-cusps.

The FIB image along the inlet centre line of the cross-slot flow shows the strain history of the experiment. This indicates that the maximum stress occurs away from the outflow centre line so that the largest extensional stress occurs before a lower steady state value. For all the cross-slot Weissenberg numbers investigated,

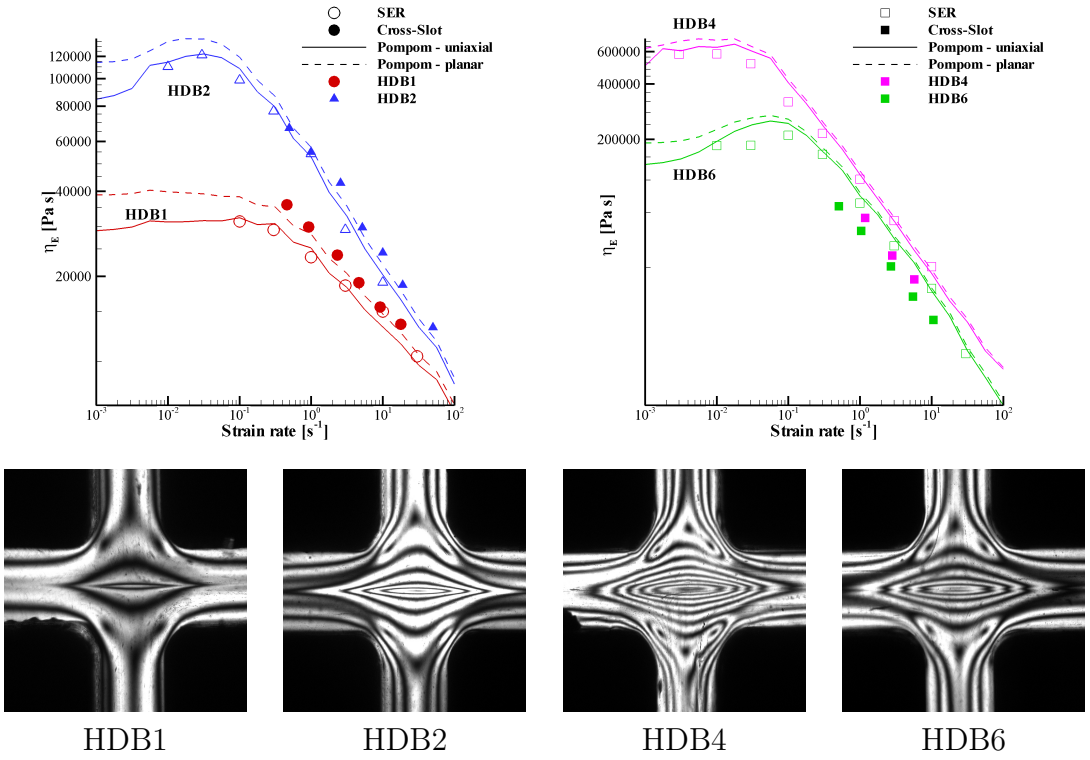

Figure 6.1: A comparison of the extensional rheology of the HDB series using SER and CSER data and FIB images taken at an initial strain rate of $1.74s^{-1}$. The comparison shows that W-cusps are a function of branching in a material as they only occur for the highly branched HDB4 and HDB6. Also, when W-cusps occur the steady state CSER data falls below cross-slot data indicating an extensional overshoot.

HDB4 and HDB6 exhibited W-cusps as they probe the strain hardening regime. An example of the variation in W-cusps with flow rate (shown as average velocity flux, defined in section 1.7), or Weissenberg number is shown in figure 6.2 for HDB6. The Weissenberg number is defined as $W_i = \dot{\varepsilon}_C \bar{\tau}_b$, where $\dot{\varepsilon}_C$ is the strain rate at the SP and $\bar{\tau}_b$ is the average relaxation time shown in table 6.1.

Similarly the FIB for all the experimentally available flow rates for the LDPEs, 1840H and Dow150R showed even sharper W-cusps than for the HDPEs. An example of this is shown in figure 6.3 where the FIB for Dow150R is shown for three flow rates. Due to the high concentration of cusps along the outflow centre line and the sharpness of the W-cusps, the W-cusps become harder to observe and

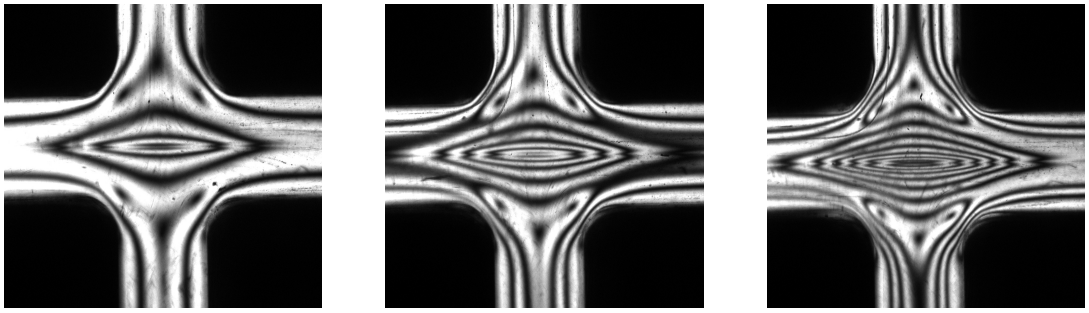

Figure 6.2: FIB images of HDB6 at three flow rates. All flow rates are in the non-linear strain hardening regime and W-cusps are exhibited for all experimental rates and the width and length of the W-cusps are similar for each flow rate.

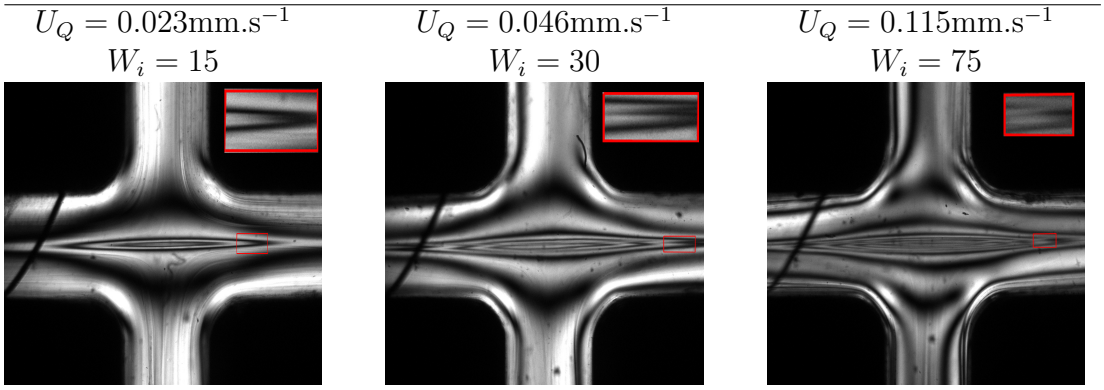

Figure 6.3: FIB images of Dow150R at three flow rates. All flow rates are in the non-linear strain hardening regime and W-cusps are exhibited for all experimental rates and the width and length of the W-cusps are similar for each flow rate.

the insets in each figure show a zoomed region to highlight the double cusping.

The LDPE 1800S provides a material with a larger content of LCB yet with a low enough viscosity to see the transition from a linear stress response to a non-linear strain hardening stress response. Figure 6.4 shows that this transition occurs at a Weissenberg number of 4.8 and the strain hardening regime coincides with W-cusps appearing along the outflow centre line.

Another phenomena associated with the observation of W-cusps is the dependence of temperature. This is illustrated for the material HDB2 in figure 6.5 where a transient W-cusps is observed at the temperature of $140°C$ for a velocity

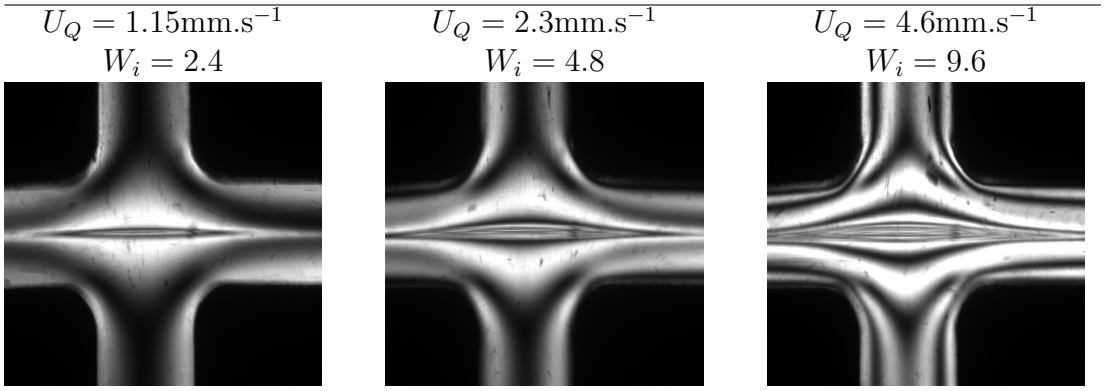

Figure 6.4: FIB images for 1800S at three flow rates. The lower viscosity of 1800S means the linear response is accessible with the cross-slot and as the flow rate increases W-cusps appear by the highest flow rate shown.

flux of $U_Q = 1.15\text{mm.s}^{-1}$, yet no W-cusps are observed at a temperature of $155°C$ ($W_i = 28$). The PSD pattern collapse that causes the vanishing of the W-cusp at steady state at $140°C$ ($W_i = 47.7$) is also seen for other LCB materials, for example HDB6 in figure 5.23. Although the number of branches will remain constant with temperature, the two relaxation times for the orientation and stretch will be shifted in equal amount, thus keeping their ratio constant. Shifting the Pompom parameters from $155°C$ to $140°C$ produces more pronounced strain hardening for a given flow rate as the relaxation times of each mode increases. This increases the Weissenberg number for the given flow rate and the resulting flow moves further into the non-linear regime.

As shown in section 5.5.1 there exists a cross-over behaviour in the steady state extensional viscosity for the LLDPE material CM3. At low and intermediate strain rates the CSER gives a higher steady state viscosity than the highest strain SER measurements, whereas at a strain rate of around $10s^{-1}$ the CSER data crosses over to predict a lower steady state value than the SER data. This coincides with the appearance of W-cusps at these higher strain rates, as shown in figure 6.6. This is the only material where both single and double cusps appear in the strain hardened regime. This suggests that there is some relaxation mechanism acting on a small enough time scale such that only large strain rates produce a sufficient Weissenberg number for the phenomena to become dominant.

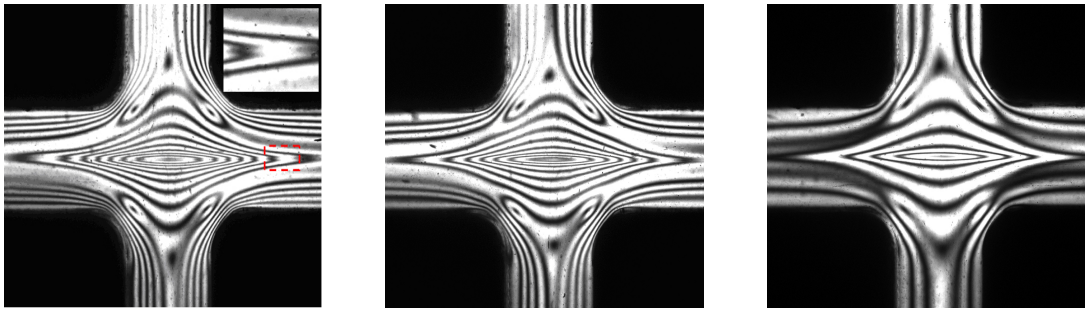

Figure 6.5: The effects of temperature on the appearance of W-cusps for HDB2 is shown at a flow rate of $U_Q = 1.15\text{mm.s}^{-1}$. At $140°C$ ($W_i = 47.7$) a transient W-cusp is found at early times which disappears as the PSD pattern collapses by steady state, whereas no W-cusps are found for HDB2 at $155°C$ ($W_i = 28$) for any flow rate.

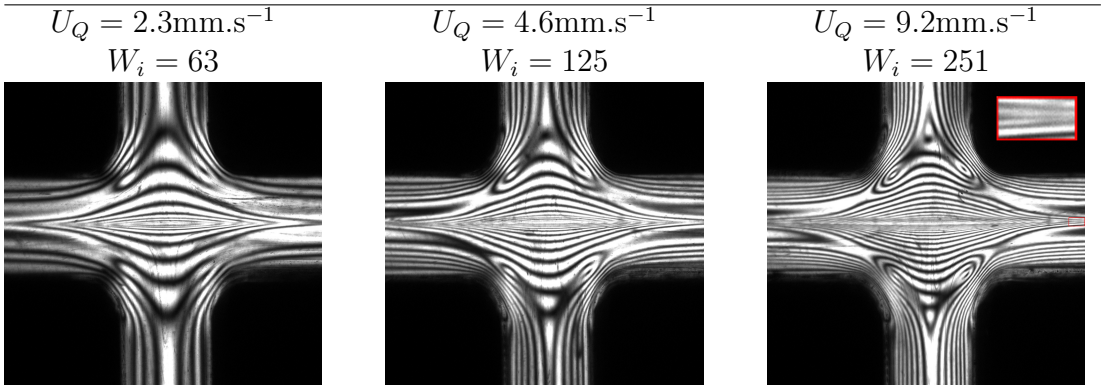

Figure 6.6: For the LLDPE CM3, the CSER and SER data cross-over at a strain rate of around $10s^{-1}$ and at a similar strain rate possible W-cusps appear in cross-slot flow. Here the transition between single and W-cusps occurs in the non-linear regime.

This series of observations provides an initial test for any constitutive model to correctly capture the rheology of W-cusps. As previously stated, the Pompom model as it stands fails to capture W-cusps for any of the materials and flow conditions mentioned. There is evidence to suggest that W-cusps are caused by a transient overshoot in extension since the FIB contours show the strain history of the material for each flow rate used. In the next section an empirical alteration to the Pompom model is introduced to produce a transient overshoot in uniaxial

extension and this model is then examined in 2D cross-slot flow.

6.2 Transient overshoot in extension

Evidence for the existence of a transient overshoot in extensional viscosity for branched polyethylenes was obtained by Bach et al. (2003). They performed uniaxial stretching experiments using a filament stretching device fitted with an active feedback device that adjusted the plate separation to give a constant extension rate at the centre of the sample. They are able to stretch to strains beyond the point at which the filament necks allowing Hencky strains of around six to be reached. For the case of a LDPE they found a transient overshoot in the extensional stress. In a subsequent paper Rasmussen et al. (2005) used the same apparatus to test two more LDPE samples. The authors show that both LDPE samples show a transient overshoot in extension for a range of extension rates and for one sample showed that an overshoot was present at two temperatures. Steady state extensional values were also able to be determined for some intermediate strain rates.

Nielsen et al. (2006) used this apparatus to study a melt of polystyrene Pompom molecules. The Pompom molecules have a narrow molar molar mass distribution and approximately $q = 2.5$ branches on each branch point. Using the previous method of measuring transient extension the authors show that there exists an overshoot in transient extension, however no steady state value was determined.

The molecular origin of this transient overshoot in extensional flow is not understood. By incorporating tube pressure into the integral molecular stretch function (MSF) constitutive model Rolon-Garrido and Wagner (2009); Wagner and Rolon-Garrido (2008) were able to fit the Pompom data in Nielsen et al. (2006). However, the existence of a tube pressure that occurs when the tubes are deformed is a controversial idea whose molecular origin is unclear. The Pompom data used did not reach steady state and so it could not be determined if the correct steady state was predicted by the model.

The Pompom constitutive model cannot produce a transient overshoot in extension. This is because once the tube segments align with the flow axis,

$\underline{\underline{K}} : \underline{\underline{S}} \simeq \dot{\varepsilon}$ and the stretch equation reduces to an autonomous first order ODE, so that λ cannot overshoot its steady state value. To produce an overshoot the Pompom model given by equations (1.6.52, 1.6.53, 1.6.54 (differential model), 1.6.48 and 1.6.49) requires an additional stretch relaxation process that depends upon $\underline{\underline{S}}$.

If this additional relaxation mechanism is driven by advection and not molecular relaxation then it must be proportional to the deformation rate of the backbone, hence the relaxation time should be of the form,

$$\frac{1}{\tau_*} = f(\underline{\underline{S}})|\underline{\underline{S}} : \underline{\underline{K}}|. \tag{6.2.1}$$

We propose that the relaxation occurs as a function of aligned backbone segments, with the measure of alignment being given by,

$$f(\underline{\underline{S}}) = C_R \left(\underline{\underline{S}} : \underline{\underline{S^T}}\right)^{\alpha}, \tag{6.2.2}$$

where the parameter α is used to define how aligned material should be to trigger this additional relaxation, typically $\alpha \gg 1$, so that the function f is very small except close to full alignment.

Finally, we introduce a second parameter, C_R, to control the contribution of this relaxation mechanism and this gives a new transient relaxation time of,

$$\frac{1}{\tau_*} = C_R \left(\underline{\underline{S}} : \underline{\underline{S^T}}\right)^{\alpha} |\underline{\underline{S}} : \underline{\underline{K}}|. \tag{6.2.3}$$

The additional relaxation time, τ_*, is added into the dynamic stretch equation in addition to the original entropic stretch relaxation time, τ_s, which gives,

$$\frac{D\lambda}{Dt} = \lambda \underline{\underline{S}} : \underline{\underline{K}} - \left(\frac{1}{\tau_s} + \frac{1}{\tau_*}\right)(\lambda - 1)\, e^{\nu^*(\lambda - 1)}, \tag{6.2.4}$$

where $\nu^* = \frac{2}{q-1}$.

Since τ_* is a function of $\underline{\underline{S}}$ it can cause a transient overshoot in extension through its own transient nature. The relaxation time becomes dominant for highly aligned tube segments, the measure of which is controlled by the parameter,

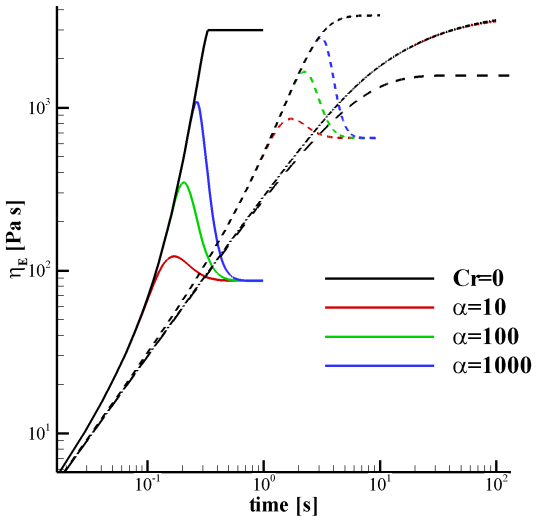

Figure 6.7: A one mode Pompom model, $\{G = 100\text{Pa}, \tau_b = 5\text{s}, q = 10, r = 4\}$, in uniaxial extension showing variations in the power law α from 10 to 1000 with $C_R = 2$. The strain rates used were $0.01s^{-1}$, $0.1s^{-1}$, $1s^{-1}$ and $10s^{-1}$. As α is increased so does the amount of alignment needed for the extra relaxation time, τ_*, to become dominant. This has the effect of delaying relaxation until a higher Hencky strain has been reached causing a bigger difference between the maximum and steady state extensional viscosity.

α. In an extensional flow the factor $\frac{1}{\tau_*}$ is small unless $S_{zz} \sim 1$ with other terms close to zero.

For small values of $\alpha \sim O(1)$, the stretch relaxation is gradual and causes no overshoot, just a lower steady state extensional viscosity. For larger values of $\alpha \sim O(100)$ this factor only becomes dominant for only very aligned material occurring at large strains, this is illustrated in figures 6.7 and 6.8. In figure 6.7 the extensional viscosity is shown for a one mode Pompom model for strain rates of 0.01, 0.1, 1 and 10 reciprocal seconds. The one mode parameters are $\{G = 100\text{Pa}, \tau_b = 5\text{s}, q = 10, r = 4\}$ and the different lines show various choices of the power α with a fixed value of $C_R = 2$. The figure shows that the steady state value of the overshoot Pompom (OPP) model does not depend on α, but the higher the value of α the more highly aligned $\underline{\underline{S}}$ must be to trigger the relaxation of τ^*. Hence, more strain hardening is experienced for higher values of the power, α.

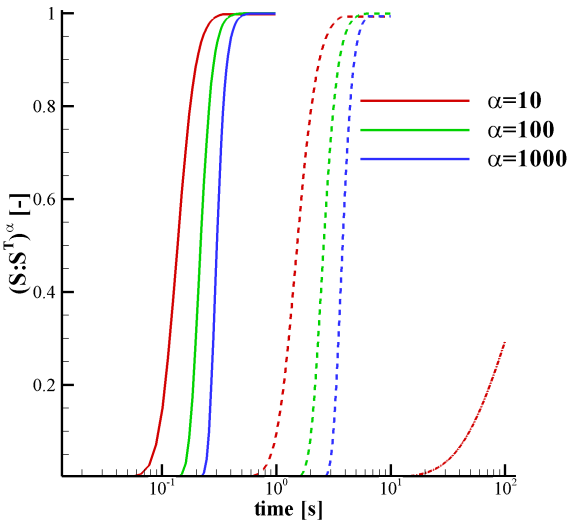

Figure 6.8: A plot of the measured alignment, $(S : S^T)^\alpha$, for the uniaxial extension shown in figure 6.7. As α is increased so does the strain taken for the measured alignment to approach unity and thus delays the transient overshoot.

Figure 6.8 shows the value of $(\underline{\underline{S}} : \underline{\underline{S}}^T)^\alpha$ for the same one mode Pompom model in uniaxial extension, seen in figure 6.7. Only the highest strain rates (1 and 10 reciprocal seconds) align enough material for τ_* to become non-trivial and for these two strain rates the various choices of α are shown. As before, the higher the value of α the longer it takes to orientate the material enough for this extra relaxation to contribute.

Since varying the power law does not alter the steady state the value of C_R can be used as an additional fitting parameter. Figure 6.9 shows the one mode Pompom model for various choices of C_R and a fixed power law, $\alpha = 100$. As the parameter C_R is increased so does the contribution of τ_* and the steady state value of extensional viscosity decreases. An important difference between variations in α and variations in C_R is the way in which each parameter affects how quickly the steady state is reached. For various choices of C_R [c.f. figure 6.9] there is little difference in the Hencky strain at which steady state is achieved (approximately a Hencky strain of 4.5). For the three choices of α in figures 6.7 and 6.8 the larger values of α reach steady state later than smaller values. This is because the larger

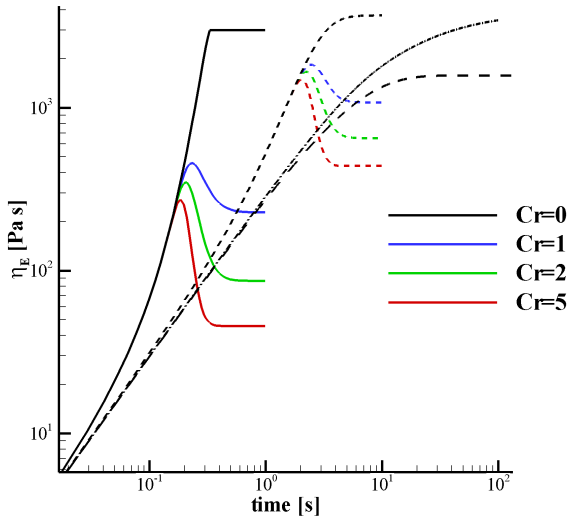

Figure 6.9: A one mode Pompom model, $\{G = 100\text{Pa}, \tau_b = 5\text{s}, q = 10, r = 4\}$, in uniaxial extension showing variations in the parameter C_R from 1 to 5 with $\alpha = 100$. The strain rates used were $0.01s^{-1}$, $0.1s^{-1}$, $1s^{-1}$ and $10s^{-1}$. The parameter C_R does not affect the strain needed to achieve an overshoot but it does affect the dominance of τ_* and thus determines the steady state extensional viscosity.

the choice of α, the more aligned the orientation must be before the overshoot relaxation becomes dominant. This in turn means that for larger values of α more strain hardening is experienced, making the difference between the maximum and steady state values of the extensional viscosity larger and delaying steady state. For the choices shown in figures 6.7 and 6.8, where $\alpha = 10, 100, 1000$ the Hencky strain at which steady state is observed is approximately $3, 4, 5$, respectively.

It is also important to consider the how the maximum stretch condition, $\lambda < q$, is affected by this additional term. Figure 6.10 shows a one mode Pompom model with $G = 100\text{Pa}$, $\tau_b = 10\text{s}$, $r = 4$ for choices of $q = 3$, 10, 20 and the overshoot parameters chosen were $\alpha = 1000$ and $C_R = 2$. In figure 6.7, the maximum stretch condition ($q = 10$) was only reached for $C_R = 0$. Lowering the value of the branching parameter to $q = 3$, means that the stretch reaches its maximum, but then relaxes back to a lower steady state value. The steady state is also lower for smaller values of q due to the effect of branch point withdrawal, i.e. that the

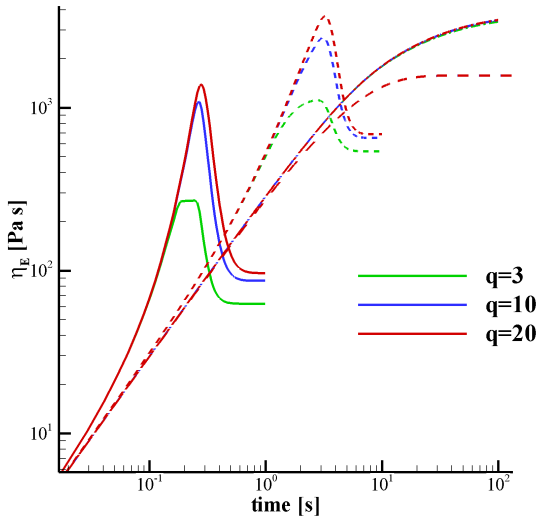

Figure 6.10: A one mode Pompom model, $\{G = 100\text{Pa}, \tau_b = 5\text{s}, r = 4\}$, in uniaxial extension showing variations in the branching priority, q, with $C_R = 2$ and $\alpha = 1000$. The strain rates used were $0.01s^{-1}$, $0.1s^{-1}$, $1s^{-1}$ and $10s^{-1}$. The figure shows how the branching priority effects the extensional viscosity in the case maximum stretch is reached ($q = 3$) and even when the maximum stretch is not reached ($q = 10$ and 20).

ν^* parameter contains a q dependence. This can be seen by comparing the cases of $q = 10$ and $q = 20$, where in both cases the maximum stretch condition is not achieved yet the steady state for $q = 10$ is lower than for $q = 20$. Thus although overshoot relaxation time, τ_* is not a function of the branching parameter, q, the branching priority still affects the steady state extensional viscosity. Since the overshoot relaxation time is a function of orientation alignment and not stretch, the relaxation becomes dominant at the same strain for each choice of branching priority, q.

In transient shear flow the extra stretch relaxation is negligible (as the orientation tensor $\underline{\underline{S}}$ does not become sufficiently aligned) and the stress response is left unchanged. However, in chapter 4 there were some discrepancies in the Pompom model at large strain amplitudes and this maybe due to inadequate modelling of stretch relaxation. It is evident that more detailed understanding of stress

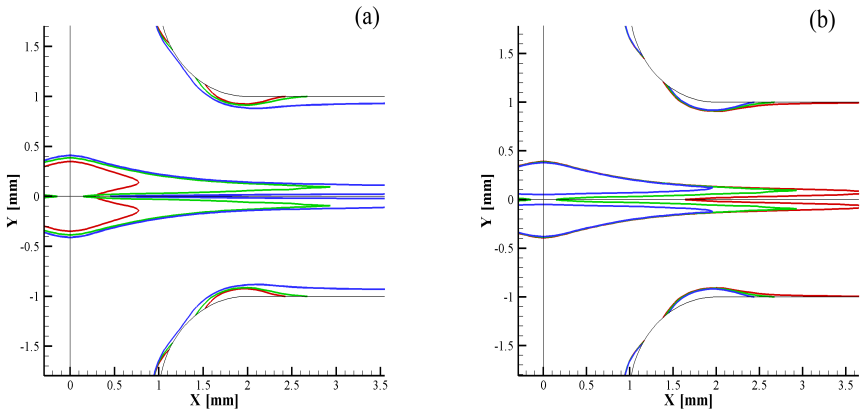

Figure 6.11: Figure a) shows the one mode Pompom model used in figure 6.7, examining how the power law α affects W-cusps in cross-slot flow. The red line shows $\alpha = 10$, the green line shows $\alpha = 100$ and the green line shows $\alpha = 1000$. Figure b) shows the one mode Pompom model used in figure 6.9, examining how the parameter C_R affects W-cusps in cross-slot flow. The red line shows $C_R = 5$, the green line shows $C_R = 2$ and the blue line shows $C_R = 1$.

relaxation is needed to fully capture all aspects of LCB melt rheology, however the model presented here is sufficient for exploring the presence of W-cusps in flow birefringence and their relationship to transient extensional flow.

In cross-slot flow the difference between the maximum extensional stress and the steady state value determines the size of the W-cusp and transient development of the extensional stress overshoot will determine the shape of the W-cusps. This is illustrated in figure 6.11 where in figure (a) the effect of varying the power law parameter on the shape of a PSD contour (of value 3kPa) for a fixed $C_R = 2$ is shown. A lower power law, $\alpha = 10$, strongly relaxes the stretch and the double cusps are shorter and wider than for a higher power law. This is analogous to the extensional viscosity shown in figure 6.7, where the lower power law relaxes faster producing the shorter cusp. The width of the W-cusps are a function of strain history. The lower power law relaxes the stretch faster than the higher power law and would exhibit a W-cusp at a lower Hencky strain and hence the W-cusps are wider.

Figure 6.11(b) shows the various choices of C_R previously shown in figure 6.9 for a fixed power law of $\alpha = 100$. Figure (b) shows one fixed PSD contour, the

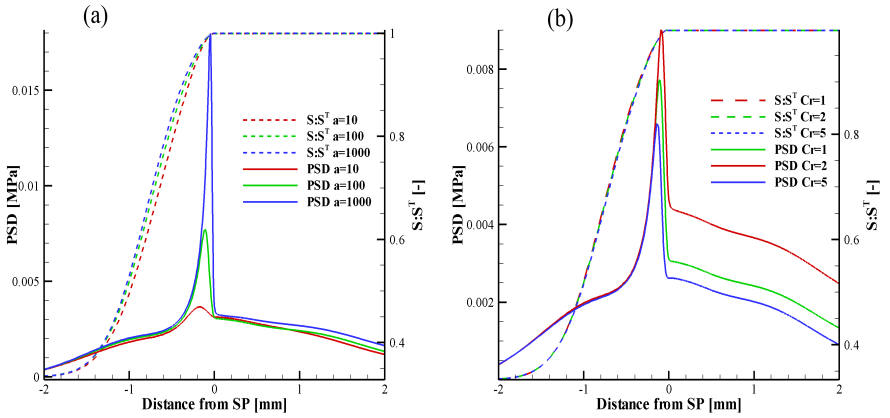

Figure 6.12: The stream line shown in figure 5.25 is plotted as a function of distance from the SP showing variations in (a) α and (b) C_R. Negative distance from the SP shows the PSD and $S : S^T$ along the centre of the inlet channel and positive distance shows the outlet channel.

same as in figure (a) of 0.3kPa. The contours are all the same width which is associated with α, however the length of the cusp is shorter for higher values of C_R where stronger stretch relaxation occurs. Unlike the case for variations in α, the parameter C_R affects both the maximum and steady state values of the extensional viscosity.

To quantify the behaviour of the OPP constitutive model figure 6.12 plots the PSD and $\underline{\underline{S}} : \underline{\underline{S}}^T$ along the stream line shown in figure 5.25 as a function of distance from the SP. In figure 6.12(a) the various choices in α from figure 6.7 are shown and figure (b) shows the choices of C_R used in figure 6.9. In figure 6.7 the value of α did not have any effect on the steady state value of the extensional viscosity, thus the differences at and downstream of the SP arise from flow modifications. The main differences in figure (a) occur in the inlet section of the stream line, upstream from the SP. Here the stress grows towards the SP and overshoots as a function of strain history, with the various power laws showing the same behaviour as in figure 6.7. The transient development of $\underline{\underline{S}} : \underline{\underline{S}}^T$ varies slightly with power law again due to flow modification.

In figure 6.12(b) the three choices of C_R have the same $\underline{\underline{S}} : \underline{\underline{S}}^T$ for all points on the stream line which shows that the power law α has the dominant effect on

flow development. The PSD is similar approaching the SP, but as the overshoot factor becomes dominant the choices of C_R affect the maximum and steady state values of the PSD in the same way as in the uniaxial stretching flow shown in figure 6.9. The smallest maximum and steady state is associated with the largest value of C_R since this provides the strongest stretch relaxation.

6.2.1 Multimode overshoot Pompom model

To parameterise the polyethylene samples in this study a multimode version of the OPP constitutive model is needed. As in chapter 2 the linear parameters $\{G_i, \tau_{b_i}\}$ are fitted to linear oscillatory data and in this section the same linear parameters as in previous sections are chosen, detailed in appendix 6.A. To simplify the fitting process the assumption is made that the overshoot parameters, $\{C_R, \alpha\}$, are the same for each mode. The Pompom non-linear parameters are fitted through trial and error using the original spectra detailed in section 2.A as a starting point. The Pompom parameters for each material modelled in this section can be found in section 6.A with the overshoot parameters used detailed in table 6.1.

The parameters in this modified model are chosen to fit both the transient extensional viscosity from the SER and the steady state measurements from the CSER. In addition for the LDPE Dow150R, experimental data is available up to Hencky strain of around 7. This data has been provided by Dr. Henrik Rasmussen and colleagues at the Technical University of Denmark, for which I would like to acknowledge their kindness and efforts in providing the data for this study. The extensional stress for Dow150R was measured using a filament stretching rheometer (FSR), the techniques of which are described in Bach et al. (2003); Rasmussen et al. (2005). The data for Dow150R from the FSR is shown in figure 6.13 for strain rates of 0.003s^{-1}, 0.01s^{-1}, 0.03s^{-1}, 0.1s^{-1} and 0.3s^{-1}. Overlayed with this data is the original SER data for Dow150R which shows excellent agreement between the two experiments for experimentally available strains. The maximum extensional viscosity measured by the FSR is higher than that achieved by the SER and for strain rates of 0.01s^{-1}, 0.03s^{-1} and 0.1s^{-1} there exist a transient overshoot in the measurements. Also shown are steady state values obtained from the CSER data, which are in reasonable agreement

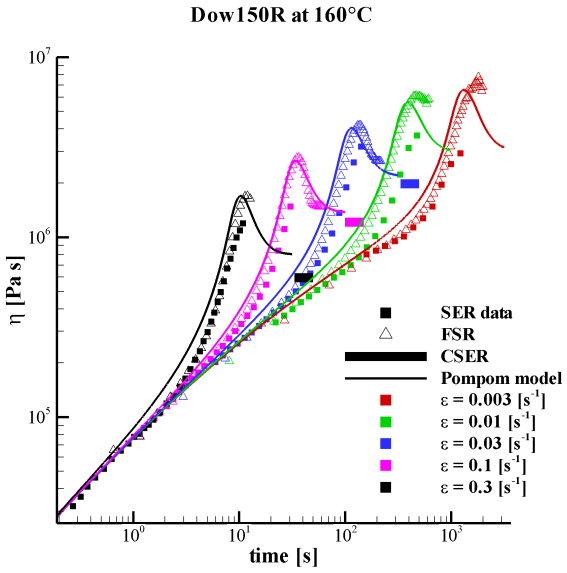

Figure 6.13: A plot comparing extensional data and OPP theory for Dow150R. Strain rates range from $0.003s^{-1}$ to $0.3s^{-1}$ and OPP parameters can be found in tables 6.1 and 6.2. The closed symbols show the SER data already considered in this work, the open symbols show new data from the FSR achieving higher Hencky strains than the SER and the blocks show the steady state predictions from CSER analysis. All three experiments agree closely and the OPP parameterisation matches the experiment very well.

for strain rates of $0.03s^{-1}$ and $0.1s^{-1}$, where the FSR measurements have reached or are near steady state.

The OPP constitutive model has been parameterised to fit the maximum extensional viscosity, as well as the steady state values for strain rates of $0.03s^{-1}$ and $0.1s^{-1}$. The OPP parameters chosen were $\alpha = 1000$ and $C_R = 0.8$. These values also capture the steady state predicted by the CSER for the strain rate $0.3s^{-1}$, where the transient data does not extend to the overshoot. The OPP parameterisation performs well except for the two slowest strain rates, where the maximum is lower than the experimental data. The parameterisation is optimized in the regime where cross-slot FIB picture are available to analyse the translation from simple uniaxial stretching to 2D cross-slot flow, and the discrepancies at the lower strain rates lie outside this regime.

For the other materials investigated in this chapter only SER and CSER data

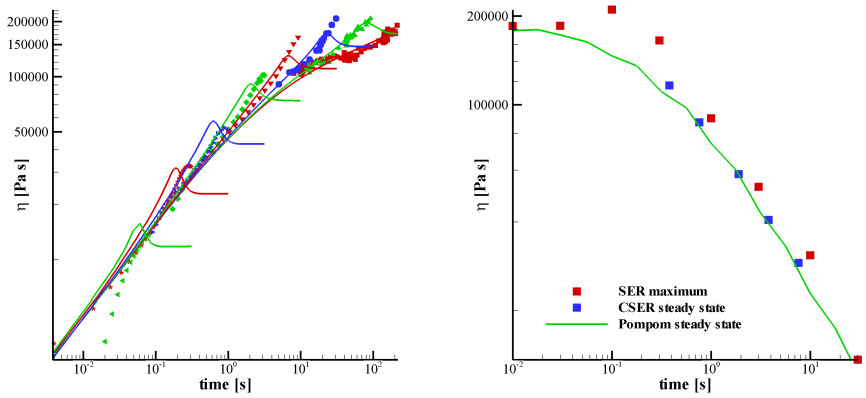

Figure 6.14: The extensional data from both the SER (left) and CSER (right) is shown for HDB6. The strain rates used range from $0.01s^{-1}$ to $30s^{-1}$. The lines show the fitted OPP parameterisation found in tables 6.1 and 6.3, with the model fitted to transient SER data and steady state CSER data.

is available. Therefore, to fit the OPP non linear parameters it is assumed that α is of the order 10^3, in agreement with the findings for Dow150R, and the parameter C_R is used to control the difference between the maximum transient value of the extensional viscosity and the steady state value. Each parameterisation is fitted to capture the transient startup flow from SER measurements and the steady state extensional viscosity from CSER analysis. Also the findings detailed in section 6.1 are used to capture the correct rheology of the transient extensional overshoot with the results of 2D cross-slot simulation discussed in the next section.

Figure 6.14 shows the comparison for HDB6 between the transient and steady state data and the predictions of the OPP spectrum given in table 6.3. A value of $\alpha = 1000$ was chosen and since cross-slot FIB pictures indicate W-cusps at all experimental rates a value of $C_R = 2$ was chosen so that there exists a transient overshoot for strain rates larger than $0.03s^{-1}$. There is a slight discrepancy between transient SER measurements and theory for strain rates of $0.1s^{-1}$ and $0.3s^{-1}$, but this will have little effect on the cross-slot analysis in the next section.

The cross-slot flow experiments on LDPE 1800S showed that W-cusps did not occur until strain rates of around $2s^{-1}$ at 140°C. The transient SER data was

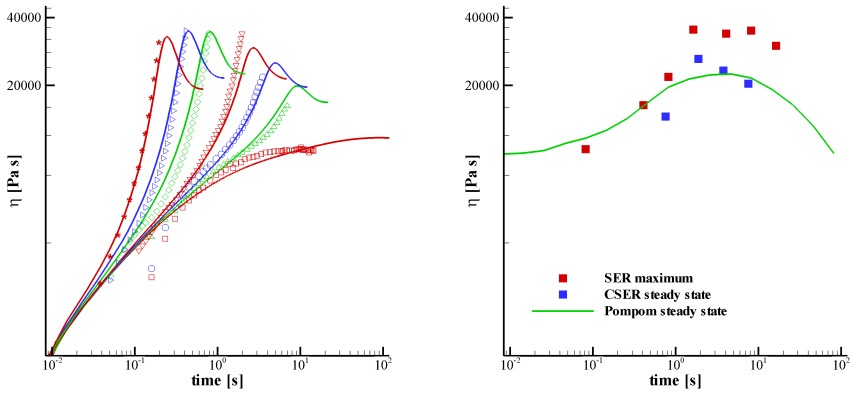

Figure 6.15: The extensional data from both the SER (left) and CSER (right) is shown for 1800S. The strain rates used range from $0.082s^{-1}$ to $24.6s^{-1}$. The lines show the fitted OPP parameterisation found in tables 6.1 and 6.2, with the model fitted to transient SER data and steady state CSER data.

measured at 155°C and then shifted using WLF theory as was previously done in chapter 2, producing shifted strain rates of $0.082s^{-1}$, $0.41s^{-1}$, $0.82s^{-1}$, $1.64s^{-1}$, $4.1s^{-1}$, $8.2s^{-1}$, $16.4s^{-1}$ and $24.6s^{-1}$, shown in figure 6.15. Again the power law, $\alpha = 1000$ and $C_R = 0.5$ is chosen to produce smaller overshoots in the stress response for strain rates less than $2s^{-1}$, with the high strain rates exhibiting a larger transient overshoot due to the strain rate dependence of τ_*.

The LLDPE CM3 exhibits strain hardening at similar flow rates to 1800S. However unlike 1800S, CM does not show W-cusps until the higher strain rate of $10s^{-1}$. This behaviour is captured using a small value of $C_R = 0.2$ and $\alpha = 1000$. In figure 6.16 this transition can be seen in the transient plot comparing theory to SER data, with a small overshoot occurring for strain rates higher than $1s^{-1}$. This produces the cross-over behaviour seen in the plot of the steady state extensional viscosity, where initially the CSER data is higher than SER data, but both theory and experimental data cross-over at a strain rate of $5s^{-1}$.

At 155°C the CSER steady state extensional viscosity measurements of the HDPE HDB2 are higher than the maximum value obtained from SER stretching experiments with only single cusps being observed for all available strain rates at 155°C. However, reducing the temperature from 155°C to 140°C produces a

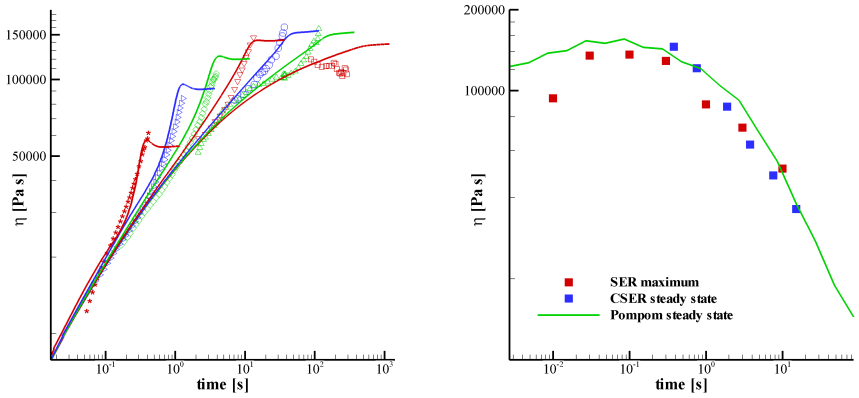

Figure 6.16: The extensional data from both the SER (left) and CSER (right) is shown for CM3. The strain rates used range from $0.01s^{-1}$ to $10s^{-1}$. The lines show the fitted OPP parameterisation found in tables 6.1 and 6.3, with the model fitted to transient SER data and steady state CSER data.

transient W-cusps at a strain rate of $1.7s^{-1}$. The transient nature of the W-cusps is a result of the relaxation of the PSD pattern with time, which is seen for all LCB materials in experiments [c.f. figure 5.23]. Since the W-cusp observed is not only transient but small in size it could be possible for a W-cusp to exist at 155°C, which is either too small to see or the PSD pattern relaxes to quickly for it to be visible. In figure 6.17 SER data is shown at 155°C and TTS shifted to 140°C using WLF theory [c.f. chapter 2]. This increases both relaxation times but the ratio of relaxation times and other non-linear parameters remain fixed.

Although the overshoot Pompom constitutive model is not fully described by molecular physics, it is still capable and flexible enough to capture a variety of rheologies in simple uniaxial extension. In the next section the OPP parameterisations discussed here are compared to FIB images to examine how overshoot rheology affects the PSD in cross-slot FIB.

6.3 Results

In this section we use the OPP constitutive model discussed in the last sections to calculate the stress distribution in cross-slot flow and compared it to the ex-

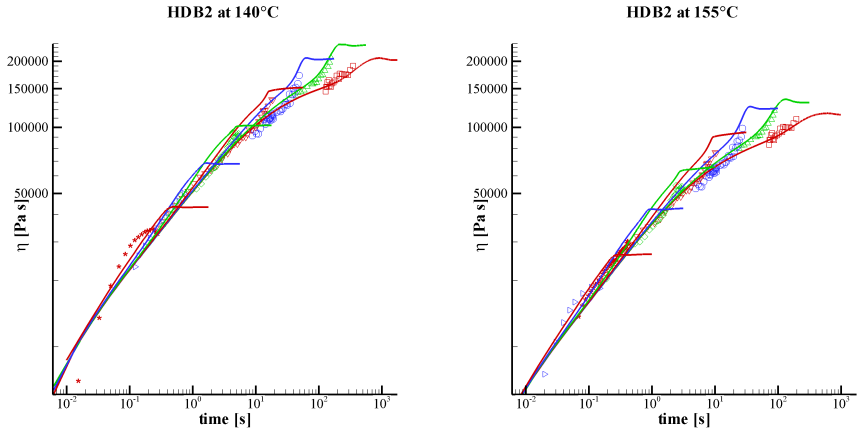

Figure 6.17: The OPP constitutive model is fitted to HDB2 at 140°C (left) and 155°C (right) on the same axis scale. The OPP parameters are given in tables 6.1 and 6.4 with only the linear parameters varying with temperature.

Table 6.1: A table showing the Pompom overshoot parameters used for fitting extensional data in figures 6.13 to 6.17. The parameters are the same for each mode in the multimode spectra given in tables 6.2 to 6.4 and are also chosen to be independent in temperature for HDB2.

material	temperature [°C]	C_R [-]	α [-]	$\bar{\tau}_b$ [s]
CM3	155°C	0.2	1000	18.0
HDB2	140°C	0.1	1000	27.4
HDB2	155°C	0.1	1000	14.8
HDB6	155°C	2.0	1000	28.0
1800S	140°C	0.5	1000	1.38
Dow150R	160°C	0.8	1000	428

perimental FIB images. All the simulations presented in this section were solved using the *euFlow* software. To resolve the W-cusping along the outflow centre line the horizontal mesh density was increased near the centre line. The solution was found to be independent on the a limit on $trace(\underline{\underline{A}})$ at a value of 10000. For all simulations in this section the PSD is shown as colour distribution and black contours of constant PSD representing the black FIB fringes. For clarity only the centre and downstream channel are shown so that the height of each image shows full cross-section of the outflow channel.

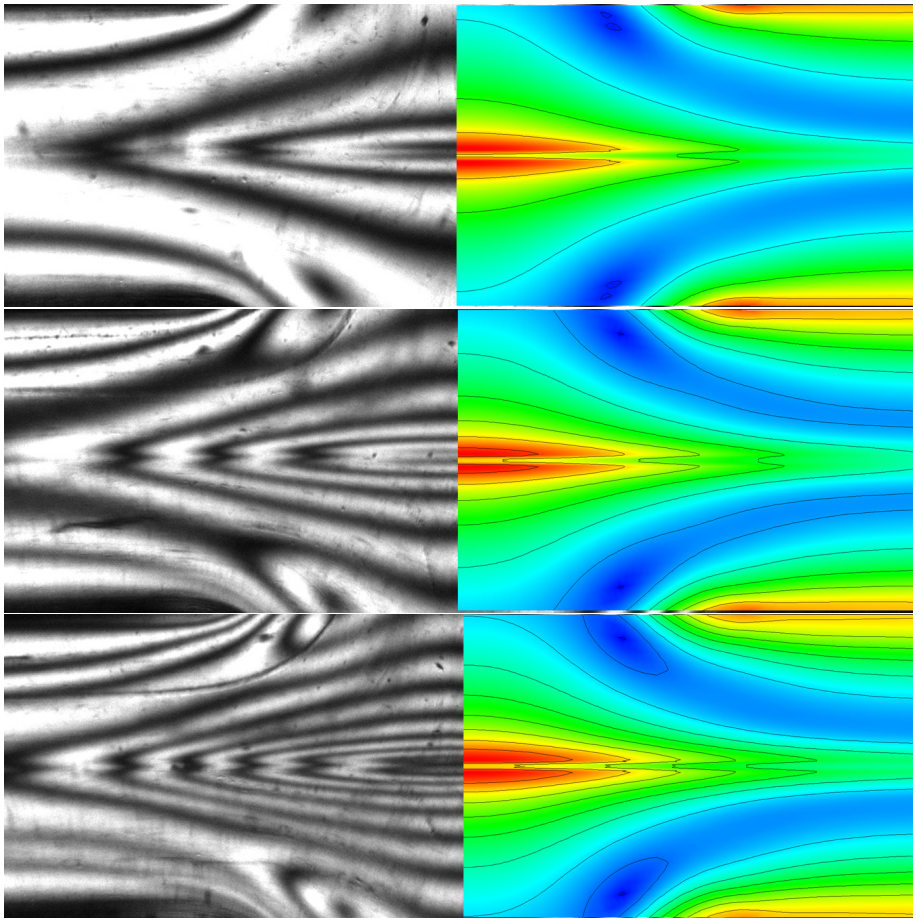

Figure 6.18: A comparison of between FIB in cross-slot flow and 2D simulations of the OPP parameterisation for HDPE HDB6. The OPP parameterisation is detailed in table 6.3 and shown in figure 6.14. The black lines in the simulations represent the black contours of the experimental PSD for initial strain rates of $\dot{\varepsilon}_C = 0.70\text{s}^{-1}$, $\dot{\varepsilon}_C = 1.74\text{s}^{-1}$ and $\dot{\varepsilon}_C = 3.48\text{s}^{-1}$ from top to bottom.

The HDPE named HDB6 shows the clearest FIB images of W-cusps. The simulation results for the OPP model are shown in figure 6.18 for three initial strain rates of $\dot{\varepsilon}_C = 0.70\text{s}^{-1}$, $\dot{\varepsilon}_C = 1.74\text{s}^{-1}$ and $\dot{\varepsilon}_C = 3.48\text{s}^{-1}$ giving Weissenberg numbers of 19.6, 48.7 and 97.4, from top to bottom. The OPP model captures the W-cusp rheology well, predicting both the form of the fringe pattern and the fringe number to within half a fringe for all three Weissenberg numbers, although the size of the W-cusps is over predicted near the SP. As with the original Pompom model the OPP model fails to capture the overall pattern collapse [c.f figure 5.23]

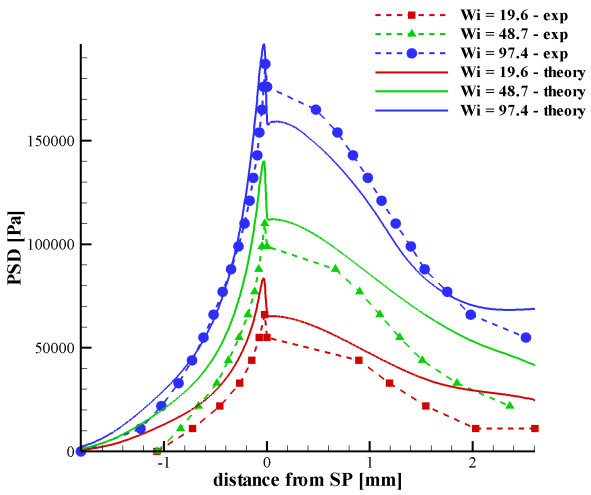

Figure 6.19: A comparison between the OPP simulations and the experimentally measured position of the FIB contours of constant PSD for HDB6 at three flow rates.

observed for all W-cusping materials and the transient development of the pattern is much faster in simulations than in experiments. In experiments the W-cusps initially occur at a strain of around 5, where as in simulations W-cusps first occur at a strain of 2.

The clarity of the experimental FIB images means that PSD measurements of the position of each fringe can be analysed across the SP stream line shown in figure 5.25, the results of which are shown in figure 6.19. The results shown in figure 6.19 confirm the visual agreement of the PSD contours. The simulations with Weissenberg numbers of 19.6 and 48.7 both over-predict the stress at all positions along the stream line, and for all Weissenberg numbers the size of PSD overshoot is over-predicted. Downstream of the SP the stress relaxation of the cusps is not predicted well. Visually this corresponds to simulations not predicting the appearance of the lower fringe orders away from the SP along the outflow centre line. This is a consequence of choosing the relaxation term to be proportional to $\underline{\underline{K}} : \underline{\underline{S}}$.

Figure 6.20 shows a similar comparison for the LDPE Dow150R comparing experimental FIB to OPP parameterisations at initial strain rates of $\dot{\varepsilon}_C = 0.035\text{s}^{-1}$, $\dot{\varepsilon}_C = 0.070\text{s}^{-1}$ and $\dot{\varepsilon}_C = 0.174\text{s}^{-1}$, corresponding to Weissenberg numbers of 15,

30 and 75, respectively. For the simulation at Weissenberg number 15 a steady state solution could not be reached. In figure 6.20 the solution is shown at a Hencky strain of 5.04 which shows the initial formation of the W-cusps at the SP only. For the other two simulations a steady state was reached and W-cusps can be observed along the whole outflow centre line. The W-cusps exhibited by Dow150R show bigger cusps than HDB6 which can be interpreted as a larger difference between the maximum extensional viscosity and the steady state value. The OPP parameterisation of Dow150R was fitted against uniaxial stretching data from the FSR which was able to measure strains of up to 7 and hence the transient extensional overshoot was modelled accurately. This is reflected in the excellent agreement between cross-slot simulations and experimental FIB with the PSD contours are accurately predicted in both number and position for all flow rates examined. Although, as with HDB6 the observed transient pattern collapse is not captured in simulations and the size of the W-cusps is slightly over predicted.

The key feature of the low viscous LCB material 1800S is the observed transition from single cusps to W-cusps associated with the transition from linear to non-linear extensional stress response. The cross-slot simulations of the OPP parameterisation discussed in the last section are compared to FIB images in figure 6.21, where as the initial strain rate is increased though $\dot{\varepsilon}_C = 1.74\text{s}^{-1}$, $\dot{\varepsilon}_C = 3.48\text{s}^{-1}$ to $\dot{\varepsilon}_C = 6.95\text{s}^{-1}$ (Weissenberg numbers of 2.4, 4.8 and 9.6, respectively). The size of the W-cusps increases and closely matches the shape and number of experimental PSD fringes. The experimental image for the largest flow rate is the poorest quality image but it seems that the OPP spectrum over predicts the number of fringes by 1-2 fringes, which is a result of the parameter values chosen.

The PSD patterns of HDB2 at two different temperatures highlighted the temperature dependence of the formation of W-cusps for the same initial strain rate of $\dot{\varepsilon}_C = 1.74\text{s}^{-1}$, giving a Weissenberg flow numbers of 47.7 at $140°C$ and 25.8 at $155°C$. Figure 6.22 shows a transient experimental W-cusp at 2.5s for a temperature of $140°C$ (top), which disappears by the steady state (middle). The bottom picture shows the flow at $155°C$ where no W-cusp can be seen for any solution time at any flow rate. The OPP simulations do show W-cusps at

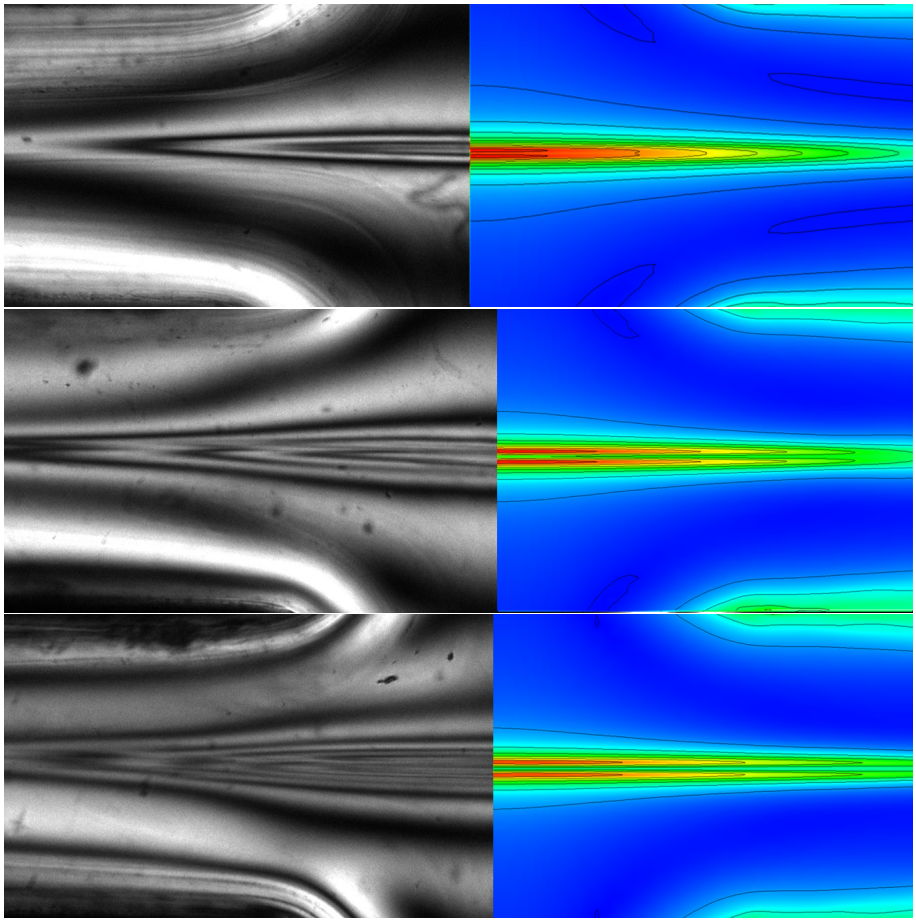

Figure 6.20: A comparison of between FIB in cross-slot flow and 2D simulations of the OPP parameterisation for LDPE Dow150R. The OPP parameterisation is detailed in table 6.2 and shown in figure 6.13. The black lines in the simulations represent the black contours of the experimental PSD for initial strain rates of $\dot{\varepsilon}_C = 0.035\text{s}^{-1}$, $\dot{\varepsilon}_C = 0.070\text{s}^{-1}$ and $\dot{\varepsilon}_C = 0.174\text{s}^{-1}$ from top to bottom.

both temperatures and the W-cusps are more pronounced at $140°C$ and so partly capturing the experimental findings. The PSD pattern does not show a collapse in the PSD pattern for the simulations at $140°C$. This finding is similar for all the W-cusping materials and is a flow feature not captured correctly by either the original Pompom model or the OPP model. HDB2 was parameterised to include a small transient overshoot, with $C_R = 0.1$ being the smallest of any material, and the resultant PSD contours have less pronounced cusping as a result. This is most evident at $140°C$ where the cross-over from single to double cusps causes

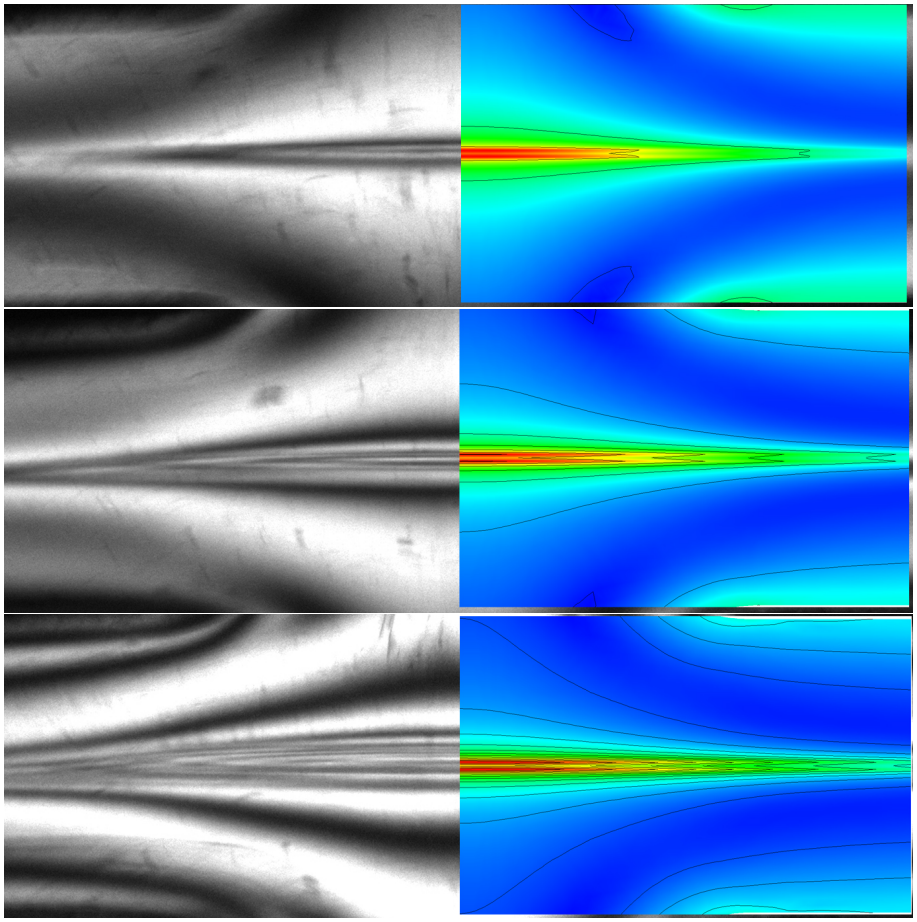

Figure 6.21: A comparison of between FIB in cross-slot flow and 2D simulations of the OPP parameterisation for LDPE 1800S. The OPP parameterisation is detailed in table 6.2 and shown in figure 6.15. The black lines in the simulations represent the black contours of the experimental PSD for initial strain rates of $\dot{\varepsilon}_C = 1.74\text{s}^{-1}$, $\dot{\varepsilon}_C = 3.48\text{s}^{-1}$ and $\dot{\varepsilon}_C = 6.95\text{s}^{-1}$ from top to bottom. The W-cusps increases in size with increasing flow rate as the strain rate increases as the flow becomes more non-linear.

the PSD contours to be much more rounded across the outflow centre line than experimental contours.

Flow modifications of the velocity gradients due to Pompom parameters especially near the SP, were modelled well by the original Pompom model and any other constitutive model should capture these developments. The OPP model was examined for each parameterisation in this chapter and the results were sim-

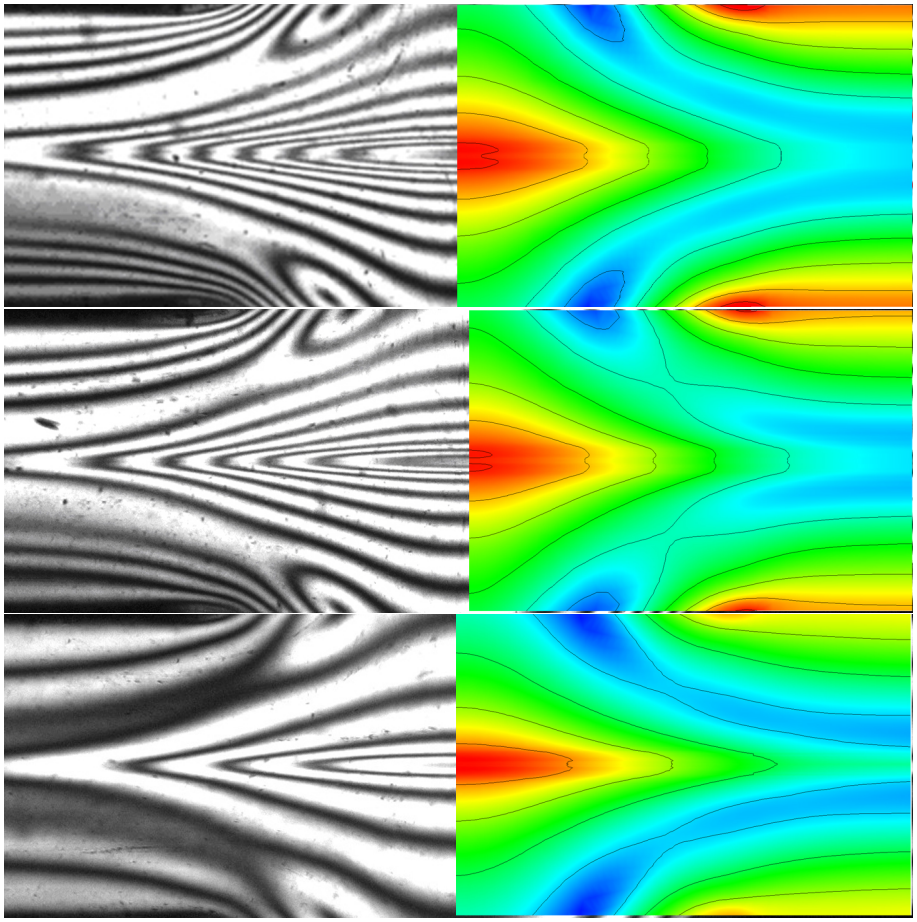

Figure 6.22: A comparison of between FIB in cross-slot flow and 2D simulations of the OPP parameterisation for HDPE HDB2. The OPP parameterisation is detailed in table 6.4 and shown in figure 6.17. The black lines in the simulations represent the black contours of the experimental PSD for initial strain rate of $\dot{\varepsilon}_C = 1.74\text{s}^{-1}$. The figure shows a transient experimental W-cusp at 2.5s for a temperature of $140°C$ (top), which disappears by the steady state (middle). The bottom picture shows the flow at $155°C$ where no experimental W-cusp can be seen for any solution time at any flow rate.

ilar to that of the original model, differing only due changes in parameterisation. An example of this is shown in figure 6.23 which is the only material in this section that LDV measurements were available. The figure shows that velocity along the SP stream line shown in figure 5.25 and compares the original Pompom model and the OPP model to experimental data and the initial Stokes prediction.

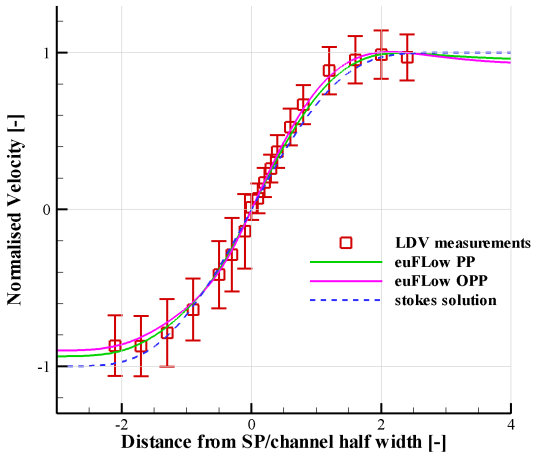

Figure 6.23: A comparison of LDV measurements of HDB2 compared with *euFlow* simulated results of both the original Pompom model and the OPP model.

The prediction of the OPP model is similar to the original model and predicts an increase in velocity along the outflow centre line near the SP and a decrease in the velocity downstream compared to the Stokes solution.

For the LLDPE CM3 the transition from single to double cusping occurs at strain rate of approximately 10s^{-1}, coinciding with an apparent cross-over from the CSER steady state data initially being higher than the SER maximum and then falling below the SER maximum at this strain rate. The comparison to experimental FIB images was made at initial strain rates of $\dot{\varepsilon}_C = 3.48\text{s}^{-1}$, $\dot{\varepsilon}_C = 6.95\text{s}^{-1}$ and $\dot{\varepsilon}_C = 13.9\text{s}^{-1}$, corresponding to Weissenberg number of 63, 125 and 251 from top to bottom in figure 6.24. The OPP model was parameterised to attempt to capture this result but figure 6.24 shows that the OPP model predicts W-cusps at all three experimental strain rates investigated. It appears to be difficult to capture this phenomena using one set of OPP parameters for all modes as each mode becomes highly aligned for all three strain rates.

Overall the OPP constitutive model exhibits W-cusps that are clearly dependent on the parameterisation used. Furthermore, fitting the OPP parameters to a combination of SER and CSER data gives W-cusps very similar to those observed in experimental FIB. We have not performed 3D simulations of the OPP

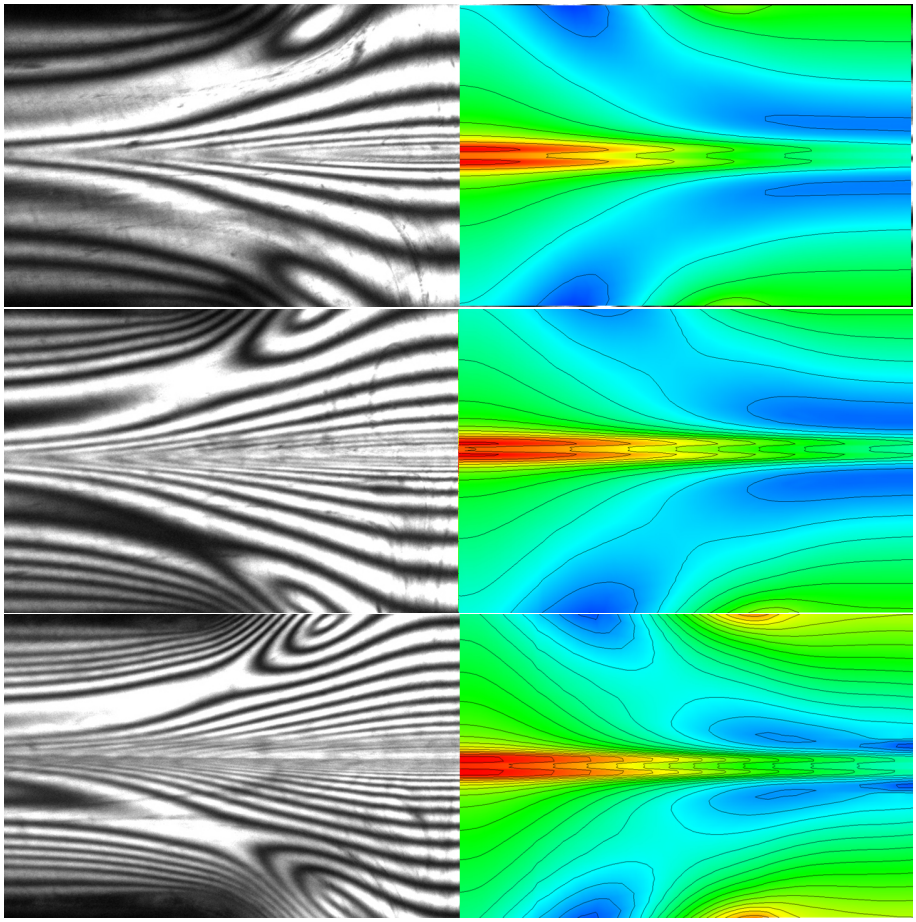

Figure 6.24: A comparison of between FIB in cross-slot flow and 2D simulations of the OPP parameterisation for LLDPE CM3. The OPP parameterisation is detailed in table 6.3 and shown in figure 6.16. The black lines in the simulations represent the black contours of the experimental PSD for initial strain rates of $\dot{\varepsilon}_C = 3.48\text{s}^{-1}$, $\dot{\varepsilon}_C = 6.95\text{s}^{-1}$ and $\dot{\varepsilon}_C = 13.9\text{s}^{-1}$ from top to bottom.

model in cross-slot flow. Although any differences from planar 2D melts are expected to be negligible based on the studies carried out in section 5.4.3 the full 3D birefringence could still have an effect on the size and width of W-cusps.

6.4 Conclusions

In chapter 5 the analysis of cross-slot FIB images predicted lower steady state extensional viscosity than the maximum value obtained from the transient SER

measurements. Also, for all the cases where this happened the experimental PSD contours showed W-cusps that the Pompom model could not predict. These findings are consistent with the observation of a transient extensional overshoot as reported by Hassager and coworkers for various LDPEs using a filaments stretching rheometer (FSR). Although the data from the FSR was only available for the LDPE named Dow150R it showed good agreement with SER and CSER data.

The Pompom constitutive model cannot produce a transient extensional overshoot due to the mathematical structure of the stretch equation. In this chapter the Pompom model was adapted to predict an overshoot. The modification is empirical and not based on an underlying relaxation mechanism. The aim being to see whether such a constitutive behaviour would reproduce the W-cusp phenomena.

An additional relaxation term was added to the stretch equation which was only dominant when molecules became highly aligned and provided a relaxation-rate proportional to the strain rate. The overshoot Pompom model (OPP) has two extra parameters to control the transient overshoot and steady state values. For simplicity these parameters are kept the same for each mode in a multimode sum. The OPP model successfully captured the rheology of Dow150R, where the transient extensional overshoot was observed using the FSR and was subsequently flexible enough to capture a variety of extensional rheologies for four other materials.

The OPP model was subsequently tested by comparing simulations to experimental FIB images from cross-slot flow. The model successfully predicts the appearance of W-cusps as a direct consequence of a transient extensional viscosity overshoot. Moreover, it is able to capture both the shape and values of the PSD contours for HDB6, Dow150R and 1800S. The OPP model still fails to capture the observed transient pattern collapse observed for W-cusping materials and as a result the size of the W-cusps is generally over estimated near the SP. The collapse was also not observed in the original Pompom model and the presence of the extra relaxation mechanism does not produce this collapse. This is most noticeable for HDB2 where at $140°C$ a W-cusp observed at 2.5s collapses to a single cusp at steady state. Despite the changes in the stress near the stagnation point the addition of the extra relaxation parameter has little effect on the predicted

flow modifications to the velocity gradient, and for HDB2 the simulation shows a similar good agreement with LDV measurements to the original Pompom model.

The OPP model does however fail to capture some of the downstream detail. This could be due to the form of the OPP relaxation term. For example if the flow is switched off, this extra relaxation factor vanishes instantly which is probably not physical. Although the OPP constitutive model can be successfully used to explore the consequences of a transient overshoot in extensional rheology, there is a need to refine this model and to obtain a molecular description of the physical processes causing this overshoot.

6.A Pompom overshoot parameters

This appendix provides a detailed list of all the Pompom parameter sets used in this chapter when modelling a transient overshoot in extensional flow.

	Dow150R, 160°C, 12 modes				1800S, 140°C, 12 modes			
Mode, i	$G_i[Pa]$	$\tau_{b,i}[s]$	$\tau_{b,i}/\tau_{s,i}$	q_i	$G_i[Pa]$	$\tau_{b,i}[s]$	$\tau_{b,i}/\tau_{s,i}$	q_i
1	64715.5	0.0040	-	1	42020.9	0.0050	-	1
2	45406.6	0.0129	-	1	9803.49	0.0100	-	1
3	23491.1	0.0415	-	1	7989.03	0.0200	-	1
4	19983.8	0.1341	-	1	5305.43	0.0398	-	1
5	12836.6	0.4329	4	7	3444.06	0.0794	2.2	12
6	8565.19	1.3978	4	9	2448.64	0.1585	2.2	14
7	5152.39	4.5138	4	11	1209.93	0.3162	2.2	15
8	2934.19	14.576	4	15	768.726	0.6310	2.2	16
9	1436.93	47.068	4	20	346.388	1.2589	2.2	17
10	635.072	151.99	3	23	99.1665	2.5119	2	18
11	176.198	490.81	2.2	40	36.4592	5.0119	2.1	23
12	45.9648	1584.9	1.5	70	18.9970	10.000	3	26

Table 6.2: A list of OPP parameters for materials 1800S and Dow150R used throughout this chapter. The transient extensional viscosity is fitted to SER data and the steady state is fitted to CSER data. For Dow150R, data was provided from Dr. Henrik Rasmussen using the method described in Bach et al. (2003). Overshoot parameters are detailed in table 6.1.

	HDB6, 155°C, 12 modes				CM3, 155°C, 12 modes			
Mode, i	$G_i[Pa]$	$\tau_{b,i}[s]$	$\tau_{b,i}/\tau_{s,i}$	q_i	$G_i[Pa]$	$\tau_{b,i}[s]$	$\tau_{b,i}/\tau_{s,i}$	q_i
1	219226	0.0009	-	1	197183	0.00631	-	1
2	179387	0.0028	-	1	49850.2	0.01954	-	1
3	37873.9	0.0093	-	1	30146.8	0.06051	-	1
4	32981.4	0.0306	-	1	17211.6	0.18738	-	1
5	18896.9	0.1009	-	1	6621.89	0.58028	-	1
6	11820.4	0.3333	-	1	3547.50	1.79699	-	1
7	6053.40	1.1009	7	2	1190.06	5.56486	6	8
8	2767.03	3.6361	7	2	383.948	17.2233	6	9
9	840.575	12.009	7	5	87.1977	53.3670	6	9
10	224.024	39.662	3	13	10.2032	165.265	4	12
11	26.7746	130.99	3	17	0.74761	511.789	4	20
12	1.94559	432.63	3	20	0.03567	1584.89	4	25

Table 6.3: A list of OPP parameters for materials HDB6 and CM3 used throughout this chapter. The transient extensional viscosity is fitted to SER data and the steady state is fitted to CSER data. Overshoot parameters are detailed in table 6.1.

	HDB2, 140°C, 12 modes				HDB2, 155°C, 12 modes			
Mode, i	$G_i[Pa]$	$\tau_{b,i}[s]$	$\tau_{b,i}/\tau_{s,i}$	q_i	$G_i[Pa]$	$\tau_{b,i}[s]$	$\tau_{b,i}/\tau_{s,i}$	q_i
1	430729	0.0025	-	1	416266	0.0010	-	1
2	91384.1	0.0072	-	1	145434	0.0028	-	1
3	83724.1	0.0204	-	1	99807.2	0.0081	-	1
4	32763.0	0.0580	-	1	44018.9	0.0231	-	1
5	12540.5	0.1653	-	1	17207.4	0.0658	-	1
6	8608.09	0.4707	-	1	9847.42	0.1874	-	1
7	3772.95	1.3405	-	1	5903.77	0.5337	-	1
8	2375.31	3.8178	10	2	2938.59	1.5199	10	2
9	874.985	10.873	15	3	1242.94	4.3288	15	3
10	30.3711	30.968	12	4	370.909	12.328	12	4
11	16.7271	88.197	10	6	79.9261	35.112	10	6
12	16.8162	251.19	1.5	8	24.9864	100.00	1.5	8

Table 6.4: A list of OPP parameters for materials HDB2 at 140°C and 155°C used throughout this chapter. The transient extensional viscosity is fitted to SER data and the steady state is fitted to CSER data. Overshoot parameters are detailed in table 6.1.

Chapter 7

Conclusions

7.1 Objectives

The subject of this thesis was to examine the rheology of long chain branched polymer melts. The Pompom constitutive model of McLeish and Larson (1998) which was subsequently developed by Blackwell et al. (2000); Inkson et al. (1999); Lee et al. (2001) was examined in a variety of flows.

The Pompom constitutive model, based on the idea of the Doi and Edwards tube model [Doi and Edwards (1986)], models the inter-molecular interactions in a polymer melt by replacing constraining entanglements with a topological tube of confinement. Molecular details such as the molecular weight of the arms and backbone as well as the number of Pompom arms then determine the governing relaxation dynamics. The relaxation of molecular section between branch points occurs via two distinct processes; a relaxation of the chain to its equilibrium length (stretch relaxation) and a slower relaxation of orientation through reptation.

My study of the Pompom model and LCB melt rheology comprises of two linked themes. First, for the Pompom model to be a reliable constitutive equation it must be able to predict the stress in a wide range of different flows with the same set of parameter values. To test the Pompom model I examine its performance against experimental data in three different flows. In particular, choosing appropriate parameter values for the Pompom model remains a challenge as some flows are more sensitive to the values of certain parameters. Second, since

in general the microstructure of a polymer melt is unknown is it possible to use experimentally determined values of the Pompom parameters to infer information on the polymer microstucture.

The overall goal would be to predict and hence synthesize the optimal polymer architecture for a given purpose, rather than investigating the suitability of an existing polymer.

7.2 Concluding remarks and future work

This thesis is focused on the multimode Pompom (mPP) constitutive model. Each Pompom mode has four parameters, $\{G_i, \tau_{b_i}, r_i, q_i\}$ and a multimode model requires many modes to captures the various time scales of a given rheology. In this work it was shown the 12 modes is sufficient for capturing the rheology of most materials. The Pompom parameters infer the molecular detail of a given polymer and so correctly parameterising the mPP model can be done to ascertain this detail. This relies on both the correct theoretical modelling of LCB polymers and experimental techniques being sensitive to the Pompom parameters.

To fit a mPP parameters experimental data is needed. Typically, the linear parameters, $\{G_i, \tau_{b_i}\}$, are fitted to the dynamic moduli and the non-linear parameters $\{r_i, q_i\}$ are fitted to transient extensional and shear data. Transient extensional data is the most sensitive to the non-linear parameters as the flow stretches the Pompom backbones and the finite limit on the stretch can be examined. Examinations of the mPP parameterisation for a given LCB polymer are limited both experimentally and theoretically. In stretching experiments the total strain achievable is often limited through sample rupture and as a result the steady state extensional flow is never established. Hence, any mPP parameterisation cannot be guaranteed to capture the correct extensional rheology of a material. From a theoretical viewpoint it was shown in chapter 2 that three different mPP spectra could be derived to give the same response in extensional flow. This demonstrates potential ambiguity when attempting to infer molecular detail for the parameter values.

In this work I looked for other flow types to help characterise the mPP model and this requires first checking the performance of the Pompom constitutive

model in each flow type. If a mPP spectra satisfies multiple experimental flow types then this indicates that the Pompom model is capable of capturing the full rheology of a material. In parameterising multiple flow types the space of compatible Pompom parameters is reduced, which reduces the ambiguity in any inferred molecular detail.

The first flow considered was a shear step-strain where a commonly observed experimental finding of polymer melts is that the relaxation modulus, $G(\gamma, t)$, is time-strain separable (TSS), i.e. that $G(\gamma, t) = G(t) \cdot h(\gamma)$, where $G(t)$ is the linear relaxation modulus and $h(\gamma)$ is a function of strain only, known as the damping function. Unlike some other constitutive models the Pompom model is not explicitly TSS. However, if a material is observed to shows TSS, the mPP spectrum for this materials should also.

It was shown in chapter 3 that Pompom spectra fitted to transient extensional and shear data did perform well in step strain, predicting experimentally observed TSS for a range of different polyethylenes. The HDPE named HDB6 was an exception, where TSS was observed experimentally the Pompom parameterisation deviated significantly from these findings.

To look at how a mPP parameterisation produces TSS I found the specific conditions required for the Pompom model to have exact TSS and thus produce a branched damping function. This was done by taking the continuous limit of $\{G, r, q\}$ as a function of orientation relaxation time, τ_b. With the conditions that for $G(\tau) \sim \tau^b$ and for constant non-linear parameters, $\{q, r\}$, the Pompom relaxation modulus is exactly TSS and as a consequence of this its relaxation modulus is factorisable. The Pompom spectra used closely approximate these conditions for exact TSS with HDB6 showing the biggest deviation. Furthermore, with parameters taken from the Pompom spectra the branched damping function showed excellent agreement with experimentally predicted damping data.

The study into shear flow is continued with the study of oscillatory shear, in particular how the stress response is affected in large amplitude oscillatory shear (LAOS). The stress response can be accurately quantified with the use of Fourier transform rheology (FTR) and much attention is focused on the third Fourier components as they are strongly dependent on the non-linear Pompom parameters.

An initial investigation into a one mode Pompom model highlighted that the absolute value of the third harmonic is strongly dependent on the relaxation ratio, r, and only weakly dependent on the branching priority, q. Furthermore, the low-strain asymptote of the third Fourier coefficient is independent of the branching priority, and so provides a unique method for examining and parameterising the stretch relaxation times, τ_{s_i}. This technique also avoids experimentally difficult large strain amplitudes.

The low strain asymptote can be used test the non-linear predictions of the branch-on-branch (BoB) rheology. This theory models reaction chemistry and produces a very detailed polymer architecture that is mapped onto a multimode Pompom spectrum that can have thousands of modes. Solving so many modes would be computationally difficult but comparisons of data at low strain is possible through asymptotic solutions. Although data is only available for three frequencies, the asymptotes give a very accurate prediction of the low strain stress response of the absolute third harmonic. This is a good indicator that the BoB spectra capture the correct rheology in non-linear SAOS and that accurate information can be inferred about the molecular structure of each material studied.

In the regime of non-linear strain amplitude, where the Fourier components deviate from this asymptote, the Pompom spectra fitted to extensional data predicted this deviation well. The spectra could be distinguished relative to branching structure when looking at the relative magnitude of the third harmonic. However, when looking at the individual components deviations appeared, where the mPP did not match the experimental measurements. Investigations into the Pompom model reveal that this is not dependent on the choice of Pompom parameters leading to the conclusion that the Pompom model fails at large strain amplitude.

In studying LAOS the low strain asymptotes were ideal for examining the dense mode spectrum produced by the BoB algorithm. However, the specific experimental measurements at low strain amplitude are still required to examine the higher Fourier coefficients as a function of frequency. Further more, this study focused on the third Fourier coefficients and potentially extra information could be learned by examining the higher Fourier coefficients for both the low strain asymptotes and in LAOS itself.

A general conclusion from shear flow is that Pompom parameterisations fitted to extensional data perform well in shear. However, the converse is not true as shear flow is relatively insensitive to the branching priority, compared to extensional flow that stretches molecules in the same direction as the flow gradient. To examine the branching structure of the Pompom model the remainder of this thesis looked at stagnation point (SP) flow in a cross-slot geometry. The SP causes the molecules to become highly stretched along the outflow centre line. This closed geometry flow does not suffer from the same instabilities occurring in free surface stretching experiments. This means that much higher total strains are achievable compared to the SER stretching rheometer, In addition by examining the flow induced birefringence (FIB) along the inlet centre line the transient growth for a given flow rate can be determined.

For polyethylenes with moderate levels of branching the Pompom model accurately predicts the flow birefringence pattern, which has a maximum value of PSD at the stagnation point. For fluids with short relaxation times so that $W_i \ll 1$ (for example the LLDPE called CM1) the pattern has four fold symmetry seen for a Newtonian flow. As relaxation times increase, this symmetry is lost and a cusped diamond pattern is produced. Increasing the flow rate and hence the Weissenberg number, produces an increasing amount of contours with high stresses along the outlet centre line. However, for polyethylene with significant proportion of LCB content this single cusp pattern gives way to doubly cusping principal stress difference (PSD) contours along the outflow centre line. This phenomenon is not reproduced by the mPP model. Although flow modifications can cause the contributions from individual modes to have a W-cusp, the total PSD remains single cusped. To investigate the rheology of the cross-slot experiments the FIB pictures, showing contours of constant PSD were interpreted as steady state extensional viscosity curves. The steady state data is dependent on accurate determination of the stress-optical coefficient (SOC) and the strain rate at the SP, along with the assumption that 3D flow effects are negligible. The initial study into the Pompom equations in cross-slot flow show that 3D effects could be neglected for this geometry and 2D simulations would provide an accurate comparison. It was then subsequently shown that flow modifications are strongly dependent on the Pompom backbone stretch, λ, and in particular variations of

the strain rate at the SP are strongly dependent on whether or not the maximum stretch conditions is reached. This implied that to correctly model flow modifications the LCB structure of a material needs to have accurately determined mPP parameters.

Using the simulated strain rate steady state extensional viscosity curves were compared to the maximum extensional viscosity achieved using the SER. For all materials with a significant LCB content the cross-slot extensional rheology (CSER) data was lower than the maximum viscosity recored with the SER and this trend coincided with the observation of W-cusps in the FIB images. Conversely for linear polymers or lightly branched materials the CSER predicted higher steady state values than the SER, where the lack of strain hardening would enhance surface flow instabilities and in these cases only single cusping appeared along the outflow centre line. The conclusion of this study is that W-cusps are consequence of a transient extensional overshoot, which has been reported in literature using other extensional rheometers [e.g. Bach et al. (2003); Rasmussen et al. (2005)]. The Pompom model as it stands cannot produce this transient extensional overshoot and hence cannot produce W-cusps.

An empirical relaxation rate was added to the ODE for the backbone stretch to produce a transient extensional overshoot by relaxing the backbone stretch when material becomes highly aligned. The OPP model can successfully capture various overshoot rheologies and these results translate into W-cusps in 2D cross-slot simulations. To ascertain the correct extensional rheology further measurements from other extensional stretching rheometers should be used to fully clarify the relation between uniaxial extension and cross-slot flow. It should also be noted that full 3D FIB is still necessary to check for differences from 2D simulations, these were not possible with the current *euFlow* software. Also more experimental data from LDV measurements would be needed to clarify the accuracy of the mPP predictions of flow modifications.

The OPP constitutive model does have limitations. Since the extra stretch relaxation is an empirical term it cannot be used to infer molecular architecture or physical relaxation. The extra relaxation term is proportional to the velocity gradient and so when the flow is stopped it would vanish instantly. In shear the extra relaxation term does not make a significant contribution. In LAOS

deviations from experimental data were found at strain amplitudes of order unity and perhaps this could be accounted for with a full molecular description of the same physical process causing the transient extensional overshoot.

Although the molecular rheological process that causes a transient extensional overshoot is not yet understood, the extensional rheology that materials exhibit in both stretching experiments and cross-slot SP flow has been successfully characterised. Furthermore, various experimental techniques in both LAOS and CSER have been identified that infer key molecular detail and provide a basis for any new molecular physics being modelled.

References

A. Abedijaberi, J. Soulages, M. Kröger, and B. Khomami. Flow of branched polymer melts in a lubricated cross-slot channel: a combined computational and experimental study. *Rheologica Acta*, 48:97–108, 2009. 175

J. Aho, V. H. Rolon-Garrido, S. Syrjala, and M. H. Wagner. Measurement technique and data analysis of extensional viscosity for polymer melts by Sentmanat extensional rheometer (SER). *Rheologica Acta*, 49(4):359–370, APR 2010a. 63

J. Aho, V. H. Rolon-Garrido, S. Syrjala, and M. H. Wagner. Extensional viscosity in uniaxial extension and contraction flow - Comparison of experimental methods and application of the molecular stress function model. *Journal of Non-Newtonian Fluid Mechanics*, 165(5-6):212–218, MAR 2010b. 63

L. A. Archer, Y. L. Chen, and R. G. Larson. Delayed slip after step strains in highly entangled polystyrene solutions. *Journal of Rheology*, 39(3):519–525, 1995. 93

D. Auhl, S. Kunamaneni, C. W Seay, C. D. McGrady, D. G. Baird, and T. C. B. McLeish. Rheological and film-casting properties of well-characterised polyethylenes with different branching structure. *AIP Conference Proceedings*, 1027:12–14, 2008. 5

R. M. A. Azzam. Propagation of partially polarized light though anisotropic media with or without depolarization: A differential 4x4 matrix calculus. *Journal of Optical Society of America*, 68(12):1756–1767, 1978. 170, 171

A. Bach, H. K. Rasmussen, and O. Hassager. Extensional viscosity for polymer

melts measured in the filament stretching rheometer. *Journal of Rheology*, 47 (2):429–441, 2003. xxxv, 195, 208, 216, 231, 238

R. C. Ball and T. C. B. McLeish. Dynamic dilution and the viscosity of star polymer melts. *Macromolecules*, 22:1911–1913, 1989. 32, 34

B. E. Bernstein, A. Kearsley, and L. J. Zapas. A study of stress relaxation with finite strain. *Trans. Soc. Rheol*, 7:391–410, 1963. 73

G. C. Berry and T. G. Fox. The viscosity of polymers and their concentrated solutions. *Advances in polymer science*, 5:261–357, 1968. 28

D. K. Bick and T. C. B. McLeish. Topological contributions to nonlinear elasticity in branched polymers. *Phys Rev Letters*, 76(14):2587–2590, 1996. 36

R. B. Bird, R. C. Armstrong, and O. Hassager. *Dynamics of Polymeric Liquids - Volume 1; Fluid Mechanics*. John Wiley and Sons, New York, 1977a. 21, 22

R. B. Bird, C. F. Curtiss, R. C. Armstrong, and O. Hassager. *Dynamics of Polymeric Liquids - Volume 2; Kinetic Theory*. John Wiley and Sons, New York, 1977b. 21, 22

G. Bishko, T. C. B. McLeish, O. G. Harlen, and R. G. Larson. Theoretical molecular rheology of branched polymers in simple and complex flows: The Pompom model. *Phys Rev Letters*, 79(12):2352–2355, 1997. 43

G. B. Bishko, O. G. Harlen, T. C. B. McLeish, and T. M. Nicholson. Numerical simulation of the transient flow of branched polymer melts through a planar contraction using the Pompom model. *Journal of Non-Newtonian Fluid Mechanics*, 82(2–3):255–273, 1999. 43

R. J. Blackwell, O. G. Harlen, and T. C. B. McLeish. Molecular drag-strain coupling in branched polymer melts. *Journal of Rheology*, 44(1):121–136, 2000. xxxiv, 34, 35, 36, 37, 39, 41, 42, 73, 78, 79, 82, 233

A. C. B. Bogaerds, W. M. H. Verbeeten, G. W. M. Peters, and F. P. T. Baaijens. 3D viscoelastic analysis of a polymer solution in a complex flow. *Computer methods in applied mechanics and engineering*, 180:413–430, 1999. 175

R. L. Burden and J. D. Faires. *Numerical Recipes*. Thomson Learning, Pacific Grove, CA, USA, 2001. 112

M. D. Chilcott and J. M. Rallison. Creeping flow of dilute polymer solutions past cylinders and spheres. *Journal of Non-Newtonian Fluid Mechanics*, 29: 381–432, 1988. 22

C. D. Chodankar, J. D. Schieber, and D. C. Venerus. Evaluation of rheological constitutive equations for branched polymers in step shear strain flows. *Rheologica Acta*, 42:123–131, 2003. 73, 91

A. W. Chow and G. G. Fuller. Response of moderately concentrated Xantham gum solutions to time-dependent flows using two colour flow birefringence. *Journal of Rheology*, 28(1):23–43, 1984. 153

N. Clemeur, R. P. G. Rutgers, and B. Debbaut. On the evaluation of some differential formulations for the Pompom constitutive model. *Rheologica Acta*, 42:217–231, 2003. 40, 41, 110, 111, 167, 168

N. Clemeur, R. P. G. Rutgers, and B. Debbaut. Numerical simulation of abrupt contraction flows using the double convected Pompom model. *Journal of Non-Newtonian Fluid Mechanics*, 117:193–209, 2004a. 40, 168

N. Clemeur, R. P. G. Rutgers, and B. Debbaut. Numerical evaluation of three dimensional effects in planar flow birefringence. *Journal of Non-Newtonian Fluid Mechanics*, 123:105–120, 2004b. 41, 151, 170, 171

R. H. Colby and M. Rubenstein. Two-parameter scaling for polymers in theta solvents. *Macromolecules*, 23(10):2753–2757, 1990. 34, 35

R. H. Colby, L. J. Fetters, and W. W. Graessley. Melt viscosity-molecular weight relationship for linear polymers. *Macromolecules*, 20:2226–2237, 1987. 28

M. W. Collis and M. R. Mackley. The melt processing of monodisperse and polydisperse polystyrene melts within a slit entry and exit flow. *Journal of Non-Newtonian Fluid Mechanics*, 128(1):29–41, 2005. 152

S Costeux, P Wood-Adams, and D Beigzadeh. Molecular structure of metallocene-catalyzed polyethylene: Rheologically relevant representation of branching architecture in single catalyst and blended systems. *Macromolecules*, 35(7):2514–2528, 2002. 52

K. D. Coventry. *Cross-Slot Rheology of Polymers. PhD Thesis*. Department of Chemical Engineering, University of Cambridge, 2006. 150, 175, 177, 180, 190

K. D. Coventry and M. R. Mackley. Cross-slot extensional flow birefringence observations of polymer melts using a multi-pass rheometer. *Journal of Rheology*, 52(2):401–415, 2008. 150, 152, 174, 177

B. J. Crosby, M. Mangnus, W. de Groot, R. Daniels, and T. C. B. McLeish. Characterization of long chain branching: Dilution rheology of industrial polyethylenes. *Journal of Rheology*, 46(2):401–426, 2002. xxxiii, 53

D. G. Crowley, F. C. Frank, M. R. Mackley, and R. G. Stephenson. Localised flow birefringence of polyethylene oxide solutions in a four roll mill. *Journal of Polymer Science, part B - Polymer physics*, 14(6):1111–1119, 1976. 149

C. Das. The branch-on-branch code. In *Computational Branch-on-Branch Rheology*, 2010. URL `http://sourceforge.net/projects/bobrheology-rheology`. 139

C. Das, N. J. Inkson, D. J. Read, and K. Kelmanson. Computational linear rheology of general branch-on-branch polymers. *Journal of Rhology*, 50(2): 207–234, 2006. xxxiii, 3, 52, 53, 139

A. R. Davies and R. S. Anderssen. Sampling localization and duality algorithms in practice. *Journal of Non-Newtonian Fluid Mechanics*, 79:235–253, 1998. 55

P. G. de Gennes. Reptation of a polymer chain in the presence of fixed obstacles. *Journal of Chemical Physics*, 55(2):572–579, 1971. 28, 29

B. Debbaut and H. Burhin. Large amplitude oscillatory shear and fourier-transform rheology for a high-density polyethylene: Experiments and numerical simulation. *Journal of Rheology*, 46(5):1155–1176, 2002. 109

J. den Doelder, R. Koopmans, M. Dees, and M. Mangnus. Pressure oscillations and periodic extrudate distortions of long-chain branched polyolefins. *Journal of Rheology*, 49(1):113–126, 2005. xxxiii, 53

M. Doi. Explanation of the 3.4 power law of viscosity of polymeric liquids on the basis of the tube model. *Journal of Polymer Science, part B; Polymer physics*, 21(5):667–684, 1983. 28

M. Doi. *Introduction to Polymer Physics*. Clarendon Press, Oxford, 1995. 21

M. Doi and S. F. Edwards. *The Theory of Polymer Dynamics*. Oxford Science Publications, Oxford, 1986. 21, 22, 27, 28, 31, 32, 35, 36, 47, 233

S. F. Edwards. A field theoretic formalism for the entanglements of a polymer network. *Computational and theoretical polymer science*, 8(2):247–252, 1998. 28

R. H. Ewolt and G. H. McKinley. On secondary loops in LAOS via self-intersection of Lissajous Bandwidth curves. *Rheologica Acta*, 49:213–219, 2010. 114

R. H. Ewolt, A. E. Hosoi, and G. H. McKinley. New measures for characterizing nonlinear viscoelasticity in large amplitude oscillatory shear. *Journal of Rheology*, 52(6):1427–1458, 2008. 114

J. D. Ferry. *Viscoelastic properties of polymers*. John Wiley and Sons inc, New York, 1961. 52, 54

G. Fleury, G. Schlatter, and R. Muller. Non-linear rheology for long chain branching characterization, comparison of two methodologies: Fourier transform rheology and relaxation. *Rheologica Acta*, 44:174–187, 2004. 56, 74, 109

F. C. Frank and M. R. Mackley. Localized flow birefringence of polyethylene oxide solutions in a two roll mill. *Journal of Polymer Science A2*, 14:1121–1131, 1976. 149

G. G. Fuller. *Optical Rheometry of Complex Fluids*. Oxford University Press, New York, 1995. 170

C. Gabriel, J. Kaschta, and H. Münstedt. Influence of molecular structure on rheological properties of polyethylenes. *Rheologica Acta*, 37:7–20, 1998. 106

R. S. Graham, T. C. B. McLeish, and O. G. Harlen. Using the Pompom equations to analyze melts in exponential shear. *Journal of Rheology*, 45(1):275–290, 2001. 107

R. S. Graham, A. E. Likhtman, T. C. B. McLeish, and S. Milner. Microscopic theory of linear, entangled polymer chains under rapid deformation including chain stretch and convective constraint release. *Journal of Rheology*, 47(5): 1171–1200, 2003. 32, 37, 121, 136

R. S. Graham, J. Bent, N. Clarke, L. R. Hutchings, R. W. Richards, T. Gough, D. M. Hoyle, O. G. Harlen, I. Grillo, D. Auhl, and T. C. B. McLeish. The long-chain dynamics in a model homopolymer blend under strong flow: small angle neuron scattering and theory. *Soft Matter*, 5:2383–2389, 2009. 6

O. G. Harlen, E. J. Hinch, and J. M. Rallison. Birefringent pipes: the steady flow of a dilute polymer solution near a stagnation point. *Journal of Non-Newtonian Fluid Mechanics*, 44:229–265, 1992. 150

O. G. Harlen, J. M. Rallison, and P. Szabo. A split Lagrangian-Eulerian method for simulating transient viscoelastic flows. *Journal of Non-Newtonian Fluid Mechanics*, 60:81–104, 1995. 43

D. G. Hassell and M. R. Mackley. Localised flow induced crystallisation of a polyethylene melt. *Rheologica Acta*, 47(4):435–446, 2008. 150

D. G. Hassell and M. R. Mackley. An experimental evaluation of the behaviour of mono and polydisperse polystyrenes in cross-slot flow. *Rheologica Acta*, 48: 543–550, 2009. 186

D. G. Hassell, D. Hoyle, D. Auhl, O. Harlen, M. R. Mackley, and T. C. B. McLeish. Effect of branching in cross-slot flow: the formation of W cusps. *Rheologica Acta*, 48:551–561, 2009. 39, 42, 150, 165, 174, 177, 186, 203

D.G. Hassell, D. Auhl, T. C. B. McLeish, O. G. Harlen, and M .R. Mackley. The effect of viscoelasticity on stress fields within polyethylene melt flow for a cross-slot and contraction-expansion slit geometry. *Rheologica Acta*, 47:821–834, 2008. xxxiii, xxxiv, 53, 55, 63, 66, 71, 150, 152, 175, 185, 186, 190, 198

R. R. Huilgol and N. Phan-Thien. *Fluid Mechanics and Viscoelasticity*. Elsevier Science, Amsterdam, 1997. 21

K. Hyun and M. Wilhelm. Establishing a new mechanical nonlinear coefficient Q from FT-Rheology: First investigation of entangled linear and comb polymer model system. *Macromolecules*, 42(1):411–422, 2009. 111

K. Hyun, K. H. Ahn, S. J. Lee, M. Sugimoto, and K. Koyama. Degree of branching of polypropylene measured from Fourier-transform rheology. *Rheologica Acta*, 46:123–129, 2006. 110

K. Hyun, E. S. Baik, K. H. Ahn, S. J. Lee, M. Sugimoto, and K. Koyama. Fourier-transform rheology under medium amplitude oscillatory shear for linear and branched polymer melts. *Journal of Rheology*, 51(6):1319–1342, 2007. 109, 110

N. J. Inkson, T. C. B. McLeish, O. G. Harlen, and D. J. Grove. Predicting low density polyethylene melt rheology in elongational and shear flows with Pompom constitutive equations. *Journal of Rheology*, 43(4):873–896, 1999. xxxiv, 36, 41, 57, 58, 78, 79, 106, 107, 192, 233

N. J. Inkson, C. Das, and D. J. Read. Monte carlo simulation for the structure of polyolefins made with two metallocene catalysts in a batch reactor. *Macromolecules*, 39:4920–4931, 2006. 1, 139, 203

H. Janeschitz-Kriegl. *Polymer Melt Rheology and Flow Birefringence*. Springer, Berlin, 1983. 149, 153

A. Keller, A. J. Müller, and J. A. Odell. Entanglements in semi-dilute solutions as revealed by elongational flow studies. *Progress in Colloid and Polymer Science*, 75:179–200, 1987. 150

T. Kotaka, A. Kojima, and M. Okamoto. Elongational flow opto-rheometry for polymer melts. 1. construction of an elongational flow opto-rheometer and some preliminary results. *Rheologica Acta*, 36:646–656, 1997. 153

K. Koyama and O. Ishizuka. Birefringence of polyethylene melt in transient elongational flow at constant strain rate. *Journal of Polymer Science: Part B: Polymer Physics*, 27:297–306, 1989. 153, 154

R. G. Larson. Constitutive relationships for polymeric materials with power-law distributions of relaxation times. *Rheologica Acta*, 24:327–334, 1985a. 73

R. G. Larson. Flows of constant stretch history for polymeric materials with power-law distributions of relaxation times. *Rheologica Acta*, 24:443–449, 1985b. 73

H. M. Laun. Prediction of elastic strains of polymer melts in shear and elongation. *Journal of Rheology*, 30(3):459–501, 1986. xxxiv, 79, 192

H. M. Laun and H. Schuch. Transient elongational viscosities and drawability of polymer melts. *Journal of Rheology*, 33(1):119–175, 1989. 192

H. M. Laun and M. Münstedt. Elongational behaviour of a low density polyethylene melt. *Rheologica Acta*, 17:415–425, 1978. 192

K. Lee, M. R. Mackley, T. C. B. McLeish, T. M. Nicholson, and O. G. Harlen. Experimental observation and numerical simulation of transient stress fangs within flowing molten polyethylene. *Journal of Rheology*, 45(6):1261–1277, 2001. 36, 38, 39, 41, 75, 233

X. Li, S. Q. Wang, and X. Wang. Nonlinearity in large amplitude oscillatory shear (LAOS) of different viscoelastic materials. *Journal of Rheology*, 53(5): 1255–1274, 2009. 114

A. E. Likhtman and T. C. B. McLeish. Quantitative theory for linear dynamics of linear entangled polymers. *Macromolecules*, 35:6332–6343, 2002. 136

D. J. Lohse, S. T. Milner, L. J. Fetters, M. Xenidou, N. Hadjichristidis, R. A. Mendelson, C. A. Garcia-Franco, and M. K. Lyon. Well-defined, model long

chain branched polyethylene. 2. melt rheological behavior. *Macromolecules*, 35: 3066–3075, 2002. 107

C. Luap, M. Karlina, T. Schweizer, and D. C. Venerus. Limit of validity of the stress-optical rule from polystyrene melts: influence of polydispersity. *Journal of Non-Newtonian Fluid Mechanics*, 138(2-3):197–203, 2006. 153

M. R. Mackley, R. T. J. Marshall, and J. B. A. F. Smeulders. The multipass rheometer. *Journal of Rheology*, 39(6):1293–1309, 1995. 152

C. W. Macosko. *Rheology, principles, measurements and applications*. Wiley-VCH, New York, 1994. 153, 190

W. C. MacSporran and R. P. Spiers. The dynamic performance of the Weissenberg rheogoniometer III. large amplitude oscillatory shearing - harmonic analysis. *Rheologica Acta*, 23:90–96, 1984. 109

A. Malmberg, C. Gabriel, T. Steffl, H. Münstedt, and B. Löfgren. Long-chain branching in metallocene-catalyzed polyethylenes investigated by low oscillatory shear and uniaxial extensional rheometry. *Macromolecules*, 35:1038–1048, 2002. 55, 56, 106, 107

G. H. McKinley and O. Hassager. The Considére condition and rapid stretching of linear and branched polymer melts. *Journal of Rheology*, 43(5):1195–1212, 1999. 75

G. H. McKinley and T. Sridhar. Filament-stretching rheometry of complex fluids. *Annual Review of Fluid Mechanics*, 34:375–415, 2002. 61

T. C. B. McLeish. Tube theory of entangled polymers. *Advances in Physics*, 51: 1379–1527, 2002. xi, 23, 29, 37, 39, 41, 73, 79

T. C. B. McLeish and R. G. Larson. Molecular constitutive equations for a class of branched polymers: The Pompom polymer. *Journal of Rheology*, 42(1): 81–110, 1998. 33, 36, 37, 39, 41, 73, 233

T. C. B. McLeish and S. T. Milner. Entangled dynamics and melt flow of branched polymers. *Advances in Physics*, 143:195–256, 1999.

T. C. B. McLeish, J. Allgaier, D. K. Bick, G. Bishko, P. Biswas, R. Blackwell, B. Blottiere, N. Clarke, B. Gibbs, D. J. Groves, A. Hakiki, R. K. Heenan, J. M. Johnson, R. Kant, D. J. Read, and R. N. Young. Dynamics of entangled H-polymers: Theory, rheology and neutron scattering. *Macromolecules*, 32: 6734–6758, 1999. 34, 72, 78

S. T. Milner and T. C. B. McLeish. Parameter-free theory for stress relaxation in star polymer melts. *Macromolecules*, 30:2159–2166, 1997. 34

S. T. Milner and T. C. B. McLeish. Reptation and contour-length fluctuations in melts of linear polymers. *Physical Review Letters*, 81(3):725–728, 1998. 31

W. Minoshima and J. L. White. Instability phenomena in tubular film and melt spinning of rheologically characterised high density, low density and linear low density polyethylenes. *Journal of Non-Newtonian Fluid Mechanics*, 19:275–302, 1986a. 63

W. Minoshima and J. L. White. A comparative experimental study of the isothermal shear and elongational rheological properties of low density, high density and linear low density polyethylenes. *Journal of Non-Newtonian Fluid Mechanics*, 29:251–274, 1986b. 63

A. J. Müller, J. A. Odell, and A. Keller. Elongational flow and rheology of monodisperse polymers in solution. *Journal of Non-Newtonian Fluid Mechanics*, 30:99–118, 1988. 150

H. Münstedt and D. Auhl. Rheological measuring techniques and their relevance for the molecular characterization of polymers. *Journal of Non-Newtonian Fluid Mechanics*, 128:62–69, 2005. 53

H. Münstedt, S. Kurzbeck, and L. Egersdörfer. Influence of molecular structure on rheological properties of polyethylenes. *Rheologica Acta*, 37:21–29, 1998. 106

J. K. Nielsen, H. K. Rasmussen, M. Denberg, K. Almdal, and O. Hassager. Nonlinear branch-point dynamics of multiarm polystyrene. *Macromolecules*, 39 (25):8844–8853, DEC 12 2006. 208

T. Neidhöfer, M. Wilhelm, and B. Debbaut. Fourier-transform rheology experiments and finite-element simulations on linear polystyrene solutions. *Journal of Rheology*, 47(6):1351–1371, 2003. 109, 126, 127

K. Osaki. On the damping function of shear relaxation modulus of entangled polymers. *Rheologica Acta*, 32:429–437, 1993. 91

A. J. Peacock. *Handbook of Polyethylene*. Marcel Dekker Inc., 2000. 3, 49

Petro-Polymers. World LDPE market. WebSite, 2009. URL `http://www.petropolymers.com/a392560-world-ldpe-market-to-reach-about.cfm`. 2

N. Phan-Thien. *Understanding Viscoelasticity, Basics of Rheology*. Springer-Verlag, Berlin, 2002. 21

W. H. Press, S. A. Teukolsky, W. T. Vetterling, B. P. Flannery, and M. Metcalf (Foreword). *Numerical Recipes in FORTRAN 90*. Cambridge University Press, UK, 1996. URL `http://www.nrbook.com`. 112

J. M. Rallison and E. J. Hinch. Do we understand the physics in the constitutive equations. *Journal of Non-Newtonian Fluid Mechanics*, 29:37–55, 1988. 22

J. Ramirez and A. E. Likhtman. Reptate: Rheology of entangled polymers, toolkit for analysis of theory and experiment. ***http://www.reptate.com***, 2007. 18, 53, 92

H. K. Rasmussen, J. K. Nielson, A. Bach, and O. Hassager. Viscosity overshoot in the start-up of uniaxial elongation of low density polyethylene melts. *Journal of Rheology*, 49(2):369–381, 2005. 195, 208, 216, 238

D. J. Read, C. Das, M. Kapnistos, D. Auhl, D. Doelder, I. Vittorias, and T. C. B. McLeish. From reactor to rheology in ldpe modeling. In *XVTH INTERNATIONAL CONGRESS ON RHEOLOGY - THE SOCIETY OF RHEOLOGY 80TH ANNUAL MEETING, PTS 1 AND 2*, volume 1027 of *AIP CONFERENCE PROCEEDINGS*, pages 424–426, 2008. 139

V. H. Rolon-Garrido and M. H. Wagner. The damping function in rheology. *Rheoloigca Acta*, 48(3):245–284, APR 2009. 208

P. E. Rouse. A theory of linear viscoelastic properties of dilute polymer solutions of coiling polymers. *Journal of Chemical Physics*, 21(7):1272–1280, 1953. 25

M. Rubinstein and R. H. Colby. *Polymer Physics*. Oxford University Press, Oxford, 2003. 21, 50

P. Rubio and M. H. Wagner. LDPE melt rheology and the Pompom model. *Journal of Non-Newtonian Fluid Mechanics*, 92:245–295, 2000. 73, 78

G. Schlatter, G. Fleury, and R. Muller. Fourier transform rheology of branched polyethylene: Experiments and models for assessing the macromolecular architecture. *Macromolecules*, 38:6492–6503, 2005. 55, 56, 109, 110

J. F. M. Schoonen, F. H. M Swartjes, G. W. M. Peters, F. P. T. Baaijens, and H. E. H Meijer. A 3D numerical/experimental study on a stagnation flow of a polyisobutylene solution. *Journal of Non-Newtonian Fluid Mechanics*, 79 (2-3):529–561, 1998. 151

O. Scrivener, C. Bernera, R. Cressely, R. Hocquart, R. Sellin, and N. S Vlachos. Dynamical behaviour of drag-reducing polymer solutions. *Journal of Non-Newtonian Fluid Mechanics*, 5:475–495, 1979. 149

M. L. Sentmanat. Miniature universal testing platform: from extensional melt rheology to solid-state deformation behavior. *Rheologica Acta*, 43(6):657–669, 2004. 52, 106

I. Sirakov, A. Ainser, M. Haouche, and J. Guillet. Three-dimensional numerical simulation of viscoelastic contraction flows using the Pompom differential constitutive model. *Journal of Non-Newtonian Fluid Mechanics*, 126:163–173, 2005. 151

J. Soulages, T. Schweizer, D.C. Venerus abd J. Hostettler, F. Mettler, M. Kröger, and H.C. Öttinger. Lubricated optical rheometer for the study of two-dimensional complex flows of polymer melts. *Journal of Non-Newtonian Fluid Mechanics*, 150:43–55, 2008. 150, 203

J. Stadler, D. Auhl, and H. Münstedt. Influence of molecular structure of polyolefins on the damping function in shear. *Macromolecules*, 41:3720–3726, 2008. 92

S. K. Sukumaran and A. E. Likhtman. Modeling entangled dynamics: Comparison between stochastic single-chain and multichain models. *Macromolecules*, 42(12):4300–4309, 2009. 29

G. I. Taylor. The formation of emulsions in definable fields of flow. *Proceedings of the Royal Society of London*, A146:501–523, 1934. 149

R. Tenchev, O. G. Harlen, P. K. Jimack, and M. K. Walkley. *Finite Element Modelling of Two- and Three-Dimensional Viscoelastic Polymer Flows*. Saxe-Coburg Publications, UK, 2008. 43

H. C. Öttinger. Thermodynamic admissibility of the Pompom model for branched polymers. *Rheologica Acta*, 40:317–321, 2001. 41, 74

H. Tobita. Simultaneous long-chain branching and random scission: I. Monte carlo simulation. *Journal of Polymer Science: Part B: Polymer Physics*, 39: 391–403, 2001. 1

S. Trinkle and C. Friedrich. Van gurp-palmen plot: A way to characterize polydispersity of linear polymers. *Rheologica Acta*, 40:322–328, 2001. 107

S. Trinkle, P. Walter, and C. Friedrich. Van gurp-palmen plot II - classification of long chain branched polymers by their topology. *Rheoligica Acta*, 41:103–113, 2002. 56, 107

J. F. Vega, A. Santamaria, A. Muñoz Escalona, and P. Lafuente. Small-amplitude oscillatory shear flow measurements as a tool to detect very low amounts of long chain branching in polyethylenes. *Macromolecules*, 31:3639–3647, 1998. 55, 106

J. F. Vega, M. Fernandez, A. Santamaria, A. Munoz-Escalona, and P. Lafuente. Rheological criteria to characterize metallocene catalyzed polyethylenes. *Macromolecules*, 200:2257–2268, 1999. 55, 106, 107

D. C. Venerus. A critical evaluation of step strain flows of entangled linear polymer liquids. *Journal of Rheology*, 49(1):277–295, 2005. 74, 121

D. C. Venerus and R. Nair. Stress relaxation dynamics of an entangled polystyrene solution following step strain flow. *Journal of Rheology*, 50(1):59–75, 2006. 74, 121

D. C. Venerus, S. H. Zhu, and H. C. Öttinger. Stress and birefringence measurements during the uniaxial elongation of polystyrene melts. *Journal of Rheology*, 43(3):795–813, 1999. 153

W. M. H. Verbeeten, G. W. M. Peters, and F. P. T. Baaijens;. Differential constitutive equations for polymer melts: the extended Pompom model. *Journal of Rheology*, 45(4):823–843, 2001. 40, 150, 167

W. M. H. Verbeeten, G. W. M. Peters, and F. P. T. Baaijens. Viscoelastic analysis of complex polymer melt flows using the extended Pompom model. *Journal of Non-Newtonian Fluid Mechanics*, 108:301–326, 2002. 175, 186

I. Vittorias and M. Wilhelm. Application FT rheology to industrial linear and branched polyethylene blends. *Macromolecular Materials Engineering*, 292: 935–948, 2007. 74, 108, 110

I. Vittorias, M. Parkinson, K. Klimke, B. Debbaut, and M. Wilhelm. Detection and quantification of industrial polyethylene branching topologies via Fourier-transform rheology, NMR and simulation using the Pompom model. *Rheologica Acta*, 46:321–340, 2007. 110

M. H. Wagner and V. H. Rolon-Garrido. Verification of branch point withdrawal in elongational flow of Pompom polystyrene melt. *Journal of Rheology*, 52(5): 1049–1068, SEP-OCT 2008. 208

M. H. Wagner and S. E. Stephenson. The irreversibility assumption of network disentanglement in flowing polymer melts and its effects on elastic recoil predictions. *Journal of Rheology*, 23(4):489–504, 1979. 73, 110

J. L. S. Wales. *The Application of Flow Birefringence to Rheological Studies of Polymer Melts*. PhD thesis, Delft University of Technology, 1976. 42, 149, 151, 171

S. Q. Wang, S. Ravindranath, P. Boukany, M. Olechnowicz, R. P. Quirk, A. Halasa, and J. Mays. Nonquiescent relaxation in entangled polymer liquids after step shear. *Phys Rev Letters*, 97:187801, 2006. 93

P. Wapperom and R. Keunings. Numerical simulation of branched polymer melts in transient complex flow using Pompom models. *Journal of Non-Newtonian Fluid Mechanics*, 97:267–281, 2001. 39

P. Wapperom, A. Leygue, and R. Keunings. Numerical simulation of large amplitude oscillatory shear of a high-density polyethylene melt using the MSF model. *Journal of Non-Newtonian Fluid Mechanics*, 130:63–76, 2005. 111

M. Wilhelm. Fourier-transform rheology. *Macromolecular Materials and Engineering*, 287:83–105, 2002. 109, 126

M. Wilhelm, D. Maring, and H. W. Spiess. Fourier-transform rheology. *Rheologica Acta*, 37:399–405, 1998. 109

M. Wilhelm, P. Reinheimer, and M. Ortseifer. High sensitivity fourier-transform rheology. *Rheologica Acta*, 38:349–356, 1999. 109

M. Wilhelm, P. Rienheimer, M. Ortseifer, T. Neidhöfer, and H. Spiess. The crossover between linear and non-linear mechanical behaviour in polymer solutions as detected by Fourier-transform rheology. *Rheologica Acta*, 29:241–246, 2000. 109

P. M. Wood-Adams and J. M. Dealy. Using rheological data to determine the branching level in metallocene polyethylenes. *Macromolecules*, 33:7481–7488, 2000. xxxiii, 53, 107

P. M. Wood-Adams, J. M. Dealy, A. W. deGroot, and O. D. Redwine. Effect of molecular structure on the linear viscoelastic behavior of polyethylene. *Macromolecules*, 33:7489–7499, 2000. 56, 57, 107

www.mupp2.co.uk. Micro-scale polymer processing (μPP^2) project. Website, 2010. URL www.mupp2.co.uk. 4, 154

W. W. Yau and S. W. Flemming. GCP data interpretation. *Journal of Applied Polymer Science*, 12:2111–2116, 1968. 51

H. Zheng, W. Yu, C. Zhou, and H. Zhang. Three-dimensional simulations of the non-isothermal cast film process of polymer melts. *Journal of Polymer Research*, 13:433–440, 2006. 6

B. H. Zimm. Dynamics of polymer molecules in dilute solution: Viscoelasticity, flow birefringence and dielectric loss. *The Journal of Chemical Physics*, 24(2): 269–278, 1956. 27

B. H. Zimm and W. H. Stockmayer. The dimensions of chain molecules containing branches and rings. *Journal of Chemical Physics*, 17(12):1301–1314, 1949. 51

B. H. Zimm, G. M. Roe, and L. F. Epstein. Solution of a characteristic value problem from the theory of chain molecules. *The Journal of Chemical Physics*, 24(2):279–280, 1956. 27